

# Lawrence Berkeley National Laboratory

## Lawrence Berkeley National Laboratory

### **Title**

X-ray and vibrational spectroscopy of manganese complexes relevant to the oxygen-evolving complex of photosynthesis

### **Permalink**

<https://escholarship.org/uc/item/9k8840ds>

### **Author**

Visser, Hendrik

### **Publication Date**

2001-05-16

X-ray and Vibrational Spectroscopy of Manganese Complexes Relevant to  
the Oxygen Evolving Complex of Photosynthesis

by

Hendrik Visser

M.S. (Agricultural University, The Netherlands) 1994

A dissertation submitted in partial satisfaction of the

requirements for the degree of

Doctor of Philosophy

in

Chemistry

in the

GRADUATE DIVISION

of the

UNIVERSITY OF CALIFORNIA, BERKELEY

Committee in charge:

Professor Kenneth Sauer, Chair

Professor Herbert L. Strauss

Professor Anastasios Melis

Spring 2001

X-ray and Vibrational Spectroscopy of Manganese Complexes Relevant to  
the Oxygen Evolving Complex of Photosynthesis

Copyright © 2001

by

Hendrik Visser

## Abstract

# X-ray and Vibrational Spectroscopy of Manganese Complexes Relevant to the Oxygen Evolving Complex of Photosynthesis

by

Hendrik Visser

Doctor of Philosophy in Chemistry

University of California, Berkeley

Professor Kenneth Sauer, Chair

Manganese model complexes, relevant to the oxygen-evolving complex (OEC) in photosynthesis, were studied with Mn K-edge X-ray absorption near-edge spectroscopy (XANES), Mn K $\beta$  X-ray emission spectroscopy (XES), and vibrational spectroscopy. A more detailed understanding was obtained of the influence of nuclearity, overall structure, oxidation state, and ligand environment of the Mn atoms on the spectra from these methods. This refined understanding is necessary for improving the interpretation of spectra of the OEC.

Mn XANES and K $\beta$  XES were used to study a di- $\mu$ -oxo and a mono- $\mu$ -oxo dinuclear Mn compound in the (III,III), (III,IV), and (IV,IV) oxidation states. XANES spectra show energy shifts of 0.8 - 2.2 eV for 1-electron oxidation-state changes and 0.4 - 1.8 eV for ligand-environment changes. The shifts observed for Mn K $\beta$  XES spectra were  $\sim$ 0.21 eV for oxidation state-changes and only  $\sim$ 0.04 eV for ligand-environment

changes. This indicates that Mn K $\beta$  XES is more sensitive to the oxidation state and less sensitive to the ligand environment of the Mn atoms than XANES. These complimentary methods provide information about the oxidation state and the ligand environment of Mn atoms in model compounds and biological systems.

A versatile spectroelectrochemical apparatus was designed to aid the interpretation of IR spectra of Mn compounds in different oxidation states. The design, based on an attenuated total reflection device, permits the study of a wide spectral range: 16,700 (600 nm) – 2250 cm<sup>-1</sup> and 1900 - 250 cm<sup>-1</sup>. A data collection protocol was introduced to deal with electrochemically non-reversible background signals. IR spectra of an adamantane-like tetra-nuclear Mn compound in two different oxidation states were obtained and analyzed by normal-mode analysis. Bridging Mn–O vibrational modes were identified by isotopic exchange (<sup>16</sup>O→<sup>18</sup>O) in the 750 - 650 cm<sup>-1</sup> and 520 - 460 cm<sup>-1</sup> ranges for the Mn<sup>IV</sup><sub>4</sub> and Mn<sup>III</sup>Mn<sup>IV</sup><sub>3</sub> species. These vibrational modes are in the same spectral range as modes that have been observed for the OEC. Using S<sub>4</sub> symmetry for the Mn<sup>IV</sup><sub>4</sub> species and C<sub>s</sub> symmetry for the Mn<sup>III</sup>Mn<sup>IV</sup><sub>3</sub> species, stretching force constants of 2.45 mdyn/Å, and 3.10 mdyn/Å were extracted for the Mn<sup>III</sup>–O and Mn<sup>IV</sup>–O bridging bonds, respectively.

# Table of Contents

## **Chapter 1: Introduction to the Oxygen-Evolving Complex of Photosystem II**

1.1 Photosynthesis	2
1.2 The oxygen evolving complex	4
1.3 References	22

## **Chapter 2: Mn K-Edge XANES and K $\beta$ XES Studies of Two Mn-oxo Binuclear Complexes. Investigation of Three Different Oxidation States Relevant to the Oxygen-Evolving Complex of Photosystem II**

2.1 Introduction	40
2.2 Experimental	46
2.3 Results	56
2.4 Discussion	73
2.5 Conclusions	79
2.6 Appendix	81
2.7 References	91

## **Chapter 3: An Attenuated Total Reflection Design for *in Situ* FTIR Spectroelectrochemical Studies**

3.1 Introduction	98
3.2 Experimental	99
3.3 Results and Discussion	103
3.4 Conclusion	110
3.5 References	111

**Chapter 4: FTIR spectra and normal-mode analysis of the Mn adamantane-like compound,  $[\text{Mn}^{\text{IV}}_4\text{O}_6(\text{bpea})_4]^{4+}$  and its reduced form,  $[\text{Mn}^{\text{III}}\text{Mn}^{\text{IV}}_3\text{O}_6(\text{bpea})_4]^{3+}$**

4.1 Introduction	114
4.2 Experimental	121
4.3 Results	125
4.4 Normal-mode analysis	135
4.5 Discussion	145
4.6 Appendix - Normal-mode analysis	
4.6.1 Definition of the G & F matrices for the adamantane-like compound	147
4.6.2 Normal-mode analysis for the $T_d$ symmetry	158
4.6.3 Normal-mode analysis for the $S_4$ symmetry	171
4.6.4 Normal-mode analysis for the $C_s$ symmetry	177
4.6.4 The gaussians used to simulate the ( $^{16}\text{O} - ^{18}\text{O}$ ) difference-difference FTIR spectrum	183
4.7 References	185

**Chapter 5: Future Directions**

5.1 X-ray spectroscopy	194
5.2 Vibrational spectroscopy	200
5.3 References	209

# List of Figures

Figure 1.1	A schematic representation of the thylakoid membrane showing all of the components involved in the light reactions.-----	3
Figure 1.2	Schematic of the major polypeptides that assemble PS II, and the cofactors of the electron transfer chain.-----	6
Figure 1.3	The five S-states of the OEC during the oxidation of water, and possible oxidation states of the manganese atoms during the catalytic cycle. —	7
Figure 1.4	Structural motifs which are relevant to the OEC of PS II, and serve as templates for Mn model compounds.-----	11
Figure 2.1	A schematic for the excitation and emission processes involved in XANES and K $\beta$ XES spectroscopy.-----	42
Figure 2.2	The linear mono- $\mu$ -oxo compound, [LMn <sup>III</sup> OMn <sup>III</sup> L] <sup>2+</sup> , with L <sup>-</sup> as the anionic <i>N,N</i> -bis(2-pyridylmethyl)- <i>N'</i> -salicylidene-1,2-diaminoethane ligand. —	44
Figure 2.3	The di- $\mu$ -oxo manganese compound [L' <sub>2</sub> Mn <sup>III</sup> O <sub>2</sub> Mn <sup>IV</sup> L' <sub>2</sub> ] <sup>3+</sup> , with L' as 1,10-phenanthroline.-----	45
Figure 2.4	Scheme of the time course for the oxidation reactions of the di- $\mu$ -oxo compound.-----	48
Figure 2.5	Scheme of the time course for the oxidation reaction of the mono- $\mu$ -oxo compound.-----	50
Figure 2.6	The EPR spectra of the di- $\mu$ -oxo compound at two different stages during the electrochemistry-----	57
Figure 2.7	The EPR spectra of the mono- $\mu$ -oxo compound at three different stages during the electrochemistry-----	59
Figure 2.8	EPR spectrum of 1.0 $\times$ 10 <sup>-3</sup> M Mn <sup>II</sup> in acetonitrile,-----	60
Figure 2.9	The Fourier-transformed Mn EXAFS spectra of the di- $\mu$ -oxo (A) and mono- $\mu$ -oxo (B) compounds in their respective pure oxidation states-----	64
Figure 2.10	The deconvoluted Mn K-edge XANES (A) and second-derivative (B) spectra of the di- $\mu$ -oxo compound in its two oxidation states-----	66



Figure 2.11	The deconvoluted Mn K-edge XANES (A) and second-derivative (B) spectra of the mono- $\mu$ -oxo compound in its three oxidation states	67
Figure 2.12	The deconvoluted Mn K-edge difference spectra for the different oxidation state transitions	68
Figure 2.13	The deconvoluted Mn K $\beta$ XES of the di- $\mu$ -oxo compound (A) and the mono- $\mu$ -oxo compound (B) in their respective oxidation states	70
Figure 2.14	The deconvoluted Mn K $\beta$ XES difference spectra for the different oxidation state transitions	71
Figure 2.15	Measured UV/vis spectra of the mono- $\mu$ -oxo compound samples	82
Figure 2.16	The deconvoluted $k^3$ -space EXAFS spectra of the pure oxidation-states of the di- $\mu$ -oxo compounds and of the mono- $\mu$ -oxo compounds.	83
Figure 2.17	Comparison of the measured and deconvoluted Mn K-edge and 2 <sup>nd</sup> der. XANES spectra for the di- $\mu$ -oxo compound.	85
Figure 2.18	Comparison of the measured and deconvoluted Mn K-edge and 2 <sup>nd</sup> der. XANES spectra for the mono- $\mu$ -oxo compound after the first oxidation step.	86
Figure 2.19	Comparison of the measured and deconvoluted Mn K-edge and 2 <sup>nd</sup> der. XANES spectra for the mono- $\mu$ -oxo compound at the end of the second oxidation step.	87
Figure 2.20	Comparison of the measured and deconvoluted Mn K $\beta$ XES spectra for the di- $\mu$ -oxo compound.	88
Figure 2.21	Comparison of the measured and deconvoluted Mn K $\beta$ XES spectra for the mono- $\mu$ -oxo compound after the first oxidation step.	89
Figure 2.22	Comparison of the measured and deconvoluted Mn K $\beta$ XES spectra for the mono- $\mu$ -oxo compound at the end of the second oxidation step.	90
Figure 3.1.	The electrochemical cell that is designed to fit onto the ASI DuraSamplIR™ ATR accessory	101
Figure 3.2	Cross section of the electrochemical cell and the stainless steel interface plate of the ATR accessory	102

Figure 3.3	FTIR absorption spectrum of 5 mM ferrocene, 0.1 M TBA(PF <sub>6</sub> ) in acetonitrile solution before electrochemistry	103
Figure 3.4	FTIR difference spectra at different times during the oxidation of a 5 mM ferrocene, 0.1 M TBA(PF <sub>6</sub> ) in acetonitrile solution.	105
Figure 3.5	FTIR difference spectra of ferricinium/ferrocene, of a 5 mM ferrocene, 0.1 M TBA(PF <sub>6</sub> ) acetonitrile solution for 4000 - 2300 cm <sup>-1</sup> range.	107
Figure 3.6	FTIR difference spectra of ferricinium/ferrocene, of a 5 mM ferrocene, 0.1 M TBA(PF <sub>6</sub> ) acetonitrile solution for the 1800 - 900 cm <sup>-1</sup> range.	108
Figure 3.7	FTIR difference spectra of ferricinium/ferrocene, of a 5 mM ferrocene, 0.1 M TBA(PF <sub>6</sub> ) acetonitrile solution for the 900 - 400 cm <sup>-1</sup> range.	109
Figure 4.1	The adamantane-like manganese compound [Mn <sup>IV</sup> <sub>4</sub> O <sub>6</sub> (bpea) <sub>4</sub> ] <sup>4+</sup> , where the ligand bpea is <i>N,N</i> -bis(2-pyridylmethyl)ethylamine.	120
Figure 4.2	The FTIR absorption and difference spectra of the solid [Mn <sup>IV</sup> <sub>4</sub> <sup>16</sup> O <sub>6</sub> (bpea) <sub>4</sub> ] <sup>4+</sup> and [Mn <sup>IV</sup> <sub>4</sub> <sup>18</sup> O <sub>6</sub> (bpea) <sub>4</sub> ] <sup>4+</sup> compounds in KBr pellets.	127
Figure 4.3	Simulation of the ( <sup>16</sup> O – <sup>18</sup> O) FTIR difference signal around 700 cm <sup>-1</sup> of the [Mn <sup>IV</sup> <sub>4</sub> O <sub>6</sub> (bpea) <sub>4</sub> ] <sup>4+</sup> compound	128
Figure 4.4	The FTIR (oxidized – reduced) difference spectra obtained with a 2.8 mM [Mn <sup>IV</sup> <sub>4</sub> <sup>16</sup> O <sub>6</sub> (bpea) <sub>4</sub> ] <sup>4+</sup> , 0.1 M TBA(PF <sub>6</sub> ) acetonitrile solution.	131
Figure 4.5	The FTIR (oxidized – reduced) difference spectra, obtained with a 2.5 mM [Mn <sup>IV</sup> <sub>4</sub> <sup>18</sup> O <sub>6</sub> (bpea) <sub>4</sub> ] <sup>4+</sup> , 0.1 M TBA(PF <sub>6</sub> ) acetonitrile solution.	132
Figure 4.6	The FTIR (oxidized – reduced) difference spectra of the <sup>16</sup> O and <sup>18</sup> O species, and the ( <sup>16</sup> O – <sup>18</sup> O) difference-difference spectrum.	133
Figure 4.7	The relation between the symmetry representations of the different overall symmetries of the Mn compound, which were used for the analysis of the two oxidation states.	136
Figure 4.8	A comparison of the observed <sup>16</sup> O and <sup>18</sup> O (oxidized-reduced) difference spectra and the ( <sup>16</sup> O – <sup>18</sup> O) difference-difference spectrum with the simulated spectra.	144
Figure 4.9	The Mn–O core of the adamantane-like compound.	148

Figure 4.10	The internal displacement vectors for the two internal coordinates, i.e. bonds and valence angles.	152
Figure 4.11	Some of the symmetry operations of the adamantane-like compound for $T_d$ symmetry.	158
Figure 5.1	Energy diagram of the Mn (M) and ligand (L) orbitals involved in the Mn K-edge XANES.	196
Figure 5.2	The mono- $\mu$ -oxo (A) and di- $\mu$ -oxo (B) compounds and the ligands that can be used to study the effect of aromaticity of the terminal ligand environment on the Mn K-edge XANES spectra.	197
Figure 5.3	The electronic energy diagram of the transitions that occur in Mn K-edge, L-edge and RIXS spectroscopy.	199
Figure 5.4	Mn complexes of interest to study the influence of replacement of one $\text{OH}^-$ or $\text{H}_2\text{O}$ by a halide.	204
Figure 5.5	The reduction of a dimer-of-dimer compound, and the conversion into an adamantane-like compound, either by chemical reaction or oxidation.	205
Figure 5.6	A biomimetic system of PS II.	208

## List of Tables

Table 1.1	Mn mono-nuclear compounds with non-bridging $O^{2-}$ , $OH^-$ , or (one or two) $OH_2$ ligated to Mn. _____	12
Tabel 1.2	Mn di-nuclear compounds with the mono- $\mu$ -oxo moiety. _____	13
Table 1.3	Mn di-nuclear compounds with the di- $\mu$ -oxo moiety. _____	14
Table 1.4	Mn tri-nuclear compounds. _____	15
Table 1.5	Mn tetra-nuclear compounds, which contain the ‘adamantane-like’, ‘dimer-of-dimer’, or ‘linear’ motif. _____	16
Table 1.6	Mn tetra-nuclear compounds with the ‘cubane’ motif. _____	17
Table 1.7	Mn tetra-nuclear compounds with the ‘butterfly’ motif. _____	18
Table 2.1	The $Mn^{III}Mn^{IV}$ and $Mn^{II}$ fractions calculated from EPR spectra of the di- $\mu$ -oxo and mono- $\mu$ -oxo sample solutions _____	62
Table 2.2	The fractions of the manganese components used to deconvolute the measured EXAFS, XANES, and $K\beta$ XES spectra _____	62
Table 2.3	A summary of the first inflection-point energy ( $1^{st}$ IPE) values of the pre-edge, and main Mn K-edge of the second-derivative XANES spectra of the mono- $\mu$ -oxo and di- $\mu$ -oxo compounds in their pure oxidation states, as well as a synopsis of the $1^{st}$ moments of the $K\beta_{1,3}$ peaks _____	72
Table 4.1	Vibrational frequency regions of IR- or Raman-active Mn–ligand modes. _____	117
Table 4.2	Published Mn–O, and Mn–halide force constants. _____	118
Table 4.3	The IR frequencies of the Mn–O modes and shifts in the modes observed in the spectra of the solid $[Mn^{IV}_4^{16}O_6(bpea)_4]^{4+}$ and $[Mn^{IV}_4^{18}O_6(bpea)_4]^{4+}$ compounds _____	126
Table 4.4	The bridging Mn–O mode IR frequencies which shift upon oxidation and isotopic exchange of the oxygens. _____	134
Table 4.5	Comparison of the observed and the calculated frequencies for the $[Mn^{IV}_4O_6(bpea)_4]^{4+}$ compound. _____	138

Table 4.6	Comparison of the observed and calculated frequencies for the $[\text{Mn}^{\text{IV}}_4\text{O}_6(\text{bpea})_4]^{4+}$ compound.	140
Table 4.7	Comparison of the observed and the calculated frequencies for the $[\text{Mn}^{\text{III}}\text{Mn}^{\text{IV}}_3\text{O}_6(\text{bpea})_4]^{3+}$ compound.	143
Table 4.8	The definition of the internal coordinates used for the normal-mode analysis of the Mn–O core of the adamantane-like compound.	149
Table 4.9	The vectorial stretching sub-matrix, $A(r)$ , of the S-matrix.	153
Table 4.10	The vectorial angular sub-matrix, $B(\alpha)$ , of the S-matrix.	154
Table 4.11	The conversion of all the bending displacement vectors into expressions of stretching vectors.	156
Table 4.12	Conversion of the inner product of the stretch displacement vectors of two connected bonds.	156
Table 4.13	Conversion of the inner product of the stretch displacement vectors of two bonds separated by one bond.	157
Table 4.14	Conversion of the inner product of the stretch displacement vectors of two bonds separated by two bonds.	157
Table 4.15	Definition of the symmetry operations for the adamantane-like compound in $T_d$ symmetry.	159
Table 4.16	The result of the $T_d$ symmetry operations working on the internal coordinates of the Mn model compound.	161
Table 4.17	The result of the of the improper rotation operations working on the internal coordinates of the Mn model compound.	162
Table 4.18	The orthogonalized symmetry bond displacement coordinates of the adamantane-like compound for the various symmetry representations, assuming the $T_d$ symmetry.	164
Table 4.19	The orthogonalized symmetry angle displacement coordinates of the adamantane-like compound for the various symmetry representations, assuming the $T_d$ symmetry.	165

Table 4.20	The calculated structural parameters of the adamantane-like compound for the $T_d$ symmetry.	169
Table 4.21	Comparison of the observed and calculated frequencies for the $Mn^{IV}_4$ adamantane-like compound, assuming $T_d$ symmetry.	170
Table 4.22	The result of the $S_4$ symmetry operations working on the internal coordinates of the Mn model compound.	172
Table 4.23	The orthogonalized symmetry bond displacement coordinates of the adamantane-like compound for the various symmetry representations, assuming the $S_4$ symmetry.	173
Table 4.24	The orthogonalized symmetry angle displacement coordinates of the adamantane-like compound for the various symmetry representations, assuming $S_4$ symmetry.	174
Table 4.25	The calculated structural parameters of the adamantane-like compound for the $S_4$ symmetry.	176
Table 4.26	The result of the $C_s$ symmetry operations working on the internal coordinate of the Mn model compound.	178
Table 4.27	The orthogonalized symmetry bond displacement coordinates of the adamantane-like compound for the various symmetry representations, assuming $C_s$ symmetry.	179
Table 4.28	The orthogonalized symmetry angle displacement coordinates of the adamantane-like compound for the various symmetry representations, assuming $C_s$ symmetry.	180
Table 4.29	The calculated structural parameters of the adamantane-like compound in $C_s$ symmetry.	182
Table 4.30	The position, width at half peak height and amplitude of the gaussian curves used to simulate the difference-difference spectrum in the 620 - 720 $cm^{-1}$ range.	183
Table 4.31	The position, width at half peak height and amplitude of the gaussian used to simulate the difference-difference spectrum in the 420 - 520 $cm^{-1}$ range.	184

## List of Abbreviations

ADP = adenosine diphosphate

ATP = adenosine triphosphate

ATR = Attenuated Total Reflection

bpea = *N,N*-bis(2-pyridylmethyl)ethylamine

bipy = 2,2'-bipyridine

cyclam = 1,4,8,11-tetraazacyclotetradecane

cyclen = 1,4,7,10-tetraazacyclododecane

di- $\mu$ -oxo compound =  $[L'_2Mn^{III}O_2Mn^{IV}L'_2](ClO_4)_3$

EPR = Electron Paramagnetic Resonance

EXAFS = Extended X-ray Absorption Fine Structure

FTIR = Fourier Transformed Infrared

HB(pz)<sub>3</sub> = hydrotris(1-pyrazolyl)borate

IPE = Inflection-Point Energy

IR = Infraed

L = *N,N*-bis(2-pyridylmethyl)-*N'*-salicylidene -1,2-diaminoethane

L' = 1,10-phenanthroline

MCT = Mercury Cadmium Telluride

MeCN = acetonitrile

mono- $\mu$ -oxo compound =  $[LMn^{III}OMn^{III}L](ClO_4)_2$

NADPH = nicotinamide adenine dinucleotide phosphate

OEC = Oxygen Evolving Complex

ox. = oxidation

phen = 1,10-phenantroline

Pheo = pheophytin

PS I = Photosystem I

PS II = Photosystem II

Q = quinone

Q<sub>A</sub> = quinone A

Q<sub>B</sub> = quinone B

QH<sub>2</sub> = hydroquinone

red. = reduction

SCE = Saturated Calomel Electrode

SERDS = Shifted-Excitation Raman Difference Spectroscopy

tacn = 1,4,7-triazacyclononane

TBA = Tertbutylammonium

TMP = tetramethylporphyrin

TMPyp = tetrakis(methylpyridinium)porphyrin

TPP = tetraphenylporphyrin

XANES = X-ray Absorption Near-Edge Spectroscopy

XAS = X-ray Absorption Spectroscopy

XES = X-ray Emission Spectroscopy



# Acknowledgments

A few years ago the old African saying ‘It takes a village to raise a child’ was made popular by Hillary Rodham-Clinton, who used it as the title for one of her books. Around that time her husband, Bill Clinton, was running for a second term as President of the USA. Bob Dole, the opposing candidate, felt the need to speak out against the title of this book during the Republican convention, by declaring that ‘it does not take a village, but a family to raise a child’. Sadly enough, he was missing the point that a village is a family of families, and that nobody is raised by just the 'nuclear' family. I would like to contend that not only a child, but also a Ph.D. is ‘raised’ by a village. Therefore, I would like to take the opportunity here to thank the various families of the village who have supported me during this long process of being able to put Dr. in front of my name.

First and foremost I would like to thank the family where it all started: my parents, brother, sister, the in-laws, and the sweetest and cutest nieces and nephews an uncle can ask for. Thanks for being there during this long journey. It all started about 28 years ago with me kicking and screaming, not wanting to go to kindergarten, because I knew this schooling stuff was going to last a while. It has not always been easy the last few years with the 6,000 miles between us, but thank you for the support from a distance.

I also would like to thank all the elementary and high-school teachers I had. Specifically, I would like to thank four high-school teachers of the DaCosta MAVO, Mr. Crezée, Mr. Warringa, Mr. van der Steen, and Mr. van Genderen, who taught me the basics of biology, chemistry, physics and mathematics, respectively. As you will notice while reading this dissertation all of these four disciplines are still there. I guess, I could blame the four of them for doing too good of a job so I never was able to make a clear-cut

choice between these four scientific disciplines...

After high school I went to the Agricultural University in Wageningen, where especially two people, Dane Bicanic and Nicu Dărdălat, got me excited about playing around with equipment and trying to come up with different kinds of contraptions to measure physical parameters. This excitement came in handy during my exchange period here at UC, Berkeley with the Klein/Sauer/Yachandra group, which ultimately resulted in my return to do my Ph.D. with this group.

And so it is time to thank the academic family I have spent the last umphhh... years with. Many thanks to my supervisor Ken Sauer, who had to read through all the Dutchisms in all of my writings (including this dissertation) and come up with novel ways of translating it into readable standard American English. I also would like to thank Mel Klein, who sadly enough is not with us anymore. Lastly, but definitely not the least, I would like to thank Vittal Yachandra, who has been a great help, and for all the on going discussions on science, world politics, and the application of Indian sayings to modern life.

The research I describe in this dissertation would not have been possible without the collaborators I had the luck to work with. Thanks to Elodie Anxolabéhère-Mallart things really started to roll, especially for Chapter 2, which was a project we did together. I also would like to thank the people who introduced and helped us to perform the Mn K $\beta$  X-ray emission spectroscopy, i.e. Uwe Bergmann, Pieter Glatzel and Steve Cramer. Chapter 3 would not have happened without Aimee Curtright bugging me and asking whether I knew any smart way of taking IR spectra of inorganic compounds in different oxidation states. When she asked I did not know any smart ways, but together I think we

came up with a pretty darn cool device, which hopefully will provide us with royalties leading to early retirement.. ;-) Chapter 4 would not have happened without the kind provision of the adamantane-like compounds by Bill Armstrong and Chris Dubé. Thanks to Heinz Frei, for the use of his IR instrumentation, and to Herbert Strauss for the discussions on performing normal-mode analysis.

Thanks also to the present and former members of the Klein/Sauer/Yachandra group Roehl, John, Emanuele, Joy, Olaf, Martin, Matthew, Wen, Johannes, Theo, Annette, Jana, and Mary. Three lab-mates especially had to endure my whining and griping about research, writing a dissertation, and all other stuff grad-students complain about. Thanks, Shelly, Karen, and Carmen for all the coffee breaks you were 'willing' to take....

A man does not live by bread alone; neither does a grad-student by a lab environment. So now it is time to thank the various 'families' outside of the lab. Especially, thanks to my former housemates Steve and Corey. It was quite an experience to live with you guys, as I am sure it also was for you. Beside these two I would like to thank a group which slowly has turned into a new-years-eve celebrations crew: Dan, Steve, Cathy, Krista, Ken, Dave (2x), Andrea, Matthew, Leslie, Emy, Bill, Christo, Nandeeni, Krista, Randy, Raymond. Hopefully, we will be able to continue to have that yearly reunion...

Then there is a whole bunch of people I have had the pleasure to meet and spend many conversations, (coffee) meetings, dinners, etc. with, enabling me to talk about something else than just academics. It was great to be in the 'real' world every now and then. Thank you Alice, Aldo, Tom, CT, Peggy, Alyosha, Patty, Cindy, Deborah, Randy, Jan, Stephanie, Robert, Karen, Beverly, Kathleen, Mary, John, Jing-Tong, Jessica, and Max.

Lastly, I would like to thank the friends that stayed friends even though there was such a distance between us. It is not always easy to keep contact when you are that far away, but somehow we were able to keep in contact. Thanks Peter, Jurgen, Ivon, Mark, Lieve, Coen, Jeroen, Gerda, and Maarten... You, the reader, might start wondering whether I will start thanking the people I met daily on the street or in the coffee shops. However, I refrain from doing so, and leave you to reading the rest of this dissertation.

Henk



To my grandparents

Hendrik van Leeuwen

Arie Visser

Hendrika Florida Looijen

Bastiaantje Visser



# **Chapter 1**

## **Introduction to the Oxygen-Evolving Complex of Photosystem II**

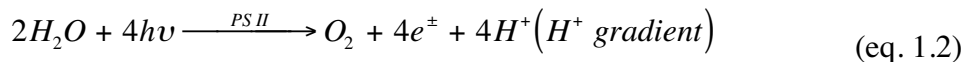


## 1.1 Photosynthesis

One of the most important processes for life on earth is photosynthesis. The conversion of light energy into chemical energy occurs in autotrophic bacteria and plants. These organisms produce the general chemical energy supply for all other organisms incapable of photosynthesis.<sup>1</sup> The mechanism of photosynthesis involves a complex interplay between many proteins and small molecules, and can be described (for green plants, algae and cyanobacteria) with the general equation 1.1:



In green plants this process is separated into different sub-processes and accomplished in chloroplasts. These organelles contain intricate membrane structures called thylakoids, where two light reactions are executed by two membrane-bound protein clusters, photosystem I (PS I) and photosystem II (PS II).<sup>2</sup> Electrons are extracted from the unlikely electron donor, H<sub>2</sub>O, by PS II and transferred to a quinone pool (Figure 1.1), which is used to establish a H<sup>+</sup>-gradient (eq. 1.2).<sup>3</sup> Water has the relatively high reduction potential of 0.815 V; therefore, PS II has to absorb several photons before water can be oxidized (see section 1.2 for a more detailed discussion).



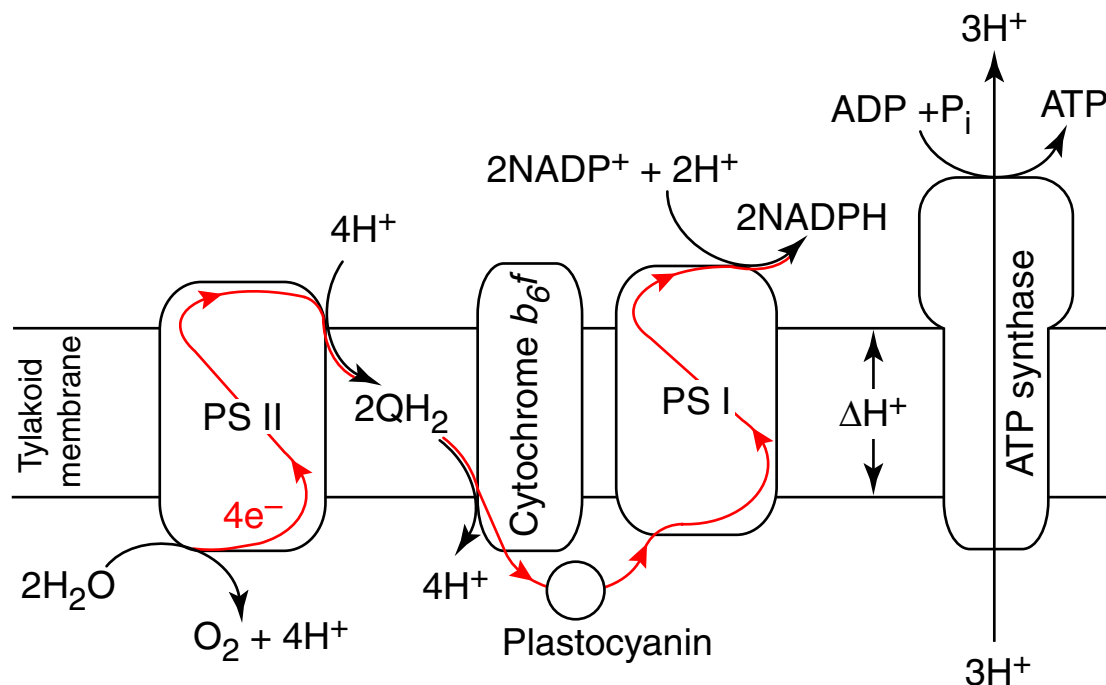


*Figure 1.1 A schematic representation of the thylakoid membrane showing all of the components involved in the light reactions. Upon absorption of photons PS II extracts electrons (indicated by red) from water and transfers these to a quinone pool (Q). The electrons are extracted from  $QH_2$  by the cytochrome  $b_6f$  complex and transferred by way of plastocyanin to PS I. Upon absorption of photons PS I transfers these electrons to  $NADP^+$ , forming the reducing agent NADPH. Both light reactions are involved in electron transfer and in the generation of a  $H^+$ -gradient. This  $H^+$ -gradient is used by ATP synthase to generate ATP, a molecule that is used as a free energy source in many biochemical reactions.*

Photosystem I receives the electrons from PS II by way of the quinone pool, the cytochrome  $b_6f$  complex, and plastocyanin (Figure 1.1).<sup>4-6</sup> Upon absorption of photons by PS I these electrons are transferred to NADPH (nicotinamide adenine dinucleotide phosphate)<sup>7</sup>, a reducing agent, via a series of ferredoxins (eq. 1.3).

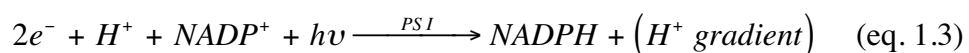
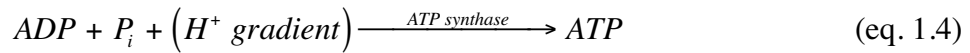
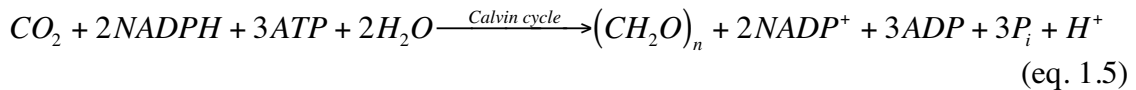


Figure 1.1 shows that Photosystems I and II, and cytochrome *b<sub>6</sub>f* are involved not only in the transfer of electrons from water to NADPH, but also in the generation of a H<sup>+</sup>-gradient. This H<sup>+</sup>-gradient is used by ATP synthase to generate ATP (adenosine triphosphate), which is a molecule that is used as a free energy source to drive unfavorable reactions in cells (eq. 1.4).<sup>8,9</sup>



The reducing agent NADPH and free energy source ATP are used in the dark reactions of the Calvin cycle to fix carbon dioxide into carbohydrates (eq. 1.5).<sup>10-12</sup> This cycle generates the biomass which ultimately is the general chemical energy supply for all other organisms incapable of photosynthesis.



## 1.2 The oxygen-evolving complex

Photosystem II is a large (300 - 400 kDa) membrane-bound complex, which contains multiple polypeptides.<sup>3</sup> The major polypeptide components of PS II are given in Figure 1.2. The process of oxidation of water and reduction of quinone B (Q<sub>B</sub>) starts with the excitation of a light-harvesting pigment-protein antenna complex located peripherally to PS II. The energy is transferred to P<sub>680</sub>, which contains two chlorophyll-*a* molecules that absorb at 680 nm. A charge separation occurs upon the excitation of P<sub>680</sub>, and an electron is transferred from P<sub>680</sub> to pheophytin (Pheo), to quinone A (Q<sub>A</sub>) and to quinone B (Q<sub>B</sub>) consecutively. Upon reception of two electrons and two protons (from the stroma

side) the resulting hydroquinone ( $Q_BH_2$ ) leaves its binding site. The vacant quinone site is filled with an oxidized  $Q_B$  from the membrane-associated quinone pool (see also Figure 1.1). The oxidized  $P_{680}^+$  is reduced by the nearby redox-active tyrosine residue ( $Y_z$ ). The tyrosine residue itself is reduced by the oxygen-evolving complex (OEC), which ultimately obtains the electrons from water.

Although great progress has been made in obtaining a high-resolution crystal structure of PS II,<sup>13</sup> most of our knowledge about the OEC has been obtained from X-ray absorption<sup>14-17</sup> and EPR spectroscopy.<sup>18-21</sup> These techniques have been used to investigate both the structure of the OEC and the mechanism of water oxidation.<sup>22-27</sup> The consensus is that the OEC contains four manganese atoms, consisting of two to three di- $\mu$ -oxo Mn-Mn moieties (Mn-Mn distance  $\approx 2.7$  Å) and one mono- $\mu$ -oxo Mn-Mn moiety (Mn-Mn distance  $\approx 3.3$  Å). In addition, two co-factors,  $Ca^{2+}$  and  $Cl^-$ , are required for water oxidation. Glutamate and aspartate provide most of the terminal ligands to the OEC, while one or two histidines are also directly ligated to manganese atoms.<sup>3,28,29</sup>

Kok et al.<sup>30</sup> proposed that water is oxidized in five stages, called S-states ( $S_0 - S_4$ ), with the index indicating the number of stored oxidizing equivalents. An electron is extracted during each of the four light-induced transitions,  $S_0 \rightarrow S_1$ ,  $S_1 \rightarrow S_2$ ,  $S_2 \rightarrow S_3$ , and  $S_3 \rightarrow [S_4] \rightarrow S_0$ . Dioxygen is released during the last transition, when the  $S_3$  state returns to the  $S_0$  state via the hypothesized  $S_4$  state, see also Figure 1.3. (For a good review of the OEC see Ref. 31)

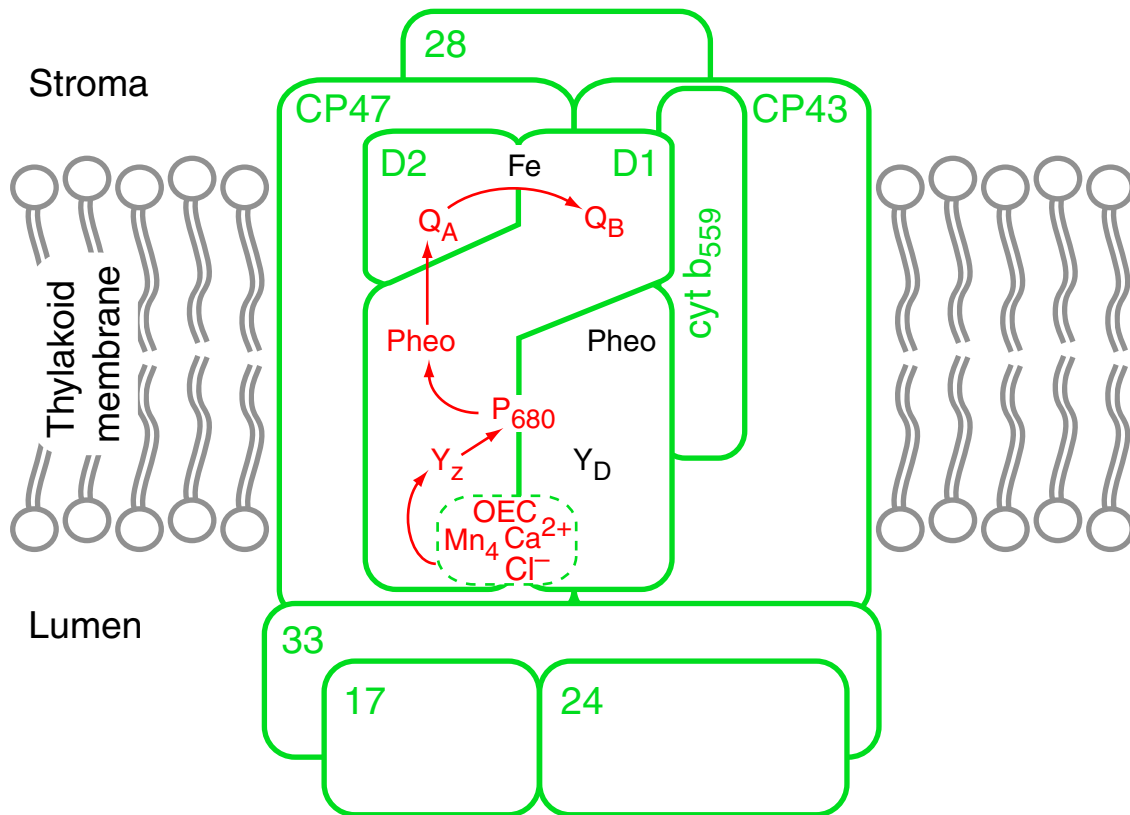


*Figure 1.2 Schematic of the major polypeptides that assemble PS II, and the cofactors of the electron transfer chain (adapted from Debus<sup>3</sup>). The 28 kDa and the two chlorophyll-containing polypeptides, CP47 and CP43, are involved in light harvesting and transfer of the energy to the reaction center  $P_{680}$ . The D1 and D2 polypeptides contain the cofactors which constitute the electron transfer chain. The cofactors are: the oxygen-evolving complex (containing  $Ca^{2+}$ ,  $Cl^-$ , and four manganese atoms), the tyrosine residue  $Y_z$ , the reaction center  $P_{680}$ , pheophytin (Pheo), and quinones A and B ( $Q_A$  &  $Q_B$ ). The red arrows indicate the direction of electron transfer between the cofactors. On the lumen side there are three external polypeptides of 33, 24 and 17 kDa, which stabilize the OEC.*

To understand the mechanism of water oxidation in more detail, it is important to know at each stage whether the extracted electrons are coming directly from bound water, from the Mn atoms, or from any other parts of the OEC. Both EPR and Mn K-edge X-

ray absorption near-edge structure (XANES)<sup>32-34</sup> have been used extensively to investigate the involvement of the Mn atoms in water oxidation. Based on the results of these techniques there is consensus that Mn is oxidized during the  $S_0 \rightarrow S_1$  and  $S_1 \rightarrow S_2$  transitions (Figure 1.3). However, there is still controversy concerning the involvement of Mn oxidation in the  $S_2 \rightarrow S_3$  transition. Roelofs et al.<sup>35</sup> concluded that there is no Mn oxidation in the  $S_2 \rightarrow S_3$  transition, based on the absence of a significant shift in the XANES spectra between  $S_2$  and  $S_3$ , and proposed that a ligand is oxidized. However, Ono et al.<sup>36</sup> and Iuzzolino et al.<sup>37</sup> concluded, based on observed shifts in their XANES data, that Mn oxidation is involved in this transition.

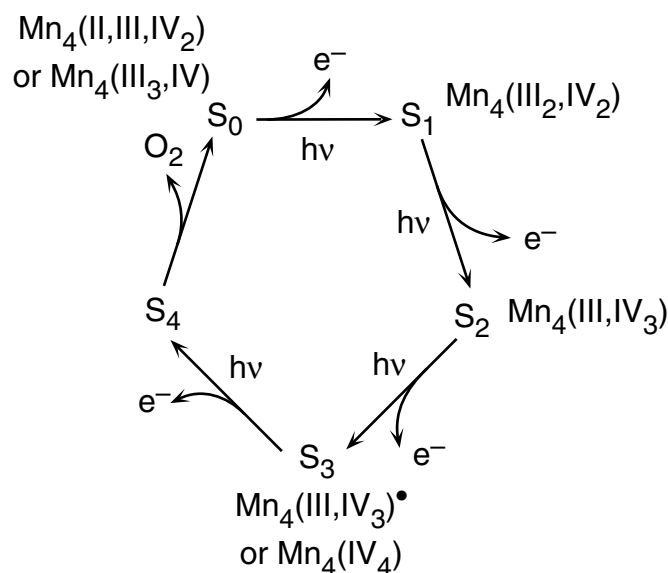


Figure 1.3 The five S-states of the OEC during the oxidation of water<sup>30</sup>, and possible oxidation states of the manganese atoms during the catalytic cycle. The state transitions from  $S_1$  to  $S_4$  are induced by excitation of  $P_{680}$  and accompanied by the release of an electron to  $Y_z^+$ . Dioxygen is released when the  $S_4$  state relaxes spontaneously to the  $S_0$  state.

Recently, Messinger et al.<sup>27</sup> performed a modified version of the experiment done by Roelofs et al.,<sup>35</sup> using XANES<sup>32-34</sup> and an additional technique, Mn K $\beta$  X-ray emission spectroscopy (K $\beta$  XES).<sup>38,39</sup> Like XANES, K $\beta$  XES is element-specific, but in comparison to XANES it has the advantage that it is more sensitive to the oxidation state and less sensitive to the ligand environment of the manganese atoms. On the basis of the results from both these techniques, it was concluded that the S<sub>2</sub>→S<sub>3</sub> transition is not Mn centered.<sup>27</sup> Nevertheless, some supporters of manganese oxidation in the S<sub>2</sub>→S<sub>3</sub> transition argue that two opposing effects, the oxidation of Mn and a structural change, cause the lack of a shift in XANES and K $\beta$  XES data. It is known that a structural change occurs in the OEC during the S<sub>2</sub>→S<sub>3</sub> transition,<sup>15</sup> which could offset the effects due to manganese oxidation. To resolve this issue, the influence of oxidation-state and structural changes on XANES and K $\beta$  XES spectra need to be studied with manganese model compounds, where the ligand environment and oxidation state can be controlled.

These Mn compounds need to have similar structural motifs that are part of the OEC. Figure 1.4 gives an overview of all the structural motifs, which either contain a Mn–Mn distance of 2.7 Å or 3.0 Å, or have terminal ligands that could be part of the OEC during its catalytic cycle. As mentioned earlier, the OEC contains two or three moieties with a 2.7 - 2.9 Å Mn–Mn distances depending on the S-state, which most likely are di- $\mu$ -oxo moieties. The oxygens of the di- $\mu$ -oxo moieties might be protonated early in the catalytic cycle. The Mn cluster also includes at least one Mn–Mn distance of about 3.3 Å, which could be an individual Mn–Mn and/or Mn–Ca mono- $\mu_2$ -oxo moiety or a mono- $\mu_3$ -oxo moiety. The majority of the terminal ligands for the Mn cluster are

carboxylate ligands, which can provide bridging between two Mn atoms or can bind to Mn in a monodentate or bidentate manner. It is also known that there are at least one or two histidine ligands.<sup>3,28,29</sup> Consequently, Mn model complexes are desired with a mixture of aromatic N ligands and carboxylate ligands to be relevant to the OEC. There is also some evidence that the co-factor  $\text{Cl}^-$  is directly ligated to one of the Mn atoms of the OEC in the  $\text{S}_3$  state,<sup>40,41</sup> and possibly in other states. During the water oxidative cycle, at least one water molecule is bound and oxidized, possibly as a terminal ligand. Therefore, Mn compounds with terminal  $\text{Cl}^-$ ,  $\text{H}_2\text{O}$ ,  $\text{HO}^-$ ,  $\text{O}^{2-}$  ligands are of interest. Additionally, Figure 1.3 shows the oxidation states of the Mn atoms in the OEC during the catalytic cycle;  $\text{Mn}^{\text{II}}$ ,  $\text{Mn}^{\text{III}}$ , or  $\text{Mn}^{\text{IV}}$ . Therefore, model compounds of the most interest contain one or more of the structural moieties in Figure 1.4 and have oxidation states that are  $\text{Mn}^{\text{II}}$ ,  $\text{Mn}^{\text{III}}$ ,  $\text{Mn}^{\text{IV}}$ , or even  $\text{Mn}^{\text{V}}$ , which has been proposed to be present in the  $\text{S}_3$  and  $\text{S}_4$  states.

A survey of the literature for Mn compounds relevant to the structure and function of the OEC is presented in Tables 1.1 through 1.7. The references in Tables 1.1 through 1.7 indicate the articles where the synthesis and structural information are provided of the Mn complexes. Compounds where the Mn atoms are connected only by alkoxide bridges ( $\text{OR}^-$ ) have been excluded from this collection, because they are less relevant to the OEC. Table 1.1 shows a list of Mn mono-nuclear compounds which contain either  $\text{O}^{2-}$ ,  $\text{OH}^-$ , or (one or two)  $\text{H}_2\text{O}$ . These mono-nuclear compounds can have 5-, 6-, or 7-coordinated Mn atoms, while the majority of the multi-nuclear compounds are 6-coordinate. Table 1.2 and 1.3 show a collection of Mn mono- $\mu$ -oxo and di- $\mu$ -oxo compounds, respectively. The majority of these compounds have a mixture of O-Mn and N-Mn ligands. Only in



two cases, are all the terminal ligands provided by oxygen. In addition, the ligating nitrogens can be separated into two types: nitrogens that are part of an aromatic system, and nitrogens that are non-aromatic. No amide residues have been identified yet as ligands to the OEC. Therefore, it would be desirable to have more mono- $\mu$ -oxo and di- $\mu$ -oxo compounds with either all oxygen ligands, or with a mixture of oxygen ligands and a few aromatic nitrogen ligands.

Table 1.4 shows a set of Mn tri-nuclear compounds, which can be used to study parts of possible intermediates during the catalytic cycle of the OEC. These tri-nuclear motifs are also part of the structures of the Mn tetra-nuclear compounds in Tables 1.5, 1.6, and 1.7. The tetra-nuclear compounds are separated into several classes. The ‘adamantane-like’, the ‘dimer-of-dimers’, and ‘linear’ Mn tetra-nuclear compounds are presented in Table 1.5. The ‘cubane’ compounds are given in Table 1.6, and the ‘butterfly’ compounds are shown in Table 1.7. The ligation of the ‘linear’, the ‘cubane’ and the ‘butterfly’ compounds consist mostly of oxygens and aromatic nitrogens, which is desirable because of their relevance to the OEC.

Many of the Mn compounds are relatively stable, and stay intact during electrochemistry. Therefore, a variety of oxidation states can be studied using the same compound. No compounds are available containing Mn and Ca, which are bridged by mono- $\mu$ -oxo or carboxylate bridges.

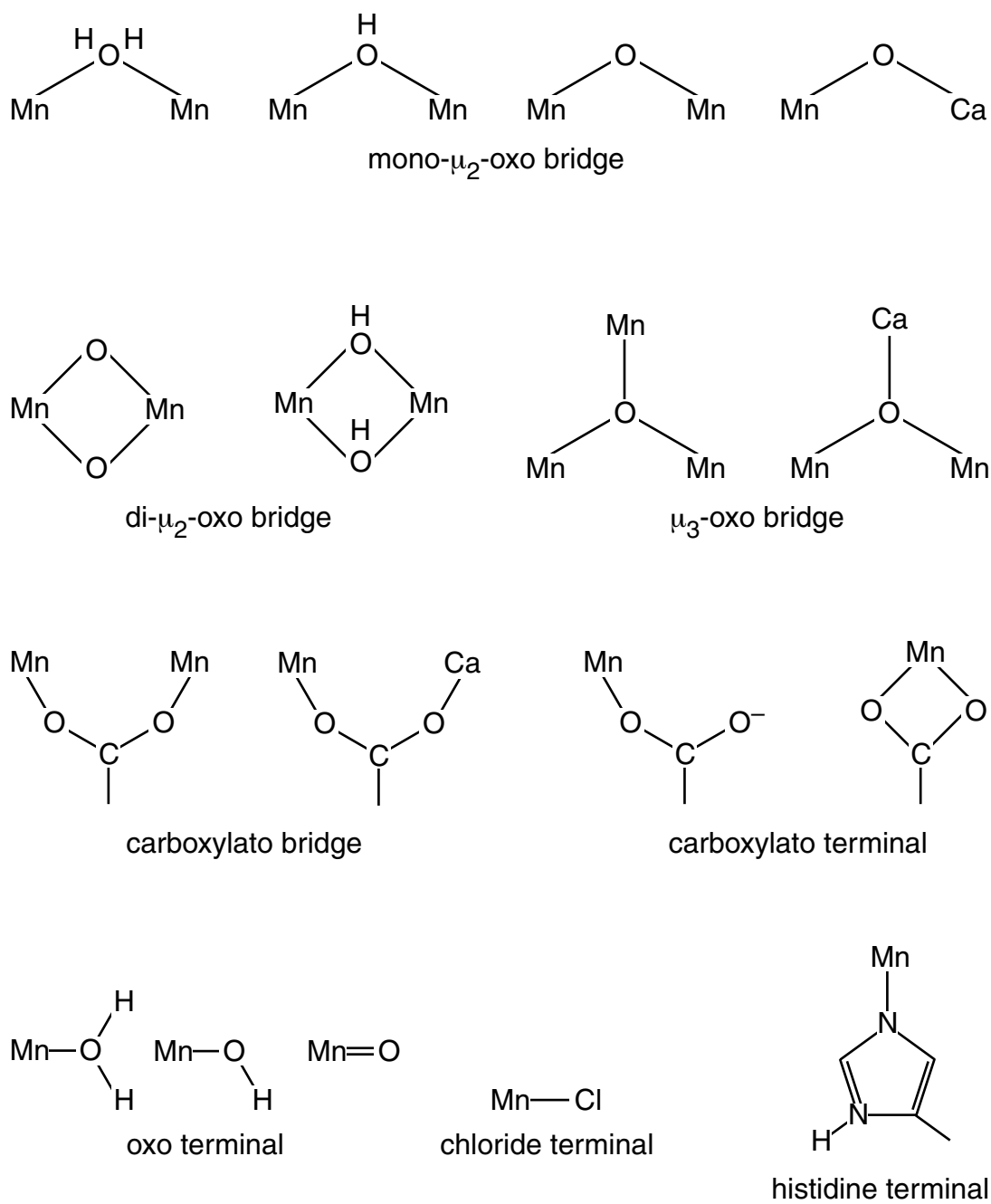


Figure 1.4 Structural motifs which are relevant to the OEC of PS II, and serve as templates for Mn model compounds.

Table 1.1 Mn mono-nuclear compounds with non-bridging  $O^{2-}$ ,  $OH^-$ , or (one or two)  $OH_2$  ligated to Mn. Four types of terminal ligands are distinguished:  $O^C$  = oxygen from carboxylate group,  $N^A$  = aromatic nitrogen,  $N^N$  = non-aromatic nitrogen, and X = either a terminal oxygen or halide.

structural unit	specifics	Mn ox. state(s)	ligand character				ref.
			$O^C$	$N^A$	$N^N$	X	
Mn=O	6-coordinate	(IV)		4		2	42
Mn≡O	5-coordinate	(V)			2	3	43
					4	1	44
HO-Mn=O	6-coordinate	(IV)		4		2	42
Mn-OH	6-coordinate	(III)			3	3	45
Mn-OH <sub>2</sub>	5-coordinate	(II)		2	2	1	46
		(III)		4		1	47-49
	6-coordinate	(III)			4	1	50
		(III)	2		3	1	51
7-coordinate	(III)	2	4		1	52	
Cl-Mn-OH <sub>2</sub>	7-coordinate	(II)		1	2	4	53
$\angle \approx 180^\circ$	6-coordinate	(III)			2	4	54
Mn-[OH <sub>2</sub> ] <sub>2</sub> $\angle \approx 180^\circ$	7-coordinate	(II)		1	2	4	55
	6-coordinate			4		2	52,56
	6-coordinate	(III)				6	57
			1	2		3	58
				4		2	48,59,60
			4			2	61
				2	4	62	
Mn-[OH <sub>2</sub> ] <sub>2</sub> $\angle \approx 90^\circ$	6-coordinate	(II)		2	2	2	63
			2			4	64
						6	65

Tabel 1.2 *Mn di-nuclear compounds with the mono- $\mu$ -oxo moiety. The number of ligands is per Mn atom. Two types of bridges are distinguished:  $O^B$  = bridging oxygen and  $O^C$  = carboxylate bridge. Three types of terminal ligand are distinguished:  $N^A$  = aromatic nitrogen,  $N^N$  = non-aromatic nitrogen, and  $X$  = either a terminal oxygen or halide (in parentheses). OAc is  $CH_3CO_2^-$ .*

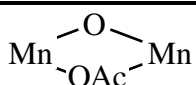
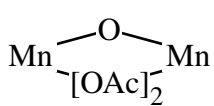
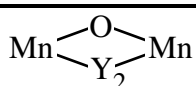
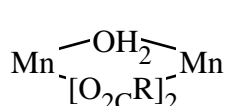
structural unit	specifics	Mn ox. state(s)	bridging		terminal			ref.
			$O^B$	$O^C$	$N^A$	$N^N$	$X$	
Mn–O–Mn	linear	(III,III)	1		5			66
		(IV,IV)	1		4	1		67,68
		(III,III), (III,IV), (IV,IV)	1		2	2	1	69
	non-linear	(III,III)	1			3	2	70
			1		3		1	71
	–	(III,III)	1	1	3	1		72
			1	1	2	2		73
	–	(II,III)	1	2	2	1		74
			1	2		3		75
		(III,III)	1	2	3			76,77
			1	2	2	1		74,78-80
			1	2		3		81-85
		(III,IV)	1	2	2	1		74
			1	2		3		81,82,84
		2 H <sub>2</sub> O	(III,III)	1	2	2		1
2 Cl	(III,III)	1	2	2		1(Cl)	87	
1 H <sub>2</sub> O & 1 OR	(III,III)	1	2	2		1	88,89	
	Y = phenyl boronate	(IV,IV)	1	2		3		90
Mn–(OH)–Mn	–	(II,II)	1		2	2	1	91
	2 OAc. bridges	(II,II)	1	2		3		82,83
	5-coordinate	(III,III)	1		4			47
	2 <sup>-</sup> O <sub>2</sub> CR terminal groups	(II,II)	1	2	2		1	92
			1	2		2	1	92
	3 OAc terminal groups		1	2	1		2	93
	2 terminal H <sub>2</sub> O & <sup>-</sup> O <sub>2</sub> CR terminal groups	(II,II)	1	2	1		2	94

Table 1.3 Mn di-nuclear compounds with the di- $\mu$ -oxo moiety. The number of ligands is per Mn atom. Two types of bridges are distinguished:  $O^B$  = bridging oxygen and  $O^C$  = carboxylate bridge. Three types of terminal ligand are distinguished:  $N^A$  = aromatic nitrogen,  $N^N$  = non-aromatic nitrogen, and X = either a terminal oxygen or halide (in parentheses). OAc is  $CH_3CO_2^-$ .


structural unit	specifics	Mn ox. state(s)	bridging		terminal			ref.
			$O^B$	$O^C$	$N^A$	$N^N$	X	
Mn-O <sub>2</sub> -Mn	5-coordinate	(III,III)	2		3			95
	Other oxidation states (III,III), (III,IV), or (IV,IV) can be electrochemically prepared	(III,III)	2		2	2		96-98
			2		3	1		97
		(III,IV)	2			4		99-101
			2		2	2		98,102-106
			2		3	1		107,108
			2		3		1	109
			2		4			110-115
			2			4		116,99
		(IV,IV)	2		2	2		98,117,118
			2		4			110,114,119
	2				3	1	120	
	2			2		2	121-124	
	2				2	2	125,126	
	2 terminal OH	(IV,IV)	2			3	1	84
	2 terminal Cl	(IV,IV)	2			3	1(Cl)	127
			2		2	1	1(Cl)	128
2 terminal F	(IV,IV)	2			3	1(F)	127	
		2		2	1	1(F)	128	
	-	(III,IV)	2	1		3		127,129
			2	1	2	1		79,128,130,131
		(IV,IV)	2	1		3		129
			2	1	2	1		78,79,132,133
	2 terminal H <sub>2</sub> O	(IV,IV)	2	1	2		1	134,135
	2 terminal Cl	(III,IV)	2	1	2		1(Cl)	136
	different terminal ligands for each Mn	(III,IV)	2	1		1 1/2	1 1/2	137
			2	1	1	1 1/2	1/2	137
Mn-(OH) <sub>2</sub> -Mn	5-coordinate	(II,II)	2		3			95
	4-coordinate	(III,III)	2				2	138

Table 1.4 Mn tri-nuclear compounds. The number of ligands is per Mn atom. Two types of bridges are distinguished:  $O^B$  = bridging oxygen and  $O^C$  = carboxylate bridge. Three types of terminal ligand are distinguished:  $N^A$  = aromatic nitrogen,  $N^N$  = non-aromatic nitrogen, and  $X$  = either a terminal oxygen or halide (in parentheses). OAc is  $CH_3CO_2^-$ .

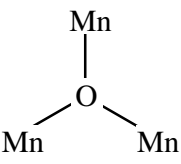
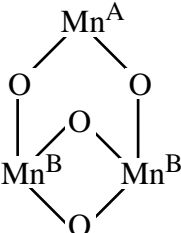
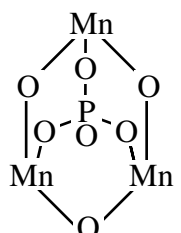
structural unit	specifics	Mn ox. state(s)	Mn	bridging		terminal			ref.
				$O^B$	$O^C$	$N^A$	$N^N$	X	
	6 $^-O_2CR$ bridges	(II,III <sub>2</sub> )	all	1	4	1			139-144
		(III <sub>3</sub> )	all	1	4	1			142,145
	& 1 H <sub>2</sub> O on Mn <sup>II</sup>	(II,III <sub>2</sub> )	II	1	4			1	141,142
			III	1	4	1			
	OH on Mn <sup>A</sup>	Mn <sup>A</sup> = III	Mn <sup>A</sup>	2		2	1	1	133
		Mn <sup>B</sup> = IV	Mn <sup>B</sup>	3		2	1		
		(IV <sub>3</sub> )	Mn <sup>A</sup>	2		2	1	1	132,133
			Mn <sup>B</sup>	3		2	1		
	F <sup>-</sup> or Cl <sup>-</sup> on Mn <sup>A</sup>	(IV <sub>3</sub> )	Mn <sup>A</sup>	2		2	1	1 (F/Cl)	146
			Mn <sup>B</sup>	3		2	1		
1 H <sub>2</sub> O per Mn <sup>B</sup>	(IV <sub>3</sub> )	Mn <sup>A</sup>	2		4			147	
		Mn <sup>B</sup>	3		2		1		
	P can be replaced by As or V <sup>V</sup>	(IV <sub>3</sub> )	all	2			3	1	148
Mn(OH)Mn(OH)Mn	4 OAc bridges	(III,II,III)	II	2	4				149
			III	1	2	3			

Table 1.5 Mn tetra-nuclear compounds, which contain the ‘adamantane-like’, ‘dimer-of-dimer’, or ‘linear’ motif. The number of ligands is per Mn atom. Two types of bridges are distinguished:  $O^B$  = bridging oxygen and  $O^C$  = carboxylate bridge. Three types of terminal ligand are distinguished:  $N^A$  = aromatic nitrogen,  $N^N$  = non-aromatic nitrogen, and  $X$  = either a terminal oxygen or halide. OAc is  $CH_3CO_2^-$ .

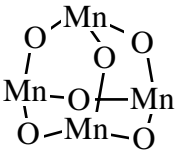
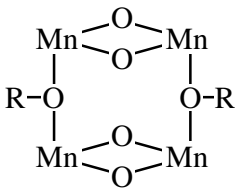
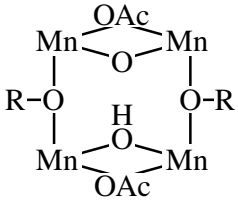
structural unit	specifics	Mn ox. state(s)	Mn	bridging		terminal			ref.
				$O^B$	$O^C$	$N^A$	$N^N$	X	
	-	(III,IV <sub>3</sub> )	all	3		2	1		150
		(IV <sub>4</sub> )	all	3		2	1		150
			all	3			3		151,152
	1 $\mu$ -oxo bridge is protonated	(IV <sub>4</sub> )	all	3			3		152
	2 $\mu$ -oxo bridges are protonated								153
	dimers linked by two $^-OR$ bridges	(III,IV) (IV,III)	all	3		2	1		154
	dimers linked by two $^-OR$ bridges H shared possibly by bridging O atoms	(III,III) (II,II)	all	2	1		1	2	155
$Mn^B-O_2-Mn^A-O_2-Mn^A-O_2-Mn^B$		(IV <sub>4</sub> )	$Mn^A$	4		2			156
			$Mn^B$	2		4			

Table 1.6 *Mn* tetra-nuclear compounds with the ‘cubane’ motif. The number of ligands is per *Mn* atom. Three types of bridges are distinguished:  $O^B$  = bridging oxygen,  $O^C$  = carboxylate bridge, and  $X^B$  = bridging that are not oxygen ligands. Three types of terminal ligand are distinguished:  $N^A$  = aromatic nitrogen,  $N^N$  = non-aromatic nitrogen, and  $X$  = either a terminal oxygen or halide (in parentheses).

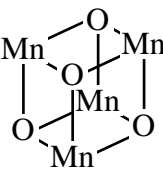
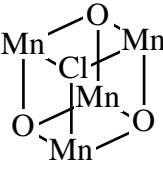
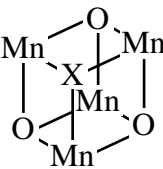
structural unit	specifics	Mn ox. state(s)	Mn	bridging			terminal			ref.
				$O^B$	$O^C$	$X^B$	$N^A$	$N^N$	$X$	
	6 ( $^-O_2PR$ ) bridges	(III <sub>2</sub> ,IV <sub>2</sub> )	all	3					3	157
		(III,IV <sub>3</sub> )	all	3					3	157, 158
 3 ( $^-O_2CR$ ) bridges	1 $Cl^-$ bridging ( $X^B$ )	(III <sub>3</sub> ,IV)	III	2	1	1(Cl)			2	159-161
			IV	3	3					
	1 $Cl^-$ bridging ( $X^B$ ) 3 $Cl^-$ terminal	(III <sub>3</sub> ,IV)	III	2	1	1(Cl)	1		1(Cl)	162-164
			IV	3	3					
	1 $Cl^-$ bridging ( $X^B$ ) 5 $Cl^-$ terminal	(III <sub>3</sub> ,IV)	III <sub>2</sub>	2	1	1(Cl)			2(Cl)	162, 165
			III	2	1	1(Cl)	1		1(Cl)	
			IV	3	3					
	1 $Cl^-$ bridging ( $X^B$ ) 6 $Cl^-$ terminal	(III <sub>3</sub> ,IV)	III	2	1	1(Cl)			2(Cl)	159
IV			3	3						
 3 ( $^-O_2CR$ ) bridge	X = H <sub>2</sub> O	(III <sub>4</sub> )	III	3	1			2	166	
			IV	3	3					
	X = Br	(III <sub>3</sub> ,IV)	III	2	1	1(Br)			2	159, 160
			IV	3	3					
	X = N <sub>3</sub> <sup>-</sup> or OCN <sup>-</sup>	(III <sub>3</sub> ,IV)	III	2	1	1(N)			2	167
			IV	3	3					
	X = OMe <sup>-</sup> or OH <sup>-</sup>	(III <sub>3</sub> ,IV)	III	3	1				2	168
										169, 170
IV			3	3					169, 171	



Table 1.7 *Mn tetra-nuclear compounds with the ‘butterfly’ motif. The number of ligands is per Mn. Two types of bridges are distinguished:  $O^B$  = bridging oxygen and  $O^C$  = carboxylate bridge. Three types of terminal ligand are distinguished:  $N^A$  = aromatic nitrogen,  $N^N$  = non-aromatic nitrogen, and  $X$  = either a terminal oxygen or halide (in parentheses).*

structural unit	specifics	Mn ox. state(s)	Mn	bridging		terminal			ref.
				$O^B$	$O^C$	$N^A$	$N^N$	$X$	
	4 $^-O_2R$ bridges between $Mn^A$ and $Mn^B$ atoms $Mn^A$ atoms 5-coordinate	$Mn^A = II$ $Mn^B = III$	$Mn^A$	1	2	2			172
			$Mn^B$	2	2	2			
	4 $^-OR$ bridge between $Mn^A$ and $Mn^B$ atoms	$(III_4)$	$Mn^A$	1			2	3	173,174
			$Mn^B$	2		2		2	
	$Mn^B$ atoms 5-coordinate	$Mn^A = II$ $Mn^B = III$	$Mn^A$	1	3	2			175,176
			$Mn^B$	2	3				
	All Mn atoms 5-coordinate	$Mn^A = II$ $Mn^B = III$	$Mn^A$	1	3			1	177
			$Mn^B$	2	3				
	one Cl per $Mn^A$ atoms	$(III_4)$	$Mn^A$	1	3	1		1(Cl)	178
			$Mn^B$	2	3	1			
		$(III_4)$	$Mn^A$	1	3			2	169
			$Mn^B$	2	3	1			
		$(III_4)$	$Mn^A$	1	3			2	169
			$Mn^B$	2	3			1	
	$(III_4)$	$Mn^A$	1	3	1		1	179	
		$Mn^B$	2	3			1		
1 $Mn^B$ atom is 5-coordinate	$(III_4)$	$Mn^A$	1	3			2	169	
		$Mn^B$	2	3	1				
		$Mn^B$	2	3					
	–	$(II,III_2,III)$	$Mn^A$	1	3	2			175
			$Mn^B$	2	4				
		$(III_4)$	$Mn^A$	1	3	2			175,180-182
			$Mn^B$	2	4				
		$(III_4)$	$Mn^A$	1	3	1		1	169,181,183,184
			$Mn^B$	2	4				
		$(III_4)$	$Mn^A$	1	3			2	169,181
		$Mn^B$	2	4					
one $H_2O$ per $Mn^A$ atoms	$(III_4)$	$Mn^A$	1	3			2	178,181,185	
		$Mn^B$	2	4					

Even though a great many Mn compounds, relevant to the OEC, have been published, only a few of these of compounds have been studied by XANES<sup>35,186-196</sup> or Mn K $\beta$  XES.<sup>46,197-199</sup> In fact, some of the compounds involved are manganese salts, such as Mn<sup>II</sup>Cl<sub>2</sub>, or oxides, such as Mn<sub>2</sub>O<sub>3</sub>, which are less relevant to the OEC.<sup>38,190,193,194,198</sup> The focus of these studies is on either the influence of an oxidation-state change<sup>191,192,196,197</sup> or a structural change<sup>186-188,195</sup> on the Mn K-edge XANES or Mn K $\beta$  XES spectra. However, no extensive comparison has been made between the two influences. Therefore, in Chapter 2, two manganese compounds in solution are studied to investigate the influence of oxidation state versus ligand environment on Mn K-edge XANES and Mn K $\beta$  XES data. One compound contains a mono- $\mu$ -oxo moiety and the other contains a di- $\mu$ -oxo moiety. The terminal ligands of the mono- $\mu$ -oxo compound are a mixture of oxygen ligands and non-aromatic and aromatic nitrogen ligands.<sup>69</sup> For the di- $\mu$ -oxo compound all the terminal ligands are aromatic nitrogen ligands.<sup>110</sup> The effects on XANES and K $\beta$  XES data of these different bridging and terminal ligands are compared to the influence of the different oxidation states: Mn<sup>III</sup>Mn<sup>III</sup>, Mn<sup>III</sup>Mn<sup>IV</sup>, and Mn<sup>IV</sup>Mn<sup>IV</sup>.

Recently, efforts have been made to add vibrational spectroscopy as an investigative tool to study the structure and mechanism of the OEC. This can be done by studying the changes during the catalytic cycle in the 1800 - 1200 cm<sup>-1</sup> range, which contains vibrations of the protein-residues ligated to the OEC.<sup>200-205</sup> Another approach is to study the Mn–ligand vibrations directly, specifically the Mn–O vibrations, which occur

in the 200 - 1000  $\text{cm}^{-1}$  range.<sup>200,206,207</sup> As for the X-ray and EPR spectroscopies, vibrational spectra of manganese model compounds are indispensable for the interpretation of the IR and Raman spectra of the OEC. Only a few Mn compounds have been analyzed by vibrational spectroscopy and normal mode analysis. This list consists of: Mn-porphyrins,<sup>42</sup>  $\text{MnO}_4^{n+}$ ,<sup>208</sup>  $\text{Mn}^{\text{VII}}\text{O}_3\text{X}$  with  $\text{X} = \text{F}$  or  $\text{Cl}^-$ ,<sup>209,210</sup>  $\text{Mn}^{\text{VI}}\text{X}_4$  with  $\text{X} = \text{F}$ ,  $\text{Cl}$ ,  $\text{Br}$  or  $\text{I}$ ,<sup>211,212</sup> and one mono- $\mu$ -oxo compound.<sup>76</sup> Only the last compound is relevant to the OEC. Consequently, more vibrational information of Mn model complexes, with different structures and oxidation states, is needed to aid the interpretation of the vibrational spectra of the OEC

Chapter 3 introduces a versatile spectroelectrochemical apparatus to study the changes in IR spectra of organic and inorganic compounds upon oxidation or reduction. In addition, an IR data collection protocol is introduced to deal with electrochemically non-reversible background signals. This apparatus and protocol enables us to study manganese compounds in different oxidation states relevant to the OEC. These studies will provide more insight into the vibrational behavior of the OEC during its catalytic cycle.

In Chapter 4, this apparatus and protocol are used to obtain IR difference spectra of an adamantane-like compound in the two oxidation states ( $\text{Mn}^{\text{III}}\text{Mn}^{\text{IV}}_3$  and  $\text{Mn}^{\text{IV}}_4$ ). The adamantane-like compound has six mono- $\mu$ -oxo bridges and a combination of non-aromatic and aromatic nitrogen containing terminal ligands.<sup>150</sup> Isotopic exchange,  $^{16}\text{O} \rightarrow ^{18}\text{O}$ , is used to distinguish Mn-O bridging modes from the terminal ligand modes. A normal-mode analysis is used to extract Mn-O stretching force constants which can be used for the analysis of vibrational spectra of the OEC. This is the first time that such an

IR and normal-mode analysis has been performed on a manganese compound in two oxidation states relevant to the OEC.

Finally, in Chapter 5 a future outlook is presented on the different techniques used to study manganese model compounds which are relevant to the understanding of the mechanism of the water-oxidation cycle.

### 1.3 References

- (1) Renger, G. *Angew. Chem.-Int. Ed. Engl.* **1987**, *26*, 643-660.
- (2) Ort, D. R.; Yocum, C. F. *Adv. Photosynth.* **1996**, *4*, 1-9.
- (3) Debus, R. J. *Biochim. Biophys. Acta* **1992**, *1102*, 269-352.
- (4) Golbeck, J. H. *Annu. Rev. Plant Physiol. Plant Molec. Biol.* **1992**, *43*, 293-324.
- (5) Golbeck, J. H. In *The Molecular Biology of Cyanobacteria*; Bryant, D. A., Ed.; Kluwer Academic Publishers: Dordrecht, 1994; pp 319-360.
- (6) Chitnis, P. R.; Xu, Q.; Chitnis, V. P.; Nechushtai, R. *Photosynthesis Research* **1995**, *44*, 23-40.
- (7) Ort, D. R.; Yocum, C. F.; Editors *Oxygenic Photosynthesis; The Light Reactions*. [In: *Adv. Photosynth.*, 1996; 4], 1996.
- (8) Boyer, P. D. *Annu. Rev. Biochem.* **1997**, *66*, 717-749.
- (9) Boyer, P. D. *Biochim. Biophys. Acta* **2000**, *1458*, 252-262.
- (10) Bassham, J. A. *Sci. Amer.* **1962**, *206*, 1-15.
- (11) Calvin, M.; Benson, A. A. *Science* **1948**, *107*, 476-480.
- (12) Calvin, M. *Angew. Chem.-Int. Ed. Engl.* **1962**, *1*, 65-75.
- (13) Zouni, A.; Jordan, R.; Schlodder, E.; Fromme, P.; Witt, H. T. *Biochim. Biophys. Acta* **2000**, *1457*, 103-105.
- (14) Kirby, J. A.; Robertson, A. S.; Smith, J. P.; Thompson, A. C.; Cooper, S. R.; Klein, M. P. *J. Am. Chem. Soc.* **1981**, *103*, 5529-5537.
- (15) Liang, W.; Roelofs, T. A.; Cinco, R. M.; Rompel, A.; Latimer, M. J.; Yu, W. O.; Sauer, K.; Klein, M. P.; Yachandra, V. K. *J. Am. Chem. Soc.* **2000**, *122*, 3399-3412.

- (16) Penner-Hahn, J. E. *Struct. Bonding (Berlin)* **1998**, *90*, 1-36.
- (17) Robblee, J. H.; Cinco, R. M.; Yachandra, V. K. *Biochim. Biophys. Acta* **2001**, *1503*, 7-23.
- (18) Liang, W.; Latimer, M. J.; Dau, H.; Roelofs, T. A.; Yachandra, V. K.; Sauer, K.; Klein, M. P. *Biochemistry* **1994**, *33*, 4923-4932.
- (19) Messinger, J.; Nugent, J. H. A.; Evans, M. C. W. *Biochemistry* **1997**, *36*, 11055-11060.
- (20) Miller, A. F.; Brudvig, G. W. *Biochim. Biophys. Acta* **1991**, *1056*, 1-18.
- (21) Peloquin, J. M.; Britt, R. D. *Biochim. Biophys. Acta* **2001**, *1503*, 96-111.
- (22) Christou, G.; Vincent, J. B. *Biochim. Biophys. Acta* **1987**, *895*, 259-274.
- (23) Renger, G. *Physiol. Plant.* **1997**, *100*, 828-841.
- (24) Hoganson, C. W.; Babcock, G. T. *Science* **1997**, *277*, 1953-1956.
- (25) Haumann, M.; Junge, W. *Biochim. Biophys. Acta* **1999**, *1411*, 86-91.
- (26) Siegbahn, P. E. M.; Crabtree, R. H. *J. Am. Chem. Soc.* **1999**, *121*, 117-127.
- (27) Messinger, J.; Robblee, J. H.; Bergmann, U.; Fernandez, C.; Glatzel, P.; Visser, H.; Cinco, R. M.; McFarlane, K. L.; Bellacchio, E.; Pizarro, S. A.; Cramer, S. P.; Sauer, K.; Klein, M. P.; Yachandra, V. K., submitted to *J. Am. Chem. Soc.*
- (28) Debus, R. J. In *Manganese and Its Role in Biological Processes*; Sigel, A., Sigel, H., Eds.; Marcel Dekker, Inc.: New York, 2000; Vol. 37, pp 657-711.
- (29) Vrettos, J. S.; Limburg, J.; Brudvig, G. W. *Biochim. Biophys. Acta* **2001**, *1503*, 229-245.
- (30) Kok, B.; Forbush, B.; McGloin, M. *Photochem. Photobiol.* **1970**, *11*, 457-475.
- (31) The whole volume of *Biochim. Biophys. Acta* **2001**, *1503*, 1-258.

- (32) Cramer, S. P. In *X-ray Absorption: Principles, Applications, Techniques of EXAFS, SEXAFS and XANES*; Koningsberger, D. C., Prins, R., Eds.; Wiley: New York, 1988; p 257.
- (33) Shulman, R. G.; Yafet, Y.; Eisenberger, P.; Blumberg, W. E. *Proc. Natl. Acad. Sci. U. S. A.* **1976**, *73*, 1384-1388.
- (34) Yachandra, V. K. In *Methods Enzymol.*; Sauer, K., Ed.; Academic Press, Inc., 1995; Vol. 246, pp 638-675.
- (35) Roelofs, T. A.; Liang, M. C.; Latimer, M. J.; Cinco, R. M.; Rompel, A.; Andrews, J. C.; Sauer, K.; Yachandra, V. K.; Klein, M. P. *Proc. Natl. Acad. Sci. U. S. A.* **1996**, *93*, 3335-3340.
- (36) Ono, T.; Noguchi, T.; Inoue, Y.; Kusunoki, M.; Matsushita, T.; Oyanagi, H. *Science* **1992**, *258*, 1335-1337.
- (37) Iuzzolino, L.; Dittmer, J.; Dörner, W.; Meyer-Klaucke, W.; Dau, H. *Biochemistry* **1998**, *37*, 17112-17119.
- (38) Peng, G.; DeGroot, F. M. F.; Hämäläinen, K.; Moore, J. A.; Wang, X.; Grush, M. M.; Hastings, J. B.; Siddons, D. P.; Armstrong, W. H.; Mullins, O. C.; Cramer, S. *P. J. Am. Chem. Soc.* **1994**, *116*, 2914-2920.
- (39) Stojanoff, V.; Hämäläinen, K.; Siddons, D. P.; Hastings, J. B.; Berman, L. E.; Cramer, S.; Smith, G. *Rev. Sci. Instrum.* **1992**, *63*, 1125-1127.
- (40) Fernandez, C.; Cinco, R. M.; Robblee, J. H.; Messinger, J.; Pizarro, S. A.; Sauer, K.; Klein, M. P.; Yachandra, V. K. In *Photosynthesis: Mechanisms and Effects*; Garab, G., Ed.; Kluwer Academic Publishers: Dordrecht, 1998; Vol. 2, pp 1399-1402.

- (41) Fernandez, C.; Cinco, R. M.; Sauer, K.; Yachandra, V. K.; Klein, M. P. *Abstr. Pap. Am. Chem. Soc.* **1998**, *216*, 436.
- (42) Czernuscewicz, R. S.; Su, Y. O.; Stern, M. K.; Macor, K. A.; Kim, D.; Groves, J. T.; Spiro, T. G. *J. Am. Chem. Soc.* **1988**, *110*, 4158-4165.
- (43) Macdonald, F. M.; Fackler, N. L. P.; Stern, C.; O'Halloran, T. V. *J. Am. Chem. Soc.* **1994**, *116*, 7431-7432.
- (44) Collins, T. J.; Powell, R. D.; Slebodnick, C.; Uffelman, E. S. *J. Am. Chem. Soc.* **1990**, *112*, 899-901.
- (45) Eichhorn, D. M.; Armstrong, W. H. *J. Chem. Soc., Chem. Commun.* **1992**, 85-87.
- (46) Peng, S.-M.; Wang, Y.; Chen, C.-K.; Lee, J.-Y.; Liaw, D.-S. *J. Chin. Chem. Soc.* **1986**, *33*, 23-33.
- (47) Cheng, B.; Cukiernik, F.; Fries, P. H.; Marchon, J.-C.; Scheidt, W. R. *Inorg. Chem.* **1995**, *34*, 4627-4639.
- (48) Williamson, M. M.; Hill, C. L. *Inorg. Chem.* **1987**, *26*, 4155-4160.
- (49) Williamson, M. M.; Hill, C. L. *Inorg. Chem.* **1986**, *25*, 4668-4671.
- (50) De, A. *Acta Crystallogr., Sect. C* **1990**, *46*, 1004-1006.
- (51) Wieghardt, K.; Bossek, U. *Z. Naturforsch., B: Chem. Sci.* **1988**, *43*, 1184.
- (52) Chan, C.-W.; Che, C.-M.; Peng, S.-M. *Polyhedron* **1993**, *12*, 2169-2173.
- (53) Palenik, G. J.; Wester, D. W. *Inorg. Chem.* **1978**, *17*, 864-870.
- (54) Horwitz, C. P.; Daily, G. C.; Tham, F. S. *Acta Crystallogr., Sect. C* **1995**, *51*, 815-816.
- (55) Pelizzi, C.; Pelizzi, G.; Predieri, G.; Resola, s. *J. Chem. Soc., Dalton Trans.* **1982**, 1349-1354.



- (56) Lee, T.-J.; Chang, Y.; Chung, C.-S.; Wang, Y.-M. *Acta Crystallogr., Sect. C* **1990**, *46*, 2360-2363.
- (57) Swarnabala, G.; Reddy, K. R.; Tirunagar, T.; Rajasekharan, M. V. *Transition Metal Chemistry* **1994**, *19*, 506.
- (58) Tang, X. S.; Chen, C. T.; Zheng, P.-J.; Tang, W.-T. *Acta Crystallogr., Sect. C* **1995**, *51*, 1268-1269.
- (59) Prince, S.; Körber, F.; Cooke, P. R.; Lindsay Smith, J. R.; Mazid, M. A. *Acta Crystallogr., Sect. C* **1993**, *49*, 1158-1160.
- (60) Byrn, M. P.; Curtis, C. J.; Hsiou, Y.; Khan, S. I.; Sawin, P. A.; Tendick, S. K.; Terzis, A.; Strouse, C. E. *J. Am. Chem. Soc.* **1993**, *115*, 9480-9497.
- (61) Lis, T.; Matuszewski, J.; Jezowska-Trzebiatowska, B. *Acta Crystallogr., Sect. B* **1977**, *33*, 1943-1946.
- (62) Aurangzeb, N.; Hulme, C. E.; McAuliffe, C. A.; Pritchard, R. G.; Watkinson, M.; Bermejo, M.; Garcia-Deibe, A.; Rey, M.; Sanmartin, J.; Sousa, A. *J. Chem. Soc., Chem. Commun.* **1994**, 1153-1155.
- (63) Goodson, P. A.; Oki, A.; Hodgson, D. J. *Inorg. Chim. Acta* **1990**, *177*, 59-64.
- (64) Lis, T. *Acta Crystallogr., Sect. B* **1980**, *36*, 701-703.
- (65) Montgomery, H.; Lingafelter, E. C. *Acta Crystallogr., Sect. C* **1968**, *24*, 1127-1128.
- (66) Vogt, L. H.; Zalkin, A.; Templeton, D. H. *Inorg. Chem.* **1967**, *6*, 1725-1730.
- (67) Schardt, B. C.; Hollander, F. J.; Hille, C. L. *J. Chem. Soc., Chem. Commun.* **1981**, 765-766.

- (68) Schardt, B. C.; Hollander, F. J.; Hille, C. L. *J. Am. Chem. Soc.* **1982**, *104*, 3964-3972.
- (69) Horner, O.; Anxolabéhère-Mallart, E.; Charlot, M. F.; Tchertanov, L.; Guilhem, J.; Mattioli, T. A.; Boussac, A.; Girerd, J.-J. *Inorg. Chem.* **1999**, *38*, 1222-1232.
- (70) Kipke, C. A.; Scott, M. J.; Gohdes, J. W.; Armstrong, W. A. *Inorg. Chem.* **1990**, *29*, 2193-2194.
- (71) Kitajima, N.; Osawa, M.; Tanaka, K.; Moro-oka, Y. *J. Am. Chem. Soc.* **1991**, *113*, 8952-8953.
- (72) Oberhausen, K. J.; O'Brien, R. J.; Richardson, J. F.; Buchanan, R. M.; Costa, R.; Latour, J. M.; Tsai, H. L.; Hendrickson, D. N. *Inorg. Chem.* **1993**, *32*, 4561-4565.
- (73) Arulsamy, N.; Glerup, J.; Hazell, A.; Hodgson, D. J.; McKenzie, C. J.; Toftlund, H. *Inorg. Chem.* **1994**, *33*, 3023-3025.
- (74) Mandal, S. K.; Armstrong, W. H. *Inorg. Chim. Acta* **1995**, *229*, 261-270.
- (75) Darovsky, A.; Kezerashvili, V.; Coppens, P.; Weyhermüller, T.; Hummel, H.; Wieghardt, K. *Inorg. Chem.* **1996**, *35*, 6916-6917.
- (76) Sheats, J. E.; Czernuszewicz, R. S.; Dismukes, G. C.; Rheingold, A. L.; Petrouleas, V.; Stubbe, J.; Armstrong, W. H.; Beer, R. H.; Lippard, S. J. *J. Am. Chem. Soc.* **1987**, *109*, 1435-1444.
- (77) Wu, F. J.; Kurtz, D. M.; Hagen, K. S.; Nyman, P. D.; Debrunner, P. G.; Vankai, V. A. *Inorg. Chem.* **1990**, *29*, 5174-5183.
- (78) Mok, H. J.; Davis, J. A.; Pal, S.; Mandal, S. K.; Armstrong, W. H. *Inorg. Chim. Acta* **1997**, *263*, 385-394.
- (79) Lal, T. K.; Mukerjee, R. *Inorg. Chem.* **1998**, *37*, 2375-2382.

- (80) Mahapatra, S.; Lal, T. K.; Mukherjee, R. *Inorg. Chem.* **1994**, *33*, 1579-1580.
- (81) Wieghardt, K.; Bossek, U.; Ventur, D.; Weiss, J. *J. Chem. Soc., Chem. Commun.* **1985**, 347-349.
- (82) Wieghardt, K.; Bossek, U.; Bonvoisin, J.; Beauvillain, P.; Girerd, J.-J.; Nuber, B.; Weiss, J.; Heinze, J. *Angew. Chem.-Int. Ed. Engl.* **1986**, *25*, 1030-1031.
- (83) Bossek, U.; Wieghardt, K.; Nuber, B.; Weiss, J. *Inorg. Chim. Acta* **1989**, *165*, 123-129.
- (84) Wieghardt, K.; Bossek, U.; Nuber, B.; Weiss, J.; Bonvoisin, J.; Corbella, M.; Vitols, S. E.; Girerd, J.-J. *J. Am. Chem. Soc.* **1988**, *110*, 7398-7411.
- (85) Hage, R.; Gunnewegh, E. A.; Niël, J.; Tjan, F. S. B.; Weyhermüller, T.; Wieghardt, K. *Inorg. Chim. Acta* **1998**, *268*, 43-48.
- (86) Ménage, S.; Girerd, J.-J.; Gleizes, A. *J. Chem. Soc., Chem. Commun.* **1988**, 431-432.
- (87) Vincent, J. B.; Tsai, H. L.; Blackman, A. G.; Wang, S.; Boyd, P. D. W.; Folting, K.; Huffman, J. C.; Lobkovsky, E. B.; Hendrickson, D. N.; Christou, G. *J. Am. Chem. Soc.* **1993**, *115*, 12353-12361.
- (88) Blackman, A. G.; Huffman, J. C.; Lobkovsky, E. B.; Christou, G. *J. Chem. Soc., Chem. Commun.* **1991**, 989-991.
- (89) Dave, B. C.; Czernuszewicz, R. S. *Inorg. Chim. Acta* **1998**, *281*, 25-35.
- (90) Bossek, U.; Hummel, H.; Weyhermüller, T.; Wieghardt, K.; Russell, S.; vanderWolf, L.; Kolb, U. *Angew. Chem.-Int. Ed. Engl.* **1996**, *35*, 1552-1554.
- (91) Tétard, E.; Rabion, A.; Verlhac, J.-B.; Guilhem, J. *J. Chem. Soc., Chem. Commun.* **1995**, 531-532.

- (92) Yu, S. B.; Lippard, S. J.; Shweky, I.; Bino, A. *Inorg. Chem.* **1992**, *31*, 3502-3504.
- (93) Coucouvanis, D.; Reynolds III, R. A.; Dunham, W. R. *J. Am. Chem. Soc.* **1995**, *117*, 7570-7571.
- (94) Caneschi, A.; Ferraro, F.; Gatteschi, D.; Melandri, M. C.; Rey, P.; Sessoli, R. *Angew. Chem.-Int. Ed. Engl.* **1989**, *28*, 1365-1367.
- (95) Kitajima, N.; Singh, U. P.; Amagai, H.; Osawa, M.; Moro-oka, Y. *J. Am. Chem. Soc.* **1991**, *113*, 7757-7758.
- (96) Goodson, P. A.; Hodgson, D. J. *Inorg. Chem.* **1989**, *28*, 3606-3608.
- (97) Goodson, P. A.; Oki, A. R.; Glerup, J.; Hodgson, D. J. *J. Am. Chem. Soc.* **1990**, *112*, 6248-6254.
- (98) Glerup, J.; Goodson, P. A.; Hazell, A.; Hazell, R.; Hodgson, D. J.; McKenzie, C. J.; Michelsen, K.; Rychlewska, U.; Toftlund, H. *Inorg. Chem.* **1994**, *33*, 4105-4111.
- (99) Goodson, P. A.; Hodgson, D. J.; Glerup, J.; Michelsen, K.; Weihe, H. *Inorg. Chim. Acta* **1992**, *197*, 141-147.
- (100) Goodson, P. A.; Hodgson, D. J. *Inorg. Chim. Acta* **1990**, *172*, 49-57.
- (101) Brewer, K. J.; Calvin, M.; Lumpkin, R. S.; Otvos, J. W.; Spreer, L. O. *Inorg. Chem.* **1989**, *28*, 4446-4451.
- (102) Collins, M. A.; Hodgson, D. J.; Michelsen, K.; Towle, D. K. *J. Chem. Soc., Chem. Commun.* **1987**, 1659-1660.
- (103) Goodson, P. A.; Glerup, J.; Hodgson, D. J.; Michelsen, K.; Pedersen, E. *Inorg. Chem.* **1990**, *29*, 503-508.

- (104) Goodson, P. A.; Glerup, J.; Hodgson, D. J.; Michelsen, K.; Weihe, H. *Inorg. Chem.* **1991**, *30*, 4909-4914.
- (105) Frapart, Y. M.; Boussac, A.; Albach, R.; Anxolabéhère-Mallart, E.; Delroisse, M.; Verlhac, J. B.; Blondin, G.; Girerd, J.-J.; Guilhem, J.; Cesario, M.; Rutherford, A. W.; Lexa, D. *J. Am. Chem. Soc.* **1996**, *118*, 2669-2678.
- (106) Horner, O.; Charlot, M.-F.; Boussac, A.; Anxolabéhère-Mallart, E.; Tchertanov, L.; Guilhem, J.; Girerd, J.-J. *Eur. J. Inorg. Chem.* **1998**, 721-727.
- (107) Towle, D. K.; Botsford, C. A.; Hodgson, D. J. *Inorg. Chim. Acta* **1988**, *141*, 167-168.
- (108) Oki, A. R.; Glerup, J.; Hodgson, D. J. *Inorg. Chem.* **1990**, *29*, 2435-2441.
- (109) Limburg, J.; Vrettos, J. S.; Chen, H. Y.; de Paula, J. C.; Crabtree, R. H.; Brudvig, G. W. *J. Am. Chem. Soc.* **2001**, *123*, 423-430.
- (110) Stebler, M.; Ludi, A.; Bürgi, H.-B. *Inorg. Chem.* **1986**, *25*, 4743-4750.
- (111) Plaksin, P. M.; Stoufer, R. C.; Mathew, M.; Palenik, G. J. *J. Am. Chem. Soc.* **1972**, *94*, 2121-2122.
- (112) Jensen, A. F.; Su, Z. W.; Hansen, N. K.; Larsen, F. K. *Inorg. Chem.* **1995**, *34*, 4244-4252.
- (113) Wilson, C.; Larsen, F. K.; Figgis, B. N. *Acta Crystallogr., Sect. C* **1998**, *54*, 1797-1799.
- (114) Dave, B. C.; Czernuszewicz, R. S. *Inorg. Chim. Acta* **1994**, *227*, 33-41.
- (115) Cooper, S. R.; Dismukes, G. C.; Klein, M. P.; Calvin, M. *J. Am. Chem. Soc.* **1978**, *100*, 7248-7252.
- (116) Hagen, K. S.; Armstrong, W. H.; Hope, H. *Inorg. Chem.* **1988**, *27*, 967-969.

- (117) Larson, E. J.; Pecoraro, V. L. *J. Am. Chem. Soc.* **1991**, *113*, 7809-7810.
- (118) Larson, E. J.; Pecoraro, V. L. *J. Am. Chem. Soc.* **1991**, *113*, 3810-3818.
- (119) Manchanda, R.; Brudvig, G. W.; Degala, S.; Crabtree, R. H. *Inorg. Chem.* **1994**, *33*, 5157-5160.
- (120) Burdinski, D.; Bothe, E.; Wieghardt, K. *Inorg. Chem.* **2000**, *39*, 105-116.
- (121) Gohdes, J. W.; Armstrong, W. H. *Inorg. Chem.* **1992**, *31*, 368-373.
- (122) Aurangzeb, N.; McAuliffe, C. A.; Pritchard, R. G.; Watkinson, M.; Bermejo, M.; Garcia-Deibe, A.; Sousa, A. *Acta Crystallogr., Sect. C* **1993**, 1945-1947.
- (123) Hoof, D. L.; Tisley, D. G.; Walton, R. A. *Inorg. Nucl. Chem. Letters* **1973**, *9*, 571-576.
- (124) Libby, E.; Webb, R. J.; Streib, W. E.; Folting, K.; Huffman, J. C.; Hendrickson, D. N.; Christou, G. *Inorg. Chem.* **1989**, *28*, 4037-4040.
- (125) Boucher, L. J.; Coe, C. G. *Inorg. Chem.* **1975**, *14*, 1289-1295.
- (126) Larson, E.; Lah, M. S.; Li, X.; Bonadies, J. A.; Pecoraro, V. L. *Inorg. Chem.* **1992**, *31*, 373-378.
- (127) Wieghardt, K.; Bossek, U.; Zsolnai, L.; Huttner, G.; Blondin, G.; Girerd, J.-J.; Babonneau, F. *J. Chem. Soc., Chem. Commun.* **1987**, 651-653.
- (128) Pal, S.; Olmstead, M. M.; Armstrong, W. H. *Inorg. Chem.* **1995**, *34*, 4708-4715.
- (129) Schäfer, K.-O.; Brittl, R.; Zwegart, W.; Lenzian, F.; Haselhorst, G.; Weyermüller, T.; Wieghardt, K.; Lubitz, W. *J. Am. Chem. Soc.* **1998**, *120*, 13104-13120.
- (130) Pal, S.; Gohdes, J. W.; Wilisch, W. C. A.; Armstrong, W. H. *Inorg. Chem.* **1992**, *31*, 713-716.

- (131) Mahapatra, S.; Das, P.; Mukherjee, R. *J. Chem. Soc., Dalton Trans.* **1993**, 217-220.
- (132) Pal, S.; Armstrong, W. H. *Inorg. Chem.* **1992**, *31*, 5417-5423.
- (133) Pal, S.; Chan, M. K.; Armstrong, W. H. *J. Am. Chem. Soc.* **1992**, *114*, 6398-6406.
- (134) Dave, B. C.; Czernuscewicz, R.; Bond, M. R.; Carrano, C. J. *Inorg. Chem.* **1993**, *32*, 3593-3594.
- (135) Reddy, K. R.; Rajasekharan, M. V.; Padhye, S.; Dahan, F.; Tuchagues, J. P. *Inorg. Chem.* **1994**, *33*, 428-433.
- (136) Bashkin, J. S.; Schake, A. R.; Vincent, J. B.; Chang, H. R.; Li, Q.; Huffman, J. C.; Christou, G.; Hendrickson, D. N. *J. Chem. Soc., Chem. Commun.* **1988**, 700-702.
- (137) Bossek, U.; Saher, M.; Weyhermüller, T.; Wieghardt, K. *J. Chem. Soc., Chem. Commun.* **1992**, 1780-1782.
- (138) Nair, B. U.; Dismukes, G. C. *J. Am. Chem. Soc.* **1983**, *105*, 124-125.
- (139) Cannon, R. D.; Jayasooriya, U. A.; Montri, L.; Saad, A. K.; Karu, E.; Bollen, S. K.; Sanderson, W. R.; Powell, A. K.; Blake, A. B. *J. Chem. Soc., Dalton Trans.* **1993**, 2005-2010.
- (140) Johnson, M. K.; Powell, D. B.; Cannon, R. D. *Spectrochim. Acta, Part A* **1981**, *37*, 995-1006.
- (141) Ribas, J.; Albela, B.; Stoeckli-Evans, H.; Christou, G. *Inorg. Chem.* **1997**, *36*, 2352-2360.
- (142) Vincent, J. B.; Chang, H. R.; Folting, K.; Huffman, J. C.; Christou, G.; Hendrickson, D. N. *J. Am. Chem. Soc.* **1987**, *109*, 5703-5711.

- (143) Baikie, R. E.; Hursthouse, M. B.; New, L.; Thornton, P.; White, R. G. *J. Chem. Soc., Dalton Trans.* **1980**, 684-685.
- (144) Baikie, R. E.; Hursthouse, M. B.; New, D. B.; Thornton, P. *J. Chem. Soc., Dalton Trans.* **1978**, 62-63.
- (145) Eppley, H. J.; deVries, N.; Wang, S. Y.; Aubin, S. M.; Tsai, H. L.; Folting, K.; Hendrickson, D. N.; Christou, G. *Inorg. Chim. Acta* **1997**, 263, 323-340.
- (146) Armstrong, W. H., personal communication.
- (147) Sarneski, J. E.; Thorp, H. H.; Brudvig, G. W.; Crabtree, R. H.; Schulte, G. K. *J. Am. Chem. Soc.* **1990**, 112, 7255-7260.
- (148) Wieghardt, K.; Bossek, U.; Nuber, B.; Weiss, J.; Gehring, S.; Haase, W. *J. Chem. Soc., Chem. Commun.* **1988**, 1145-1146.
- (149) Kitajima, N.; Osawa, M.; Imai, S.; Fujisawa, K.; Moro-oka, Y.; Heerwegh, K.; Reed, C. A.; Boyd, P. D. W. *Inorg. Chem.* **1994**, 33, 4613-4614.
- (150) Dubé, C. E.; Wright, D. W.; Pal, S.; Bonitatebus, P. J.; Armstrong, W. H. *J. Am. Chem. Soc.* **1998**, 120, 3704-3716.
- (151) Wieghardt, K.; Bossek, U.; Gebert, W. *Angew. Chem.-Int. Ed. Engl.* **1983**, 22, 328-329.
- (152) Hagen, K. S.; Westmoreland, T. D.; Scott, M. J.; Armstrong, W. H. *J. Am. Chem. Soc.* **1989**, 111, 1907-1909.
- (153) Dubé, C. E.; Wright, D. W.; Armstrong, W. H. *J. Am. Chem. Soc.* **1996**, 118, 10910-10911.
- (154) Chan, M. K.; Armstrong, W. H. *J. Am. Chem. Soc.* **1991**, 113, 5055-5057.
- (155) Stibrany, R. T.; Gorun, S. M. *Angew. Chem.-Int. Ed. Engl.* **1990**, 29, 1156-1158.



Chapter 1

- (156) Philouze, C.; Blondin, G.; Ménage, S.; Auger, N.; Girerd, J.-J.; Vigner, D.; Lance, M.; Nierlich, M. *Angew. Chem.-Int. Ed. Engl.* **1992**, *31*, 1629-1631.
- (157) Ruettinger, W. F.; Campana, C.; Dismukes, G. C. *J. Am. Chem. Soc.* **1997**, *119*, 6670-6671.
- (158) Ruettinger, W. F.; Ho, D. M.; Dismukes, G. C. *Inorg. Chem.* **1999**, *38*, 1036-+.
- (159) Wang, S.; Tsai, H. L.; Libby, E.; Folting, K.; Streib, W. E.; Hendrickson, D. N.; Christou, G. *Inorg. Chem.* **1996**, *35*, 7578-7589.
- (160) Wang, S.; Tsai, H. L.; Streib, W. E.; Christou, G.; Hendrickson, D. N. *J. Chem. Soc., Chem. Commun.* **1992**, 1427-1429.
- (161) Wang, S.; Folting, K.; Streib, W. E.; Schmitt, E. A.; McCusker, J. K.; Hendrickson, D. N.; Christou, G. *Angew. Chem.-Int. Ed. Engl.* **1991**, *30*, 305-306.
- (162) Hendrickson, D. N.; Christou, G.; Schmitt, E. A.; Libby, E.; Bashkin, J. S.; Wang, S.; Tsai, H.-L.; Vincent, J. B.; Boyd, P. D. W.; Huffman, J. C.; Folting, K.; Li, Q.; Streib, W. E. *J. Am. Chem. Soc.* **1992**, *114*, 2455-2471.
- (163) Wemple, M. W.; Tsai, H. L.; Folting, K.; Hendrickson, D. N.; Christou, G. *Inorg. Chem.* **1993**, *32*, 2025-2031.
- (164) Li, Q.; Vincent, J. B.; Libby, E.; Chang, H. R.; Huffman, J. C.; Boyd, P. D. W.; Christou, G.; Hendrickson, D. N. *Angew. Chem.-Int. Edit. Engl.* **1988**, *27*, 1731-1733.
- (165) Bashkin, J. S.; Chang, H.-R.; Streib, W. E.; Huffman, J. C.; Hendrickson, D. N.; Christou, G. *J. Am. Chem. Soc.* **1987**, *109*, 6502-6504.

- (166) Aromí, G.; Aubin, S. M. J.; Bolcar, M. A.; Christou, G.; Eppley, H. J.; Folting, K.; Hendrickson, D. N.; Huffman, J. C.; Squire, R. C.; Tsai, H.-L.; Wang, S.; Wemple, M. W. *Polyhedron* **1998**, *17*, 3005-3020.
- (167) Wemple, M. W.; Adams, D. M.; Hagen, K. S.; Folting, K.; Hendrickson, D. N.; Christou, G. *J. Chem. Soc., Chem. Commun.* **1995**, 1591-1593.
- (168) Aromí, G.; Wemple, M. W.; Aubin, S. J.; Folting, K.; Hendrickson, D. N.; Christou, G. *J. Am. Chem. Soc.* **1998**, *120*, 5850-5851.
- (169) Wang, S.; Wemple, M. S.; Yoo, J.; Folting, K.; Huffman, J. C.; Hagen, K. S.; Hendrickson, D. N.; Christou, G. *Inorg. Chem.* **2000**, *39*, 1501-1513.
- (170) Wemple, M. S.; Adams, D. M.; Folting, K.; Henderickson, D. N.; Christou, G. *J. Am. Chem. Soc.* **1995**, *117*, 7275-7276.
- (171) Wang, S.; Tsai, H. L.; Hagen, K. S.; Hendrickson, D. N.; Christou, G. *J. Am. Chem. Soc.* **1994**, *116*, 8376-8377.
- (172) Grillo, V. A.; Knapp, M. J.; Bollinger, J. C.; Hendrickson, D. N.; Christou, G. *Angew. Chem.-Int. Ed. Engl.* **1996**, *35*, 1818-1820.
- (173) Sunatsuki, Y.; Shimada, H.; Matsuo, T.; Nakamura, M.; Kai, F.; Matsumoto, N.; Re, N. *Inorg. Chem.* **1998**, *37*, 5566-5574.
- (174) Sunatsuki, Y.; Shimada, H.; Matsuo, T.; Nakamura, M.; Kai, F.; Matsumoto, N.; Re, N. *Inorg. Chem.* **1999**, *38*, 2756.
- (175) Vincent, J. B.; Christmas, C.; Chang, H.-R.; Li, Q. Y.; Boyd, P. D. W.; Huffman, J. C.; Hendrickson, D. N.; Christou, G. *J. Am. Chem. Soc.* **1989**, *111*, 2086-2097.
- (176) Christmas, C.; Vincent, J. B.; Huffman, J. C.; Christou, G.; Chang, H.-R.; Hendrickson, D. N. *J. Chem. Soc., Chem. Commun.* **1987**, 1303-1305.

- (177) Kulawiec, R. J.; Crabtree, R. H.; Brudvig, G. W.; Schulte, G. K. *Inorg. Chem.* **1988**, *27*, 1309-1311.
- (178) Wemple, M. W.; Coggin, D. K.; Vincent, J. B.; McCusker, J. K.; Streib, W. E.; Huffman, J. C.; Hendrickson, D. N.; Christou, G. *J. Chem. Soc., Dalton Trans.* **1998**, 719-725.
- (179) Libby, E.; Folting, K.; Huffman, C. J.; Huffman, J. C.; Christou, G. *Inorg. Chem.* **1993**, *32*, 2549-2556.
- (180) Vincent, J. B.; Christmas, C.; Huffman, C. J.; Christou, G.; Chang, H.-R.; Hendrickson, D. N. *J. Chem. Soc., Chem. Commun.* **1987**, 236-238.
- (181) Wemple, M. W.; Tsai, H. L.; Wang, S.; Claude, J. P.; Streib, W. E.; Huffman, J. C.; Hendrickson, D. N.; Christou, G. *Inorg. Chem.* **1996**, *35*, 6437-6449.
- (182) Albela, B.; El Fallah, M. S.; Ribas, J.; Folting, K.; Christou, G.; Hendrickson, D. N. *Inorg. Chem.* **2001**, *40*, 1037-1044.
- (183) Libby, E.; McCusker, J. K.; Schmitt, E. A.; Folting, K.; Hendrickson, D. N.; Christou, G. *Inorg. Chem.* **1991**, *30*, 3486-3495.
- (184) Bouwman, E.; Bolcar, M. A.; Libby, E.; Huffman, J. C.; Folting, K.; Christou, G. *Inorg. Chem.* **1992**, *31*, 5185-5192.
- (185) Wang, S.; Huffman, J. C.; Folting, K.; Streib, W. E.; Lobkovsky, E. B.; Christou, G. *Angew. Chem.-Int. Ed. Engl.* **1991**, *30*, 1672-1674.
- (186) Baldwin, M. J.; Stemmler, T. L.; Riggs-Gelasco, P. J.; Kirk, M. L.; Penner-Hahn, J. E.; Pecoraro, V. L. *J. Am. Chem. Soc.* **1994**, *116*, 11349-11356.
- (187) Caudle, M. T.; Riggs-Gelasco, P.; Gelasco, A. K.; Penner-Hahn, J. E.; Pecoraro, V. L. *Inorg. Chem.* **1996**, *35*, 3577-3584.

- (188) Cinco, R. M.; Rompel, A.; Visser, H.; Aromí, G.; Christou, G.; Sauer, K.; Klein, M. P.; Yachandra, V. K. *Inorg. Chem.* **1999**, *38*, 5988-5998.
- (189) DeRose, V. J.; Mukerji, I.; Latimer, M. J.; Yachandra, V. K.; Sauer, K.; Klein, M. *P. J. Am. Chem. Soc.* **1994**, *116*, 5239-5249.
- (190) Kirby, J. A.; Goodin, D. B.; Wydrzynski, T.; Robertson, A. S.; Klein, M. P. *J. Am. Chem. Soc.* **1981**, *103*, 5537-5542.
- (191) Pecoraro, V. L.; Hsieh, W.-Y. In *Manganese and Its Role in Biological Processes*; Sigel, A., Sigel, H., Eds.; Marcel Dekker Inc.: New York, 2000; Vol. 37, pp 429-504.
- (192) Penner-Hahn, J. E.; Fronko, R. M.; Pecoraro, V. L.; Yocum, C. F.; Betts, S. D.; Bowlby, N. R. *J. Am. Chem. Soc.* **1990**, *112*, 2549-2557.
- (193) Stemmler, T. L.; Sossong, T. M., Jr.; Goldstein, J. I.; Ash, D. E.; Elgren, T. E.; Kurtz, D. M.; Penner-Hahn, J. E. *Biochemistry* **1997**, *36*, 9847-9858.
- (194) Yachandra, V. K.; Derose, V. J.; Latimer, M. J.; Mukerji, I.; Sauer, K.; Klein, M. *P. Science* **1993**, *260*, 675-679.
- (195) Chan, M. K. Ph.D. thesis, University of California, Berkeley, 1986.
- (196) Kuzek, D.; Pace, R. J. *Biochim. Biophys. Acta* **2001**, *1503*, 123-137.
- (197) Bergmann, U.; Grush, M. M.; Horne, C. R.; DeMarois, P.; Penner-Hahn, J. E.; Yocum, C. F.; Wright, D. W.; Dubé, C. E.; Armstrong, W. H.; Christou, G.; Eppley, H. J.; Cramer, S. P. *J. Phys. Chem. B* **1998**, *102*, 8350-8352.
- (198) Grush, M. M.; Christou, G.; Hämäläinen, K.; Cramer, S. P. *J. Am. Chem. Soc.* **1995**, *117*, 5895-5896.

- (199) Grush, M. M. Ph.D. (LBNL publ. 38973) thesis, University of California, Davis, 1996.
- (200) Chu, H.-A.; Hillier, W.; Law, N. A.; Sackett, H.; Haymond, S.; Babcock, G. T. *Biochim. Biophys. Acta* **2000**, *1459*, 528-532.
- (201) Noguchi, T.; Ono, T. A.; Inoue, Y. *Biochim. Biophys. Acta* **1993**, *1143*, 333-336.
- (202) Noguchi, T.; Ono, T. A.; Inoue, Y. *Biochim. Biophys. Acta* **1995**, *1232*, 59-66.
- (203) Noguchi, T.; Inoue, Y.; Tang, X. S. *Biochemistry* **1999**, *38*, 10187-10195.
- (204) Noguchi, T.; Sugiura, M. *Biochemistry* **2000**, *39*, 10943-10949.
- (205) Steenhuis, J. J.; Hutchison, R. S.; Barry, B. A. *J. Biol. Chem.* **1999**, *274*, 14609-14616.
- (206) Chu, H. A.; Hillier, W.; Law, N. A.; Babcock, G. T. *Biochim. Biophys. Acta* **2001**, *1503*, 69-82.
- (207) Cua, A.; Stewart, D. H.; Reifler, M. J.; Brudvig, G. W.; Bocian, D. F. *J. Am. Chem. Soc.* **2000**, *122*, 2069-2077.
- (208) Gonzalez-Vilchez, F.; Griffith, W. P. *J. Chem. Soc., Dalton Trans.* **1972**, 1416-1421.
- (209) Varetti, E. L.; Müller, A. Z. *Anorg. Allg. Chem.* **1978**, *422*, 230-234.
- (210) Varetti, E. L.; Filgueira, R. R.; Müller, A. *Spectrochim. Acta, Part A* **1981**, *37*, 369-373.
- (211) Edwards, H. G. M.; Ware, M. J.; Woodward, L. A. *Chem. Commun.* **1968**, 540-541.
- (212) Edwards, H. G. M.; Woodward, L. A.; Gall, M. J.; Ware, M. J. *Spectrochim. Acta* **1970**, *26A*, 287-290.

# Chapter 2

**Mn K-Edge XANES and K $\beta$  XES Studies of Two Mn-oxo Binuclear Complexes. Investigation of Three Different Oxidation States Relevant to the Oxygen-Evolving Complex of Photosystem II**

## 2.1 Introduction

In green plants and cyanobacteria, light-induced water oxidation is performed by a membrane-bound protein cluster, photosystem II (PS II). This protein cluster contains an active site, the oxygen-evolving complex (OEC), where water binds and is oxidized during four consecutive photon-induced electron extractions. In the absence of high-resolution crystallographic information, most of the structural information about the OEC comes from X-ray absorption spectroscopy (XAS) and EPR studies on PS II<sup>1-9</sup> and on model complexes.<sup>10-15</sup> These techniques have been used to investigate both the structure of the OEC and the mechanism of water oxidation.<sup>16-21</sup> The consensus is that the OEC contains four manganese atoms, consisting of two to three di- $\mu$ -oxo Mn-Mn moieties and one mono- $\mu$ -oxo Mn-Mn moiety. Kok et al.<sup>22</sup> proposed that water is oxidized in five stages, called S-states ( $S_0$  -  $S_4$ ), with the index indicating the number of stored oxidizing equivalents. An electron is extracted during each of the first four light-induced transitions,  $S_0 \rightarrow S_1$ ,  $S_1 \rightarrow S_2$ ,  $S_2 \rightarrow S_3$  and  $S_3 \rightarrow [S_4] \rightarrow S_0$ . Dioxygen is released during the last transition, when the  $S_3$  state returns to the  $S_0$  state via the hypothesized  $S_4$  state.

To understand the mechanism of water oxidation in more detail, it is important to know at each stage whether the extracted electrons are coming directly from bound water, from the Mn atoms, or from any other parts of the OEC. Both EPR and Mn K-edge X-ray absorption near-edge structure (XANES) have been used extensively to investigate the involvement of the Mn atoms in water oxidation. Based on the results of these techniques there is consensus that Mn is oxidized during the  $S_0 \rightarrow S_1$  and  $S_1 \rightarrow S_2$  transitions. However, there is still controversy concerning the involvement of Mn

oxidation in the  $S_2 \rightarrow S_3$  transition. Roelofs et al.<sup>23</sup> concluded that there is no Mn oxidation in the  $S_2 \rightarrow S_3$  transition, based on the absence of a significant shift in the XANES spectra between  $S_2$  and  $S_3$ , and proposed that a ligand is oxidized. However, Ono et al.<sup>24</sup> and Iuzzolino et al.<sup>25</sup> concluded, based on observed shifts in their XANES data, that Mn oxidation is involved in this transition.

Recently, Messinger et al.<sup>21</sup> performed a modified version of the experiment done by Roelofs et al.,<sup>23</sup> using XANES and an additional technique, Mn  $K\beta$  X-ray emission spectroscopy ( $K\beta$  XES).<sup>26,27</sup> Like XANES,  $K\beta$  XES is element-specific, but in comparison to XANES it has the advantage that it is more sensitive to the oxidation state and less sensitive to the ligand environment of the manganese atoms.

XANES results from the excitation of a 1s electron (K-shell) to a higher, bound orbital (Figure 2.1). The higher the oxidation state of the metal, the more positive the overall charge of the atom, and the more energy is required to excite an electron out of an orbital.<sup>28</sup> The first formally allowed electric-dipole transition is the  $1s \rightarrow 4p$  transition. Due to the size of the 4p orbital, it overlaps with p-orbitals of the ligands, either through  $\sigma$  or  $\pi$  bonding. Consequently, this transition is sensitive to the oxidation state and the ligand environment of the metal. For certain symmetries around the metal, the formally electric-dipole forbidden  $1s \rightarrow 3d$  transition can be observed, occurring at a lower energy than the main edge transitions.<sup>29</sup> This transition is due to mixing of metal 3d and 4p orbitals and gives information about the ligand as well as about the oxidation state and symmetry of the metal complex.<sup>30,31</sup> To increase the sensitivity of XANES, absorption is detected as an excitation spectrum by measuring the  $K\alpha$  fluorescence of the Mn atoms.<sup>32</sup>



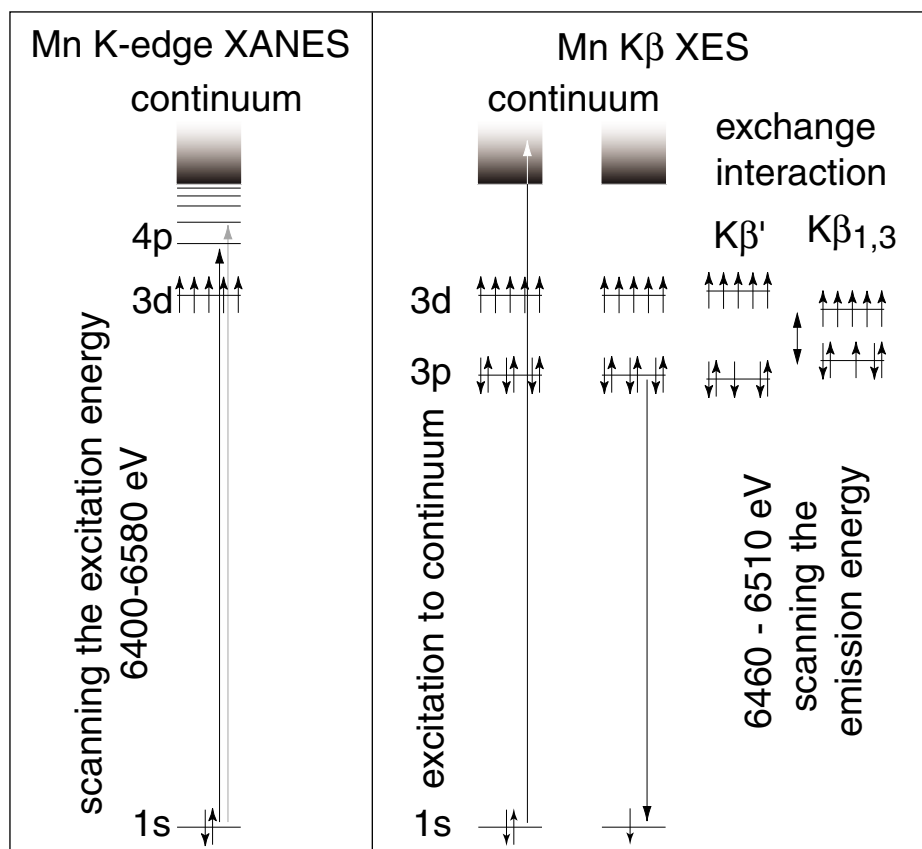


Figure 2.1 A schematic for the excitation and emission processes involved in XANES and  $K\beta$  XES spectroscopy. XANES spectra reflect the transition energy of  $1s$  electrons excited to higher bound states, which depends on the overall charge and ligand environment of the metal.<sup>28</sup> To enhance sensitivity, the absorption spectra are collected as excitation spectra using Mn  $K\alpha$  fluorescence detection.  $K\beta$  XES arise from the emission of a  $3p$  electron to  $1s$  hole, which is formed following X-ray absorption. In a simplified model, two final spin states exist with either a constructive ( $K\beta_{1,3}$ ) or destructive ( $K\beta'$ ) spin exchange interaction between the unpaired  $3p$  and  $3d$  electrons. The magnitude of the interaction depends on the number of unpaired  $3d$  electrons, which is related to the oxidation state of the metal. For a more accurate model, the ligand-field multiplet formalism needs to be applied, taking into account spin-spin and spin-orbit interactions, ligand-field splitting, and Jahn-Teller distortions.<sup>27</sup>

In contrast to XANES,  $K\beta$  XES detects the X-ray emission from the relaxation of a 3p electron to a 1s hole, which is created by excitation of a 1s electron into the continuum (Figure 2.1). In a simplified model, two final states exist due to a constructive ( $K\beta_{1,3}$ ) or destructive ( $K\beta'$ ) spin-exchange interaction between the unpaired electrons in the 3p and 3d orbitals.<sup>33,34</sup> The magnitude of the exchange interaction depends on the number of unpaired electrons in the 3d orbital. Increasing the oxidation state of the metal decreases the number of unpaired 3d electrons, in the high spin case; concomitantly, the spin exchange interaction decreases. Accordingly, the  $K\beta_{1,3}$  transition shifts to a higher and the  $K\beta'$  transition shifts to a lower energy.<sup>27,35-37</sup> Compared to the 4p orbitals, the 3p orbitals have less overlap with the ligand orbitals, because they are smaller and more buried within the electronic shells. Therefore,  $K\beta$  XES is less sensitive to the ligand environment compared to XANES. The  $K\beta_{1,3}$  transition is better resolved than the  $K\beta'$  transition due to a difference in relaxation processes.<sup>38</sup> Hence, the  $K\beta_{1,3}$  transition is used here as an indicator of the oxidation state of the metal.

A more accurate view on  $K\beta$  XES requires the ligand-field multiplet formalism. For example, in the atomic picture, a  $Mn^{II}$  atom has five 3d electrons ( ${}^6S$  term state) and one unpaired 3p electron ( ${}^2S$ ) after  $K\beta$  emission. A variety of spin multiplet states exists when the spin-spin exchange interaction is included; two of the main states are the  ${}^7P$  (part of  $K\beta_{1,3}$ ) and the  ${}^5P$  (part of  $K\beta'$ ) symmetry. Using this formalism enables inclusion of other symmetry-dependent perturbations such as spin-orbit coupling, ligand-field splitting, Jahn-Teller distortion and, in case of multi-nuclear compounds, spin-spin interaction between different metal atoms. Each of these perturbations will split the spin states into a multiplet of states, causing an asymmetric broadening of the observed

emission peaks. This indicates that there is some dependence of the ligand environment on  $K\beta$  XES spectra.

On the basis of the results from both these techniques, it was concluded that no manganese oxidation accompanies the  $S_2 \rightarrow S_3$  transition.<sup>21</sup> Nevertheless, some supporters of manganese oxidation in the  $S_2 \rightarrow S_3$  transition argue that two opposing effects cause the lack of a shift in XANES and  $K\beta$  XES data. A structural change occurs in the OEC during the  $S_2 \rightarrow S_3$  transition,<sup>3</sup> which could offset the effects due to manganese oxidation. To resolve this issue, the influence of oxidation-state and structural changes on XANES and  $K\beta$  XES spectra needs to be established. To address this question, two manganese compounds in solution are studied here to investigate the influence of oxidation state versus ligand environment on XANES and  $K\beta$  XES data.

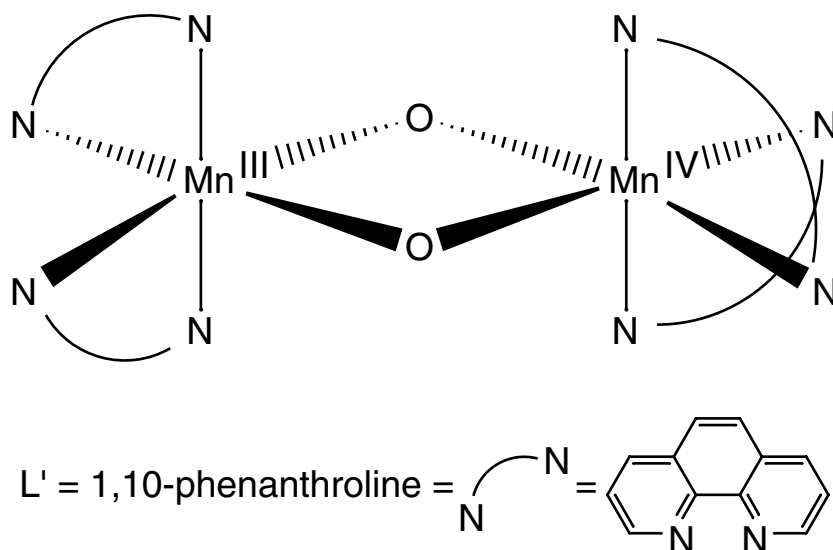


Figure 2.2 The di- $\mu$ -oxo manganese compound  $[L'_2 Mn^{III}O_2Mn^{IV}L'_2]^{3+}$ , with  $L'$  as 1,10-phenanthroline.<sup>10,39,40</sup>

The two compounds studied are the di- $\mu$ -oxo bridged compound  $[\text{L}'_2\text{Mn}^{\text{III}}\text{O}_2\text{Mn}^{\text{IV}}\text{L}'_2](\text{ClO}_4)_3$ , where L' is 1,10-phenanthroline<sup>10</sup> (Figure 2.2) and the mono- $\mu$ -oxo bridged compound  $[\text{LMn}^{\text{III}}\text{OMn}^{\text{III}}\text{L}](\text{ClO}_4)_2$ , where L<sup>-</sup> is the mono-anionic *N,N*-bis(2-pyridylmethyl)-*N'*-salicylidene-1,2-diaminoethane ligand<sup>41</sup> (Figure 2.3). The di- $\mu$ -oxo compound has a diamond-core  $\text{Mn}^{\text{III}}\text{-O}_2\text{-Mn}^{\text{IV}}$  unit with a Mn–Mn distance of 2.75 Å. One reversible wave is observed in the cyclic voltammetry at  $E^{1/2} = +1.26$  V vs. SCE of a  $[(\text{L}')_2\text{Mn}^{\text{III}}\text{O}_2\text{Mn}^{\text{IV}}(\text{L}')_2]^{3+}$  acetonitrile solution for the  $(\text{Mn}^{\text{III}}\text{Mn}^{\text{IV}} \rightleftharpoons \text{Mn}^{\text{IV}}\text{Mn}^{\text{IV}} + e^\pm)$  couple.<sup>10,39,40</sup> The mono- $\mu$ -oxo compound contains a linear  $\text{Mn}^{\text{III}}\text{-O-Mn}^{\text{III}}$  unit with a Mn–Mn distance of 3.52 Å. Cyclic voltammetry of a solution of  $[\text{LMn}^{\text{III}}\text{OMn}^{\text{III}}\text{L}]^{2+}$  in acetonitrile shows two reversible waves at  $E_1^{1/2} = +0.54$  V vs. SCE and at  $E_2^{1/2} = +0.99$  V vs. SCE. for the  $(\text{Mn}^{\text{III}}\text{Mn}^{\text{III}} \rightleftharpoons \text{Mn}^{\text{III}}\text{Mn}^{\text{IV}} + e^\pm)$  and  $(\text{Mn}^{\text{III}}\text{Mn}^{\text{IV}} \rightleftharpoons \text{Mn}^{\text{IV}}\text{Mn}^{\text{IV}} + e^\pm)$  couples, respectively.<sup>42-45</sup>

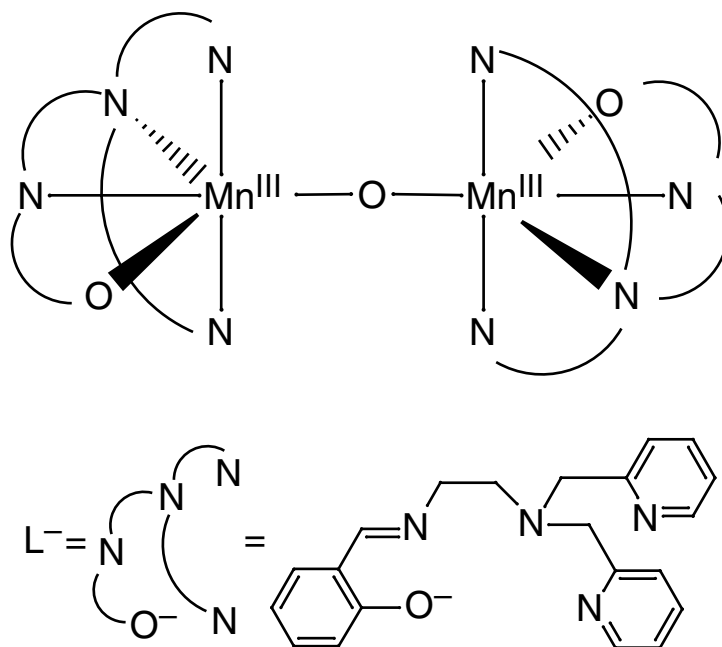


Figure 2.3 The linear mono- $\mu$ -oxo compound,  $[\text{LMn}^{\text{III}}\text{OMn}^{\text{III}}\text{L}]^{2+}$ , with L<sup>-</sup> as the anionic *N,N*-bis(2-pyridylmethyl)-*N'*-salicylidene-1,2-diaminoethane ligand.<sup>41,42</sup>

Samples of the different oxidation states of both compounds are made by preparative bulk electrolysis. To determine the extent of the influence of oxidation state and ligand environment on the Mn K-edge XANES and K $\beta$  XES spectra, pure oxidation-state compound spectra are required. However, the electrochemical preparation of the different oxidation states for each compound is not 100% complete. Therefore, UV/vis and EPR spectroscopies are used to determine the manganese species present in the electrochemical solutions. This information is used to deconvolute the measured spectra into pure oxidation state spectra. EXAFS spectroscopy is used as an additional tool to verify the integrity of the electrochemically prepared compounds. By comparing the different oxidation states for each compound, the effect of manganese oxidation on XANES and K $\beta$  XES data is studied. The influence of ligands is investigated by comparing the spectra of the two compounds in equivalent manganese oxidation states. This is the first such study of structurally homologous Mn compounds in different oxidation states using XAS and K $\beta$  XES methodology.

## 2.2 Experimental

**Preparation of di- $\mu$ -oxo compound samples:** Synthesis of the di- $\mu$ -oxo compound,  $[\text{L}'_2\text{Mn}^{\text{III}}\text{O}_2\text{Mn}^{\text{IV}}\text{L}'_2](\text{ClO}_4)_3$  with L' as 1,10-phenanthroline, is adapted from the published procedure by Cooper et al.<sup>10</sup> The IR spectrum of the recrystallized solid compound was recorded to determine the purity, and it matches the published data.<sup>10</sup> Electrochemistry of  $[\text{L}'_2\text{Mn}^{\text{III}}\text{O}_2\text{Mn}^{\text{IV}}\text{L}'_2]^{3+}$  in acetonitrile shows one anodic wave at +1.26 V vs. SCE, corresponding to the  $(\text{Mn}^{\text{III}}\text{Mn}^{\text{IV}} \rightleftharpoons \text{Mn}^{\text{IV}}\text{Mn}^{\text{IV}} + e^\pm)$  couple. The

$[\text{L}'_2\text{Mn}^{\text{IV}}\text{O}_2\text{Mn}^{\text{IV}}\text{L}'_2]^{4+}$  cation is prepared from a  $1.7 \times 10^{-4}$  M  $\text{Mn}^{\text{III}}\text{Mn}^{\text{IV}}$  di- $\mu$ -oxo compound solution at +1.4 V vs. SCE under an argon atmosphere at room temperature. Figure 2.4 shows a scheme of the two compound fractions as a function of time during electrochemistry. Samples are extracted at different times during the electrolysis experiment for XAS,  $\text{K}\beta$  XES, UV/vis and quantitative EPR. In the nomenclature of the electrochemical samples, the first letter denotes the kind of compound, 'di' refers to the di- $\mu$ -oxo compound, and 'mono' refers to the mono- $\mu$ -oxo compound. The Roman numerals between brackets indicate the desired oxidation state of the compound. Different extraction time-points are indicated by subscripts. The samples from the di- $\mu$ -oxo compound,  $[\text{L}'_2\text{Mn}^{\text{III}}\text{O}_2\text{Mn}^{\text{IV}}\text{L}'_2] (\text{ClO}_4)_3$ , are designated **di(III,IV)**, **di(IV,IV)<sub>A</sub>**, and **di(IV,IV)<sub>B</sub>**.

UV/vis spectroscopy could not be used to follow the progress of the electrolysis of the di- $\mu$ -oxo compound, because the strong absorption bands of the  $\text{Mn}^{\text{III}}\text{Mn}^{\text{IV}}$  and  $\text{Mn}^{\text{IV}}\text{Mn}^{\text{IV}}$  species are obscured by the absorption of free terminal ligand, 1,10-phenanthroline. However, the starting  $\text{Mn}^{\text{III}}\text{Mn}^{\text{IV}}$  di- $\mu$ -oxo compound is EPR-active ( $S=1/2$ , with a distinctive 16-line spectrum) and the  $\text{Mn}^{\text{IV}}\text{Mn}^{\text{IV}}$  species is EPR-silent ( $S=0$ ).<sup>47</sup> Therefore, the EPR spectra of the **di(IV,IV)** samples are used to determine the degree of completion of the oxidation step by measuring the decline in the  $\text{Mn}^{\text{III}}\text{Mn}^{\text{IV}}$  species.

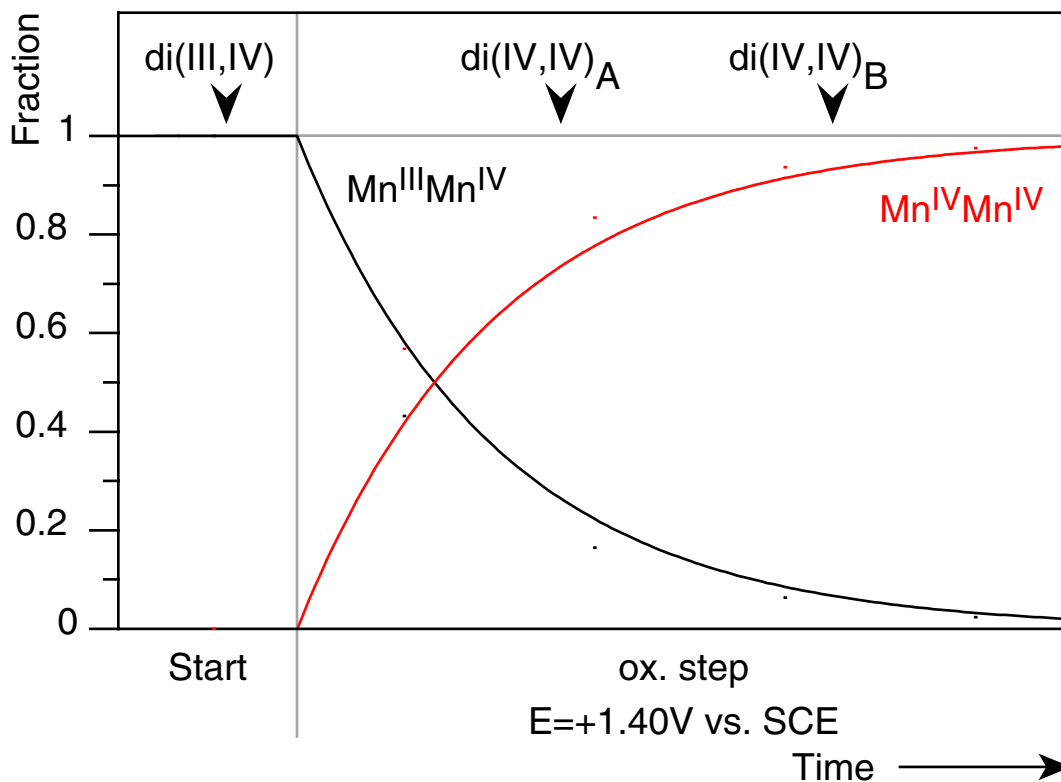


Figure 2.4 Scheme of the time course for the oxidation reaction of the  $\text{di-}\mu\text{-oxo}$  compound. The arrows indicate sample extractions. The  $\text{Mn}^{\text{III}}\text{Mn}^{\text{IV}}$  compound ( $\text{di(III,IV)}$ ) is an EPR-active  $\text{di-}\mu\text{-oxo}$  species. The  $\text{Mn}^{\text{IV}}\text{Mn}^{\text{IV}}$  species is stable and EPR-silent. The EPR spectra of the  $\text{di(IV,IV)}$  samples are analyzed to determine the decline in the  $\text{Mn}^{\text{III}}\text{Mn}^{\text{IV}}$  concentration. The EPR spectrum of the starting sample ( $\text{di(III,IV)}$ ) is used as the pure  $\text{Mn}^{\text{III}}\text{Mn}^{\text{IV}}$  quantitative standard.

**Preparation of mono- $\mu$ -oxo compound samples:** Synthesis of the mono- $\mu$ -oxo compound,  $[\text{LMn}^{\text{III}}\text{OMn}^{\text{III}}\text{L}](\text{ClO}_4)_2$  with  $\text{L}^-$  as the mono-anionic *N,N*-bis(2-pyridylmethyl)-*N'*-salicylidene-1,2-diaminoethane ligand is according to the procedure by Horner et al.<sup>41</sup> The mono- $\mu$ -oxo compound is recrystallized, and it was determined that the IR spectrum agrees with the published data.<sup>41</sup> Cyclic voltammetry of  $[\text{LMn}^{\text{III}}\text{OMn}^{\text{III}}\text{L}]^{2+}$  in acetonitrile shows two reversible anodic waves at: +0.54 V vs. SCE for the  $(\text{Mn}^{\text{III}}\text{Mn}^{\text{III}} \rightleftharpoons \text{Mn}^{\text{III}}\text{Mn}^{\text{IV}} + e^\pm)$  couple and at +0.99 V vs. SCE for the  $(\text{Mn}^{\text{III}}\text{Mn}^{\text{IV}} \rightleftharpoons \text{Mn}^{\text{IV}}\text{Mn}^{\text{IV}} + e^\pm)$  couple.<sup>41,42</sup> The cation  $[\text{LMn}^{\text{III}}\text{OMn}^{\text{IV}}\text{L}]^{3+}$  is prepared from a  $5.0 \times 10^{-4}$  M  $\text{Mn}^{\text{III}}\text{Mn}^{\text{III}}$  mono- $\mu$ -oxo compound solution by bulk electrolysis at  $E = +0.85$  V vs. SCE under argon atmosphere at  $-35$  °C. To prepare the  $[\text{LMn}^{\text{IV}}\text{OMn}^{\text{IV}}\text{L}]^{4+}$  cation, the potential is raised to +1.3 V vs. SCE. Figure 2.5 shows a scheme of the different mono- $\mu$ -oxo compound fractions during the two electrochemical steps. At different times during the electrochemical experiment, samples are extracted for XAS,  $\text{K}\beta$  XES, UV/vis and quantitative EPR as indicated in Figure 2.5. The samples from the mono- $\mu$ -oxo compound,  $[\text{LMn}^{\text{III}}\text{OMn}^{\text{III}}\text{L}](\text{ClO}_4)_2$ , are designated by **mono(III,III)**, **mono(III,IV)**, and **mono(IV,IV)<sub>A</sub>** through **mono(IV,IV)<sub>F</sub>**.



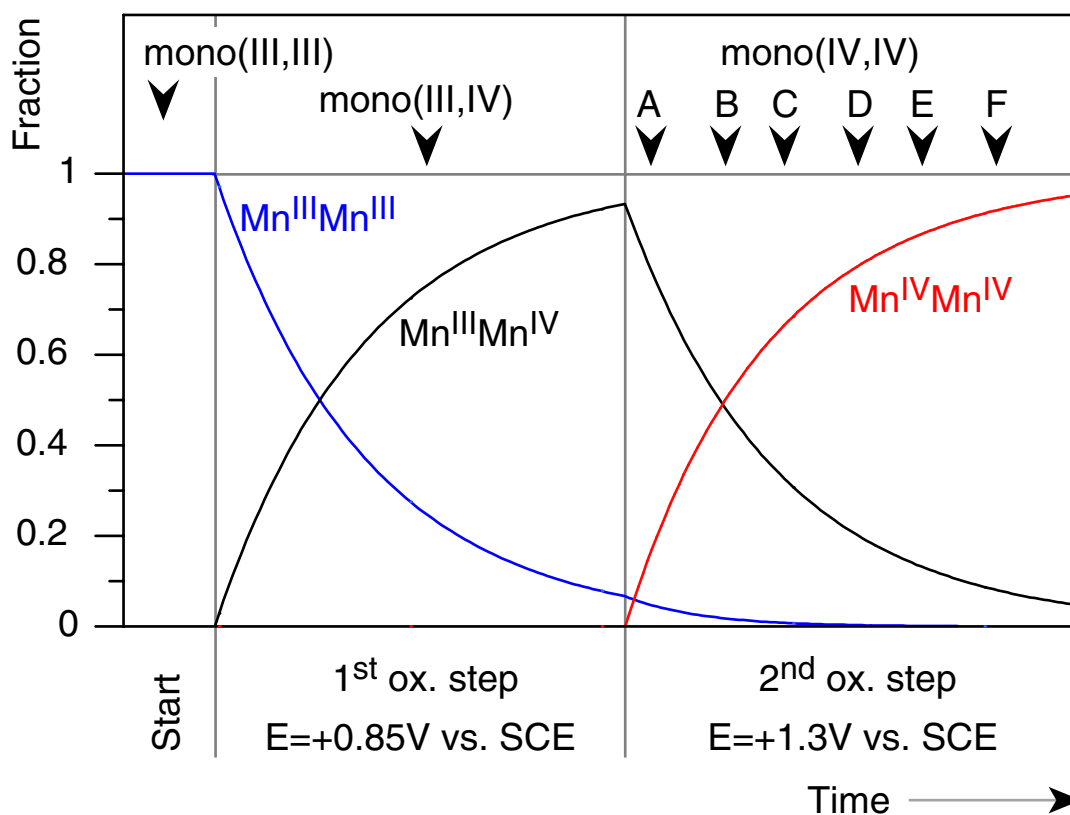


Figure 2.5 Scheme of the time course for the oxidation reactions of the mono- $\mu$ -oxo compound. The arrows indicate sample extractions. UV/vis absorption coefficients of the  $\text{Mn}^{\text{III}}\text{Mn}^{\text{III}}$  and  $\text{Mn}^{\text{III}}\text{Mn}^{\text{IV}}$  compounds are used to determine the starting concentration (**mono(III,III)**), and the degree of completion of the first oxidation step (**mono(III,IV)**). The  $\text{Mn}^{\text{III}}\text{Mn}^{\text{IV}}$  compound is the only EPR-active mono- $\mu$ -oxo species; it has a distinctive 18-line spectrum. When water is present in the electrochemical solution, the  $\text{Mn}^{\text{IV}}\text{Mn}^{\text{IV}}$  species decomposes into  $\text{Mn}^{\text{II}}$ , which has a distinctive six-line EPR spectrum. Therefore, the EPR spectra of the **mono(IV,IV)** samples are analyzed to determine the decline in the  $\text{Mn}^{\text{III}}\text{Mn}^{\text{IV}}$  concentration and the appearance of the decomposition product  $\text{Mn}^{\text{II}}$ . The EPR spectrum of sample **mono(III,IV)** is used as the  $\text{Mn}^{\text{III}}\text{Mn}^{\text{IV}}$  quantitative standard, and a  $\text{MnCl}_2$  acetonitrile solution as the  $\text{Mn}^{\text{II}}$  quantitative EPR standard.

UV/vis absorption is used to determine the extent of the first oxidation step (sample **mono(III,IV)**), i.e. the ratio between the  $\text{Mn}^{\text{III}}\text{Mn}^{\text{III}}$  and  $\text{Mn}^{\text{III}}\text{Mn}^{\text{IV}}$  species. To monitor the progress of the second oxidation step, EPR spectroscopy is used, because the  $\text{Mn}^{\text{III}}\text{Mn}^{\text{IV}}$  species has a distinctive 18-line spectrum ( $S=1/2$ ) and the  $\text{Mn}^{\text{III}}\text{Mn}^{\text{III}}$  and  $\text{Mn}^{\text{IV}}\text{Mn}^{\text{IV}}$  species are both EPR-silent ( $S=0$ ). Using this signal, the EPR spectra of the **mono(IV,IV)** samples are analyzed to determine the decline in the  $\text{Mn}^{\text{III}}\text{Mn}^{\text{IV}}$  fraction. By subtracting the  $\text{Mn}^{\text{III}}\text{Mn}^{\text{IV}}$  fractions from 1.0, the increasing  $\text{Mn}^{\text{IV}}\text{Mn}^{\text{IV}}$  fraction in the **mono(IV,IV)** samples is calculated. When water is present in the electrolyte, the  $\text{Mn}^{\text{IV}}\text{Mn}^{\text{IV}}$  species is unstable<sup>41</sup> and decomposes into  $\text{Mn}^{\text{II}}$ , which has a distinctive six-line EPR signal ( $S=5/2$ ). Even though great care is taken to keep solvents dry, a small amount of decomposition is observed. Therefore, EPR is used to correct the  $\text{Mn}^{\text{IV}}\text{Mn}^{\text{IV}}$  fraction for this small amount of decomposition. To determine the  $\text{Mn}^{\text{II}}$  fraction in the **mono(IV,IV)** samples a  $1.0 \times 10^{-3}$  M  $\text{MnCl}_2$  electrolyte solution is used as an analog for the decomposed compound.

**Cyclic voltammetry and bulk electrolysis.** For electrochemical experiments an electrolyte solution of 0.2 M tetrabutylammonium perchlorate (Puriss Fluka) in high-quality acetonitrile (Burdick & Jackson) is used. For each complex, cyclic voltammetry is run before electrolysis. A platinum disk of 1.5 mm diameter is used as a working electrode for cyclic voltammetry. For bulk electrolysis in a double-jacketed cylindrical cell, a cylindrical Pt grid of about 20 mm diameter is used as a working electrode. The auxiliary electrode is made of a Pt grid in a glass tube with a fritted glass disk at the end to separate the electrode from the sample solution. The reference electrode is  $\text{Ag}/\text{AgClO}_4$  in 0.1 M  $\text{TBA}(\text{ClO}_4)$  acetonitrile (270 mV more positive than SCE). Cyclic voltammetry

and bulk electrolysis are conducted using a BAS CV-27 Voltammetry Controller. Bulk electrolysis for the di- $\mu$ -oxo compound is performed at room temperature and it is performed at  $-35\text{ }^{\circ}\text{C}$  for the mono- $\mu$ -oxo compound.

To minimize degradation during electrochemistry, the electrolyte solution is dried by running it through an  $\text{Al}_2\text{O}_3$  column. Additionally, the final solutions are carefully degassed in the electrochemical cell with argon for approximately 30 min. The entire electrochemical cell is situated in a glove bag, which is flushed with dry nitrogen to decrease product degradation during the transfer of solutions. The oxidized samples are transferred from the electrolysis cell to the X-ray sample holders and precision EPR tubes using nitrogen-flushed pipettors, and immediately frozen in liquid nitrogen.

**UV/vis spectroscopy.** Absorbance measurements are recorded on an AVIV 14DS UV-VIS-NIR Spectrophotometer (AVIV, Lakewood, NJ) with a bandwidth of 0.25 nm, a step size of 1 nm, and an averaging time of 0.1 s per measured wavelength. Absorption spectra are baseline-corrected using an electrolyte solution. All measurements are conducted in a 0.2 mm pathlength demountable quartz cell (T-19, NSG Precision Cells, Inc.).

**EPR spectroscopy.** Low-temperature X-band ( $\sim 9.2\text{ GHz}$ ) EPR spectra are recorded using a Varian E-109 EPR spectrometer with a TE102 cavity and magnetic field modulation at 100 kHz. All spectra are measured at 20 K using an Air Products LTR liquid helium cryostat. Modulation amplitudes for the di- $\mu$ -oxo and mono- $\mu$ -oxo compounds are 25 G and 20 G, respectively. The microwave power is  $1\text{ }\mu\text{W}$  for the di- $\mu$ -oxo compound and  $100\text{ }\mu\text{W}$  for the mono- $\mu$ -oxo compounds. Quantitative EPR is performed with precision EPR tubes from Wilmad (706 PQ), with a  $\pm 3\%$  volume error.

EPR spectra of the XAS samples are measured in the same Lucite holders that are used for the X-ray experiments.

**Mn K-edge X-ray absorption spectroscopy.** Mn K-edge absorption spectra are collected at the wiggler beamline 7-3 at Stanford Synchrotron Radiation Laboratory (SSRL) with SPEAR operating at ring currents of 40 - 100 mA at 3.0 GeV. The X-ray beam is used unfocused, with an energy-scanning Si[220] double-crystal monochromator detuned to 50% to attenuate higher harmonics.<sup>48</sup> The Mn absorption spectra are recorded as fluorescence excitation spectra<sup>32</sup>, using an energy-resolving 13-element Ge detector (Canberra Instruments).<sup>49</sup> Ionization chamber detectors ( $I_0$ ,  $I_1$  and  $I_2$ ) are filled with dinitrogen gas. Absorption is related to the fluorescence signal divided by the incident flux ( $A = F/I_0$ ).<sup>32</sup> A  $\text{KMnO}_4$  standard, placed between the rear ionization chambers  $I_1$  and  $I_2$ , is used to monitor the energy calibration and resolution. The  $\text{KMnO}_4$  standard has a narrow pre-edge line at 6543.3 eV, the full width at half height is less than 1.7 eV in the absorption spectrum ( $\log(I_1/I_2)$ ). To reduce radiation damage, samples are kept in a gaseous helium atmosphere at ambient pressure and at a temperature of  $10 \pm 1$  K, using a liquid helium flow cryostat (Oxford Instruments CF 1208).

XANES spectra are collected from 6520 to 6580 eV, with a step size of 0.2 eV. Reproducibility of the Mn K-edge energy in these conditions is typically  $\pm 0.1$  eV.<sup>23</sup> EXAFS spectra are collected from 6530 - 7100 eV. The 6540 - 6550 eV region is measured in 0.25 eV steps to obtain an accurate energy calibration using the  $\text{KMnO}_4$  standard. The rest of the pre-edge and edge region, 6530 - 6576 eV, is measured in 1.0 eV steps. The EXAFS region, 6576 - 7100 eV, is measured in equal  $k$ -range (eq. 1) steps of  $0.05 \text{ \AA}^{-1}$ .

Data analysis for the Mn K-edge XANES and EXAFS has been published earlier<sup>23,48,50</sup> and is described here briefly. For both types of data (XANES and EXAFS), a linear pre-edge background is removed from the spectra. Subsequently, the post-edge region (6630 - 7100 eV) is fit with a quadratic polynomial and normalized to the absorption of one free Mn atom, i.e. the amplitude of the polynomial at 6558.0 eV is set to 1. For XANES, the first inflection-point energy (IPE) of the second-derivative spectrum is taken as an indicator of the Mn K-edge energy for each compound. Derivatives of the spectra are obtained by analytically deriving a third-order polynomial fit to the data over a sliding  $\pm 1.5$  eV interval for each data point.

In addition, the EXAFS data are used to determine the integrity of the electrochemically prepared compounds. Therefore, only the radial distribution of backscatterers for the Mn atoms is of interest; no additional effort is taken to fit this radial distribution to specific elements. A quadratic polynomial fit is removed from the post-edge region of the EXAFS spectrum. Subsequently, the EXAFS spectrum is converted from  $E$ -space to  $k$ -space, the photoelectron wave vector ( $\text{\AA}^{-1}$ ), as described in eq. 2.1:<sup>51</sup>

$$k = \left( \frac{2\pi}{h} \right) \sqrt{2m_e(E - E_0)} \quad (\text{eq. 2.1})$$

where  $k$  is the photon electron wave vector ( $\text{\AA}^{-1}$ ),  $h$  is Planck's constant,  $m_e$  is the electron mass, and  $E$  is the X-ray energy.  $E_0$  is the Mn ionization threshold energy, which is chosen to be the same for all compounds to enable comparison of  $k$ -space and Fourier-transformed spectra.  $E_0$  is chosen to be 6558.0 eV, which is the average energy of the first edge maximum for all the model compounds. The EXAFS data are weighted by  $k^3$  and forward Fourier-transformed into  $R$ -space ( $\text{\AA}$ ); the  $k^3$ -range is 3.5 - 11.6  $\text{\AA}^{-1}$ .

Due to the quality of the data, no low-frequency background removal is necessary in the  $k^3$ -data.

**Mn K $\beta$  X-ray emission spectroscopy.** K $\beta$  XES spectra are collected at the wiggler beamline 10-2 at Stanford Synchrotron Radiation Laboratory (SSRL) with SPEAR operating at ring currents of 40 - 100 mA at 3.0 GeV. The X-ray beam at 9.2 keV is focused to a 1 mm  $\times$  4 mm spot, with a flux of approximately  $3 \times 10^{11}$  photons/sec. Samples are positioned at a 45° angle to the X-ray beam. Variations in the incident beam intensity ( $I_0$ ) are monitored using an ionization-chamber detector filled with dinitrogen gas. The fluorescence emission spectra are measured using a high-resolution crystal-array spectrometer, which consists of a solid-state detector positioned in the focus of eight Bragg-diffracting Si(440) crystals.<sup>52</sup> The resolution under our experimental conditions is  $\sim 1.0$  eV; a detailed description is given in Bergmann et al.<sup>52</sup> Samples are protected from radiation damage by keeping them in a gaseous helium atmosphere at ambient pressure and at a temperature of  $10 \pm 1$  K, using a liquid helium flow cryostat (Oxford Instruments CF 1208). Energy calibration and reproducibility are monitored by assigning the 1<sup>st</sup> moment of a solid Mn<sub>2</sub>O<sub>3</sub> sample to 6490.40 eV. Using these procedures a energy-determination accuracy of  $\leq 0.01$  eV within a run and  $\leq 0.03$  eV between runs is achieved. The di- $\mu$ -oxo compound spectra were collected in a separate run from the mono- $\mu$ -oxo compound spectra.

K $\beta$  XES spectra are collected from 6467.2 to 6510.9 eV at 5 sec/point. The step size ranges from 0.1 to 0.24 eV. The K $\beta$  XES spectra of the dilute compounds have a linear background resulting from Compton scattering. This background is determined by aligning spectral regions that are oxidation-state independent, i.e. outside the 6470 -

6505 eV range, to those of concentrated Mn oxides (MnO, Mn<sub>2</sub>O<sub>3</sub>, and MnO<sub>2</sub>). The result is then fit with a linear function and subtracted from the experimental data. To simplify mathematical operations, the spectra are splined onto a grid of 0.1 eV energy steps. Concomitantly, the integrated area from 6468 to 6510 eV of each spectrum is normalized to 1. The 1<sup>st</sup> moment,  $\langle E \rangle$ , of the K $\beta_{1,3}$  peak is calculated between 6485 and 6495 eV using eq. 2.2, and is used as an energy indicator.

$$\langle E \rangle = \frac{\sum_i E_i \cdot I_i}{\sum_i I_i} \quad (\text{eq. 2.2})$$

where  $I_i$  is the background-corrected emission intensity at each energy  $E_i$ .

## 2.3 Results

### Analysis of di- $\mu$ -oxo compound solutions

Figure 2.6 presents the EPR spectra of different samples during the electrochemistry of the di- $\mu$ -oxo compound (also see Figure 2.4). The EPR spectrum of the **di(III,IV)** sample matches the published spectrum for the Mn<sup>III</sup>Mn<sup>IV</sup> di- $\mu$ -oxo compound in acetonitrile.<sup>47</sup> Only a small amount of the Mn<sup>III</sup>Mn<sup>IV</sup> species signal remains in the **di(IV,IV)<sub>B</sub>** EPR spectrum. The Mn<sup>III</sup>Mn<sup>IV</sup> fraction of the **di(IV,IV)** sample is calculated by subtracting a fractional part of the **di(III,IV)** EPR spectrum from the **di(IV,IV)** spectrum to obtain the minimal least-square value of the residual spectrum. Table 2.1 shows that, during the electrolysis, the Mn<sup>III</sup>Mn<sup>IV</sup> fraction decreases over time to 0.19 and 0.04 for the **di(IV,IV)<sub>A</sub>** and **di(IV,IV)<sub>B</sub>** samples, as indicated in Figure 2.4. Table 2.2 summarizes the fractions and errors that are used to calculate pure oxidation-state X-ray spectra of the di- $\mu$ -oxo compound from sample **di(III,IV)** and **di(IV,IV)<sub>B</sub>**.

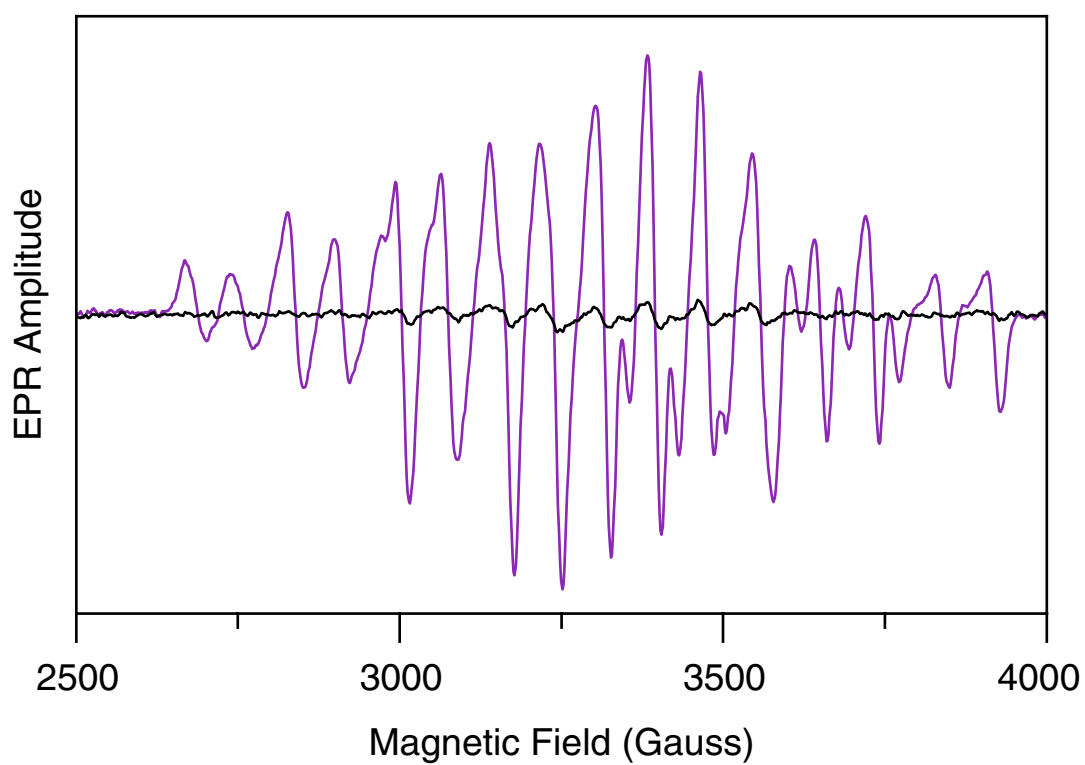


Figure 2.6 The EPR spectra of the  $di-\mu$ -oxo compound at two different stages during the electrochemistry: sample **di(III,IV)**, the starting solution (purple); and sample **di(IV,IV)<sub>B</sub>**, the final solution after the oxidation step (black).



### Analysis of mono- $\mu$ -oxo compound solutions

The EPR spectra of different samples during the electrochemistry of the mono- $\mu$ -oxo compound solution are shown in Figure 2.7. As expected, the starting solution, sample **mono(III,III)**, has no significant EPR signals, because the  $\text{Mn}^{\text{III}}\text{Mn}^{\text{III}}$  species is EPR-silent. Sample **mono(III,IV)** shows the characteristic 18-line EPR spectrum of the  $\text{Mn}^{\text{III}}\text{Mn}^{\text{IV}}$  mono- $\mu$ -oxo compound in acetonitrile.<sup>41</sup> This indicates that, during the first oxidation step, the  $\text{Mn}^{\text{III}}\text{Mn}^{\text{III}}$  species is oxidized to the EPR-active  $\text{Mn}^{\text{III}}\text{Mn}^{\text{IV}}$  species (Figure 2.5). The degree of conversion during the first oxidation step is calculated from a UV/vis spectrum of sample **mono(III,IV)** (see Appendix 2.6) and published absorption coefficient data of the  $\text{Mn}^{\text{III}}\text{Mn}^{\text{III}}$  and  $\text{Mn}^{\text{III}}\text{Mn}^{\text{IV}}$  species.<sup>41</sup> The reliability of this method is examined by comparing the total concentration of the  $\text{Mn}^{\text{III}}\text{Mn}^{\text{III}}$  and  $\text{Mn}^{\text{III}}\text{Mn}^{\text{IV}}$  with the starting  $\text{Mn}^{\text{III}}\text{Mn}^{\text{III}}$  mono- $\mu$ -oxo compound concentration. Using a least-square fit for the UV/vis absorption values at 335, 380, 400, 480, 495, and 550 nm (data not shown) the  $\text{Mn}^{\text{III}}\text{Mn}^{\text{III}} : \text{Mn}^{\text{III}}\text{Mn}^{\text{IV}}$  ratio is calculated to be 23 : 77 ( $\pm 7$ ). This shows that the first oxidation step is not complete for sample **mono(III,IV)**. The starting concentration of the  $\text{Mn}^{\text{III}}\text{Mn}^{\text{III}}$  species, sample **mono(III,III)**, is calculated to be  $0.50 \pm 0.02$  mM from UV/vis data at 380 and 495nm (see Appendix 2.6). The total concentration of the  $\text{Mn}^{\text{III}}\text{Mn}^{\text{III}}$  and  $\text{Mn}^{\text{III}}\text{Mn}^{\text{IV}}$  species of sample **mono(III,IV)** is calculated to be  $0.49 \pm 0.02$  mM, which is well within the error of the starting concentration.

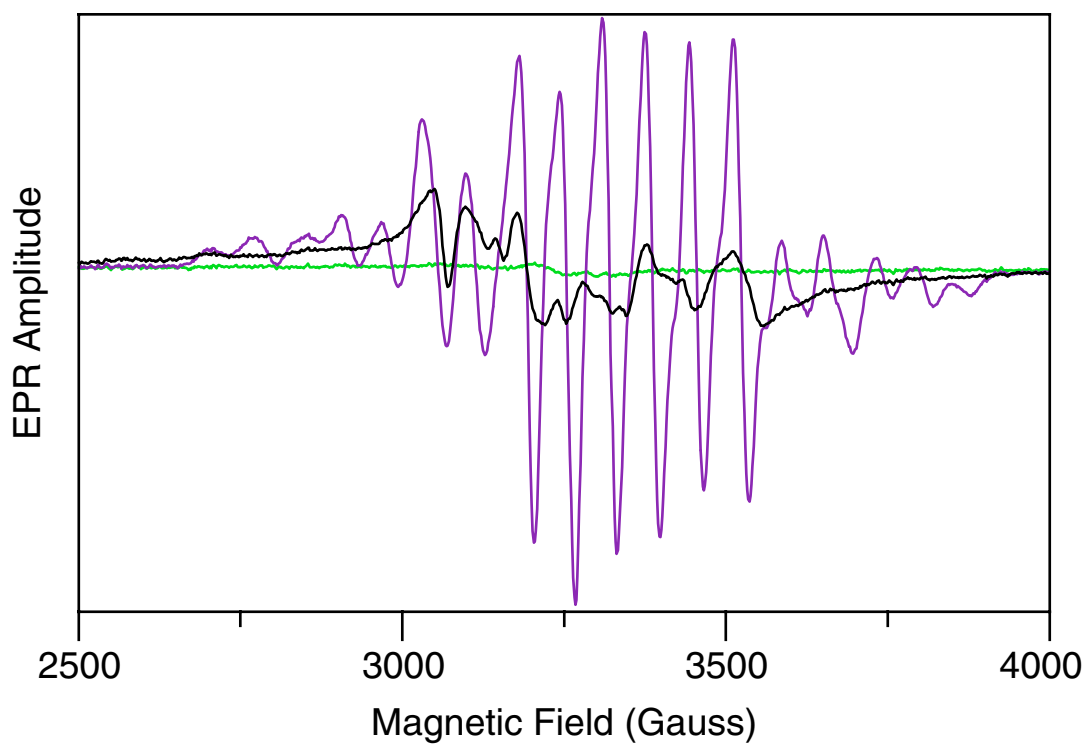


Figure 2.7 The EPR spectra of the mono- $\mu$ -oxo compound at three different stages during the electrochemistry: sample **mono(III,III)**, the starting solution (green); sample **mono(III,IV)**, the solution after the first oxidation step (purple); sample **mono(IV,IV)<sub>F</sub>**, the final solution during the second oxidation step (black).

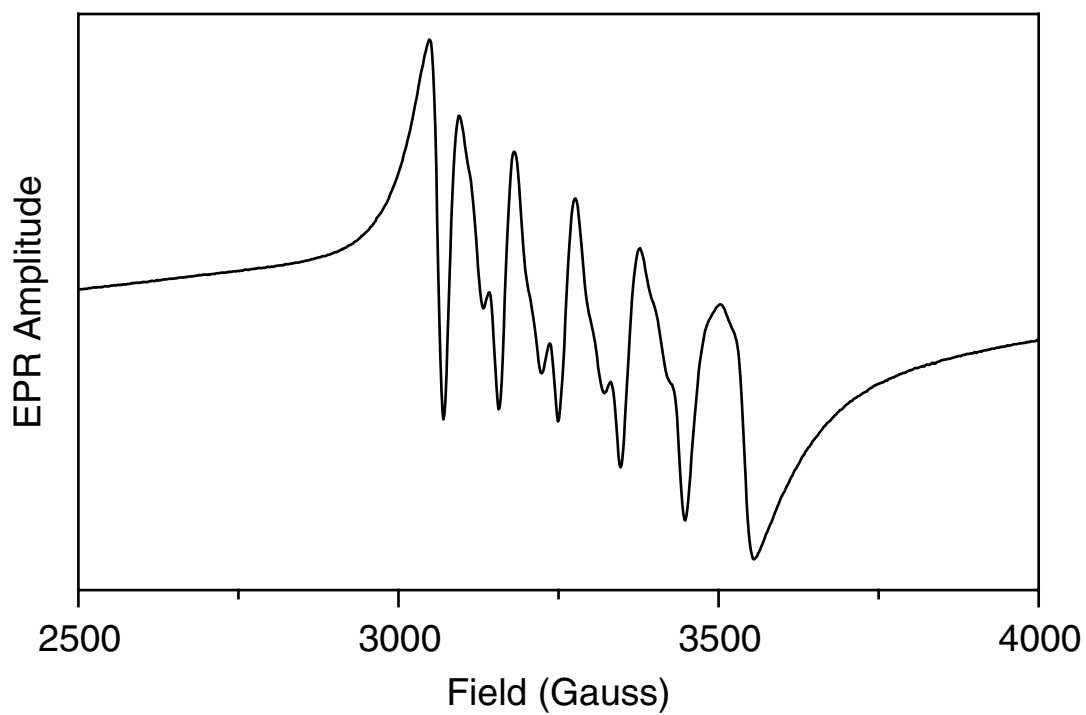


Figure 2.8 EPR spectrum of  $1.0 \times 10^{-3}$  M  $Mn^{II}$  in acetonitrile, which was used to calculate the amount of decomposition of the mono- $\mu$ -oxo compound after the second oxidation step.

The decrease in  $\text{Mn}^{\text{III}}\text{Mn}^{\text{IV}}$  during the second oxidation step of the mono- $\mu$ -oxo compound is followed by EPR spectroscopy, analogous to the di- $\mu$ -oxo compound. Figure 2.7 shows that the  $\text{Mn}^{\text{III}}\text{Mn}^{\text{IV}}$  EPR signal in the **mono(IV,IV)<sub>F</sub>** sample spectrum is greatly decreased. This indicates that most of the  $\text{Mn}^{\text{III}}\text{Mn}^{\text{IV}}$  species has been oxidized during the second oxidation step (Figure 2.5). However, the EPR spectrum of the **mono(IV,IV)<sub>F</sub>** contains an additional six-line EPR signal, which resembles that of free  $\text{Mn}^{\text{II}}$  in acetonitrile (data not shown). This shows that a small amount of the newly formed  $\text{Mn}^{\text{IV}}\text{Mn}^{\text{IV}}$  species has decomposed into  $\text{Mn}^{\text{II}}$ . The amount of the  $\text{Mn}^{\text{III}}\text{Mn}^{\text{IV}}$  species and  $\text{Mn}^{\text{II}}$  present in the **mono(IV,IV)** samples are determined by minimizing the least-square value of the residue EPR spectra, which is the **mono(IV,IV)** spectra minus fractional parts of the the **mono(III,IV)** EPR spectrum, as the  $\text{Mn}^{\text{III}}\text{Mn}^{\text{IV}}$  reference, and the  $\text{Mn}^{\text{II}}$  EPR spectrum (Figure 2.8). Table 2.1 presents the contribution of the **mono(III,IV)** and  $\text{Mn}^{\text{II}}$  spectra to the various **mono(IV,IV)** sample spectra. The  $\text{Mn}^{\text{III}}\text{Mn}^{\text{IV}}$  fraction increases first during the second oxidation step (**mono(IV,IV)<sub>A</sub>**) before it decreases (**mono(IV,IV)<sub>A</sub>** to **mono(IV,IV)<sub>F</sub>**). This initial increase is due to the incomplete first oxidation step, as was determined by UV/vis spectroscopy. At the start of the second oxidation step, more  $\text{Mn}^{\text{III}}\text{Mn}^{\text{IV}}$  species is initially formed from the remaining  $\text{Mn}^{\text{III}}\text{Mn}^{\text{III}}$  than is oxidized into  $\text{Mn}^{\text{IV}}\text{Mn}^{\text{IV}}$  (Figure 2.5). Table 2.1 also shows that only a very small fraction (3%) of  $\text{Mn}^{\text{IV}}\text{Mn}^{\text{IV}}$  species decomposes into  $\text{Mn}^{\text{II}}$ . The final oxidation state fractions of the mono- $\mu$ -oxo samples used to deconvolute the measured sample X-ray spectra into pure oxidation-state spectra are given in Table 2.2.

Table 2.1 The  $Mn^{III}Mn^{IV}$  and  $Mn^{II}$  fractions calculated from EPR spectra of the di- $\mu$ -oxo and mono- $\mu$ -oxo sample solutions at different stages during the electrolysis, see also Figures 2.6 and 2.7.

	di			mono						
	(III,IV)	(IV,IV)		(III,IV)	(IV,IV)					
		A	B		A	B	C	D	E	F
$Mn^{III}Mn^{IV}$	1	0.19	0.04	0.77	0.85	0.48	0.25	0.15	0.09	0.05
$Mn^{II}$	–	–	–	–	0.01	0.02	0.02	0.02	0.03	0.03

Table 2.2 The fractions of the manganese components used to deconvolute the measured EXAFS, XANES, and  $K\beta$  XES spectra into pure oxidation-state spectra of the mono- $\mu$ -oxo and di- $\mu$ -oxo compounds.

		$Mn^{III}Mn^{III}$	$Mn^{III}Mn^{IV}$	$Mn^{IV}Mn^{IV}$	$Mn^{II}$
di	(III,IV)	–	1.0	–	–
	(IV,IV) <sub>B</sub>	–	0.04 ± 0.01	0.96 ± 0.01	–
mono	(III,III)	1.0	–	–	–
	(III,IV)	0.23 ± 0.07	0.77 ± 0.07	–	–
	(IV,IV) <sub>F</sub>	–	0.05 ± 0.01	0.92 ± 0.02	0.03 ± 0.01

### Analysis of EXAFS data

Figure 2.9 presents the deconvoluted EXAFS spectra of the di- $\mu$ -oxo compound (A) and mono- $\mu$ -oxo compound (B) in their respective pure oxidation states. No major structural changes in the compounds occur upon oxidation.<sup>10,41</sup> Therefore, only small alterations in the EXAFS spectra are expected between the different oxidation states. For the di- $\mu$ -oxo compound (A), the Fourier peak at  $R' \approx 2.4 \text{ \AA}$  (see inset), containing Mn–Mn back-scatter contributions, shows a slight decrease in apparent distance upon oxidation from  $\text{Mn}^{\text{III}}\text{Mn}^{\text{IV}}$  to  $\text{Mn}^{\text{IV}}\text{Mn}^{\text{IV}}$ . The Mn–N/O Fourier peaks at  $R' < 2 \text{ \AA}$  show a small decrease in apparent distance and intensity upon oxidation of the di- $\mu$ -oxo compound. The intensity and apparent distance of the Fourier peak at  $R' \approx 3 \text{ \AA}$  (see inset) of the mono- $\mu$ -oxo compound (B), which contains Mn–Mn back-scatter contributions, are nearly independent of oxidation state. Oxidation-state dependence is observed for the Fourier peaks at  $R' < 2 \text{ \AA}$  (Mn–N/O back-scatter). The intensity of these peaks in the  $\text{Mn}^{\text{III}}\text{Mn}^{\text{III}}$  and  $\text{Mn}^{\text{III}}\text{Mn}^{\text{IV}}$  states is reduced by a factor of about two relative to that observed in the  $\text{Mn}^{\text{IV}}\text{Mn}^{\text{IV}}$  state. This may be caused by a distribution of distances due to the Jahn-Teller effect from  $\text{Mn}^{\text{III}}$  and the mixed valence nature of the  $\text{Mn}^{\text{III}}\text{Mn}^{\text{IV}}$  species. The changes observed in the Mn–Mn Fourier peak are minor and indicate that no major structural changes have occurred, thus the compounds have remained intact throughout the electrochemical oxidation steps.

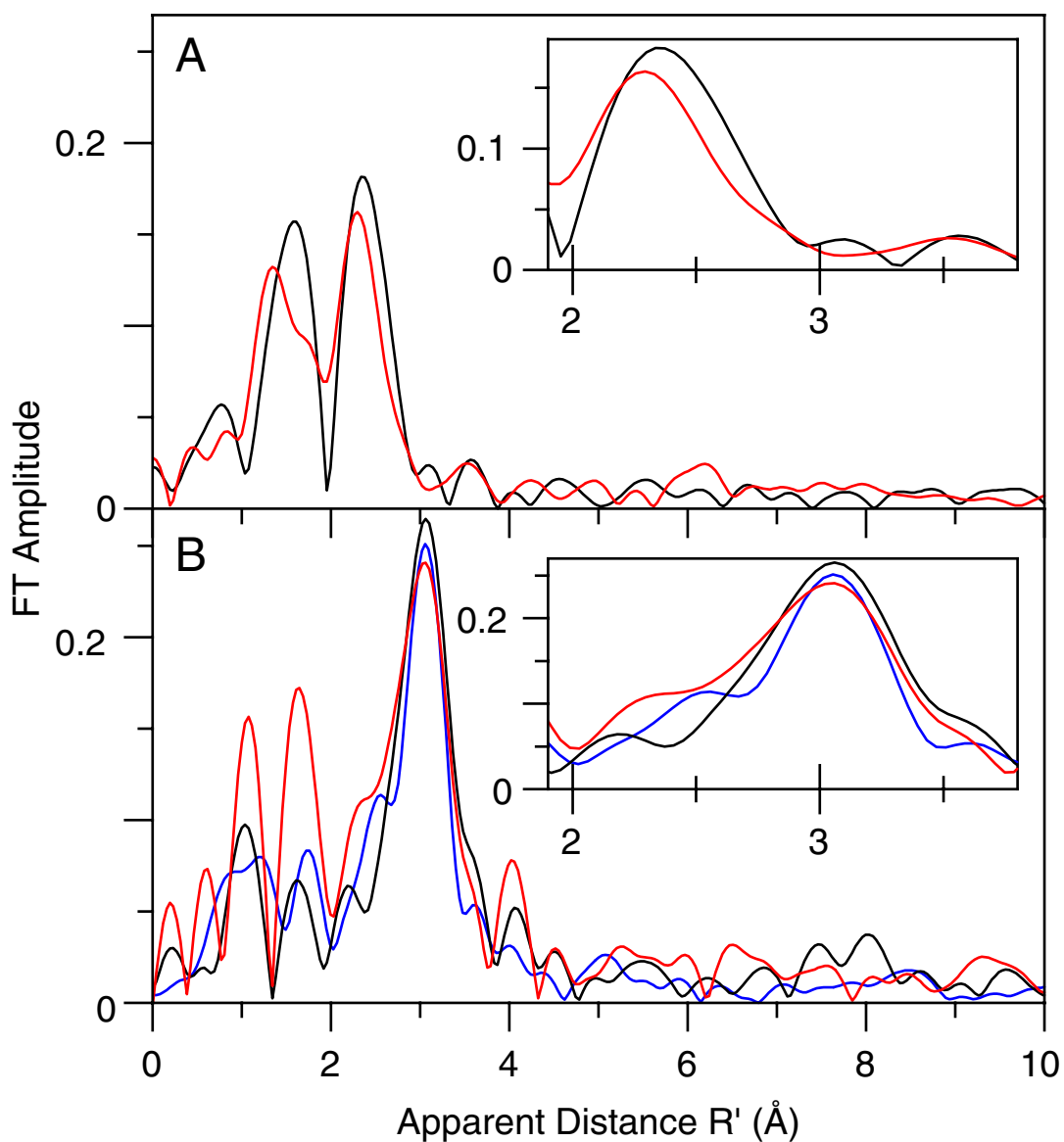


Figure 2.9 The Fourier-transformed Mn EXAFS spectra of the di- $\mu$ -oxo (A) and mono- $\mu$ -oxo (B) compounds in their respective pure oxidation states:  $\text{Mn}^{\text{III}}\text{Mn}^{\text{III}}$  (blue),  $\text{Mn}^{\text{III}}\text{Mn}^{\text{IV}}$  (black), and  $\text{Mn}^{\text{IV}}\text{Mn}^{\text{IV}}$  (red). The insets present the 1.9 - 3.8 Å range, which contains the Mn-Mn Fourier peak for each compound.

### Analysis of XANES and K $\beta$ XES data

The Mn K-edge XANES and the second-derivative spectra of the di- $\mu$ -oxo and mono- $\mu$ -oxo compounds are shown in Figures 2.10 and 2.11. Oxidation of Mn<sup>III</sup> to Mn<sup>IV</sup> for each compound causes all K-edges to shift to a higher energy and change in shape slightly. This behavior is reversible, i.e. when the higher oxidation states are reduced, the Mn K-edges shift to lower energy (data not shown). The magnitude of the shift depends on the type of compound. An indicator of the magnitude of edge shifts are the changes in first inflection-point energies (IPEs), which are indicated by the arrows in Figures 2.10B and 2.11B and summarized in Table 2.3. The Mn K-edge shift for the oxidation of the di- $\mu$ -oxo compound (Mn<sup>III</sup>Mn<sup>IV</sup>  $\rightarrow$  Mn<sup>IV</sup>Mn<sup>IV</sup>) is 2.2 eV. The shift in energy for the first oxidation step of the mono- $\mu$ -oxo compound (Mn<sup>III</sup>Mn<sup>III</sup>  $\rightarrow$  Mn<sup>III</sup>Mn<sup>IV</sup>) is 1.0 eV, and it is 0.8 eV for the second oxidation step (Mn<sup>III</sup>Mn<sup>IV</sup>  $\rightarrow$  Mn<sup>IV</sup>Mn<sup>IV</sup>). Each shift is smaller than that observed for the di- $\mu$ -oxo compound. The pre-edge features also change upon oxidation of the compounds. The shift in the pre-edge IPE for the di- $\mu$ -oxo compound is 0.6 eV. For the first oxidation step of the mono- $\mu$ -oxo compound this shift is 0.8 eV, similar to that of the di- $\mu$ -oxo compound. However, the shift in pre-edge IPE for the second oxidation step is only 0.1 eV. The shape of the Mn K-edge is also highly dependent on the type of compound. In comparison to the di- $\mu$ -oxo species, the mono- $\mu$ -oxo species Mn K-edges have less structure.



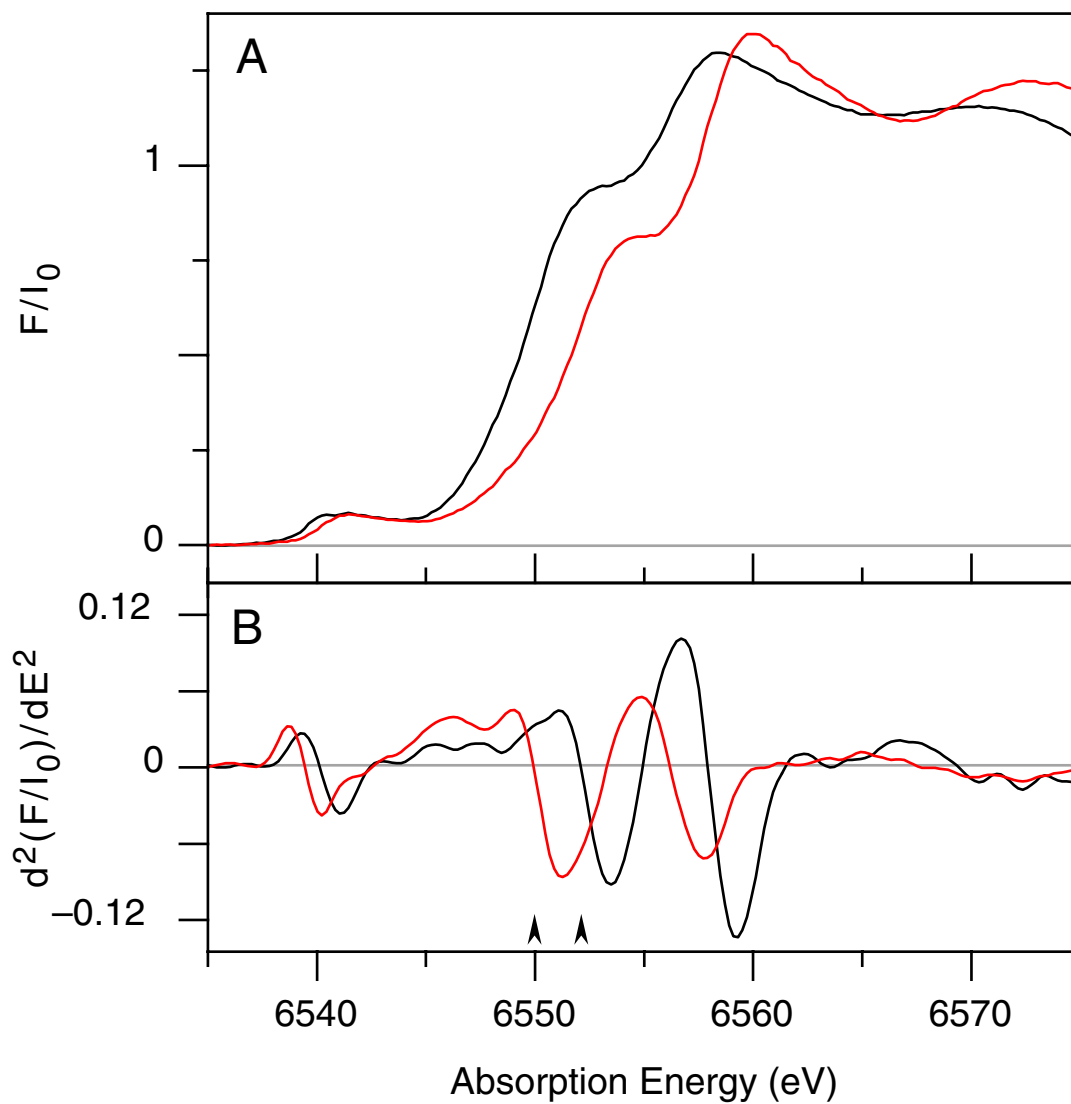


Figure 2.10 The deconvoluted Mn K-edge XANES (A) and second-derivative (B) spectra of the di- $\mu$ -oxo compound in its two oxidation states:  $Mn^{III}Mn^{IV}$  (black) and  $Mn^{IV}Mn^{IV}$  (red). The arrows in the second-derivative spectra indicate the first inflection-point energy for the two oxidation states:  $Mn^{III}Mn^{IV} = 6549.9$  eV and  $Mn^{IV}Mn^{IV} = 6552.1$  eV.

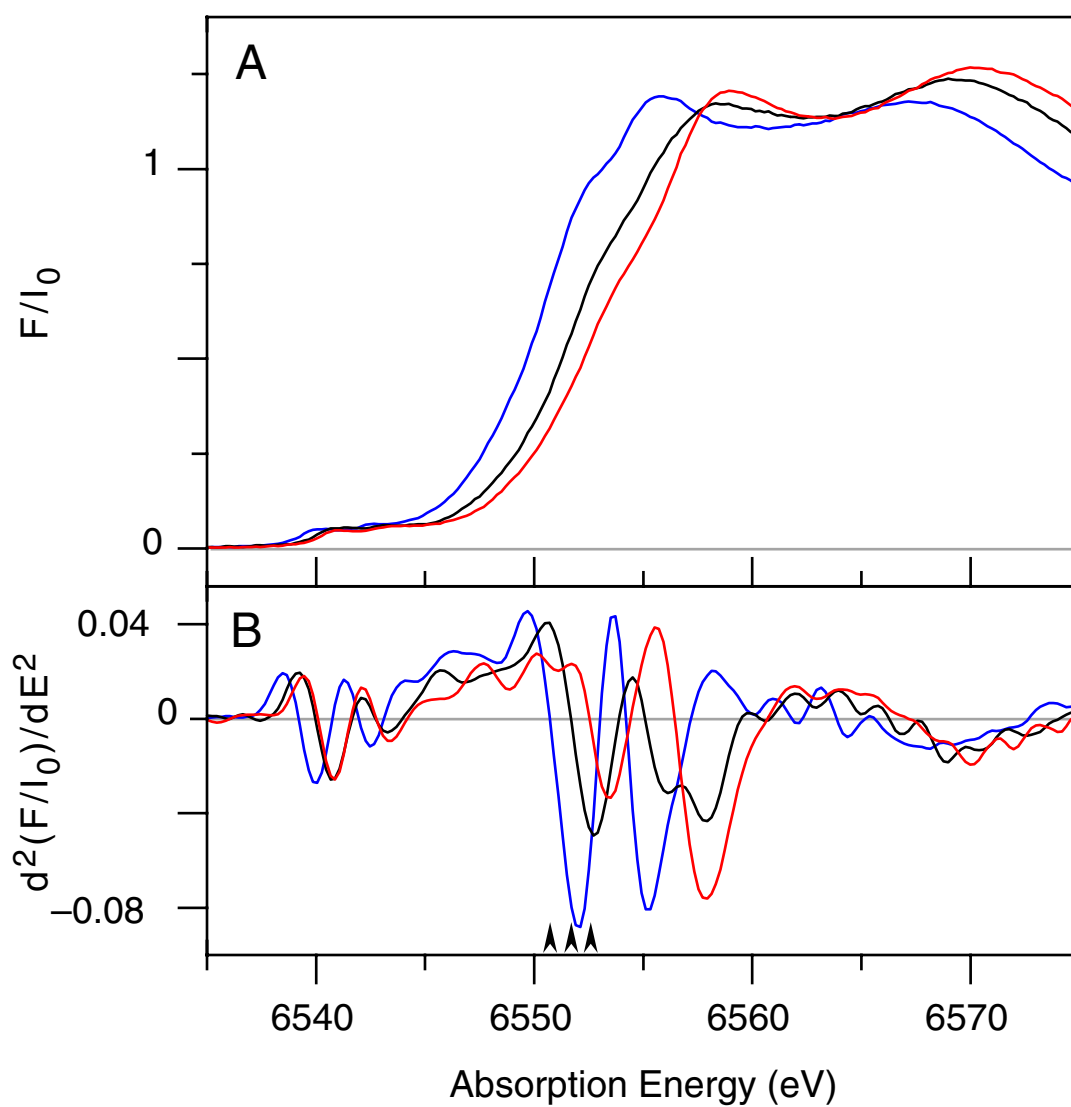


Figure 2.11 The deconvoluted Mn K-edge XANES (A) and second-derivative (B) spectra of the mono- $\mu$ -oxo compound in its three oxidation states:  $Mn^{III}Mn^{III}$  (blue),  $Mn^{III}Mn^{IV}$  (black), and  $Mn^{IV}Mn^{IV}$  (red). The arrows in the second-derivative spectra indicate the first inflection-point energy for each of the three oxidation states:  $Mn^{III}Mn^{III} = 6550.7$  eV,  $Mn^{III}Mn^{IV} = 6551.7$  eV, and  $Mn^{IV}Mn^{IV} = 6552.5$  eV.

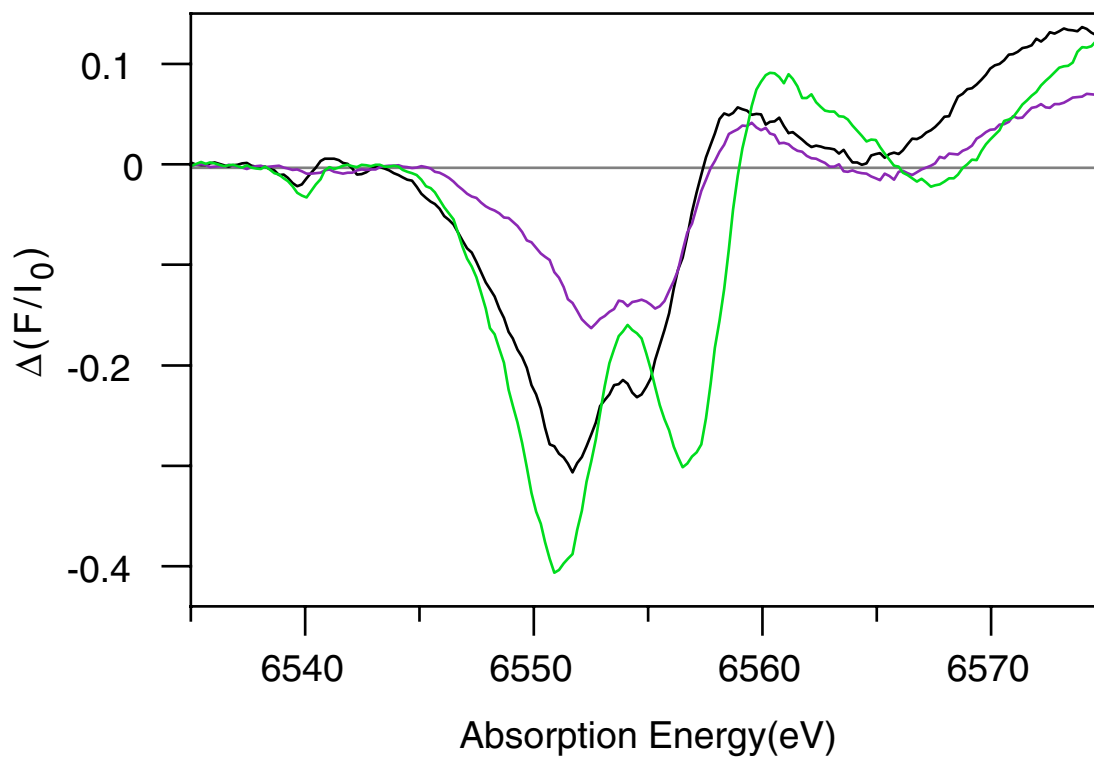


Figure 2.12 The deconvoluted Mn K-edge difference spectra for the different oxidation state transitions of the di- $\mu$ -oxo compound;  $Mn^{IV}Mn^{IV} - Mn^{III}Mn^{IV}$  (green), and of the mono- $\mu$ -oxo compound:  $Mn^{III}Mn^{IV} - Mn^{III}Mn^{III}$  (black) and  $Mn^{IV}Mn^{IV} - Mn^{III}Mn^{IV}$  (purple).

The difference Mn K-edge XANES spectra for the oxidation-state transitions are presented in Figure 2.12. The difference spectra show similar structures for the oxidation state transitions of each compound, i.e. two broad negative peaks in the 6545 - 6558 eV range and a weak broad positive peak at 6561 eV. However, the energy and intensity of the peaks depend on the ligand environment and starting oxidation state of the compound. The di- $\mu$ -oxo compound also shows a feature at  $\sim$ 6540.0 eV in the pre-edge region. The first oxidation step of the mono- $\mu$ -oxo compound shows a feature at  $\sim$ 6539.8 eV, with a smaller intensity than that of the di- $\mu$ -oxo compound. No significant change is observed in the pre-edge region for the second oxidation step of the mono- $\mu$ -oxo compound.

Figure 2.13 presents the Mn K $\beta$  XES spectra of the di- $\mu$ -oxo (A) and mono- $\mu$ -oxo (B) compounds in their respective oxidation states. The weaker K $\beta'$  peak is at  $\sim$ 6476 eV and the stronger K $\beta_{1,3}$  peak occurs at  $\sim$ 6491 eV.<sup>38</sup> The insets present the K $\beta_{1,3}$  emission on an expanded scale. Figure 2.13 shows that, upon oxidation of the di- $\mu$ -oxo and mono- $\mu$ -oxo compounds, the K $\beta_{1,3}$  peak shifts to a lower energy. First moments are used to quantify the magnitude of the shift of the K $\beta_{1,3}$  peak; they are summarized in Table 2.3. The shift in first moments is  $\sim$ 0.21 eV to lower energy for each oxidation step, indicating that the changes observed between the compounds are very similar. Support for this observation is shown in Figure 2.14, which presents the Mn K $\beta$  XES difference spectra of the oxidation steps of the compounds. The K $\beta_{1,3}$  XES difference spectra are all similar in shape, intensity and energy, within the error of the measurements. Each difference spectrum shows an increase in intensity at  $\sim$ 6490 eV and a decrease at  $\sim$ 6492 eV upon oxidation, with a zero-crossing of  $\sim$ 6491 eV.

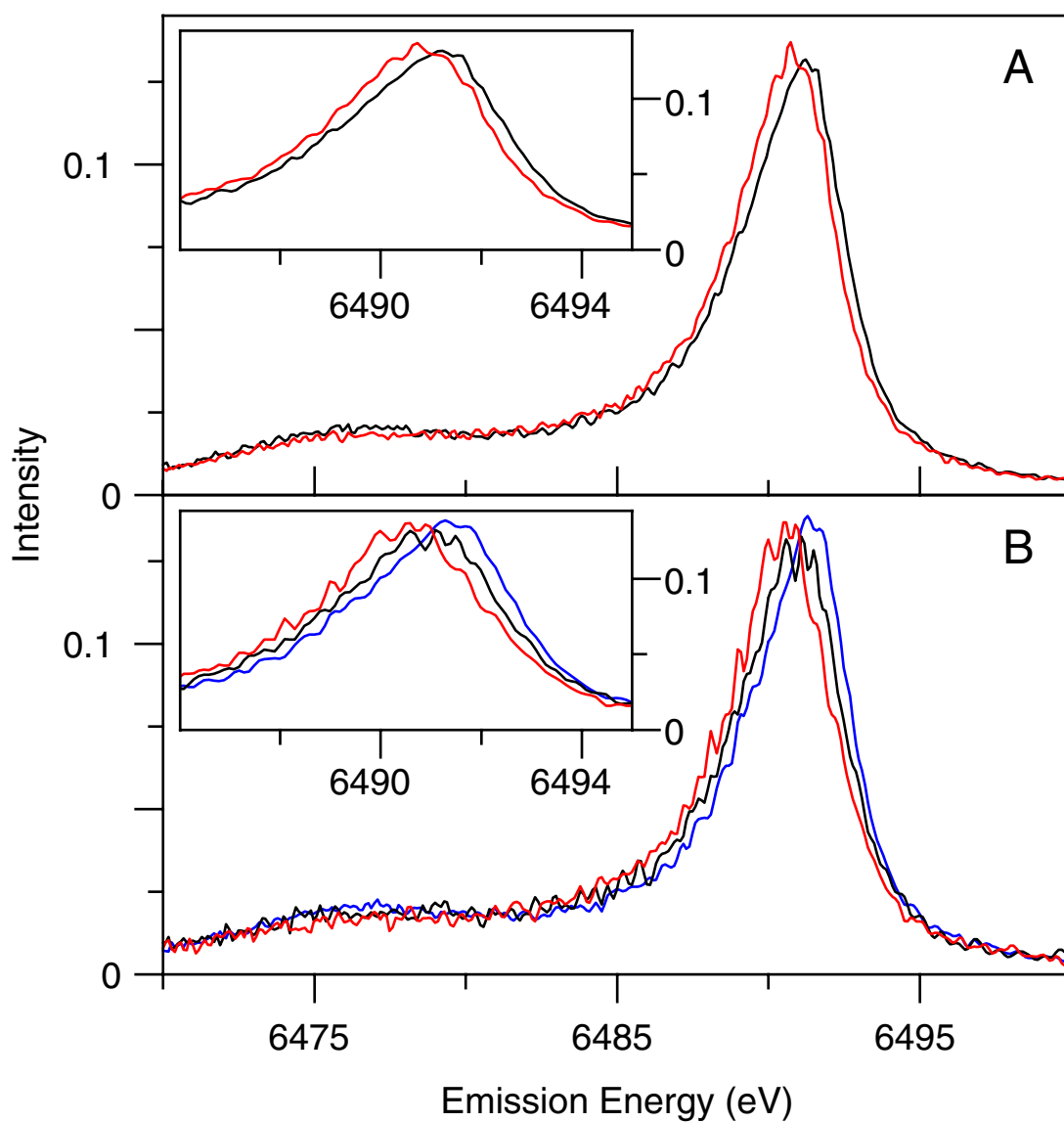


Figure 2.13 The deconvoluted Mn  $K\beta$  XES of the di- $\mu$ -oxo compound (A) and the mono- $\mu$ -oxo compound (B) in their respective oxidation states:  $Mn^{III}Mn^{III}$  (blue),  $Mn^{III}Mn^{IV}$  (black), and  $Mn^{IV}Mn^{IV}$  (red). The spectra show the entire spectral region with the two emission bands:  $K\beta'$  (weak, left) and  $K\beta_{1,3}$  (strong, right). The insets show the Mn  $K\beta_{1,3}$  XES spectra on an expanded scale.

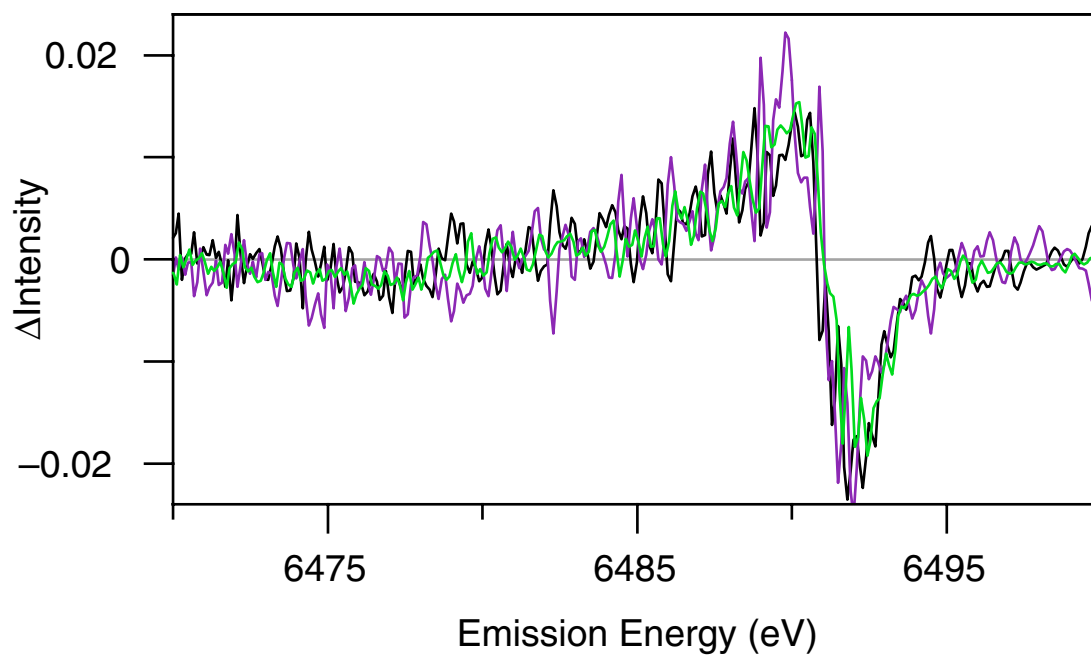


Figure 2.14 The deconvoluted Mn K $\beta$  XES difference spectra for the different oxidation state transitions of the di- $\mu$ -oxo compound:  $Mn^{IV}Mn^{IV} - Mn^{III}Mn^{IV}$  (green), and of the mono- $\mu$ -oxo compound:  $Mn^{III}Mn^{IV} - Mn^{III}Mn^{III}$  (black) and  $Mn^{IV}Mn^{IV} - Mn^{III}Mn^{IV}$  (purple).

**Table 2.3** A summary of the first inflection-point energy ( $1^{\text{st}}$  IPE) values of the pre-edge, and main Mn K-edge of the second-derivative XANES spectra of the mono- $\mu$ -oxo and di- $\mu$ -oxo compounds in their pure oxidation states, as well as a synopsis of the  $1^{\text{st}}$  moments of the  $K\beta_{1,3}$  peaks of the mono- $\mu$ -oxo and di- $\mu$ -oxo compound in their pure oxidation states. The di- $\mu$ -oxo compound and mono- $\mu$ -oxo compound spectra were collected during different runs. Therefore, when the  $K\beta_{1,3}$  first moments of the mono- $\mu$ -oxo compound are compared to those of the di- $\mu$ -oxo compound, an error of  $\pm 0.02$  eV is present in addition to the error values shown below.

mono- $\mu$ -oxo Compound		Mn K-edge XANES				Mn $K\beta$ XES	
		pre-edge IPE (eV)	$\Delta$ (eV)	Edge $1^{\text{st}}$ IPE (eV)	$\Delta$ (eV)	$1^{\text{st}}$ moment $K\beta_{1,3}$ (eV)	$\Delta$ (eV)
di- $\mu$ -oxo	III,IV	$6539.5 \pm 0.1$	0.6	$6549.9 \pm 0.1$	2.2	$6490.21 \pm 0.01$	-0.20
	IV,IV	$6540.1 \pm 0.1$		$6552.1 \pm 0.1$		$6490.01 \pm 0.01$	
mono- $\mu$ -oxo	III,III	$6539.2 \pm 0.1$	0.8	$6550.7 \pm 0.1$	1.0	$6490.39 \pm 0.01$	-0.21
	III,IV	$6540.0 \pm 0.1$		$6551.7 \pm 0.2$		$6490.18 \pm 0.03$	
	IV,IV	$6540.1 \pm 0.1$	0.1	$6552.5 \pm 0.2$	0.8	$6489.96 \pm 0.03$	-0.22

## 2.4 Discussion

### Deconvolution into pure oxidation-state spectra

The trends observed in the XANES and K $\beta$  XES spectra rely on the quality of deconvolution of the measured data into pure oxidation compound spectra. Mn K-edge XANES and K $\beta$  XES are element-specific; therefore, only manganese-containing components and their ratios in the electrochemical solutions will affect these spectra. In addition to the degree of completion of the electrochemical reactions, two other concerns are addressed below: purity of the starting materials, and possible decomposition products.

**Di- $\mu$ -oxo compound solutions** - No contamination is evident in the IR spectrum of the recrystallized di- $\mu$ -oxo compound (data not shown) relative to the published spectrum.<sup>10</sup> Furthermore, no other EPR signals are present, apart from the EPR signal of the starting material in the spectrum of sample **di(IV,IV)<sub>B</sub>** (Figure 2.6). Decomposition of the di- $\mu$ -oxo compounds is not considered an issue, because both the Mn<sup>III</sup>Mn<sup>IV</sup> and Mn<sup>IV</sup>Mn<sup>IV</sup> species are reported to be stable in a variety of solutions, including acetonitrile.<sup>10,39</sup> The oxidation of the di- $\mu$ -oxo compound goes almost to completion (96%; Table 2.2). Therefore, the correction needed to obtain the deconvoluted pure oxidation-state X-ray spectra is minor. The change in IPE (XANES) and 1<sup>st</sup>-moment (K $\beta$  XES) values are less than the inherent errors of each method when the raw and deconvoluted data are compared (see Appendix 2.6).

**Mono- $\mu$ -oxo compound solutions** - To determine the purity of the recrystallized mono- $\mu$ -oxo compound we recorded an IR spectrum of the solid starting material (data not shown) and a UV/vis spectrum of the starting electrochemical solution (see Appendix



2.6). Both match the published spectra.<sup>41</sup> Furthermore, the EPR spectrum of the starting solution shows no EPR signal (Figure 2.7). None of these three spectroscopies show evidence of contamination in the starting material. Horner et al.<sup>41</sup> determined that, of the three oxidation states, only the most oxidized species is unstable and decomposes to free  $\text{Mn}^{\text{II}}$  when water is present in the electrolyte solution. Although great care is taken to keep the electrolyte solution dry, a small decomposition is observed for the **mono(IV,IV)** samples (< 3%, Table 2.1).

UV/vis spectroscopy indicated that the first oxidation step of the mono- $\mu$ -oxo compound is the least complete of all of the oxidation reactions (77%). This was confirmed by the increase in EPR amplitude of the  $\text{Mn}^{\text{III}}\text{Mn}^{\text{IV}}$  species in the **mono(IV,IV)<sub>A</sub>** spectrum. Nevertheless, the correction needed to obtain the pure  $\text{Mn}^{\text{III}}\text{Mn}^{\text{IV}}$  oxidation state X-ray spectra is relatively small. Differences of 0.3 eV in IPE (XANES) and 0.05 eV in 1<sup>st</sup>-moment ( $\text{K}\beta$  XES) values are observed when the raw and deconvoluted spectra are compared (Appendix 2.6). The conversion during the second oxidation step is almost complete for the **mono(IV,IV)<sub>F</sub>** sample (92%  $\text{Mn}^{\text{IV}}\text{Mn}^{\text{IV}}$ ). Therefore, only minor corrections for the incomplete oxidation and decomposition are needed to obtain the pure  $\text{Mn}^{\text{IV}}\text{Mn}^{\text{IV}}$  oxidation-state X-ray spectra are minor (the correction fractions of the  $\text{Mn}^{\text{IV}}\text{Mn}^{\text{IV}}$  species and  $\text{Mn}^{\text{II}}$  are in Table 2.2). When the raw and deconvoluted spectra are compared (see Appendix 2.6), a change of 0.1 eV in the IPE (XANES) value is observed and only a 0.05 eV change in 1<sup>st</sup>-moment ( $\text{K}\beta$  XES) value.

#### **Analysis of EXAFS data**

No major changes occur in the Fourier-transformed EXAFS spectra between different oxidation-state species, except for the shorter back-scatter distances of the

Mn<sup>IV</sup>Mn<sup>IV</sup> mono- $\mu$ -oxo species. This is also evident for the  $k^3$ -space spectra, where the oscillation patterns of the pure oxidation state spectra change only slightly upon oxidation (see Appendix 2.6). The intensity of the Fourier peaks at 0 - 2 Å depends on the distribution of the Mn–N/O back-scatter distances. In the case of a large distribution in metal-back-scatter distances, high disorder is present and smaller intensities of the Fourier peaks are observed.<sup>51</sup> Changes in oxidation state of the Mn atoms alter bond distances, which influences the intensity of these Fourier peaks. However, these peaks do not give information on whether the compound is a monomer or dimer. Therefore, the focus in the Fourier-transformed EXAFS spectra is the Mn–Mn back-scatter peak at  $R' > 2.0$  Å. If the dimer breaks apart into monomers, this Fourier peak should disappear. Figure 2.9 shows that no major changes occur for the Fourier peaks at  $R' \approx 2.4$  Å, in the di- $\mu$ -oxo spectra or at  $R' \approx 3$  Å in the mono- $\mu$ -oxo spectra. This indicates that the Mn–Mn backscattering contribution remains intact, and the di- $\mu$ -oxo and mono- $\mu$ -oxo samples consist of manganese dimers.

Additional evidence is available that the mono- $\mu$ -oxo compound is not decomposing during the oxidation steps. Multiple scattering from the central oxygen atom enhances the back-scattering of the Mn–Mn vector, because the Mn–O–Mn moiety is linear.<sup>53-56</sup> This causes a higher intensity for this Mn–Mn Fourier peak than for the di- $\mu$ -oxo compounds (Figure 2.9). Among the different oxidation states no major changes are observed in the intensity of the peaks near  $R' \approx 3$  Å. This can be the case only if the linear Mn–O–Mn moiety stays intact for the different mono- $\mu$ -oxo species.

### **Oxidation-state changes and ligand effects on XANES and K $\beta$ XES spectra**

The Mn K-edge XANES spectra shift to higher energy upon each oxidation step of the mono- $\mu$ -oxo ( $[\text{Mn}^{\text{III}}]_2 \rightarrow \text{Mn}^{\text{III}}\text{Mn}^{\text{IV}} \rightarrow [\text{Mn}^{\text{IV}}]_2$ ) and di- $\mu$ -oxo compound ( $\text{Mn}^{\text{III}}\text{Mn}^{\text{IV}} \rightarrow [\text{Mn}^{\text{IV}}]_2$ ). This is expected, because the overall charge of the atom increases when a manganese atom is oxidized. Consequently, more energy is required to excite an electron from the 1s to the 4p or higher orbitals.<sup>28,57,58</sup>

The Mn K-edge energy and shape do not depend solely on the oxidation state of the manganese atoms (Figures 2.10 and 2.11), but also on the ligand environment. This is caused by mixing of the ligand and the manganese atomic orbitals.<sup>57</sup> It is possible that a change in structure and ligand environment will have an even greater influence on the main-edge energy and shape than a change in oxidation state. For example, it would be expected from an oxidation state point-of-view that the  $\text{Mn}^{\text{III}}\text{Mn}^{\text{IV}}$  di- $\mu$ -oxo compound edge would have a higher energy than that of the  $\text{Mn}^{\text{III}}\text{Mn}^{\text{III}}$  mono- $\mu$ -oxo compound. However, as shown in Table 2.3, the  $\text{Mn}^{\text{III}}\text{Mn}^{\text{III}}$  mono- $\mu$ -oxo compound has a higher IPE value than the  $\text{Mn}^{\text{III}}\text{Mn}^{\text{IV}}$  di- $\mu$ -oxo species. This difference in edge energy (and shape) is caused by differences in structure and ligand environment between the di- $\mu$ -oxo and mono- $\mu$ -oxo compounds. For example, in case of the linear mono- $\mu$ -oxo species, the bridging oxygen has the unusual hybridization of sp, which is different from the bridging oxygens in the di- $\mu$ -oxo compound or even other mono- $\mu$ -oxo compounds.<sup>13</sup> Therefore, the mixing of the oxygen and the manganese orbitals is different, and consequently the region and shape of the K-edge will differ. Beside these major differences in the bridging oxygen ligands, there are also differences in the terminal ligands of the di- $\mu$ -oxo and mono- $\mu$ -oxo compound. The di- $\mu$ -oxo compound has only aromatic terminal ligands,

while the mono- $\mu$ -oxo compound has a mixture of aromatic and non-aromatic ligands. Aromatic ligands have unoccupied  $\pi^*$  orbitals which can have strong  $\pi$  back-bonding interactions with the manganese d-orbitals. These interactions are different for non-aromatic orbitals. Therefore, the shape and region of the XANES spectra are also dependent on the terminal ligands.

All oxidation steps of the mono- $\mu$ -oxo and di- $\mu$ -oxo compounds involve removal of an electron from  $\text{Mn}^{\text{III}}$  to produce  $\text{Mn}^{\text{IV}}$ , without any major changes in ligand environment (see also Analysis of EXAFS).<sup>39,40,42,43</sup> Therefore, no major changes are expected for the difference spectra of the two oxidation steps of mono- $\mu$ -oxo compound. However, Figure 2.12 shows that the shape, intensity and peak energy of the main XANES K-edge difference features do depend on the starting oxidation state of the compound. The same applies to the pre-edge, where in the case of the mono- $\mu$ -oxo compound, a difference feature is observed for the first oxidation step ( $[\text{Mn}^{\text{III}}]_2 \rightarrow \text{Mn}^{\text{III}}\text{Mn}^{\text{IV}}$ ). However, no such feature is observed for the second oxidation step ( $\text{Mn}^{\text{III}}\text{Mn}^{\text{IV}} \rightarrow [\text{Mn}^{\text{IV}}]_2$ ). This dependence of the difference spectra on the kind of oxidation step indicates that the two Mn atoms are affecting each other in some way. This behavior can be explained in two possible ways: differences in delocalization of charge or exchange coupling through the bridging oxygen(s). If valence delocalization occurs, the first oxidation step should present a  $[\text{Mn}^{3+}]_2 \rightarrow [\text{Mn}^{3.5+}]_2$  transition and the second oxidation step would present a  $[\text{Mn}^{3.5+}]_2 \rightarrow [\text{Mn}^{4+}]_2$  transition. This could explain the changes in difference spectra between the two oxidation steps, because the two oxidation steps are not the same. However, Horner et al.<sup>41</sup> found that the mono- $\mu$ -oxo oxidation-state species are valence-trapped (Robin-Day class I).<sup>59</sup> Therefore, the

interaction between the Mn atoms needs to happen via the bridging oxygen. This explanation is supported by the fact that the mono- $\mu$ -oxo species are strongly anti-ferromagnetically coupled.<sup>41</sup> This again exemplifies how important the bridging ligands can be to the changes observed in the Mn K-edge XANES spectra upon oxidation.

The 1<sup>st</sup> moments of the  $K\beta_{1,3}$  peak energy are equal, within the error of the method, for the mono- $\mu$ -oxo and the di- $\mu$ -oxo compound in their  $Mn^{III}Mn^{IV}$  or  $Mn^{IV}Mn^{IV}$  oxidation state (Table 2.3, add  $\pm 0.02$  eV to error values when di- $\mu$ -oxo and mono- $\mu$ -oxo are compared). This indicates that the energy of the  $K\beta_{1,3}$  peak is determined mostly by the oxidation state of the manganese atom rather than the ligand environment. This is also evident from the difference spectra of the mono- $\mu$ -oxo and the di- $\mu$ -oxo compound (Figure 2.14). Not only are the energies of the maximum, minimum and zero crossing the same for the difference spectra of all the oxidation transitions, but the intensity is also similar. This also shows that the shape of the  $K\beta_{1,3}$  peak is less ligand-dependent than it is for XANES.  $K\beta$  XES reflect the transition of a 3p electron to a 1s hole.<sup>27</sup> The energy of the 3p level is affected by the magnitude of the 3p–3d exchange interaction. This exchange interaction is mainly determined by the number of unpaired electrons in the 3d level and is less affected by changes in the energy of the 3d levels due to ligand-field interactions. In addition, the 3p orbitals are smaller than the 3d and 4p orbitals, and therefore have less overlap with the 2p and  $\pi$  orbitals of the ligand environment. Thus, the 3p orbitals ( $K\beta$  XES) are less sensitive to the ligand environment than the 4p orbitals (XANES).

## 2.5 Conclusions

Due to the purity, low degree of decomposition, and high degree of completion of the oxidation reactions, the measured data needed only small corrections to obtain the pure oxidation-state spectra for each compound. This is evident from the minor differences between measured and deconvoluted data. This enabled us to study the dependence of Mn K-edge XANES and Mn K $\beta$  XES spectra on ligand environment and oxidation state for these two specific compounds in solution with a high degree of reliability.

The Mn K-edge XANES spectra give information on both the oxidation state of the manganese atoms and on their ligand environment. These spectra show energy shifts of 0.8 - 2.2 eV for oxidation-state changes and 0.4 - 1.8 eV for ligand-environment changes. This dependence on oxidation state and ligand environment is especially evident in the XANES difference spectra. Therefore, care must be exercised when correlating the Mn K-edge energies to manganese oxidation states without taking into account the nature of the ligand environment. This is especially a problem when sets of compounds with different ligand structures, different nuclearities, and different analysis methods to determine edge positions are used to infer oxidation-state information about biological systems, such as in Kuzek et al.<sup>60</sup> However, there is a correlation between manganese oxidation state and Mn K-edge energy if the ligand environment stays the same, i.e. the edge shift to a higher energy upon oxidation within a given compound. No such correlation exists for the pre-edge feature, which shows an energy shift of 0.8 eV for the first oxidation step of the mono- $\mu$ -oxo compound, but only 0.1 eV for the second

oxidation step. This difference in behavior of the main Mn K-edge and pre-edge is because each feature is due to transitions to different molecular orbitals.

The K $\beta$  XES spectra show an energy shift of  $\sim 0.21$  eV for oxidation state-changes and only  $\sim 0.04$  eV for ligand-environment changes. Therefore, this method is less dependent on the ligand environment of the manganese atoms than on the oxidation states. Additional compounds are being studied to see whether there is indeed such a strong correlation between oxidation state and K $\beta_{1,3}$  peak energy. Furthermore, multiplet calculations are being performed to enhance our theoretical understanding of K $\beta$  XES spectra. Based on currently available data, K $\beta$  XES seems to be an accurate method to determine the oxidation state of manganese atoms, in model compounds and biological systems, such as PS II.<sup>21</sup> The study of the different behavior of the XANES pre-edge and main edge in conjunction with K $\beta$  XES can provide much information about the character of the ligand environment of manganese atoms. In conclusion, Mn K-edge XANES and K $\beta$  XES are complementary methods, which give a wealth of information about oxidation state and ligand environment of the manganese atoms in model compounds and biological systems.<sup>21</sup>

## 2.6 Appendix

### *UV/vis spectra of the mono(III,III) and mono(III,IV) samples*

Figure 2.15 presents the UV/vis spectra of the **mono(III,III)** and **mono(III,IV)** samples of the mono- $\mu$ -oxo compound. The **mono(III,IV)** spectrum is used to calculate the degree of conversion during the first oxidation step, from the published absorption coefficient data and the UV/vis absorption values at 335, 380, 400, 480, 495, and 550nm, using a least-square fit. The **mono(III,III)** spectrum is used to calculate the starting mono- $\mu$ -oxo compound concentration of UV/vis absorption at 380 and 495nm, which is used as a control of the least-square fit method. (See Results - analysis of mono- $\mu$ -oxo compound.)

### *$k^3$ -space EXAFS spectra*

Figures 2.16A and B present the  $k^3$ -space XANES spectra of the oxidation-state species of the di- $\mu$ -oxo and mono- $\mu$ -oxo species, respectively. These spectra, along with the Fourier-transformed XANES spectra (Figure 2.9) are used to determine the integrity of the samples. If the compounds are decomposing, the Mn–Mn backscattering contribution would disappear, which greatly influences the frequency, amplitude and phase components of the  $k^3$ -space XANES spectra. However, only minor changes are observed, indicating that no decomposition occurred of the di- $\mu$ -oxo and mono- $\mu$ -oxo moieties. The slight changes observed are due to the changes in bond distances.



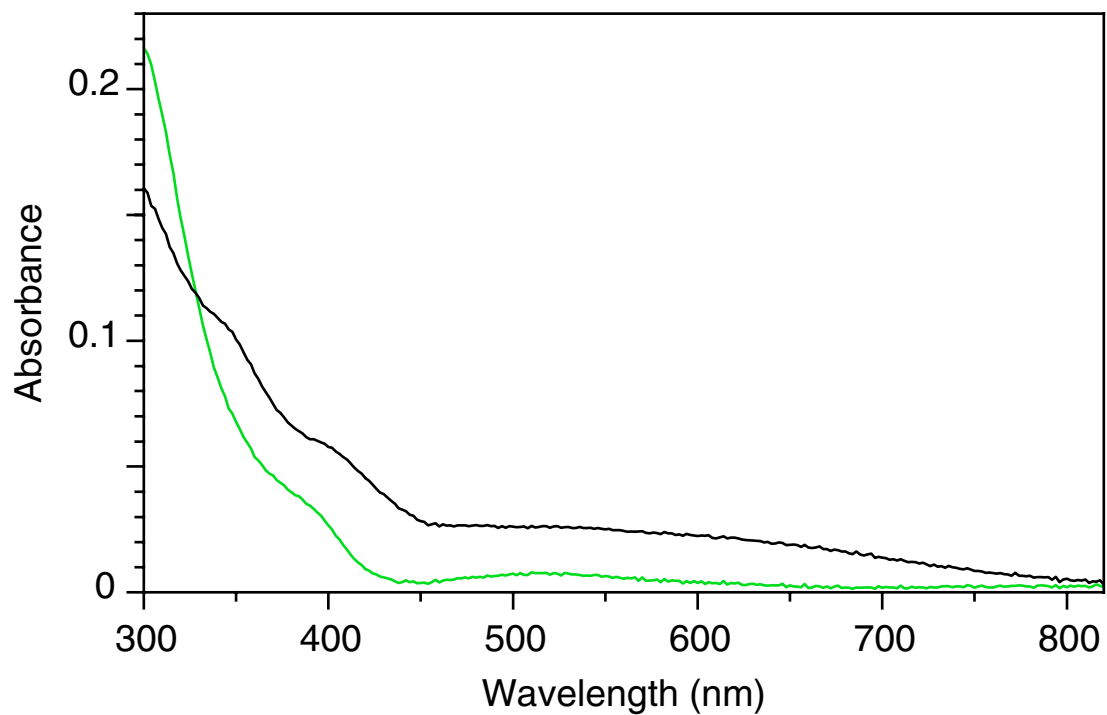


Figure 2.15 Measured UV/vis spectra of the mono- $\mu$ -oxo compound samples **mono(III,III)** (green) and **mono(III,IV)** (black), i.e. the starting solution, and the solution at the end of the first oxidation step ( $Mn^{III}Mn^{III} \rightarrow Mn^{III}Mn^{IV}$ ), respectively.

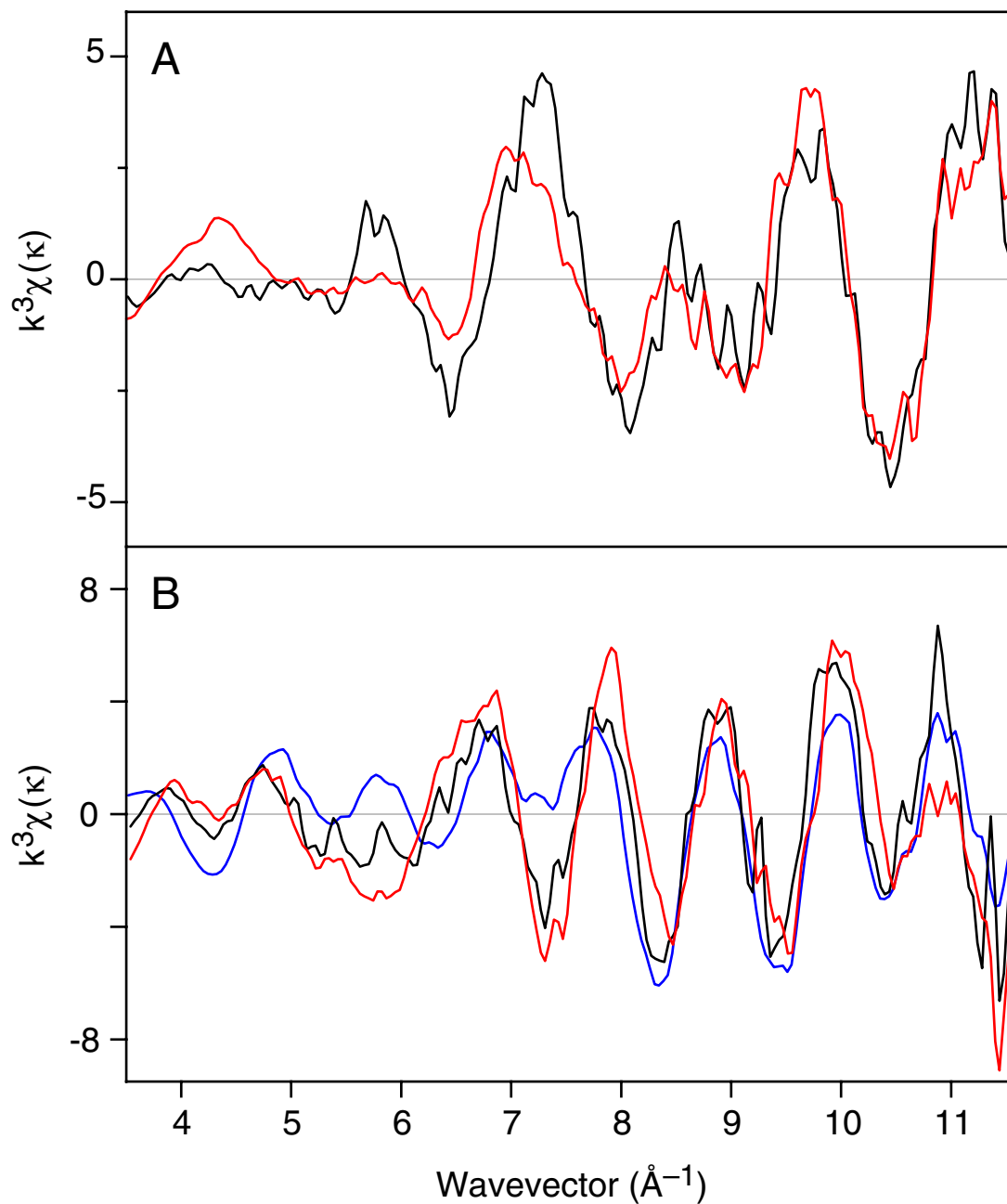


Figure 2.16 (A) The deconvoluted  $k^3$ -space EXAFS spectra of the pure oxidation-state  $\text{Mn}^{\text{III}}\text{Mn}^{\text{IV}}$  (black) and  $\text{Mn}^{\text{IV}}\text{Mn}^{\text{IV}}$  (red) species of the di- $\mu$ -oxo compounds. (B) The deconvoluted  $k^3$ -space EXAFS spectra of the pure oxidation-state  $\text{Mn}^{\text{III}}\text{Mn}^{\text{III}}$  (blue),  $\text{Mn}^{\text{III}}\text{Mn}^{\text{IV}}$  (black), and  $\text{Mn}^{\text{IV}}\text{Mn}^{\text{IV}}$  (red) species of the mono- $\mu$ -oxo compounds.

### ***Measured vs. Deconvoluted XANES spectra***

Figures 2.17, 2.18 and 2.19 present the measured and deconvoluted Mn K-edge XANES spectra for the  $\text{Mn}^{\text{IV}}\text{Mn}^{\text{IV}}$  di- $\mu$ -oxo species and the  $\text{Mn}^{\text{III}}\text{Mn}^{\text{IV}}$  and  $\text{Mn}^{\text{IV}}\text{Mn}^{\text{IV}}$  mono- $\mu$ -oxo species, respectively. As can be seen from Figure 2.17, the correction made to obtain the pure oxidation-state spectrum for the  $\text{Mn}^{\text{IV}}\text{Mn}^{\text{IV}}$  di- $\mu$ -oxo species has a minor effect. However there are some slight differences observed for the  $\text{Mn}^{\text{III}}\text{Mn}^{\text{IV}}$  and  $\text{Mn}^{\text{IV}}\text{Mn}^{\text{IV}}$  mono- $\mu$ -oxo species between the measured and deconvoluted spectra (Figure 2.18 and 2.19).

### ***Measured vs. deconvoluted Mn K $\beta$ XES spectra***

Figures 2.20, 2.21 and 2.22 present the measured and deconvoluted Mn K $\beta$  XES spectra for the  $\text{Mn}^{\text{IV}}\text{Mn}^{\text{IV}}$  di- $\mu$ -oxo species and the  $\text{Mn}^{\text{III}}\text{Mn}^{\text{IV}}$  and  $\text{Mn}^{\text{IV}}\text{Mn}^{\text{IV}}$  mono- $\mu$ -oxo species, respectively. As can be seen from Figure 2.20, the correction made to obtain the pure  $\text{Mn}^{\text{IV}}\text{Mn}^{\text{IV}}$  di- $\mu$ -oxo spectrum is so small that differences between the measured and pure oxidation-state spectra are hard to detect, as is the case for the XANES spectrum. However, there are some slight differences observed, for the  $\text{Mn}^{\text{III}}\text{Mn}^{\text{IV}}$  and  $\text{Mn}^{\text{IV}}\text{Mn}^{\text{IV}}$  mono- $\mu$ -oxo species, between the measured and deconvoluted spectra (Figure 2.21 and 2.22).

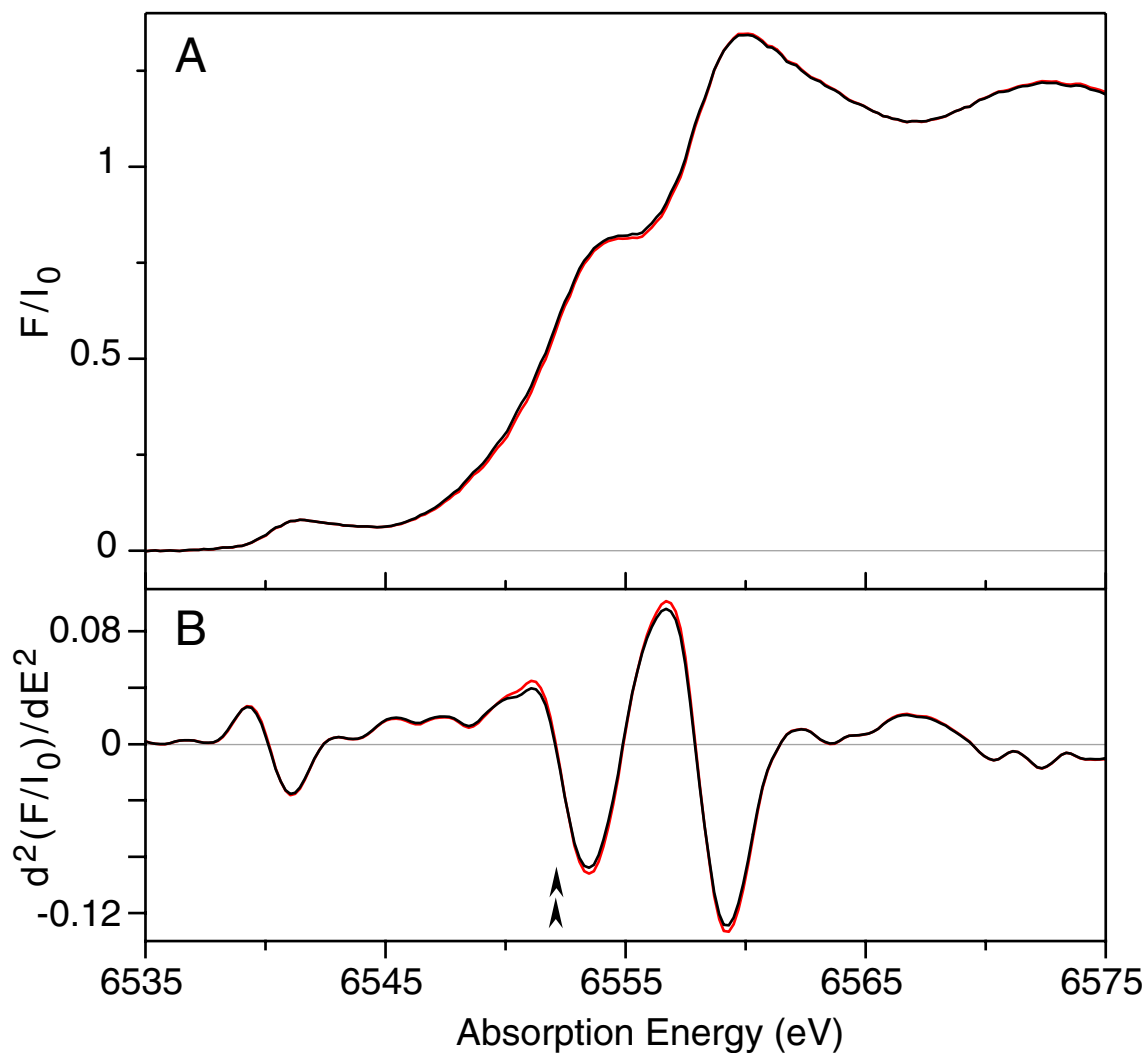


Figure 2.17 Comparison of the measured and deconvoluted Mn K-edge and 2<sup>nd</sup> derivative XANES spectra for the di- $\mu$ -oxo compound. The measured spectrum is of sample **di(IV,IV)<sub>B</sub>** (black) and the deconvoluted pure oxidation-state spectrum (red) is of the  $Mn^{IV}Mn^{IV}$  di- $\mu$ -oxo species. Arrows indicate the first inflection-point energy of the Mn K-edge XANES spectra of sample **di(IV,IV)<sub>B</sub>**, 6552.1 eV, and the  $Mn^{IV}Mn^{IV}$  species at 6552.1 eV.

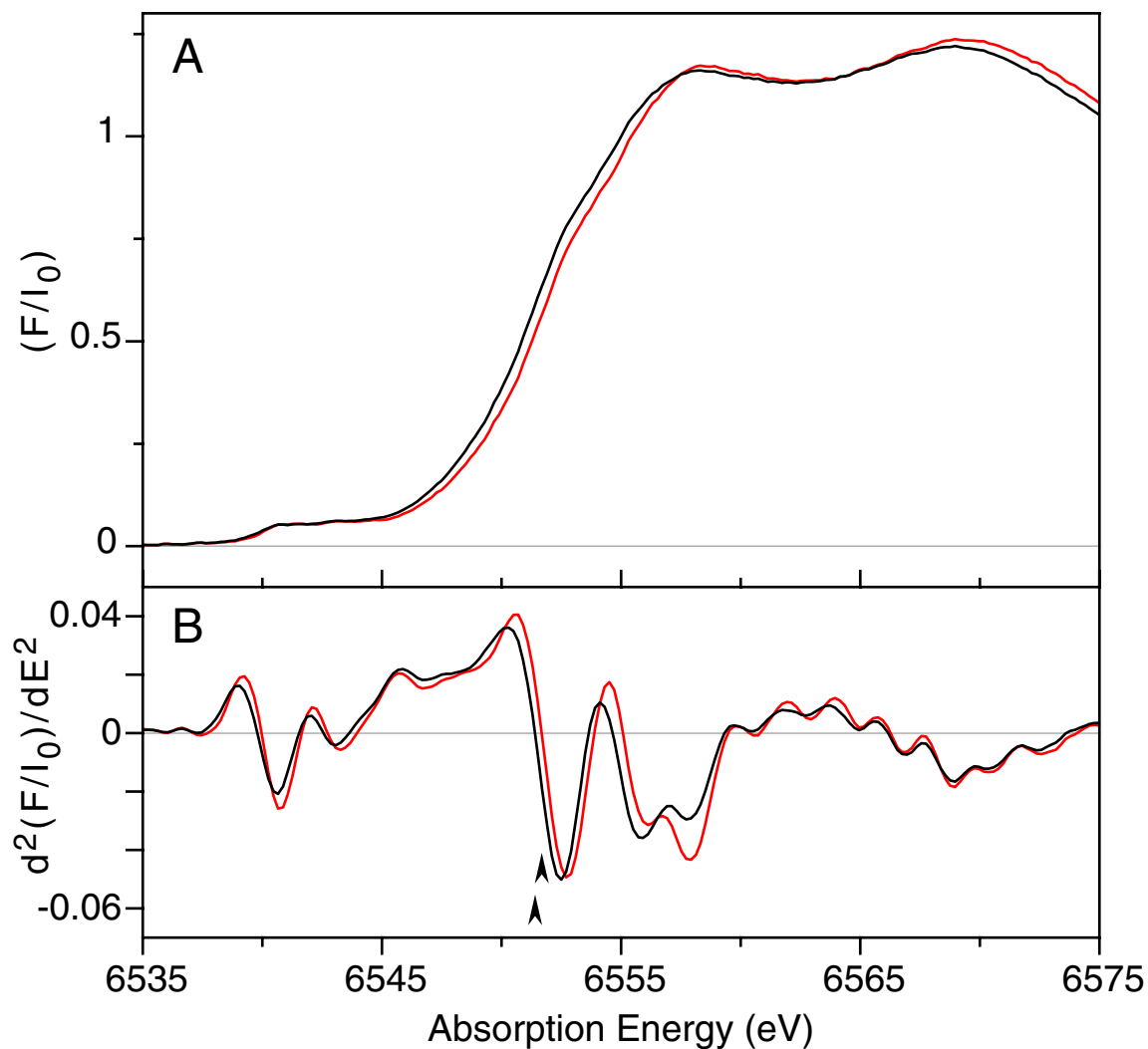


Figure 2.18 Comparison of the measured and deconvoluted Mn K-edge and 2<sup>nd</sup> derivative XANES spectra for the mono- $\mu$ -oxo compound after the first oxidation step. The measured spectrum is of sample **mono(III,IV)** (black) and the deconvoluted pure oxidation-state spectrum (red) is of the  $Mn^{III}Mn^{IV}$  mono- $\mu$ -oxo species. Arrows indicate the first inflection-point energy of the Mn K-edge XANES spectra of sample **mono(III,IV)**, 6551.4 eV, and the  $Mn^{III}Mn^{IV}$  species at 6551.7 eV.

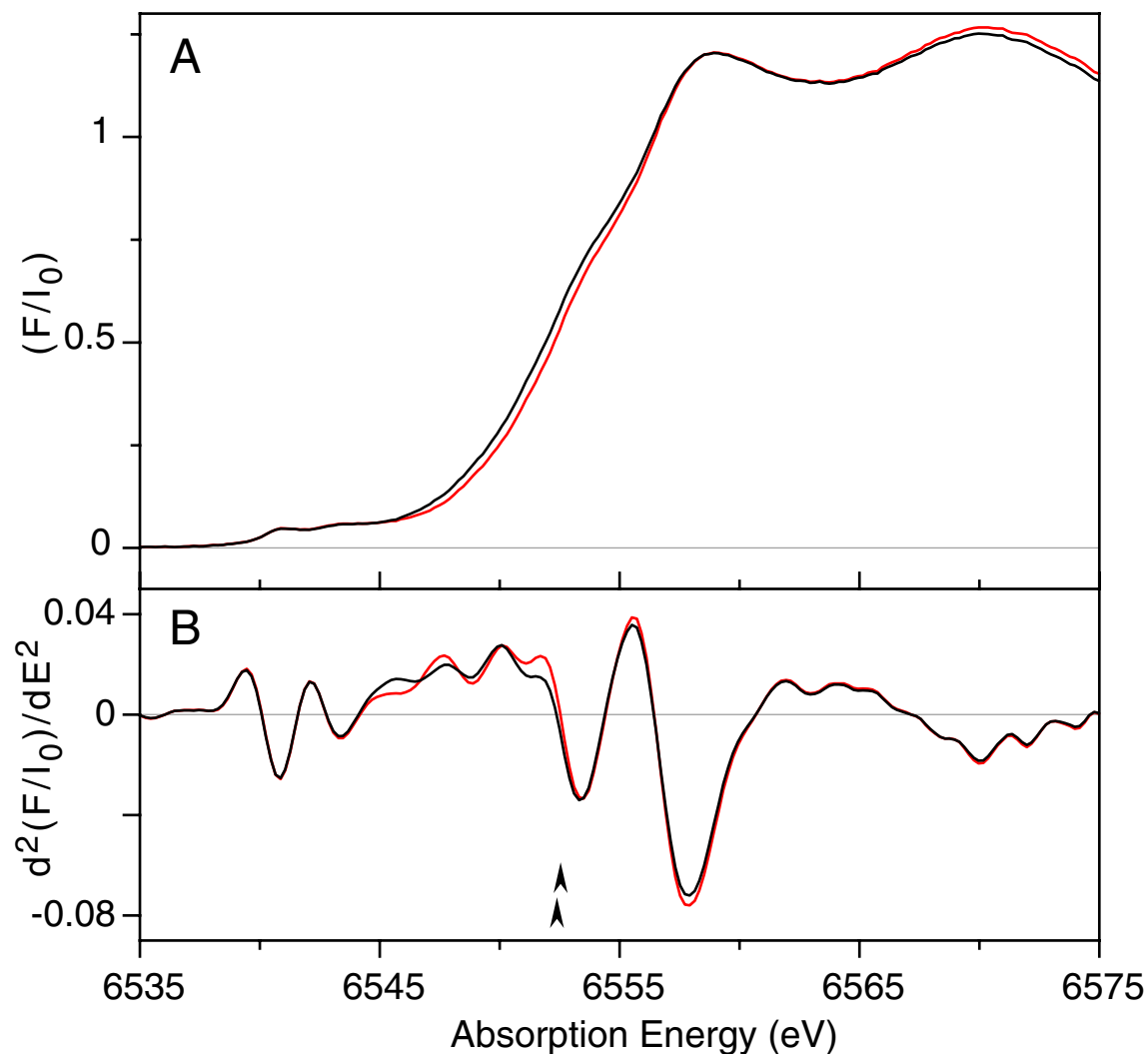


Figure 2.19 Comparison of the measured and deconvoluted Mn K-edge and 2<sup>nd</sup> derivative XANES spectra for the mono- $\mu$ -oxo compound at the end of the second oxidation step. The measured spectrum is of sample **mono(IV,IV)<sub>F</sub>** (black) and the deconvoluted pure oxidation-state spectrum (red) is of the  $Mn^{IV}Mn^{IV}$  mono- $\mu$ -oxo species. Arrows indicate the first inflection-point energy of the Mn K-edge XANES spectra of sample **mono(IV,IV)<sub>F</sub>**, 6552.4 eV, and the  $Mn^{IV}Mn^{IV}$  species at 6552.5 eV.

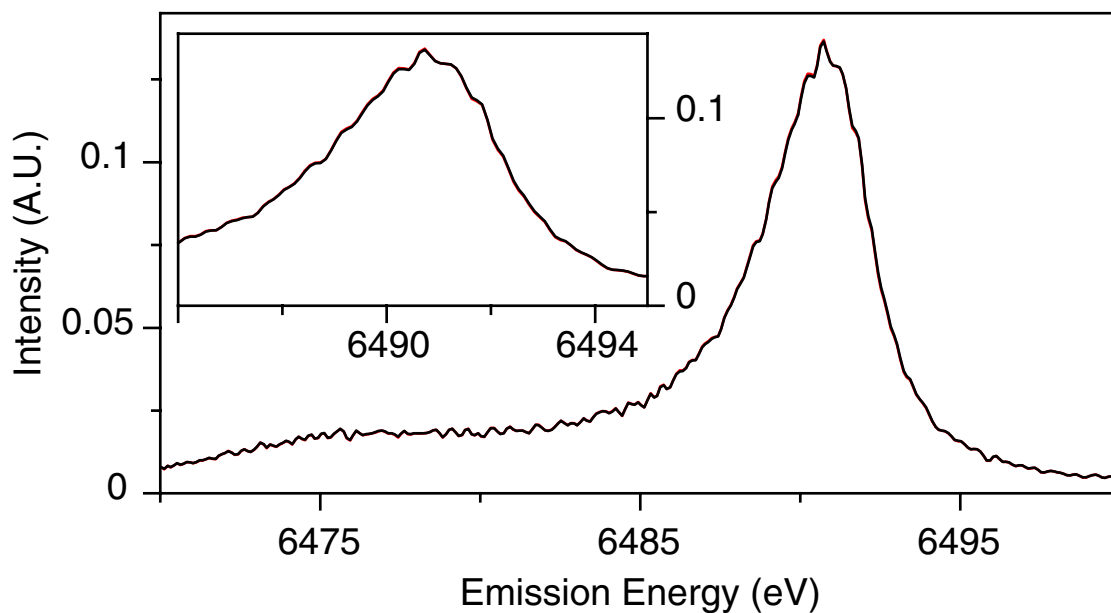


Figure 2.20 Comparison of the measured and deconvoluted Mn  $K\beta$  XES spectra for the di- $\mu$ -oxo compound. The measured spectrum is of sample  $di(IV,IV)_B$  (black) and the deconvoluted pure oxidation-state spectrum (red) is of the  $Mn^{IV}Mn^{IV}$  species, both have a 1<sup>st</sup> moment of 6490.01 eV.

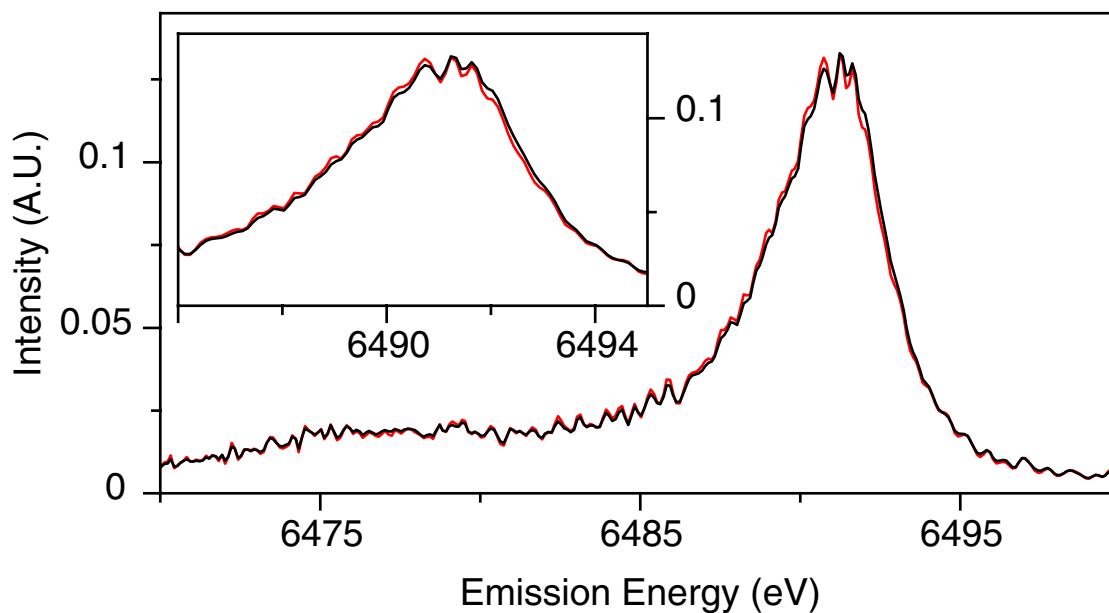


Figure 2.21 Comparison of the measured and deconvoluted Mn  $K\beta$  XES spectra for the mono- $\mu$ -oxo compound after the first oxidation step. The measured spectrum is of sample **mono(III,IV)** (black) and the deconvoluted pure oxidation-state spectrum (red) is of the  $Mn^{III}Mn^{IV}$  mono- $\mu$ -oxo species, with first moments 6490.23 eV and 6490.18 eV, respectively.



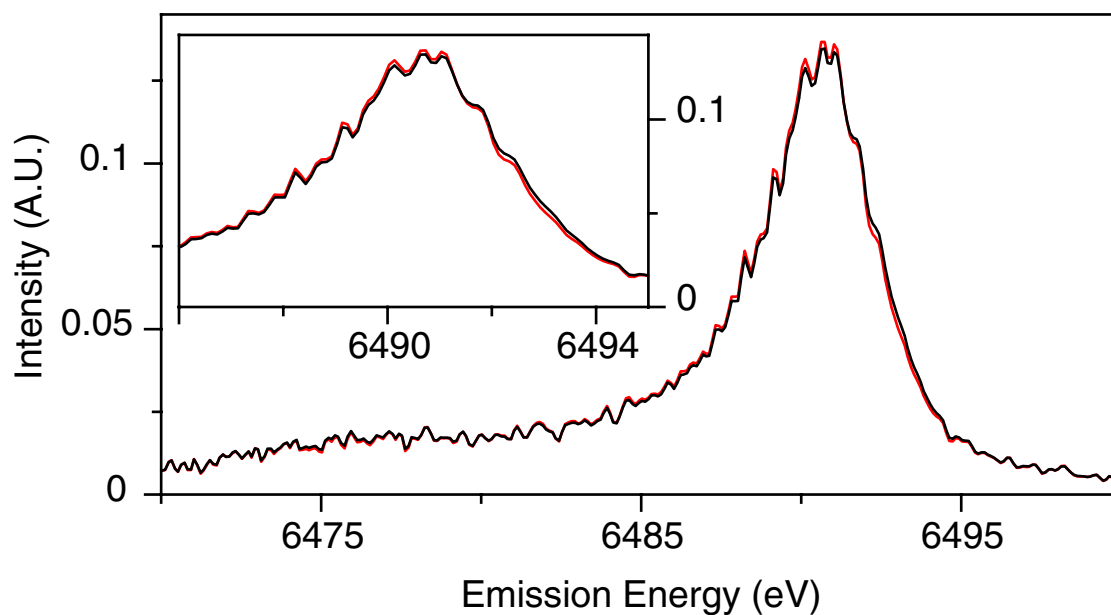


Figure 2.22 Comparison of the measured and deconvoluted Mn  $K\beta$  XES spectra for the mono- $\mu$ -oxo compound at the end of the second oxidation step. The measured spectrum is of sample **mono(IV,IV)<sub>F</sub>** (black) and the deconvoluted pure oxidation-state spectrum (red) is of the  $Mn^{IV}Mn^{IV}$  mono- $\mu$ -oxo species, with 1<sup>st</sup> moments 6490.01 eV and 6489.96 eV, respectively.

## 2.7 References

- (1) Kirby, J. A.; Goodin, D. B.; Wydrzynski, T.; Robertson, A. S.; Klein, M. P. *J. Am. Chem. Soc.* **1981**, *103*, 5537-5542.
- (2) Yachandra, V. K.; Sauer, K.; Klein, M. P. *Chem. Rev.* **1996**, *96*, 2927-2950.
- (3) Liang, W.; Roelofs, T. A.; Cinco, R. M.; Rompel, A.; Latimer, M. J.; Yu, W. O.; Sauer, K.; Klein, M. P.; Yachandra, V. K. *J. Am. Chem. Soc.* **2000**, *122*, 3399-3412.
- (4) Penner-Hahn, J. E. *Struct. Bonding (Berlin)* **1998**, *90*, 1-36.
- (5) Liang, W.; Latimer, M. J.; Dau, H.; Roelofs, T. A.; Yachandra, V. K.; Sauer, K.; Klein, M. P. *Biochemistry* **1994**, *33*, 4923-4932.
- (6) Miller, A. F.; Brudvig, G. W. *Biochim. Biophys. Acta* **1991**, *1056*, 1-18.
- (7) Messinger, J.; Robblee, J. H.; Yu, W. O.; Sauer, K.; Yachandra, V. K.; Klein, M. P. *J. Am. Chem. Soc.* **1997**, *119*, 11349-11350.
- (8) Peloquin, J. M.; Britt, R. D. *Biochim. Biophys. Acta* **2001**, *1503*, 96-111.
- (9) Robblee, J. H.; Cinco, R. M.; Yachandra, V. K. *Biochim. Biophys. Acta* **2001**, *1503*, 7-23.
- (10) Cooper, S. R.; Calvin, M. *J. Am. Chem. Soc.* **1977**, *99*, 6623-6630.
- (11) Kirby, J. A.; Robertson, A. S.; Smith, J. P.; Thompson, A. C.; Cooper, S. R.; Klein, M. P. *J. Am. Chem. Soc.* **1981**, *103*, 5529-5537.
- (12) Wieghardt, K. *Angew. Chem.-Int. Edit. Engl.* **1989**, *28*, 1153-1172.
- (13) Pecoraro, V. L.; Baldwin, M. J.; Gelasco, A. *Chem. Rev.* **1994**, *94*, 807-826.
- (14) Cinco, R. M.; Rompel, A.; Visser, H.; Aromí, G.; Christou, G.; Sauer, K.; Klein, M. P.; Yachandra, V. K. *Inorg. Chem.* **1999**, *38*, 5988-5998.

- (15) Pecoraro, V. L.; Hsieh, W.-Y. In *Manganese and Its Role in Biological Processes*; Sigel, A., Sigel, H., Eds.; Marcel Dekker Inc.: New York, 2000; Vol. 37, pp 429-504.
- (16) Christou, G.; Vincent, J. B. *Biochim. Biophys. Acta* **1987**, *895*, 259-274.
- (17) Renger, G. *Physiol. Plant.* **1997**, *100*, 828-841.
- (18) Hoganson, C. W.; Babcock, G. T. *Science* **1997**, *277*, 1953-1956.
- (19) Haumann, M.; Junge, W. *Biochim. Biophys. Acta* **1999**, *1411*, 86-91.
- (20) Siegbahn, P. E. M.; Crabtree, R. H. *J. Am. Chem. Soc.* **1999**, *121*, 117-127.
- (21) Messinger, J.; Robblee, J. H.; Bergmann, U.; Fernandez, C.; Glatzel, P.; Visser, H.; Cinco, R. M.; McFarlane, K. L.; Bellacchio, E.; Pizarro, S. A.; Cramer, S. P.; Sauer, K.; Klein, M. P.; Yachandra, V. K., manuscript submitted to *J. Am. Chem. Soc.*
- (22) Kok, B.; Forbush, B.; McGloin, M. *Photochem. Photobiol.* **1970**, *11*, 457-475.
- (23) Roelofs, T. A.; Liang, M. C.; Latimer, M. J.; Cinco, R. M.; Rompel, A.; Andrews, J. C.; Sauer, K.; Yachandra, V. K.; Klein, M. P. *Proc. Natl. Acad. Sci. U.S.A.* **1996**, *93*, 3335-3340.
- (24) Ono, T.; Noguchi, T.; Inoue, Y.; Kusunoki, M.; Matsushita, T.; Oyanagi, H. *Science* **1992**, *258*, 1335-1337.
- (25) Iuzzolino, L.; Dittmer, J.; Dörner, W.; Meyer-Klaucke, W.; Dau, H. *Biochemistry* **1998**, *37*, 17112-17119.
- (26) Stojanoff, V.; Hämäläinen, K.; Siddons, D. P.; Hastings, J. B.; Berman, L. E.; Cramer, S.; Smith, G. *Rev. Sci. Instrum.* **1992**, *63*, 1125-1127.

- (27) Peng, G.; DeGroot, F. M. F.; Hämmäläinen, K.; Moore, J. A.; Wang, X.; Grush, M. M.; Hastings, J. B.; Siddons, D. P.; Armstrong, W. H.; Mullins, O. C.; Cramer, S. P. *J. Am. Chem. Soc.* **1994**, *116*, 2914-2920.
- (28) Shulman, R. G.; Yafet, Y.; Eisenberger, P.; Blumberg, W. E. *Proc. Natl. Acad. Sci. U. S. A.* **1976**, *73*, 1384-1388.
- (29) Roe, A. L.; Schneider, D. J.; Mayer, R. J.; Pyrz, J. W.; Widom, J.; Que, L., Jr. *J. Am. Chem. Soc.* **1984**, *106*, 1676-1681.
- (30) DuBois, J. L.; Mukherjee, P.; Stack, T. D. P.; Hedman, B.; Solomon, E. I.; Hodgson, K. O. *J. Am. Chem. Soc.* **2000**, *122*, 5775-5787.
- (31) Westre, T. E.; Kennepohl, P.; DeWitt, J. G.; Hedman, B.; Hodgson, K. O.; Solomon, E. I. *J. Am. Chem. Soc.* **1997**, *119*, 6297-6314.
- (32) Jaklevic, J.; Kirby, J. A.; Klein, M. P.; Robertson, A. S.; Brown, G. S.; Eisenberger, P. *Solid State Commun.* **1977**, *23*, 679-682.
- (33) Tsutsumi, K.; Nakamori, H. *J. Phys. Soc. Jpn.* **1968**, *25*, 1419-1424.
- (34) Tsutsumi, K.; Nakamori, H.; Ichikawa, K. *Phys. Rev. B: Condens. Matter* **1976**, *13*, 929-933.
- (35) Sanner, V. H. Ph. D. thesis, Uppsala University, 1941.
- (36) Tsutsumi, K. *J. Phys. Soc. Jpn.* **1959**, *14*, 1696-1706.
- (37) Urch, D. S.; Wood, P. R. *X-Ray Spectrom.* **1978**, *7*, 9-11.
- (38) Taguchi, M.; Uozumi, T.; Kotani, A. *J. Phys. Soc. Jpn.* **1997**, *66*, 247-256.
- (39) Stebler, M.; Ludi, A.; Bürgi, H.-B. *Inorg. Chem* **1986**, *25*, 4743-4750.
- (40) Manchanda, R.; Brudvig, G. W.; Degala, S.; Crabtree, R. H. *Inorg. Chem.* **1994**, *33*, 5157-5160.

- (41) Horner, O.; Anxolabéhère-Mallart, E.; Charlot, M. F.; Tchertanov, L.; Guilhem, J.; Mattioli, T. A.; Boussac, A.; Girerd, J.-J. *Inorg. Chem.* **1999**, *38*, 1222-1232.
- (42) Anxolabéhère-Mallart, E.; Visser, H.; Bergman, U.; Cramer, S. P.; Girerd, J.-J.; Sauer, K.; Yachandra, V. K.; Klein, M. P. *J. Inorg. Biochem.* **1999**, *74*, 66.
- (43) Poussereau, S. Ph.D. thesis, Université de Paris-Sud, 1999.
- (44) Albela, B.; Chottard, G.; Girerd, J.-J., submitted for publication.
- (45) Although the cation resulting from the second oxidation process has been shown to possess some phenoxyl radical character,<sup>39,46</sup> further experiments showed that this radical is not stable and that it evolves rapidly into the  $[\text{Mn}^{\text{IV}}\text{Mn}^{\text{IV}}]^{4+}$  cation.<sup>42-44</sup>
- (46) Schnepf, R.; Sokolowski, A.; Müller, J.; Bachler, V.; Wieghardt, K.; Hildebrandt, P. *J. Am. Chem. Soc.* **1998**, *120*, 2352-2364.
- (47) Cooper, S. R.; Dismukes, G. C.; Klein, M. P.; Calvin, M. *J. Am. Chem. Soc.* **1978**, *100*, 7248-7252.
- (48) DeRose, V. J.; Mukerji, I.; Latimer, M. J.; Yachandra, V. K.; Sauer, K.; Klein, M. *J. Am. Chem. Soc.* **1994**, *116*, 5239-5249.
- (49) Cramer, S. P.; Tench, O.; Yocum, M.; George, G. N. *Nucl. Instrum. Methods Phys. Res. A* **1988**, *266*, 586-591.
- (50) Latimer, M. J.; DeRose, V. J.; Mukerji, I.; Yachandra, V. K.; Sauer, K.; Klein, M. *P. Biochemistry* **1995**, *34*, 10898-10909.
- (51) Teo, B. K. *EXAFS: Basic Principles and Data Analysis*; Springer-Verlag: New York, 1986.
- (52) Bergmann, U.; Cramer, S. P. In *SPIE Conference on Crystal and Multilayer Optics*; SPIE: San Diego, CA, 1998; Vol. 3448, pp 198-210.

- (53) Liu, H. B. I.; Filipponi, A.; Gavini, N.; Burgess, B. K.; Hedman, B.; Di Cicco, A.; Natoli, C. R.; Hodgson, K. O. *J. Am. Chem. Soc.* **1994**, *116*, 2418-2423.
- (54) Westre, T. E.; Di Cicco, A.; Filipponi, A.; Natoli, C. R.; Hedman, B.; Solomon, E. I.; Hodgson, K. O. *J. Am. Chem. Soc.* **1994**, *116*, 6757-6768.
- (55) Scott, M. J.; Zhang, H. H.; Lee, S. C.; Hedman, B.; Hodgson, K. O.; Holm, R. H. *J. Am. Chem. Soc.* **1995**, *117*, 568-569.
- (56) Laplaza, C. E.; Johnson, M. J. A.; Peters, J. C.; Odom, A. L.; Kim, E.; Cummins, C. C.; George, G. N.; Pickering, I. J. *J. Am. Chem. Soc.* **1996**, *118*, 8623-8638.
- (57) Cramer, S. P. In *X-ray Absorption: Principles, Applications, Techniques of EXAFS, SEXAFS and XANES*; Koningsberger, D. C., Prins, R., Eds.; Wiley: New York, 1988; p 257.
- (58) Yachandra, V. K. In *Methods Enzymol.*; Sauer, K., Ed.; Academic Press, Inc., 1995; Vol. 246, pp 638-675.
- (59) Robin, M. B.; Day, P. *Adv. Inorg. Chem. Radiochem.* **1967**, *10*, 247-422.
- (60) Kuzek, D.; Pace, R. J. *Biochim. Biophys. Acta* **2001**, *1503*, 123-137.



# Chapter 3

## **An Attenuated Total Reflection Design for *in Situ* FTIR Spectroelectrochemical Studies**



### 3.1 Introduction

*In situ* FTIR spectroelectrochemistry has proven useful for elucidating the structure of chemical intermediates and studying the redox chemistry of a wide range of molecules. In the past, many *in situ* infrared spectroelectrochemistry designs have been proposed and developed.<sup>1-3</sup> These designs range from transmission electrochemical cells, using minigrad electrodes,<sup>4-9</sup> to designs utilizing reflectance methods with either totally reflective<sup>10-12</sup> or transparent<sup>13-16</sup> electrodes. These techniques have addressed the problem of absorption of IR radiation by bulk solvent, but most designs do have other problems. For example, minigrad electrodes have scattering problems, and thin-cell transmittance designs in general are sensitive to leakage and are difficult to purge of oxygen. Because previous reflectance methods have measured the electrochemical species near and on the electrodes, their spectra may differ from the species in the bulk solution. Transparent electrodes generally have specific IR features, which can block important spectral regions. Also, reflectance approaches have had limited success in obtaining IR spectra using both highly reflective and conductive electrode materials.<sup>12-16</sup>

The versatile *in situ* infrared spectroelectrochemistry design presented here has a wide spectral range: 16,700  $\text{cm}^{-1}$  - 2250  $\text{cm}^{-1}$  and 1900 - 250  $\text{cm}^{-1}$ . It requires a small total sample volume (0.7 mL) which can be purged easily. The design is resistant to a variety of solvents, and different types of electrodes can be utilized. Good signal-to-noise is obtained for concentrations of ferrocene as low as 1 mM. The design is based on an attenuated total reflection (ATR) device that was developed for following chemical reactions *in situ* using FTIR spectroscopy.<sup>17,18</sup> This device is modified to perform

preparative electrochemistry, permitting measurement of the IR spectrum of the bulk solution near an ATR window. The system is tested with ferrocene, and the resulting IR spectra are compared to spectra previously published using transmission electrochemical cells.<sup>5,9</sup> The system has been successfully applied to analysis of nanosecond IR spectra of a series of substituted  $[\text{Ru}(\text{bpy})_3]^{2+}$  complexes. Transient MLCT excited-state IR features were identified by comparison with oxidized and reduced species.<sup>19</sup> In addition, this method has been used to study changes in the vibrational features of  $[\text{Mn}_4\text{O}_6(\text{bpea})_4]^{4+}$  upon reduction, at concentrations of  $\sim 2$  mM (see Chapter 4).<sup>20</sup>

### 3.2 Experimental

**Spectroelectrochemical apparatus:** The spectroelectrochemical apparatus consists of a home-built electrochemical cell designed to interface with an ASI DuraSampIIR™ (Applied Systems Inc., Annapolis, MD) ATR accessory. The IR beam passes through a KRS-5 support element and a 3 mm diamond sensing window of the ATR device, providing a wide spectral range of  $16,700\text{ cm}^{-1} - 250\text{ cm}^{-1}$ , with a small opaque region of  $2250 - 1900\text{ cm}^{-1}$ . Figure 3.1 shows the electrochemical cell, including the clamp that attaches the cell to the stainless steel interface plate of the ATR accessory. The electrochemical cell, constructed from a Teflon disk, is bolted to the clamp. A slot is excavated from this disk to make space for the reference and auxiliary electrode, and a small circular cavity inside this slot provides contact between bulk solution and diamond sensing window. Figure 3.2 gives a sideview of the cell along the long axis of the slot in the disk, which requires a sample volume of approx. 0.7 mL. A seal between the Teflon

disk and interface plate of the ATR device is provided by a butyl O-ring (which is resistant to acetonitrile).

**Electrochemistry:** The working electrode consists of a Pt wire (0.5 mm dia.) connected to a 6 mm diameter disk of Pt gauze (52 mesh woven of 0.1 mm dia. wire). The auxiliary electrode is similarly constructed with Pt gauze and is placed inside a fritted glass tube to allow electrochemical contact while minimizing diffusion of electrochemical products. A non-aqueous ( $\text{CH}_3\text{CN}$ , 0.1 M TBA( $\text{PF}_6$ )) Ag/AgClO<sub>4</sub> reference electrode is used. This electrode is isolated from the bulk solution by an additional electrolyte bridge (a glass tube fitted with a vycor tip), which is changed between samples to avoid contamination (Figure 3.2). The interface plate of the ATR accessory is grounded by connection to the ground of the voltammeter.

The electrolyte solution (0.1 M TBA( $\text{PF}_6$ ) in acetonitrile) is dried over  $\text{Al}_2\text{O}_3$ , bubbled with Ar, and kept under a constant flow of Ar throughout the experiment. To minimize evaporation and the resultant change in compound concentration, the Ar is bubbled through dry  $\text{CH}_3\text{CN}$  ( $\text{Al}_2\text{O}_3$ ). Ferrocene is obtained from Aldrich. The electrochemistry is conducted using a BAS CV-27 Voltammetry Controller. Oxidation of the ferrocene is performed at +0.6 V and reduction at -0.4 V vs the Ag/AgClO<sub>4</sub> reference electrode ( $E_{1/2}[\text{ferrocene}] = +0.1 \text{ V}$ ).

**FTIR spectroscopy:** The FTIR spectra are collected using a Bruker IFS88 FTIR spectrometer, using a broad band MCT detector (lower cut-off  $400 \text{ cm}^{-1}$ ). Before each experiment, the absorption spectrum is checked at the  $1375 \text{ cm}^{-1}$  and  $1038 \text{ cm}^{-1}$  acetonitrile peaks, and if the values are not  $\sim 0.13$  and  $\sim 0.09$  respectively, the working electrode is adjusted to remove air bubbles that are presumably trapped on the diamond

window below the working electrode. All spectra are taken at a resolution of  $4\text{ cm}^{-1}$ , and absorption spectra consist of 100 averaged scans. Spectra taken during electrochemistry are recorded in rapid scan mode (128 ms per scan) and 100 scans are averaged into a scan group (12.8 s).

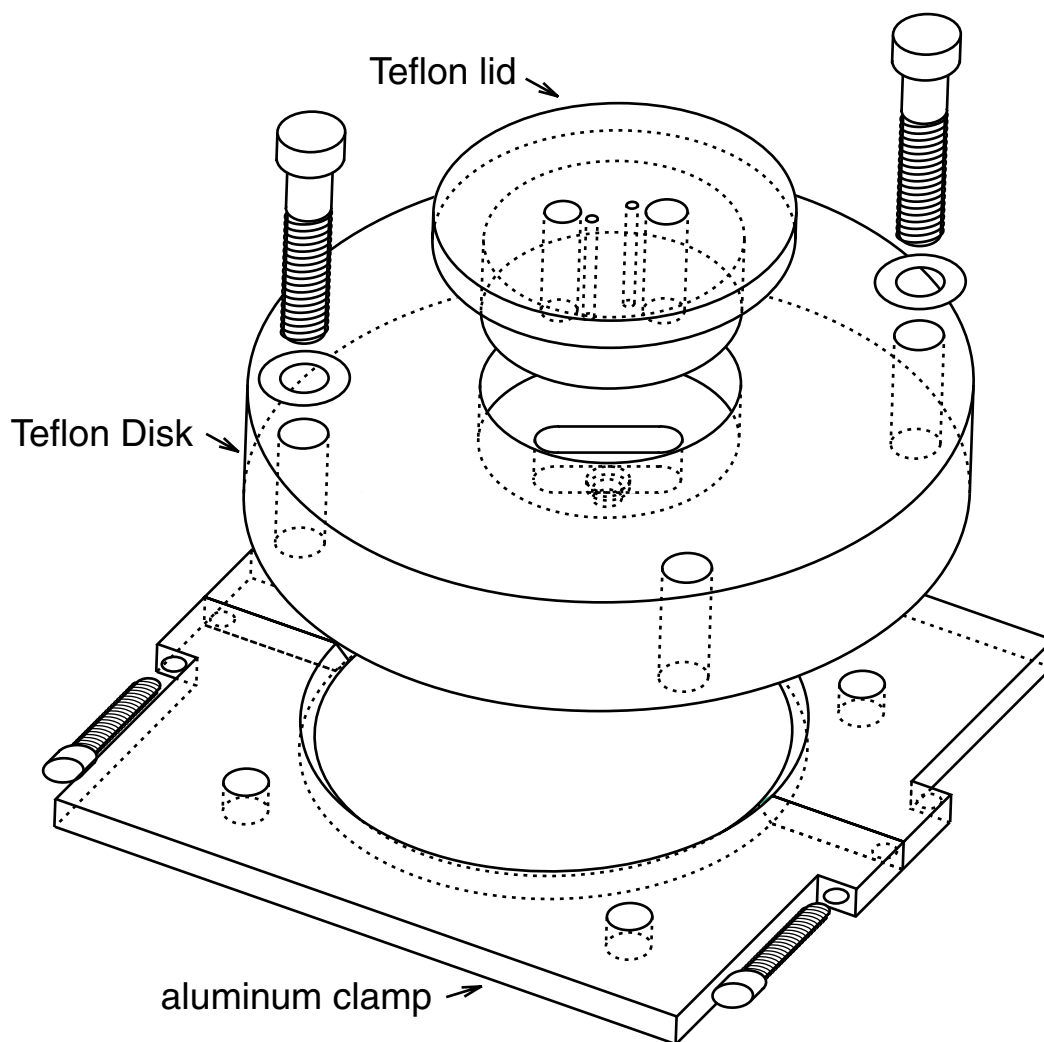


*Figure 3.1. The electrochemical cell that is designed to fit onto the ASI DuraSamplIR™ ATR accessory, consisting of an aluminum base clamp, a Teflon disk from which the cell compartment is excavated and a Teflon, airtight lid. A total sample volume of approximately 0.7 mL is required.*

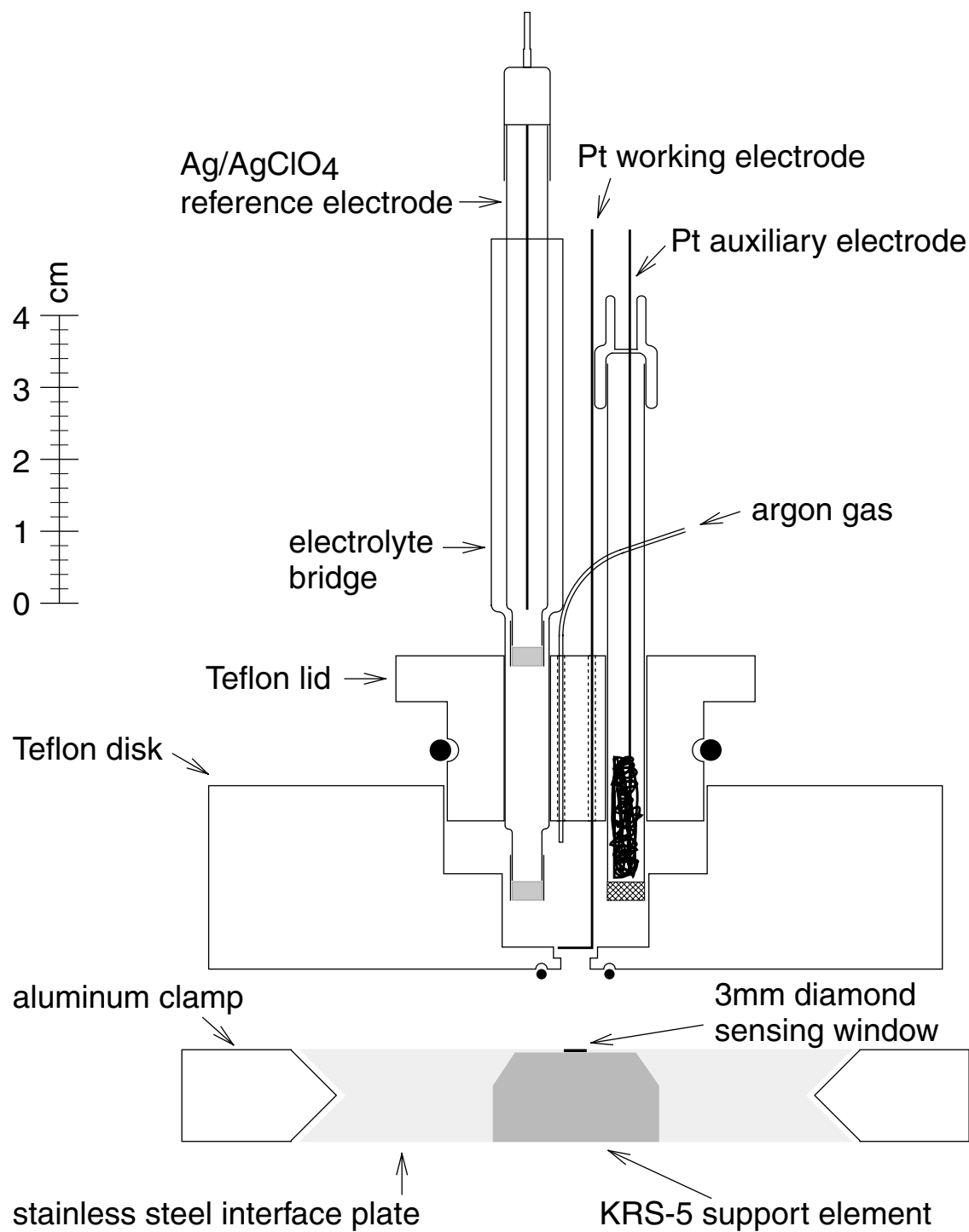


Figure 3.2 Cross section of the electrochemical cell and the stainless steel interface plate of the ATR accessory, along the long axis of the excavated slot. A total sample volume of approximately 0.7 mL is required.

### 3.3 Results and Discussion

Figure 3.3 shows the FTIR absorption spectrum of a 5 mM ferrocene electrolyte solution in the spectroelectrochemical cell, which is dominated by the bulk solvent and electrolyte. Characteristic peaks of ferrocene, such as those at 1107 and 1005  $\text{cm}^{-1}$ , are too small to be observed. Therefore, it is necessary to obtain difference spectra of the solution before and after electrochemistry. The advantage of taking difference spectra is that signals that do not change upon redox chemistry are eliminated, and only the relevant signals remain.

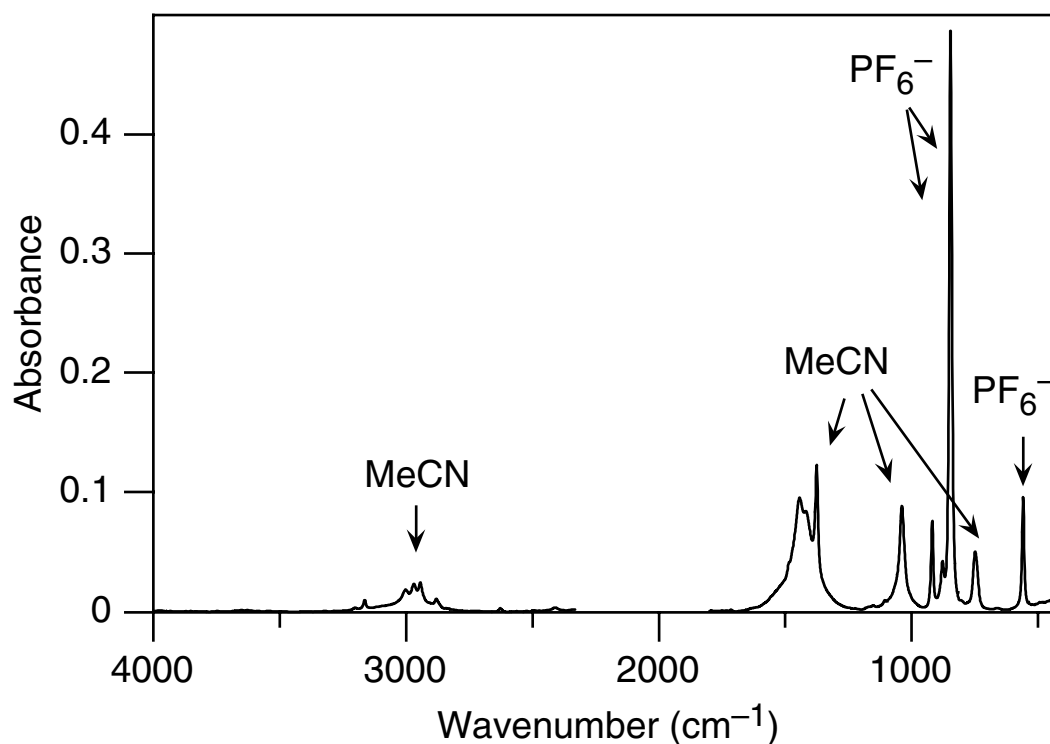


Figure 3.3 FTIR absorption spectrum of 5 mM ferrocene, 0.1 M TBA(PF<sub>6</sub>) in acetonitrile solution before electrochemistry (average of 100 scans at 4  $\text{cm}^{-1}$  resolution).

Figure 3.4 shows the FTIR absorption difference spectra during the oxidation ( $\text{Fe}^{\text{II}}$  to  $\text{Fe}^{\text{III}}$ ) of a 5 mM ferrocene solution, 0.1 M TBA( $\text{PF}_6$ ) in acetonitrile. A decrease of the ferrocene peaks at 1107 and 1005  $\text{cm}^{-1}$  can be observed as a function of time (corresponding to scan-group number in Figure 3.4) after starting the oxidation. The signals associated with the oxidized ferrocene attain their maximum after roughly 6 scan groups (600 scans is about 80 s). When electrochemistry is performed on low concentrations of electrochemical species certain background signals arise, such as at 1040  $\text{cm}^{-1}$ . These bands can be distinguished here due to their different dynamic behavior relative to those associated with ferrocene. In addition to their difference in dynamic behavior to ferrocene, the mentioned background signals are electrochemically non-reversible.

Based on these differences of the signals, an experimental procedure is performed where IR spectra are taken while alternating between oxidation and reduction periods. This enables us to make a distinction between reversible (ferrocene/ferricinium) and non-reversible (solvent and electrolyte) signals. These electrochemical periods, consisting of 16 scan groups (~205 s), are chosen to minimize the rise of the solvent signals, while maximizing the ferrocene signal. To obtain the difference spectra, the last 12 scan groups before oxidation (or reduction) are averaged and subtracted from the average of scan group 5-16 after oxidation (or reduction). The first 4 scan groups are not used because of their small signal contribution. Figures 3.5, 3.6 and 3.7 show the difference spectra obtained for the first oxidation (purple) and reduction (blue) periods. All difference spectra are presented such that features due to ferricinium are positive and ferrocene are negative. Consequently, reversible features have the same sign in both the oxidation and

reduction spectra, and non-reversible features have the opposite sign. Reversible features are indicated with arrows.

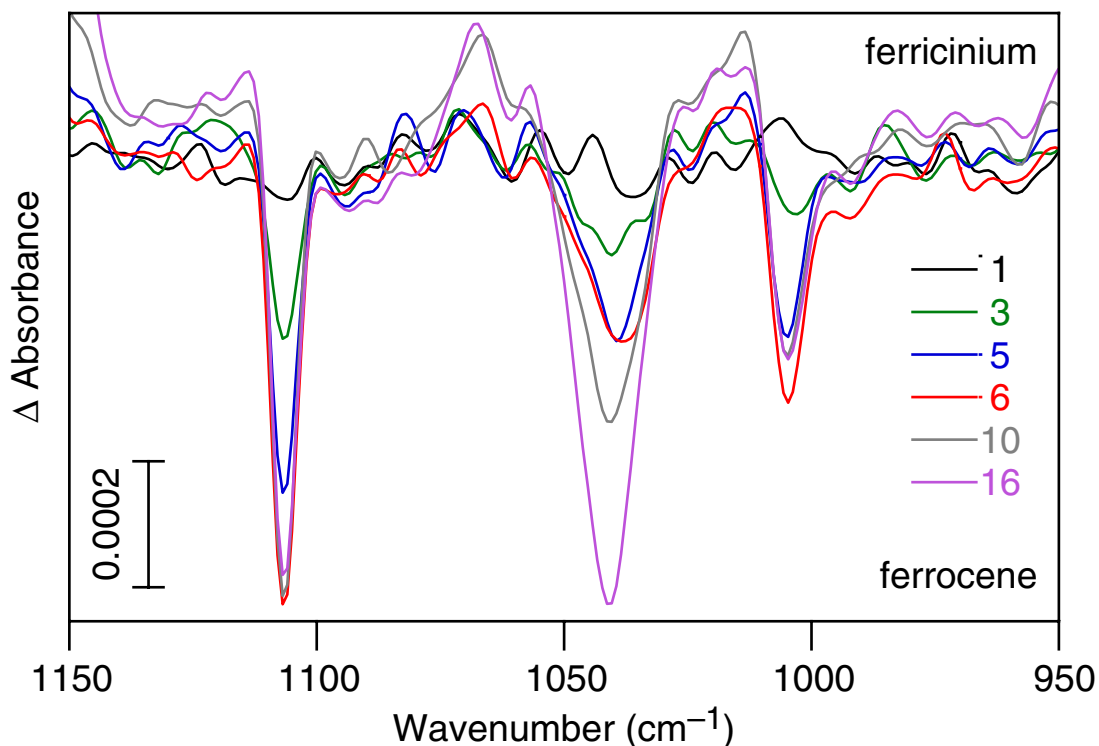


Figure 3.4 FTIR difference spectra at different times during the oxidation of a 5 mM ferrocene, 0.1 M TBA(PF<sub>6</sub>) in acetonitrile solution. The numbers refer to the scan group taken after starting the electrochemistry (each scan group contains 100 scans of 128 ms), from which one scan group taken before electrochemistry is subtracted. Spectra are measured at a 4 cm<sup>-1</sup> resolution (ferricinium has positive peaks and ferrocene has negative peaks).

Two types of non-reversible features can be distinguished by their different dynamic behavior. The features at 840 and 550 cm<sup>-1</sup> are due to the counter ion PF<sub>6</sub><sup>-</sup> (see also Figure 3.3). These signals are expected to be reversible, because PF<sub>6</sub><sup>-</sup> is the counter ion to the ferrocene/ferricinium couple. However, even though great care is taken to prevent evaporation of acetonitrile, a constant increase in concentration is observed,



which overwhelms the reversible behavior of the counter ion features. (Reversibility of  $\text{PF}_6^-$  has been observed in other experiments.) These are the only two features that occur when no potential is applied to an electrolyte solution, i.e. without ferrocene present. However, when a potential is applied to the electrolyte solution, non-reversible signals occur, such as at  $2900\text{ cm}^{-1}$  in Figure 3.5, at  $1478\text{ cm}^{-1}$  and  $1040\text{ cm}^{-1}$  in Figure 3.6, and at  $740\text{ cm}^{-1}$  in Figure 3.7. This indicates, that these non-reversible features are due to decomposition of the electrolyte solution. All these features are underneath acetonitrile absorption peaks (see Figures 3.3 and 3.7). Therefore, the non-reversible features are most likely due to changes of acetonitrile.

Each oxidation and reduction period is performed twice and averaged. The sum spectrum (black) is obtained by subtracting a fraction of the averaged reduction spectrum from the oxidation spectrum. The fraction is chosen so that all non-reversible features due to the acetonitrile are minimized over the whole spectral range ( $4000\text{ cm}^{-1}$  -  $400\text{ cm}^{-1}$ ). This fraction is 0.82 for the sum spectra in Figures 3.5, 3.6 and 3.7. The sum spectra show several signals due to the ferrocene/ferricinium species. Upon oxidation of ferrocene, new vibrational features appear at  $3114$ ,  $1419$ ,  $1014$ ,  $458$ , and  $440\text{ cm}^{-1}$ . Vibrational features at  $1107$ ,  $1005$ ,  $819$ ,  $494$ , and  $479\text{ cm}^{-1}$  disappear due to the formation of ferricinium. The difference features at  $1107$ ,  $1014$ , and  $1005\text{ cm}^{-1}$  agree with previously published data,<sup>5,9,10</sup> indicating that this spectroelectrochemical design and method of data acquisition is viable with low concentrations of electrochemical species. To the knowledge of the authors, this is the first time that the IR difference features at  $3114$ ,  $1419$ ,  $819$ ,  $494$ ,  $479$ ,  $458$ , and  $440\text{ cm}^{-1}$  have been observed and assigned to vibrational changes of ferrocene when oxidized into ferricinium. The inset of Figure 3.6

shows the sum difference spectrum for a 1 mM ferrocene solution. Even though the spectrum is noisy, the two features at 1107 and 1005  $\text{cm}^{-1}$  can be observed. With more signal-to-noise averaging, i.e. averaging more oxidation and reduction steps, one could presumably go to even lower concentrations.

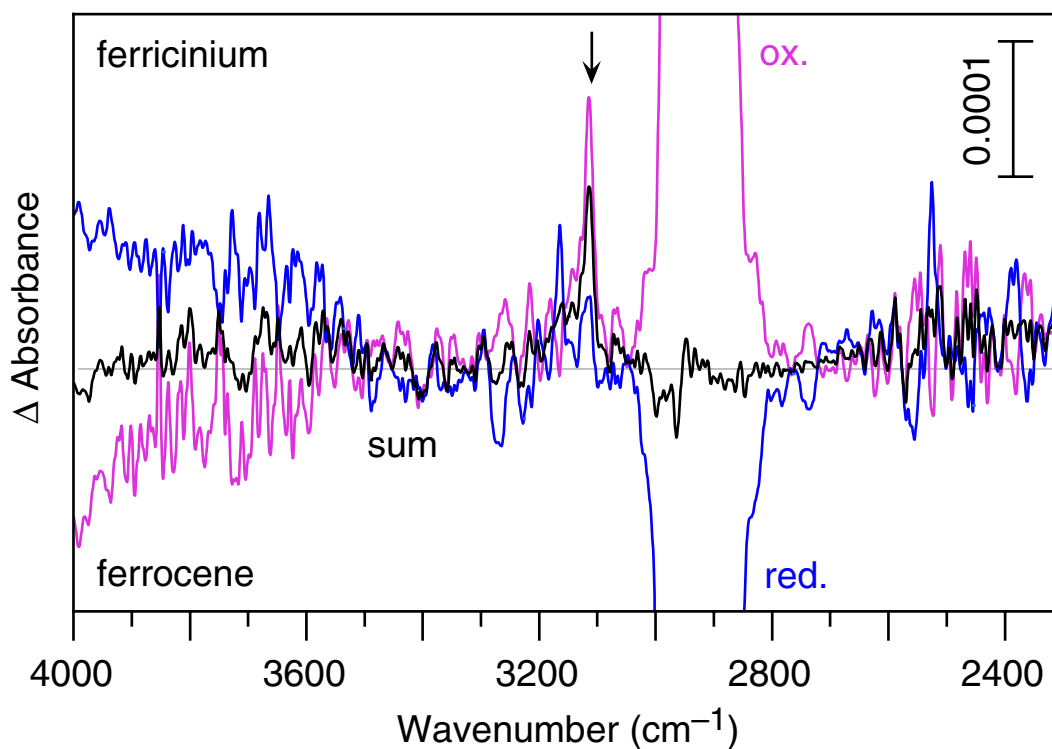


*Figure 3.5 FTIR difference spectra of ferricinium/ferrocene, of a 5 mM ferrocene, 0.1 M TBA(PF<sub>6</sub>) acetonitrile solution for 4000 - 2300  $\text{cm}^{-1}$  range. Each graph shows difference spectra of the first oxidation (purple) step, first reduction (blue) step, and the averaged sum of two oxidations and two reduction steps (black). Arrows indicate reversible absorption peaks that can be ascribed to either ferrocene or ferricinium. Spectra are taken at 4  $\text{cm}^{-1}$  resolution.*

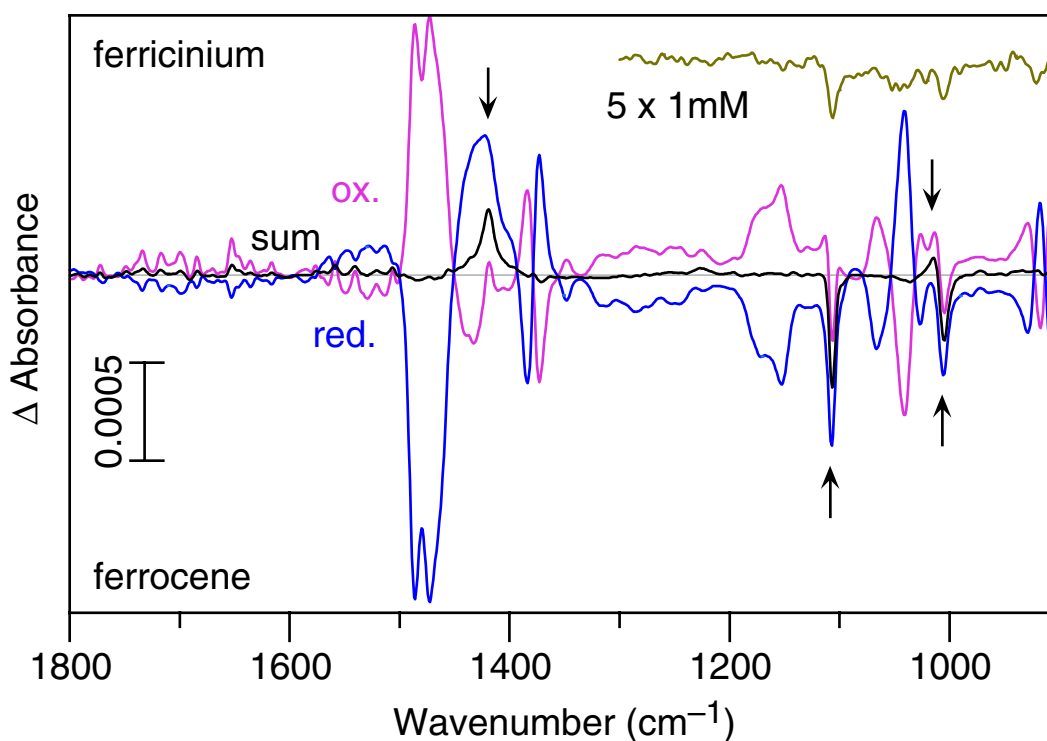


Figure 3.6 FTIR difference spectra of ferricinium/ferrocene, of a 5 mM ferrocene, 0.1 M TBA(PF<sub>6</sub>) acetonitrile solution for the 1800 - 900 cm<sup>-1</sup> range. Each graph shows difference spectra of the first oxidation (purple) step, first reduction (blue) step, and the averaged sum of two oxidations and two reduction steps (black). Arrows indicate reversible absorption peaks that can be ascribed to either ferrocene or ferricinium. The inset is the sum difference spectrum of a 1 mM ferrocene electrolyte solution (brown). Spectra are taken at 4 cm<sup>-1</sup> resolution.

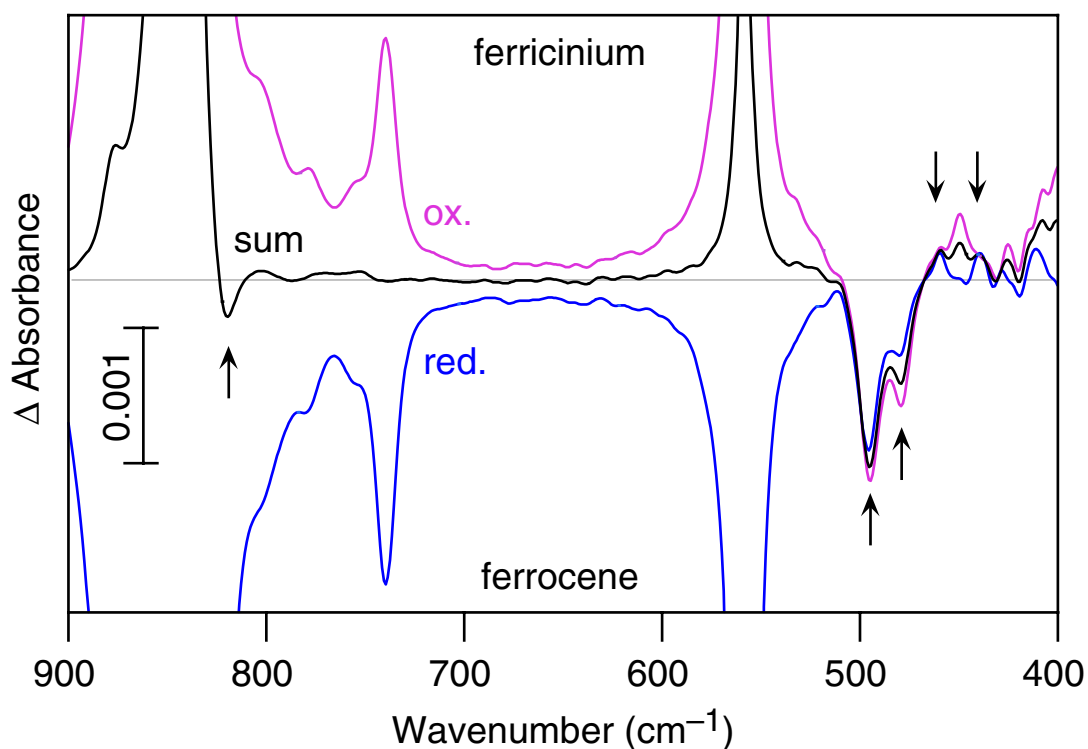


Figure 3.7 FTIR difference spectra of ferricinium/ferrocene, of a 5 mM ferrocene, 0.1 M TBA( $\text{PF}_6$ ) acetonitrile solution for the 900 - 400  $\text{cm}^{-1}$  range. Each graph shows difference spectra of the first oxidation (purple) step, first reduction (blue) step, and the averaged sum of two oxidations and two reduction steps (black). Arrows indicate reversible absorption peaks that can be ascribed to either ferrocene or ferricinium. Spectra are taken at 4  $\text{cm}^{-1}$  resolution.

### 3.4 Conclusion

Figures 3.4, 3.5, 3.6, and 3.7 show that FTIR difference spectra of ferrocene in different oxidation state can be obtained using the spectroelectrochemical design. The sensitivity of the method is enhanced by applying the experimental protocol of alternation between oxidation and reduction periods. This protocol enables us to eliminate the non-reversible background signals. Consequently, good signal to noise ratios of ferrocene for concentrations as low as 1 mM are obtained. This spectroelectrochemical design and experimental protocol also have been used successfully to study the vibrational features of  $[\text{Mn}_4\text{O}_6(\text{bpea})_4]^{4+}$  and the reduced species, at concentrations of  $\sim 2$  mM (Chapter 4).<sup>20</sup> In addition, this method has been applied to identify features in nanosecond excited-state IR spectra of asymmetrically substituted  $[\text{Ru}(\text{bpy})_3]^{2+}$ -type complexes at concentrations of 5-10 mM.<sup>19</sup> IR features corresponding to  $\text{Ru}^{\text{III}}(\text{bpy})$  and the reduced ligand ( $\text{bpy}^-$ ) were identified by comparison of the spectra from the transient MCLT excited-state IR with that of the electrochemically prepared species. This indicates, that spectroelectrochemical design and experimental protocol can be used for variety of inorganic complexes.

A drawback of this design is that the response time of the compound signal is dependent on the rate of diffusion. Therefore, the dynamic behavior during electrochemistry is dependent on the size of the studied compound and the distance between working electrode and sensing window. To eliminate the diffusion dependence the bulk solution needs to be stirred, accelerating the rate of electrochemistry, improving the signal-to-noise ratio, and reducing background signal problems. To facilitate this enhancement a stir rod could be added through the Teflon lid and a basket shaped

working electrode could be used, instead of a disk shaped one.

Several other permutations of the cell can be envisioned. For example, the total volume could be reduced using micro reference and auxiliary electrodes. The Pt working electrode could be of another electrode material, for example reticulated vitreous carbon. If experiments at a lower temperature are required a cooling jacket could be added in the Teflon disk around the cell slot (the ASI DuraSampIIR™ ATR accessory is stated to give reproducible results down to about 230 K). The flexibility of our design allows for these and other modifications.

### 3.5 References

- (1) Heineman, W. R. *J. Chem. Ed.* **1983**, *60*, 305-308.
- (2) Ashley, K. *Talanta* **1991**, *38*, 1209-1218.
- (3) Foley, J. K.; Pons, S. *Anal. Chem.* **1985**, *57*, 945A-956A.
- (4) Hartl, F.; Luyten, H.; Nieuwenhuis, H. A.; Schoemaker, G. C. *Appl. Spectrosc.* **1994**, *48*, 1522-1528.
- (5) Krejcik, M.; Danek, M.; Hartl, F. *J. Elec. Chem.* **1991**, *317*, 179-187.
- (6) Flowers, P. A.; Mamantov, G. *Anal. Chem.* **1989**, *61*, 190-192.
- (7) Yao, C. L.; Capdevielle, F. J.; Kadish, K. M.; Bear, J. L. *Anal. Chem.* **1989**, *61*, 2805-2809.
- (8) Nevin, W. A.; Lever, A. B. P. *Anal. Chem.* **1988**, *60*, 727-730.
- (9) Bullock, J. P.; Boyd, D. C.; Mann, K. R. *Inorg. Chem.* **1987**, *26*, 3084-3086.
- (10) Rosa-Montanez, M. E.; De Jesus-Cardona, H.; Cabrera-Martinez, C. R. *Anal.*

*Chem.* **1998**, *70*, 1007-1011.

- (11) Klima, J.; Kratochvilova, K.; Ludvik, J. *J. Electroanal. Chem.* **1997**, *427*, 57-61.
- (12) Best, S. P.; Clark, R. J. H.; McQueen, R. C. S.; Cooney, R. P. *Rev. Sci. Instrum.* **1987**, *58*, 2071-2074.
- (13) Kulesza, P. J.; Malik, M. A.; Denca, A.; Strojek, J. *Anal. Chem.* **1996**, *68*, 2442-2446.
- (14) Ping, Z.; Neugebauer, H.; Neckel, A. *Electrochim. Acta* **1996**, *41*, 767-772.
- (15) Bae, I. T.; Sandifer, M.; Lee, Y. W.; Tryk, D. A.; Sukenik, C. N.; Scherson, D. A. *Anal. Chem.* **1995**, *67*, 4508-4513.
- (16) Neugebauer, H.; Nauer, G.; Brinda-Konopik, N. *J. Electroanal. Chem.* **1981**, *122*, 381-385.
- (17) Sheridan, R. E.; Rein, A. *J. R&D* **1991**, *33*, 100-102.
- (18) Milosevic, M.; Sting, D.; Rein, A. *Spectroscopy* **1995**, *10*, 44-49.
- (19) Curtright, A. E.; McCusker, J. K. *J. Phys. Chem. A* **1999**, *103*, 7032-7041.
- (20) Visser, H.; Dubé, C. E.; Armstrong, W. H.; Sauer, K.; Yachandra, V. K., manuscript in preparation.

# Chapter 4

**FTIR spectra and normal-mode analysis of the  
Mn adamantane-like compound,  
[Mn<sup>IV</sup><sub>4</sub>O<sub>6</sub>(bpea)<sub>4</sub>]<sup>4+</sup> and its reduced form,  
[Mn<sup>III</sup>Mn<sup>IV</sup><sub>3</sub>O<sub>6</sub>(bpea)<sub>4</sub>]<sup>3+</sup>**



## 4.1 Introduction

The supply of the world's oxygen is a by-product of the water oxidation process carried out by organisms of oxygenic photosynthesis, such as cyanobacteria and green plants. Water oxidation takes place in a trans-membrane protein cluster, Photosystem II (PS II), where it is catalyzed by the oxygen-evolving complex (OEC). A photon-induced electron abstraction from the OEC occurs during each of the first four state transitions of the catalytic cycle ( $S_0 \rightarrow S_1$ ,  $S_1 \rightarrow S_2$ ,  $S_2 \rightarrow S_3$ ,  $S_3 \rightarrow [S_4] \rightarrow S_0$ ).<sup>1</sup> Dioxygen is released when the  $S_3$  state returns to the  $S_0$  state, via the hypothesized  $S_4$  state.

Although great progress has been made in obtaining a high-resolution crystal structure of PS II,<sup>2</sup> most of our knowledge about the OEC has been obtained from X-ray absorption<sup>3-7</sup> and EPR spectroscopy.<sup>8-11</sup> From these studies, it is known that the OEC contains four manganese atoms which are arranged in two to three di- $\mu$ -oxo moieties and one mono- $\mu$ -oxo moiety. In addition, two co-factors,  $Ca^{2+}$  and  $Cl^-$ , are required for water oxidation. One or two histidines are directly ligated to one of the manganese atoms of the OEC, while glutamate and aspartate provide most of the other the terminal ligands to the OEC.<sup>12-14</sup> During the first two state transitions ( $S_0 \rightarrow S_1$ ,  $S_1 \rightarrow S_2$ ) an electron is abstracted from Mn.<sup>15-18</sup> However, during the third state transition ( $S_2 \rightarrow S_3$ ) X-ray spectroscopy studies indicate that oxidation of manganese is unlikely; an electron may instead be extracted from a nearby ligand.<sup>15,16</sup> The synthesis and study of a wide variety of manganese model compounds have been critical for the interpretation of the X-ray and EPR spectra of the OEC.<sup>3,19-25</sup>

Recently vibrational spectroscopy has been added as an investigative tool to study the structure and mechanism of the OEC. Changes during the catalytic cycle in the 1800 - 1200  $\text{cm}^{-1}$  range, which contains vibrations of the protein-residues ligated to the OEC<sup>26-31</sup> are complemented by those of the Mn–ligand vibrations, specifically the Mn–O vibrations, which occur in the 200 - 1000  $\text{cm}^{-1}$  range (Table 4.1).<sup>26,32</sup> However, several complications arise in measuring and interpreting the Mn–ligand vibrations by either infrared or Raman spectroscopy.

In infrared spectroscopy, the Mn–ligand vibration region is obscured by the absorption of water present in the biological preparations. Additionally, most detectors have a low signal to noise ratio for frequencies below 600  $\text{cm}^{-1}$ . Nevertheless, Chu et al.<sup>26,32,33</sup> were able to obtain IR difference spectra of the  $S_1 \rightarrow S_2$  transition of the OEC in the 350 - 1000  $\text{cm}^{-1}$  range, using a helium bolometer detector and special IR filters<sup>34</sup> which improved the signal–to–noise–ratio. They have identified a Mn–O–Mn vibration at 625  $\text{cm}^{-1}$  in the  $S_1$  state, which shifts to 606  $\text{cm}^{-1}$  in the  $S_2$  state (596  $\text{cm}^{-1}$  in the  $^{18}\text{O}$ -treated sample).

To apply Raman spectroscopy to the OEC successfully, the fluorescence of chlorophylls and carotenoids present in PS II, needs to be addressed. Recently, Cua et al.<sup>35</sup> have worked around this complication and obtained low frequency (220 - 620  $\text{cm}^{-1}$ ) Resonance Raman spectra. An excitation wavelength of 820 nm was used, which is outside the main absorption of the pigments, and which coincides with an electronic transition of the Mn cluster.<sup>36-39</sup> To mitigate the remainder of the fluorescence from the pigments, the technique of shifted-excitation Raman difference spectroscopy

(SERDS)<sup>40,41</sup> was utilized. Two absorption frequencies at 348 cm<sup>-1</sup> and 476 cm<sup>-1</sup> were tentatively assigned to Mn–O vibrations and are sensitive to isotopic exchange of D for H. Such vibrational assignments of the OEC are supported by the studies of known manganese compounds.

As for the X-ray and EPR spectroscopies, vibrational spectra of manganese model compounds are indispensable for the interpretation of the IR and Raman spectra of the OEC. Table 4.1 gives the vibrational frequencies observed for a variety of Mn moieties in manganese compounds. Different kinds of Mn–O stretching modes occur in the 500 - 900 cm<sup>-1</sup> range, while Mn–O bending modes occur in the 300 - 450 cm<sup>-1</sup>. Mn-halide vibrations can occur from 100 cm<sup>-1</sup> to 720 cm<sup>-1</sup>, depending on the oxidation state of the manganese. Mn-terminal/chelating ligand vibrations occur in the 100 - 400 cm<sup>-1</sup> range. In addition, other vibrations of the ligating molecule occur in the 200 - 1000 cm<sup>-1</sup> range. Consequently, conclusive identification of specific Mn–ligand vibrations is complicated. Therefore, a more extensive understanding of vibrational spectra is required. Isotopic exchange, such as <sup>16</sup>O→<sup>18</sup>O, is necessary to positively distinguish Mn–O vibrations from those of the terminal ligating molecule. Additionally, isotopic exchange is also necessary to identify modes that are indicative of the oxidation state of the Mn atoms. Normal-mode analysis of the compound is required to understand the pattern of the identified vibrations and to extract force constants. These force constants can be used to predict and analyze the vibrational spectra of other compounds and the OEC

Table 4.1 Vibrational frequency regions of IR- or Raman-active Mn–ligand modes.

Type of compound	Ox. state	Type	Range (cm <sup>-1</sup> )	Ref.
(porphyrin)Mn=O	Mn <sup>IV</sup>	stretch	711 - 757	42
	Mn <sup>V</sup>	stretch	970 - 981	43,44
(MnO <sub>4</sub> ) <sup>x-</sup>	Mn <sup>V</sup>	stretch	763 - 838	45-47
		bend	316 - 349	45,47
	Mn <sup>VI</sup>	stretch bend	814 - 888 325 - 332	45,48,49 45
Mn–O–Mn mono- $\mu$ -oxo	Mn <sup>III</sup> Mn <sup>III</sup>	stretch	551 - 764	52-55
	Mn <sup>III</sup> Mn <sup>IV</sup>	stretch	681	56
	Mn <sup>IV</sup> Mn <sup>IV</sup>	stretch	794	57
Mn–O <sub>2</sub> –Mn di- $\mu$ -oxo	Mn <sup>III</sup> Mn <sup>IV</sup>	stretch	589 - 700	20,52,56,58-63
	Mn <sup>IV</sup> Mn <sup>IV</sup>	stretch	640 - 705	20,52,56,63-67
Mn–O <sub>3</sub> –Mn tri- $\mu$ -oxo	Mn <sup>IV</sup> Mn <sup>IV</sup>	stretch	670 - 701	68,69
Mn–X X = halide	Mn <sup>II</sup> –Cl	stretch	158-347	70-73
	Mn <sup>II</sup> –Br	stretch	138-226	70,72,73
	Mn <sup>II</sup> –I	stretch	108 - 193	72,73
	Mn <sup>VII</sup> -Cl	stretch	453 - 459	74
	Mn <sup>VII</sup> -F	stretch	710 - 716	75
Mn–X <sub>2</sub> –Mn	Mn <sup>II</sup> Cl <sub>2</sub> Mn <sup>II</sup>	stretch	160 - 210	76-78
	Mn <sup>II</sup> Br <sub>2</sub> Mn <sup>II</sup>	stretch	115 - 175	77,78
	Mn <sup>II</sup> I <sub>2</sub> Mn <sup>II</sup>	stretch	103	78
Mn–terminal/chelating ligand; non-halide	Mn <sup>II</sup> –N	stretch	230 - 240	76
	Mn <sup>II</sup> –O	stretch	335 - 377	70,76
	Mn <sup>III</sup> –N	stretch	175 - 342	77-79

Table 4.2 Published Mn–O, and Mn–halide force constants.

Type of compound	Force constants (mdyn/Å)		Ref.
[HO–Mn <sup>III</sup> –OH](TMPyp) (solv. CH <sub>2</sub> Cl <sub>2</sub> )	$f_{\text{Mn-OH}} = 2.46$		42
[HO–Mn <sup>IV</sup> –O](TMPyp) (solv. CH <sub>2</sub> Cl <sub>2</sub> )	$f_{\text{Mn-O}} = 3.43$ $f_{\text{Mn-OH}} = 2.6$	$f_{\text{O-H}} = 7.2$ $f_{\text{Mn-OH/O-H}} = 0.3$	42
[Cl–Mn <sup>IV</sup> –O](TMP) (solv. CH <sub>3</sub> CN)	$f_{\text{Mn-O}} = 4.15$		42
[Cl–Mn <sup>IV</sup> –O](TPP) (solv. CH <sub>2</sub> Cl <sub>2</sub> )	$f_{\text{Mn-O}} = 4.15$		42
[Mn <sup>V</sup> O <sub>4</sub> ] <sup>3-</sup> (aq.)	$f_{\text{Mn-O}} = 5.01$ $f_{\text{Mn-O/Mn-O}} = 0.39$	$f_{\alpha} = 0.39$ $f_{\alpha\alpha} = 0.02$	45
[Mn <sup>VI</sup> O <sub>4</sub> ] <sup>2-</sup> (aq.)	$f_{\text{Mn-O}} = 4.88$ $f_{\text{Mn-O/Mn-O}} = 0.45$	$f_{\alpha} = 0.35$ $f_{\alpha\alpha} = 0.07$	45
[Mn <sup>VII</sup> O <sub>4</sub> ] <sup>-</sup> (aq.)	$f_{\text{Mn-O}} = 5.79$ $f_{\text{Mn-O/Mn-O}} = 0.28$	$f_{\alpha} = 0.59$ $f_{\alpha\alpha} = 0.1$	45
Mn <sup>VII</sup> O <sub>3</sub> F	$f_{\text{Mn-O}} = 6.33$ $f_{\text{Mn-O/Mn-O}} = 0.29$	$f_{\text{Mn-F}} = 4.27 - 4.40$	74,75
Mn <sup>VII</sup> O <sub>3</sub> Cl	$f_{\text{Mn-O}} = 6.31$ $f_{\text{Mn-O/Mn-O}} = 0.24$	$f_{\text{Mn-Cl}} = 2.56$	74
Mn <sup>VI</sup> Cl <sub>4</sub>	$f_{\text{Mn-Cl}} = 1.31 - 1.40$		72,73
Mn <sup>VI</sup> Br <sub>4</sub>	$f_{\text{Mn-Br}} = 1.17$		72,73
Mn <sup>VI</sup> I <sub>4</sub>	$f_{\text{Mn-I}} = 0.76 - 1.01$		72,73
[Mn <sup>III</sup> <sub>2</sub> O(O <sub>2</sub> CCH <sub>3</sub> ) <sub>2</sub> (HB(pz) <sub>3</sub> ) <sub>2</sub> ]	$f_{\text{Mn-O}} = 3.34$	$f_{\text{Mn-O/Mn-O}} = 0.74$	55

\*TMPyp = tetrakis(methylpyridinium)porphyrin; TMP = tetramethylporphyrin;  
 TPP = tetraphenylporphyrin; HB(pz)<sub>3</sub> = hydrotris(1-pyrazolyl)borate

Table 4.2 presents a list of the few force constants that have been previously published. From this table several trends can be observed. For example, the higher the manganese oxidation state, the stronger the Mn–O bond. This is true for the porphyrin compounds and, to a lesser extent, the  $[\text{MnO}_4]^{x-}$  compounds, with the  $[\text{Mn}^{\text{VI}}\text{O}_4]^{2-}$  compound as an exception. A stronger Mn–O bond can cause the vibrations to have a higher frequency, as can be seen in Table 4.1, for the porphyrin and the  $[\text{MnO}_4]^{x-}$  compounds. However, the  $\mu$ -oxo bridged compounds in Table 4.1 show that this is not always true. The bond strength is determined not only by the oxidation state of the manganese but also by the electronegativity of the bridging and terminal ligands, which can be seen for the  $\text{MnO}_3\text{X}$  and the  $\text{MnX}_4^{2-}$  compounds. The Mn–ligand interaction is also influenced by the strength of the other Mn–ligand bonds. This can be seen by comparing the  $\text{MnO}_3\text{X}$  compounds with the  $[\text{MnO}_4]^-$  compound. Force constants also are altered slightly when a compound is a solid or when it is in solution. Even though some trends can be observed, only the last compound in Table 4.2 contains a moiety which is relevant to the OEC. Therefore, more vibrational studies are required of manganese compounds in oxidation states relevant to the OEC.

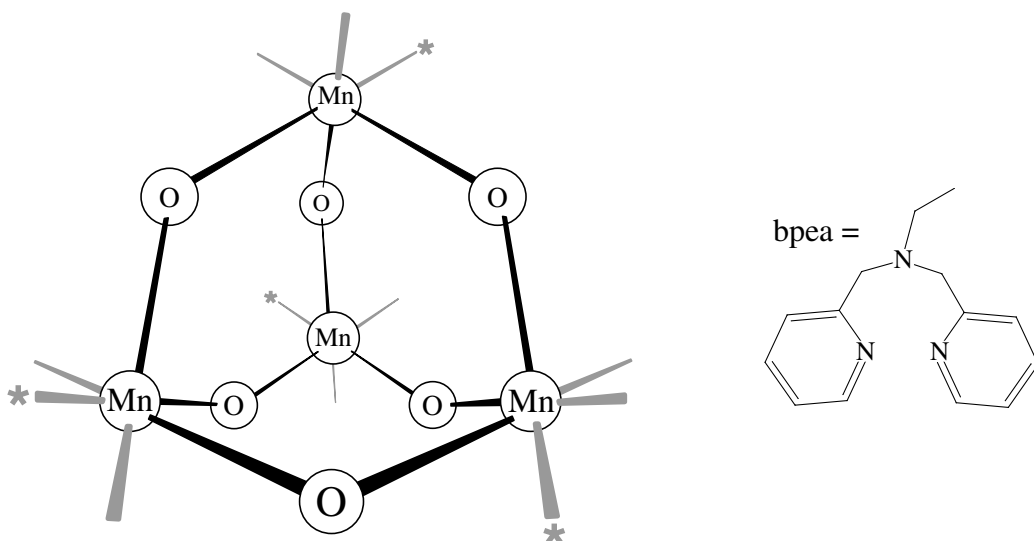


Figure 4.1 The adamantane-like manganese compound  $[\text{Mn}^{\text{IV}}_4\text{O}_6(\text{bpea})_4]^{4+}$ , where the ligand bpea is *N,N*-bis(2-pyridylmethyl)ethylamine.

This chapter presents IR spectra and a normal-mode analysis of the tetranuclear adamantane-like Mn compound  $[\text{Mn}^{\text{IV}}_4\text{O}_6(\text{bpea})_4]^{4+}$ , where bpea is the terminal ligand *N,N*-bis(2-pyridylmethyl)ethylamine (Figure 4.1).<sup>80</sup> The ligand, bpea, has one non-aromatic nitrogen (indicated by an asterisk in Figure 4.1) and two aromatic nitrogens ligated to Mn. Due to the structure of bpea, the compound approaches  $S_4$  symmetry. This compound has an infrared Mn–O–Mn stretch mode at  $709\text{ cm}^{-1}$ , which shifts to  $675\text{ cm}^{-1}$  upon  $^{16}\text{O}$  to  $^{18}\text{O}$  exchange.<sup>80</sup> This frequency is close to  $730\text{ cm}^{-1}$ , which was identified as a Mn–O vibration for the structurally analogous  $[\text{Mn}^{\text{IV}}_4\text{O}_6(\text{tacn})_4]^{4+}$ , where tacn is 1,4,7-triazacyclononane.<sup>81</sup> In contrast to bpea, tacn has three equivalent non-aromatic nitrogens ligated to Mn with the compound close to  $T_d$  symmetry.

The bpea compound in acetonitrile has a reversible wave in the cyclic voltammogram at  $E^{1/2} = 0.104$  V versus SCE (Standard Calomel Electrode), for the ( $\text{Mn}^{\text{IV}}_4 \rightleftharpoons \text{Mn}^{\text{III}}\text{Mn}^{\text{IV}}_3 + e^-$ ) redox couple. An attenuated total reflection design for spectroelectrochemical studies, presented in Chapter 3,<sup>82</sup> is used to obtain IR difference spectra of the adamantane-like compound in the two oxidation states. Using this electrochemical method, the reversibility of the redox couple is advantageously utilized to distinguish IR frequencies of the compound versus non-reversible background signals. Additionally, isotopic exchange,  $^{16}\text{O} \rightarrow ^{18}\text{O}$ , is used to distinguish Mn–O bridging modes from the terminal ligand modes. This is the first time that such an IR and normal-mode analysis has been performed on a manganese compound in two oxidation states relevant to the OEC.

## 4.2 Experimental

**Preparation of adamantane-like compound.** Synthesis and isotopic exchange of the bridging oxygen atoms,  $^{16}\text{O} \rightarrow ^{18}\text{O}$ , of the  $[\text{Mn}^{\text{IV}}_4\text{O}_6(\text{bpea})_4]^{4+}$  compound was performed as described in Dubé et al.,<sup>80</sup> where bpea is *N,N*-bis(2-pyridylmethyl)ethylamine, the counter ion is either  $\text{Br}^-$  or  $\text{ClO}_4^-$ . During the isotopic exchange a 90% replacement of  $^{16}\text{O}$  by  $^{18}\text{O}$  was achieved.<sup>80</sup>

**Electrochemistry.** A home-built spectroelectrochemical apparatus (described in Chapter 3)<sup>82</sup> was used to measure the IR spectra of the redox species during electrochemistry. The apparatus consists of an electrochemical cell made of Teflon, which interfaces with an ASI DuraSampIIR™ (Applied Systems Inc., Annapolis, MD)



ATR accessory.<sup>83,84</sup> The ATR device has a wide spectral range of 16,700 – 250  $\text{cm}^{-1}$ , and a small opaque region of 2250 – 1900  $\text{cm}^{-1}$ . Pt gauze was used for both the working and counter electrode. To minimize diffusion of electrochemical products but allow electrochemical contact, the counter electrode was placed inside a glass tube with a fritted glass disk at the end. The non-aqueous ( $\text{CH}_3\text{CN}$ , 0.1 M TBA( $\text{PF}_6$ )) Ag/AgClO<sub>4</sub> reference electrode was isolated from the bulk solution by an additional electrolyte bridge (a glass tube fitted with a vycor tip), which was changed between samples to avoid contamination.

Before each experiment the electrolyte solution, 0.1 M TBA( $\text{PF}_6$ ) in acetonitrile, was dried over  $\text{Al}_2\text{O}_3$  and bubbled with Ar. Sample solutions of  $\sim 2.8$  mM  $[\text{Mn}^{\text{IV}}_4 \text{}^{16}\text{O}_6(\text{bpea})_4](\text{ClO}_4)_4$  or  $\sim 2.5$  mM  $[\text{Mn}^{\text{IV}}_4 \text{}^{18}\text{O}_6(\text{bpea})_4](\text{ClO}_4)_4$  dissolved in electrolyte solution were prepared, with a total volume of 0.8 mL. During the electrochemistry the sample solution was under a constant purge of Ar. The Ar was bubbled through dry acetonitrile ( $\text{Al}_2\text{O}_3$ ) to minimize evaporation and the consequent change in compound concentration. Electrochemistry was conducted using a BAS CV-27 Voltammetry Controller. Reduction of the  $\text{Mn}^{\text{IV}}_4$  complex was performed at  $-0.7$  V and oxidation at  $+0.3$  V vs. the Ag/AgClO<sub>4</sub> reference electrode ( $E^{1/2} = -0.2$  V vs. Ag/AgClO<sub>4</sub>, and  $+0.10$  V vs. SCE)<sup>80</sup>.

**IR spectroscopy.** A Bruker IFS88 FTIR spectrometer was used to collect the infrared data. The spectrometer contains a KBr beam-splitter and a broad band MCT detector (lower cut-off 400  $\text{cm}^{-1}$ ). KBr disks were used to obtain the IR spectra of both the solid  $^{16}\text{O}$  and  $^{18}\text{O}$  adamantane-like  $[\text{Mn}^{\text{IV}}_4\text{O}_6(\text{bpea})_4]\text{Br}_4$  compounds, at a resolution of 1  $\text{cm}^{-1}$ , each sample spectrum was averaged over 100 scans.

The IR spectra during the electrochemistry were taken at a resolution of  $4\text{ cm}^{-1}$  and were recorded in rapid scan mode (128 ms per scan). The spectra were collected as described previously in Chapter 3 and are briefly summarized here.<sup>82</sup> The experiments were performed by alternating between reduction and oxidation conditions, enabling a distinction to be made between reversible and non-reversible signals. Each experiment had a redox sequence of: ox., red., ox., red., ox., where ox. represents oxidizing and red. is reducing conditions. This sequence enables us to calculate two reduction difference spectra, during the reduction of the  $\text{Mn}^{\text{IV}}_4$  species (ox. – red.), and two oxidation spectra, during the oxidation of the  $\text{Mn}^{\text{III}}\text{Mn}^{\text{IV}}_3$  species (red. – ox.).

During a reduction or oxidation period, 1600 scans were taken and averaged into 16 separate groups (100 scans per group). To enhance the signal to noise ratio, the earlier spectra with small signal intensity were discarded. To determine what groups need to be discarded, the time profile of various signals during the electrochemistry was studied. Reversible signals will have successive maxima and minima in the signal intensity during the experiment. The averaged maxima and minima were subtracted from each other to obtain the reduction and oxidation difference spectra.

After each experiment the solution was put under oxidizing conditions for about 30 min, to return the sample to the oxidized state. This conversion was not complete; consequently, the IR difference signals of this solution were smaller than for the first experiment. This procedure was repeated twice for each sample,  $^{16}\text{O}$  and  $^{18}\text{O}$ . The averaged reduction and oxidation spectra were calculated by weighting the spectra of each experiment by the intensity of the reversible  $1030/1022\text{ cm}^{-1}$  difference signal. This corrected the differences in intensity due to the incomplete oxidation between

experiments.

All of the difference spectra are presented such that features due to the oxidized species  $\text{Mn}^{\text{IV}}_4$  are positive and those for the reduced species  $\text{Mn}^{\text{III}}\text{Mn}^{\text{IV}}_3$  are negative. Consequently, reversible features have the same sign in both the reduction and oxidation spectra, and non-reversible features have the opposite sign. Therefore, when the averaged reduction and oxidized spectra are added the non-reversible back-ground signals are eliminated and only the reversible features remain.

**Normal-mode analysis** of the adamantane-like compound, which is described in detail in Appendix 4.6, was performed by using the *FG*-matrix method as introduced by Wilson, Decius and Scott.<sup>85</sup> The linear algebra calculations of the normal-mode analysis were performed using Mathematica 3.0 (Wolfram Research). The frequencies of the normal modes were matched with the observed frequencies by varying the force constants in steps of 0.05 mdyn/Å. The bending and stretching modes were assumed to have no interactions, i.e. the bending force constants were set at zero during the calculations (see Appendix 4.6 for the effect this has on the stretching modes). The stretch force constants used for the  $[\text{Mn}^{\text{IV}}_4\text{O}_6(\text{bpea})_4]^{4+}$  compound simulations are: (1) the stretching force constant of the  $\text{Mn}^{\text{IV}}\text{-O}$  bonds,  $f_{r,\text{IV}}$ , and (2) the two stretching coupling constants between two adjacent bonds with oxygen,  $f_{r,\text{Or}}$ , or manganese,  $f_{r,\text{Mnr}}$ , at the apex. In the normal mode simulations of the  $[\text{Mn}^{\text{III}}\text{Mn}^{\text{IV}}_3\text{O}_6(\text{bpea})_4]^{3+}$  compound the stretch force constant of the  $\text{Mn}^{\text{III}}\text{-O}$  bonds,  $f_{r,\text{III}}$ , is added as a variable. It is assumed that the oxidation state of the manganese has no influence on the stretch coupling constants.

### 4.3 Results

#### *FTIR spectra of the $[\text{Mn}^{\text{IV}}_4\text{O}_6(\text{bpea})_4]^{4+}$ compound*

Isotopic exchange of the bridging oxygen atoms,  $^{16}\text{O} \rightarrow ^{18}\text{O}$ , is used to distinguish Mn–O vibrational modes of the adamantane-like compound from the other modes which do not involve oxygen atoms, such as vibrations of bpea, the terminal ligand molecule. The FTIR absorption spectra of the  $[\text{Mn}^{\text{IV}}_4^{16}\text{O}_6(\text{bpea})_4]^{4+}$  (black) and  $[\text{Mn}^{\text{IV}}_4^{18}\text{O}_6(\text{bpea})_4]^{4+}$  (red) compounds are shown in Figure 4.2. Differences between the vibrational modes of the two isotopic species are indicated by arrows. Two apparent changes are observed for the  $^{16}\text{O}$  vibrational modes at  $707\text{ cm}^{-1}$  and  $510\text{ cm}^{-1}$  which shift to  $674\text{ cm}^{-1}$  and  $490\text{ cm}^{-1}$ , respectively, in the  $^{18}\text{O}$  spectrum. A weak absorption band at about  $1016\text{ cm}^{-1}$  is observed for the  $^{16}\text{O}$  compound which is not present in the  $^{18}\text{O}$  spectrum. This vibrational mode could be the first overtone of the  $510\text{ cm}^{-1}$  mode. However, the  $^{18}\text{O}$  band of this overtone mode, expected to be around  $980\text{ cm}^{-1}$ , cannot be observed. Therefore, the band observed at  $1016\text{ cm}^{-1}$  is most likely not an overtone, but possibly due to some kind of contamination. All the other bands that do not shift upon the  $^{16}\text{O} \rightarrow ^{18}\text{O}$  exchange are most likely due to vibrational modes of the terminal ligand, bpea.

Another possible Mn–O mode, detected as a weak shoulder at  $\sim 745\text{ cm}^{-1}$  in the  $^{16}\text{O}$  absorption spectra, is not present in the  $^{18}\text{O}$  spectrum. This transition is more evident in the  $^{16}\text{O}$ – $^{18}\text{O}$  difference spectrum (blue curve in Figure 4.2). In the difference spectrum the weak shoulder at  $745\text{ cm}^{-1}$  is a strong, broad vibrational mode which overlaps the  $707/674\text{ cm}^{-1}$  difference signal. It is not clear where the  $^{18}\text{O}$  companion of this broad band appears. However, in the difference spectrum the  $707\text{ cm}^{-1}$  signal is weaker than the  $674\text{ cm}^{-1}$  signal. Upon isotopic exchange, only the frequency of vibrational modes is

expected to shift not the intensity of the transition. Therefore, this change in signal intensity is possibly an indication that the  $^{18}\text{O}$  companion of the  $745\text{ cm}^{-1}$  peak is underneath the  $707\text{ cm}^{-1}$ . Figure 4.3 shows that the difference signal around  $700\text{ cm}^{-1}$  can be simulated by two  $^{16}\text{O}$ -absorption bands at  $745\text{ cm}^{-1}$  and  $707\text{ cm}^{-1}$  (black curves), and two  $^{18}\text{O}$ -absorption bands at  $705\text{ cm}^{-1}$  and  $674\text{ cm}^{-1}$  (red curves). This indicates that the  $745\text{ cm}^{-1}$  mode indeed shifts to  $705\text{ cm}^{-1}$  upon isotopic exchange, and is underneath the  $^{16}\text{O}$  species  $707\text{ cm}^{-1}$  mode in the difference spectrum. All of the observed IR modes, their bandwidth at half peak height, and their isotopic shifts are summarized in Table 4.3.

*Table 4.3 The IR frequencies of the Mn–O modes and shifts in the modes observed in the spectra of the solid  $[\text{Mn}^{\text{IV}}_4\text{O}_6(\text{bpea})_4]^{4+}$  and  $[\text{Mn}^{\text{IV}}_4\text{O}_6(\text{bpea})_4]^{4+}$  compounds, with the bandwidth at half the peak height between parentheses.*

$^{16}\text{O}$ ( $\text{cm}^{-1}$ )	$^{18}\text{O}$ ( $\text{cm}^{-1}$ )	$\Delta$ ( $\text{cm}^{-1}$ )	Comment
510 (20)	490 (20)	20	
707 (14)	674 (14)	32	
~745 (20)	~705 (20)	~40	determined by gaussian fit
1016 (8)	?	–	possible overtone of $510\text{ cm}^{-1}$

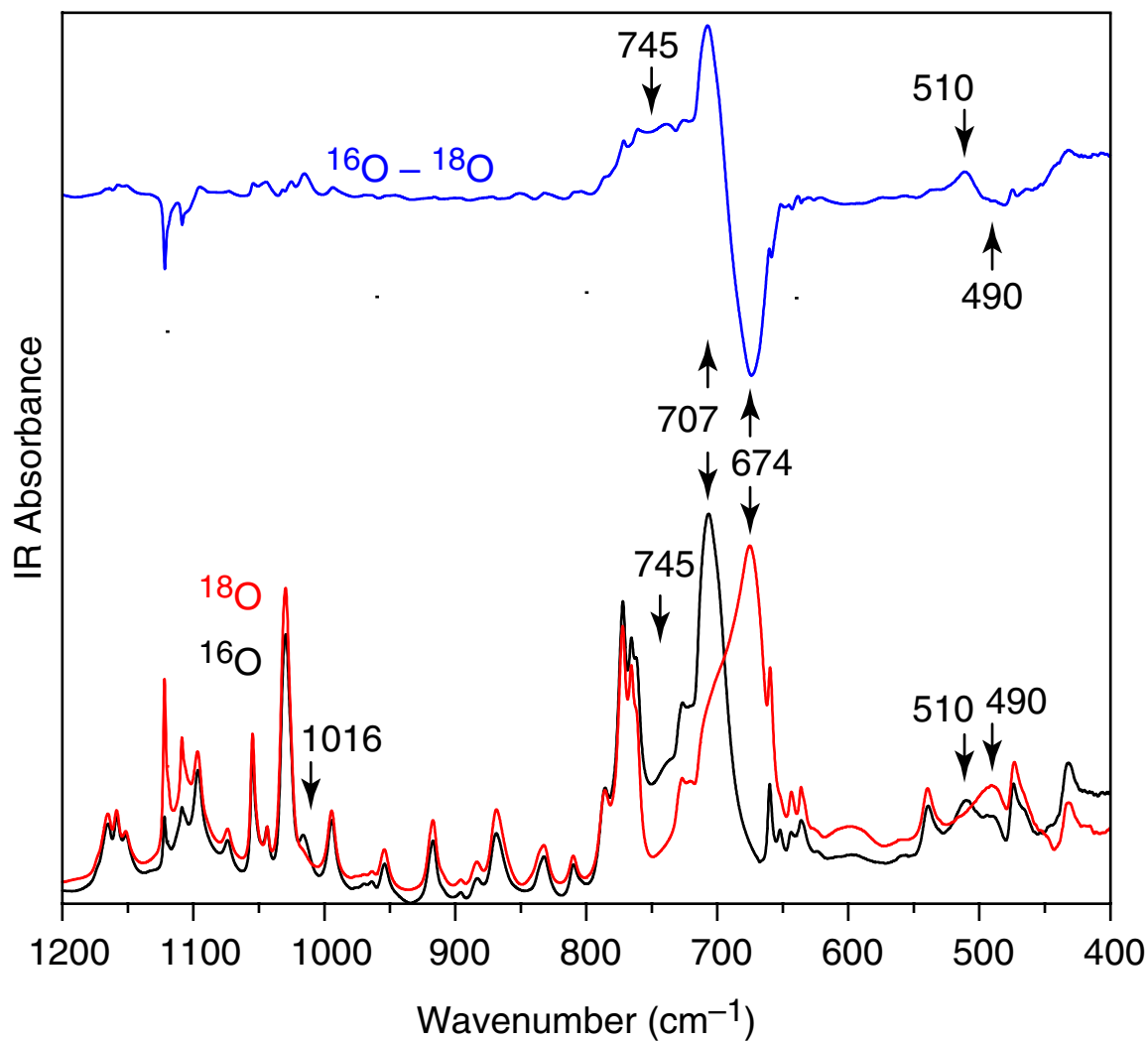


Figure 4.2 The FTIR absorption and difference spectra of the solid  $[\text{Mn}_4^{IV}\text{O}_6(\text{bpea})_4]^{4+}$  and  $[\text{Mn}_4^{IV}\text{O}_6(\text{bpea})_4]^{4+}$  compounds in KBr pellets, at a resolution of  $1 \text{ cm}^{-1}$ . Arrows indicate frequencies of major difference peaks between the two isotopic spectra.

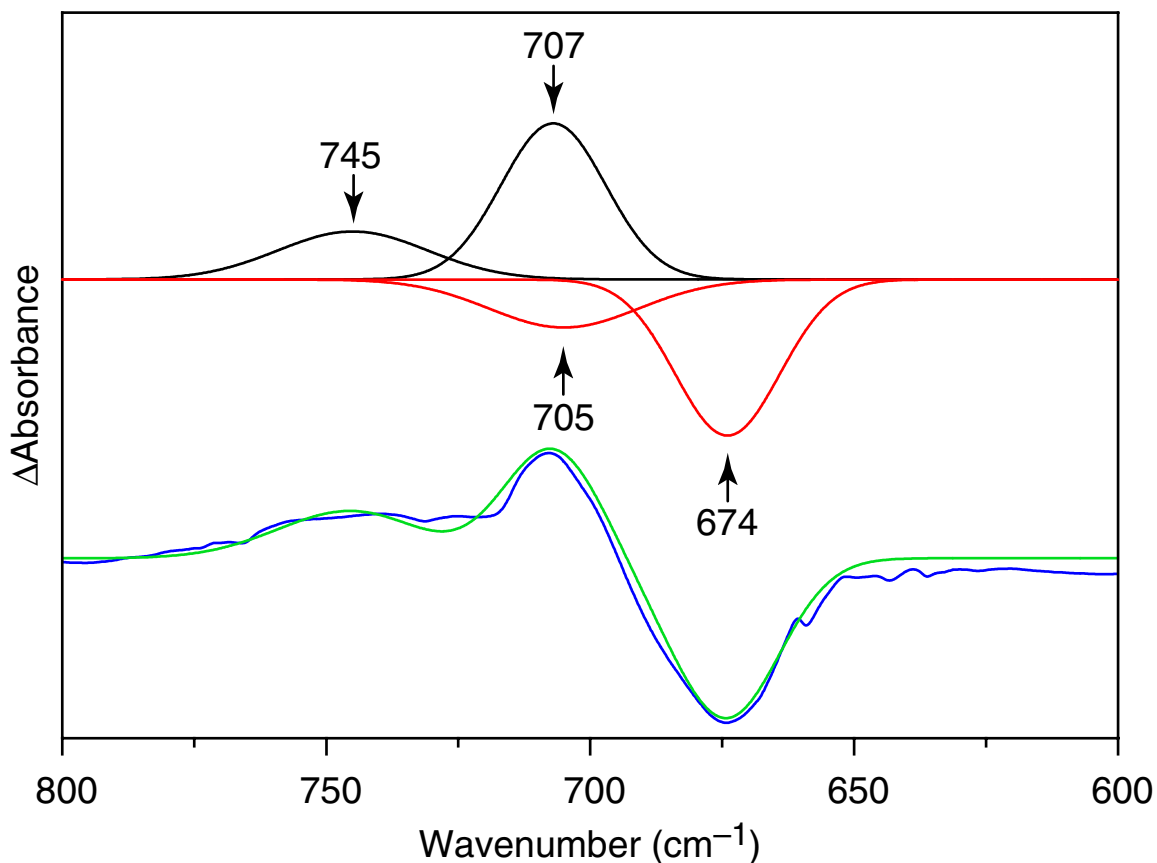


Figure 4.3 Simulation of the ( $^{16}\text{O} - ^{18}\text{O}$ ) FTIR difference signal around  $700\text{ cm}^{-1}$  of the  $[\text{Mn}^{\text{IV}}_4\text{O}_6(\text{bpea})_4]^{4+}$  compound (blue line), fitted with four gaussian absorption curves (black and red lines, green is the sum of the gaussian curves). The two positive black gaussian curves represent the absorption bands of the  $^{16}\text{O}$  species at  $745\text{ cm}^{-1}$  and  $707\text{ cm}^{-1}$ , with bandwidths at half height of  $20\text{ cm}^{-1}$  and  $14\text{ cm}^{-1}$ , respectively. The two negative red curves are the companion modes of the  $^{18}\text{O}$  species at  $705\text{ cm}^{-1}$  and  $674\text{ cm}^{-1}$ , with identical bandwidths and intensity as the  $^{16}\text{O}$  gaussian curves.

***FTIR (oxidized – reduced) difference spectra of the adamantane-like compound***

Figures 4.4 and 4.5 give the FTIR (oxidized – reduced) difference spectra measured for the  $^{16}\text{O}$  and  $^{18}\text{O}$  compounds, respectively. In both figures the positive signals are due to the  $\text{Mn}^{\text{IV}}_4$  oxidation state, and the negative signals are due to the  $\text{Mn}^{\text{III}}\text{Mn}^{\text{IV}}_4$  oxidation state. Each figure contains the reduction (purple), the oxidation (blue), and the sum spectra (black). A distinction is made between reversible and non-reversible signals by comparing the reduction and oxidation spectra. Reversible signals have the same sign for the reduction and oxidation spectra, but non-reversible signals have opposite sign.

Both figures show non-reversible signals at  $1100\text{ cm}^{-1}$ ,  $917\text{ cm}^{-1}$ ,  $739\text{ cm}^{-1}$ , and  $624\text{ cm}^{-1}$ , which are most likely due to decomposition of the solvent (see also Chapter 3).<sup>82</sup> The sum spectra are obtained by adding the Red. and a fraction of Ox. spectrum together, in order to minimize the non-reversible signals over the whole spectral range ( $400 - 4000\text{ cm}^{-1}$ , higher frequency data not shown). In Figures 4.4 and 4.5 the non-reversible signals are absent or reduced greatly in intensity in the sum spectra. The signals at  $877\text{ cm}^{-1}$ ,  $844\text{ cm}^{-1}$ , and  $560\text{ cm}^{-1}$  in Figures 4.4 and 4.5 are due to small changes in the concentration of the electrolyte anion  $\text{PF}_6^-$  (see also Chapter 3).<sup>82</sup>

Two different types of reversible signals can be observed by comparing the sum spectra in Figure 4.4 and 4.5. The first group of reversible signals, indicated by black arrows, correspond to modes that have the same energy position for the  $^{16}\text{O}$  and  $^{18}\text{O}$  difference-spectra. When directly compared in Figure 4.6, the signals at  $1162/1154\text{ cm}^{-1}$ ,  $1054/1048\text{ cm}^{-1}$ ,  $1030/1022\text{ cm}^{-1}$ ,  $669/659\text{ cm}^{-1}$ , and at  $773\text{ cm}^{-1}$  do not shift upon  $^{16}\text{O} \rightarrow ^{18}\text{O}$  exchange, indicating that no Mn–O modes are involved. These reversible



signals are assigned to the changes in the vibrational modes of the bpea terminal-ligand molecule, caused by the change in Mn–bpea interaction upon a change in the Mn oxidation state. The second group of reversible signals is dependent on the isotopic state of the oxygens, and therefore bridging Mn–O modes are involved. Some of these signals are indicated by red arrows, such as the broad difference signal at  $\sim 710\text{ cm}^{-1}$ , which shifts to  $\sim 680\text{ cm}^{-1}$  upon isotopic  $^{16}\text{O}\rightarrow^{18}\text{O}$  exchange. Another possible reversible signal, sensitive to isotopic exchange, can be observed around  $500\text{ cm}^{-1}$  in Figure 4.4. A positive feature is present at  $510\text{ cm}^{-1}$ , which could be due to the  $\text{Mn}^{\text{IV}}_4$  oxidation state, while a negative feature occurs at  $494\text{ cm}^{-1}$ , possibly due to the  $\text{Mn}^{\text{III}}\text{Mn}^{\text{IV}}_3$  oxidation state. This pattern is repeated in Figure 4.5, at  $493\text{ cm}^{-1}$  and  $481\text{ cm}^{-1}$ , respectively.

The direct comparison of the  $^{16}\text{O}$  and  $^{18}\text{O}$  difference spectra in Figure 4.6 shows that several changes occur between the two spectra in the  $550 - 400\text{ cm}^{-1}$  range. However, it is difficult to distinguish the reversible signals that are sensitive or non-sensitive to isotopic exchange. To eliminate the non-isotopic sensitive signals the difference-difference spectrum of the  $^{16}\text{O}$  and  $^{18}\text{O}$  difference spectra is obtained (Figure 4.6). This exposes the reversible signals sensitive to  $^{16}\text{O}\rightarrow^{18}\text{O}$  exchange. Two strong bands appear, a negative signal at  $490\text{ cm}^{-1}$  and a positive signal at  $448\text{ cm}^{-1}$ . These two signals indicate effects on the Mn–O modes caused by redox changes of the adamantane-like compound. However, additional information from the normal-mode analysis is needed to completely understand the changes observed in the  $550 - 400\text{ cm}^{-1}$  range of the difference-difference spectrum. All of the observed signals, isotopic shifts and redox shifts of reversible features that are sensitive to  $^{16}\text{O}\rightarrow^{18}\text{O}$  exchange are summarized in Table 4.4

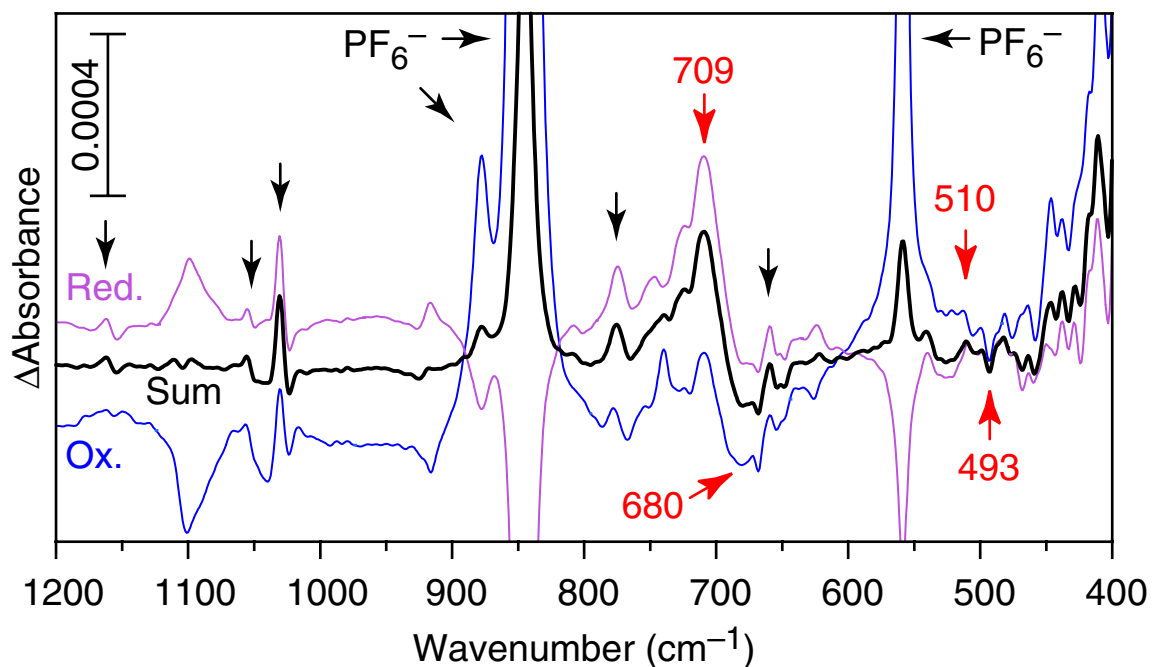


Figure 4.4 The FTIR (oxidized – reduced) difference spectra obtained with a 2.8 mM  $[\text{Mn}^{\text{IV}}_4^{16}\text{O}_6(\text{bpea})_4]^{4+}$ , 0.1 M TBA( $\text{PF}_6$ ) acetonitrile solution. The average sum spectrum (black) is the sum of the averaged reduction spectrum (purple) and the averaged oxidized spectrum (blue). Reversible signals are indicated by black and red arrows, with the red arrows sensitive to the  $^{16}\text{O} \rightarrow ^{18}\text{O}$  isotopic exchange. Positive reversible signals are due to the  $\text{Mn}^{\text{IV}}_4$  oxidation state, and negative signals due to the  $\text{Mn}^{\text{III}}\text{Mn}^{\text{IV}}_4$  oxidation state.

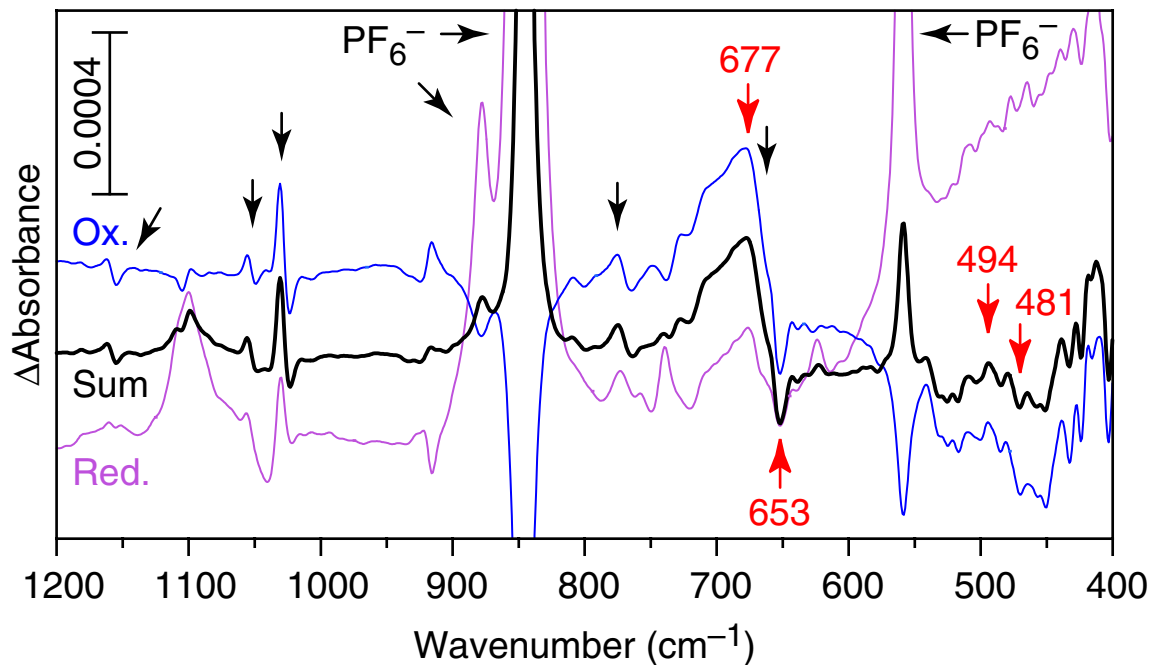


Figure 4.5 The FTIR (oxidized – reduced) difference spectra, obtained with a 2.5 mM  $[\text{Mn}^{\text{IV}}_4^{18}\text{O}_6(\text{bpea})_4]^{4+}$ , 0.1 M TBA( $\text{PF}_6$ ) acetonitrile solution. The sum spectrum (black) is the sum of the averaged reduction spectrum (purple) and the averaged oxidized spectrum (blue). Reversible signals are indicated by black and red arrows, with the red arrows sensitive to the  $^{16}\text{O} \rightarrow ^{18}\text{O}$  isotopic exchange. Positive reversible signals are due to the  $\text{Mn}^{\text{IV}}_4$  oxidation state, and negative signals due to the  $\text{Mn}^{\text{III}}\text{Mn}^{\text{IV}}_4$  oxidation state.

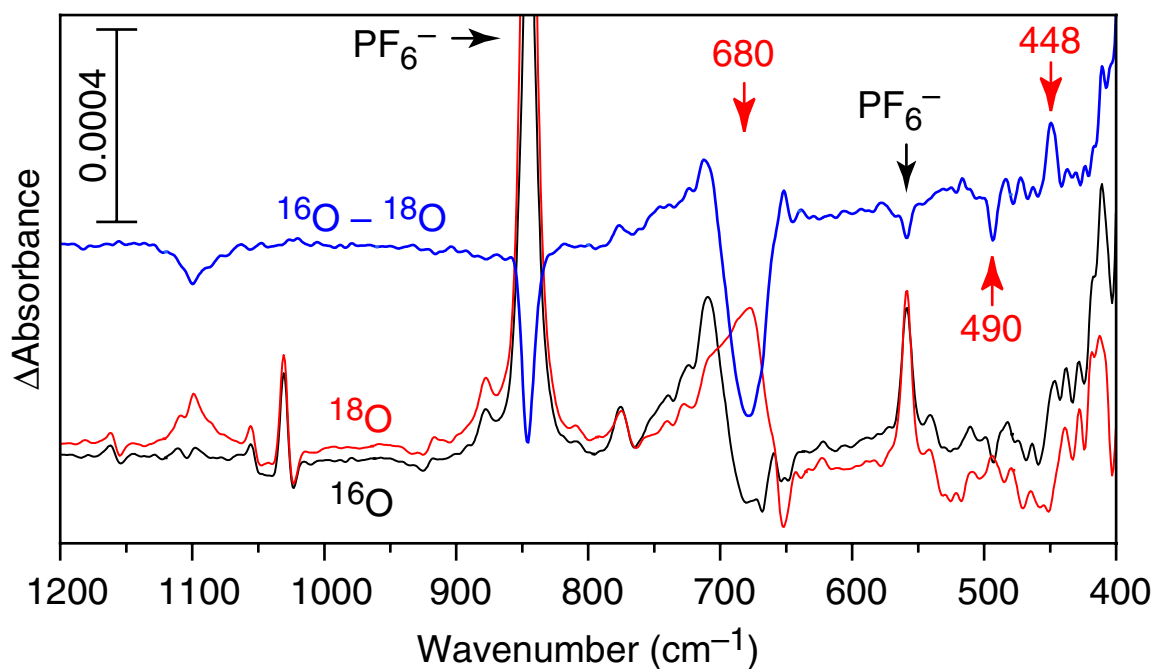


Figure 4.6 The FTIR (oxidized – reduced) difference spectra of the  $^{16}\text{O}$  (black) and  $^{18}\text{O}$  (red) species, and the ( $^{16}\text{O} - ^{18}\text{O}$ ) difference-difference spectrum (blue). The red arrows indicate the two regions sensitive to  $^{16}\text{O} \rightarrow ^{18}\text{O}$  exchange.

Table 4.4 The bridging Mn–O mode IR frequencies which shift upon oxidation and isotopic exchange of the oxygens.  $\Delta_{iso}$  are the shifts observed in the modes due to the  $^{16}\text{O} \rightarrow ^{18}\text{O}$  exchange.  $\Delta_{E\text{-chem}}$  are the shifts observed in the modes due to reduction of the  $\text{Mn}^{\text{IV}}_4$  to the  $\text{Mn}^{\text{III}}\text{Mn}^{\text{IV}}_3$  oxidation state.

	$^{16}\text{O}$ ( $\text{cm}^{-1}$ )	$^{18}\text{O}$ ( $\text{cm}^{-1}$ )	$\Delta_{iso}$ ( $\text{cm}^{-1}$ )
$\text{Mn}^{\text{IV}}_4$	510	494	16
$\text{Mn}^{\text{III}}\text{Mn}^{\text{IV}}_3$	493	481	12
$\Delta_{E\text{-chem}}(\text{cm}^{-1})$	17	13	
$\text{Mn}^{\text{IV}}_4$	709	677	32
$\text{Mn}^{\text{III}}\text{Mn}^{\text{IV}}_3$	680	653	27
$\Delta_{E\text{-chem}}(\text{cm}^{-1})$	29	24	
$\text{Mn}^{\text{IV}}_4$	~735	?	–
$\text{Mn}^{\text{III}}\text{Mn}^{\text{IV}}_3$	~700	?	–
$\Delta_{E\text{-chem}}(\text{cm}^{-1})$	35	?	

#### 4.4 Normal-mode analysis

Several vibrational modes in the IR spectra of the adamantane-like compound are identified as Mn–O core vibrations, by isotopic  $^{16}\text{O} \rightarrow ^{18}\text{O}$  exchange of the bridging oxygens. These modes are observed at  $510\text{ cm}^{-1}$ ,  $707\text{ cm}^{-1}$ , and  $745\text{ cm}^{-1}$  for the oxidized state of the compound,  $\text{Mn}^{\text{IV}}_4$  (Table 4.3). Upon reduction of the compound to  $\text{Mn}^{\text{III}}\text{Mn}^{\text{IV}}_3$ , the  $510\text{ cm}^{-1}$  vibrational mode shifts to  $\sim 490\text{ cm}^{-1}$ , and the  $707\text{ cm}^{-1}$  mode shifts to  $680\text{ cm}^{-1}$ . It is not clear where the  $745\text{ cm}^{-1}$  mode is shifting to (Table 4.4). To understand the IR spectra of the adamantane-like compound in more detail a normal-mode analysis is required. Such an analysis will aid the assignment of the observed bands, and enable us to extract specific information about the Mn–O bonds.

The adamantane-like compound contains 146 atoms and has 432 vibrational modes. A complete analysis of this many modes is complicated. Therefore some simplifications are necessary. Our main interest is in Mn–O modes, therefore we focus on the Mn–O core. This approach implicates several assumptions - (1) the terminal bpea ligand vibrational modes are independent of the Mn–O modes, (2) the Mn–N(bpea) interaction is much weaker than that of the bridging Mn–O ligand (a more detailed discussion is given in Appendix 4.6). As a result of these simplifications the number of atoms involved reduces to 10 and the number of vibrational modes to 24. Beside this reduction in atoms involved, some additional assumptions about the symmetry of the adamantane-like compound are necessary to simplify the normal mode calculations. If the influence of the terminal bpea ligand on the compound is ignored, the overall  $T_d$  symmetry can be applied for the  $\text{Mn}^{\text{IV}}_4$  compound. However, if the influence of the bpea on the compound is included, the highest symmetry possible for the  $\text{Mn}^{\text{IV}}_4$  compound is

$S_4$  symmetry. Upon reduction of the compound to  $Mn^{III}Mn^{IV}_3$  the highest possible symmetry is  $C_s$ , when the influence of the terminal bpea ligand on the compound is ignored. Including the bpea in the symmetry analysis causes the compound to have  $C_1$  symmetry, which is close to  $C_s$  symmetry. No normal-mode analysis was performed for the overall  $C_1$  symmetry, because no significant additional information is obtained by including the  $C_1$  symmetry in this analysis. Figure 4.7 shows the relation between the symmetry terms of the normal modes for the  $T_d$ ,  $S_4$ , and  $C_s$  symmetries.

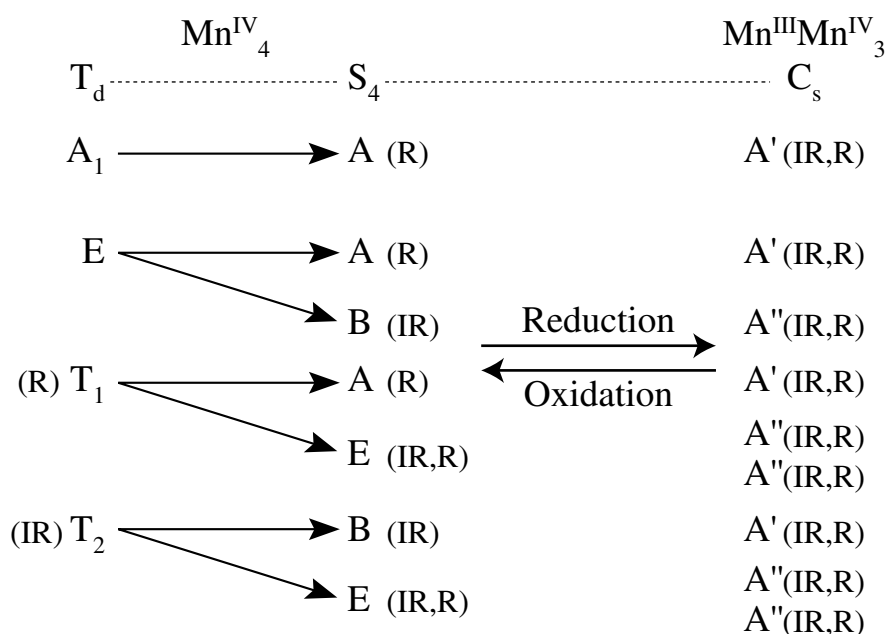


Figure 4.7 The relation between the symmetry representations of the different overall symmetries of the Mn compound, which were used for the analysis of the two oxidation states. When the influence of the terminal ligand, bpea, on the compound is ignored, the  $T_d$  and the  $C_s$  symmetry apply to the  $Mn^{IV}_4$  and  $Mn^{III}Mn^{IV}_3$  compounds, respectively. When the influence of bpea on the compound is included the  $S_4$  symmetry applies to the  $Mn^{IV}_4$  species. IR and R indicate whether a symmetry term is infrared or Raman active.

*Normal-mode analysis of Mn<sup>IV</sup><sub>4</sub> compound - T<sub>d</sub> symmetry*

When an overall T<sub>d</sub> symmetry for the [Mn<sup>IV</sup><sub>4</sub>O<sub>6</sub>(bpea)<sub>4</sub>]<sup>4+</sup> compound is assumed, the 24 vibrations are divided into 2A<sub>1</sub>, 2E, 2T<sub>1</sub>, and 4T<sub>2</sub> symmetry representations. Figure 4.7 shows that only the triply degenerate vibrational modes with the T<sub>2</sub> symmetry are infrared active. If the bending modes are ignored, i.e. the bending force constants are set at zero, the symmetry representations of the stretch vibrations are: A<sub>1</sub>, E, T<sub>1</sub>, and 2T<sub>2</sub> (see Appendix 4.6). Consequently, only two IR-active stretching modes are anticipated. However, the IR absorption and difference spectra of the Mn<sup>IV</sup><sub>4</sub> compound show at least three strong absorption bands in Figure 4.2 at 510 cm<sup>-1</sup>, 707cm<sup>-1</sup>, and 745cm<sup>-1</sup>. Nevertheless, a normal mode calculation was attempted to match two T<sub>2</sub> modes to these absorption bands. Table 4.5 presents a normal-mode analysis which assigns the 510 cm<sup>-1</sup> and 745 cm<sup>-1</sup> vibrational modes to the T<sub>2</sub> representation. The calculated values are similar to the observed values, including their isotopic shift. The mode at 707 cm<sup>-1</sup> is assigned to the IR inactive T<sub>1</sub> representation. However, this mode becomes partially active when the T<sub>d</sub> symmetry breaks down, as can be seen in Figure 4.7.



Table 4.5 Comparison of the observed and the calculated frequencies for the  $[Mn^{IV}_4O_6(bpea)_4]^{4+}$  compound. Calculated frequencies are from the normal-mode analysis where overall  $T_d$  symmetry is assumed, with  $f_{r^{IV}} = 3.15$  mdyn/Å,  $f_{rOr} = 0.55$ ,  $f_{rMnr} = 0.20$  mdyn/Å, and the bending force constants are kept zero (see also Appendix 4.6).

$T_d$	$^{16}O$ (cm $^{-1}$ )		$^{18}O$ (cm $^{-1}$ )		$\Delta$ (cm $^{-1}$ )	
	Obs.	Calc.	Obs.	Calc.	Obs.	Calc.
$T_2$	745	746	705	709	40	37
	510	508	490	492	20	16
$T_1$	707	706	677	673	30	33
E	–	511	–	496	–	15
$A_1$	–	503	–	485	–	18

#### *Normal-mode analysis of $Mn^{IV}_4$ compound - $S_4$ symmetry*

When the symmetry of the bpea ligand is included, i.e. overall  $S_4$  symmetry is assumed, the  $T_2$  degenerate levels of the  $T_d$  symmetry split into the two IR-active E and B symmetry representations (Figure 4.7). Additionally, other vibrational modes become IR active compared to the  $T_d$  symmetry. One absorption band is derived from the  $T_1$  symmetry representation, which splits into an IR-active doubly degenerate band (symmetry representation E) and a Raman-active band (symmetry representation A). The other new IR absorption band comes from the degenerate E symmetry representation, and separates into an IR- (symmetry representation B) and Raman- (symmetry representation A) active vibration.

Table 4.6 presents the results of the normal-mode analysis, assuming the  $S_4$  symmetry. The vibrational modes are organized as for the  $T_d$  symmetry. The calculated values are similar to the observed values, including their isotopic shift. The  $745\text{ cm}^{-1}$  feature is calculated to be an absorption band consisting of three vibrational modes; one at  $742\text{ cm}^{-1}$  and two at  $748\text{ cm}^{-1}$ . This splitting in the  $T_2$  representation is supported by the broad bandwidth of  $20\text{ cm}^{-1}$  observed for this mode. A similar situation occurs for the  $510\text{ cm}^{-1}$  mode, where the  $T_2$  mode splits into one  $489\text{ cm}^{-1}$  and two  $506\text{ cm}^{-1}$  modes. Additionally, a new active mode in the  $S_4$  symmetry occurs at  $512\text{ cm}^{-1}$ , which is derived from the E representation in the  $T_d$  symmetry. This new band also contributes to the broad bandwidth of  $20\text{ cm}^{-1}$  observed for the  $510\text{ cm}^{-1}$  mode. Therefore, the bandwidths of both the  $510\text{ cm}^{-1}$  and  $745\text{ cm}^{-1}$  are indications that a symmetry of  $S_4$  or lower is required to explain the spectra of the  $\text{Mn}^{\text{IV}}_4$  adamantane-like compound.

Table 4.6 indicates that the  $707\text{ cm}^{-1}$  band is derived from the  $T_1$  symmetry representation, as suggested earlier. When the overall  $S_4$  symmetry is assumed, this band splits into an IR- and Raman-active doubly degenerate mode at  $707\text{ cm}^{-1}$ , and a Raman-active mode at  $705\text{ cm}^{-1}$ . This band has a bandwidth of about  $14\text{ cm}^{-1}$  (Table 4.3), which suggests that the doubly degenerate mode has slightly split, indicating that the adamantane-like compound has a slightly distorted  $S_4$  symmetry.

Table 4.6 Comparison of the observed and calculated frequencies for the  $[Mn^{IV}_4O_6(bpea)_4]^{4+}$  compound. Calculated frequencies are for the normal-mode analysis where the overall  $S_4$  symmetry is assumed, with  $f_{r_{iv}} = 3.10$  mdyn/Å,  $f_{r_{or}} = 0.50$ ,  $f_{r_{Mnr}} = 0.20$  mdyn/Å, and the bending force constants are kept zero (see also Appendix 4.6). (The normal modes are organized as in the  $T_d$  Table 4.5.)

$S_4$	$^{16}O$ (cm $^{-1}$ )		$^{18}O$ (cm $^{-1}$ )		$\Delta$ (cm $^{-1}$ )	
	Obs.	Calc.	Obs.	Calc.	Obs.	Calc.
B	745	742	705	706	40	36
E		748		711		37
B	510	489	490	473	20	16
E		506		490		16
A	707	705	674	672	33	33
E		707		673		34
A	–	504	–	487	–	17
B		512		497		15
A	–	491	–	474	–	17

#### *Normal-mode analysis of $Mn^{III}Mn^{IV}_3$ compound - $C_s$ symmetry*

Upon reduction of the  $Mn^{IV}_4$  compound, the  $Mn^{III}Mn^{IV}_3$  species is formed. This reduced species approaches an overall  $C_s$  symmetry when the symmetry of the bpea ligand is ignored. Figure 4.7 shows that all of the degeneracies break apart upon reduction of the  $[Mn^{IV}_4O_6(bpea)_4]^{4+}$  compound and all vibrational modes become IR and Raman active. Consequently, not only are shifts in peaks anticipated due to reduction of the compound, but also broadening of the previously degenerate modes, and possibly new modes in the IR spectra.

The broad reversible difference signal at  $\sim 710\text{ cm}^{-1}$  resembles the signature of the  $^{16}\text{O}-^{18}\text{O}$  difference spectrum of the solid  $[\text{Mn}^{\text{IV}}_4\text{O}_6(\text{bpea})_4]^{4+}$  compound (Figure 4.3). However, unlike isotopic exchange, redox chemistry causes changes in bond lengths, bond angles, bond strengths, and consequently, the overall symmetry of the compound. This results in different frequency shifts for each vibrational mode, including possible shifts to higher energy. Due to the change in overall symmetry certain modes will also become IR active or inactive, and the isotopic shifts will also alter. Therefore, simulating the difference signal in the  $750 - 650\text{ cm}^{-1}$  and  $520 - 460\text{ cm}^{-1}$  ranges is not straightforward.

To reduce the complexity of the normal mode calculations of the  $[\text{Mn}^{\text{III}}\text{Mn}^{\text{IV}}_3\text{O}_6(\text{bpea})_4]^{3+}$  compound some additional assumptions, beside symmetry considerations, are necessary about the force constant variables. The stretching force constants of all  $\text{Mn}^{\text{IV}}-\text{O}$  bonds are kept at the calculated value of the solid state  $[\text{Mn}^{\text{IV}}_4\text{O}_6(\text{bpea})_4]^{4+}$  compound,  $f_{r,\text{IV}} = 3.10\text{ mdyn}/\text{\AA}$ . No distinction is made between force constants of the Jahn-Teller distorted and non-Jahn-Teller distorted  $\text{Mn}^{\text{III}}-\text{O}$  bonds, i.e. only one type of  $f_{r,\text{III}}$  is used. In addition, no distinction is made between  $\text{Mn}^{\text{III}}-\text{O}$  and  $\text{Mn}^{\text{IV}}-\text{O}$  bonds when the stretching coupling constants are considered. Therefore, there are only two types of stretching coupling constants: with either oxygen,  $f_{r,\text{O}}$ , or manganese,  $f_{r,\text{Mn}}$ , at the apex.

Using the overall  $C_s$  symmetry and these force constant variables, the normal modes of the  $[\text{Mn}^{\text{III}}\text{Mn}^{\text{IV}}_3\text{O}_6(\text{bpea})_4]^{3+}$  compound were calculated from the difference signals of the  $(\text{Mn}^{\text{IV}}_4-\text{Mn}^{\text{III}}\text{Mn}^{\text{IV}}_3)$  difference spectra and the  $(^{16}\text{O} - ^{18}\text{O})$  difference-difference spectrum. Four different objectives were sought with the normal mode

calculation. The first objective was to try to simulate the difference signals in the 620 - 720  $\text{cm}^{-1}$  range for both the  $^{16}\text{O}$  and  $^{18}\text{O}$  spectra. The second objective was to roughly match the  $^{16}\text{O} - ^{18}\text{O}$  difference-difference signal in this range. The third objective was to simulate the difference signals in the 420 -520  $\text{cm}^{-1}$  range for both the  $^{16}\text{O}$  and  $^{18}\text{O}$  spectra. The final objective was to obtain a simulation that matches the  $^{16}\text{O} - ^{18}\text{O}$  difference-difference signal in this range, especially the positive signals around 510  $\text{cm}^{-1}$  and 450  $\text{cm}^{-1}$  and the negative band at  $\sim 490 \text{ cm}^{-1}$ .

Table 4.7 presents the calculated frequencies which gave a reasonable simulation of the difference and difference-difference signals, as shown in Figure 4.8. Normal-mode calculations give only the absorption frequencies of the normal modes; they do not give any information about the width or intensity of these transitions. Therefore, the intensities and bandwidths are based on the information that was obtained from the solid state spectra (see appendix 4.6 for the exact values). Figure 4.8 shows that the simulated spectra match the measured spectra reasonably well in the 620 -720  $\text{cm}^{-1}$  range. There are slight differences between frequencies and bandwidths, but the overall simulated spectra contain all of the observed elements. The  $^{18}\text{O}$  difference spectrum has the poorest match, which is due to the fact that the isotopic exchange is only 90% complete. Therefore, the  $^{18}\text{O}$  difference spectrum contains also signals of adamantane-like compounds with various  $^{16}\text{O}/^{18}\text{O}$  ratios. This mixture of isotopic species causes the observed signal to be broader than the calculated one.

It was more difficult to match the simulated signals with the calculated signals in the 420 -520  $\text{cm}^{-1}$  range. All of the vibrational modes have major changes upon reduction of the  $\text{Mn}^{\text{IV}}_4$  adamantane-like compound. Therefore it is difficult to match all

of the calculated changes with the observed shifts in this range. Nevertheless, the simulations match the observed spectra reasonably well, especially the difference-difference spectrum. Only slight shifts in some of the normal modes are needed to improve the match between simulated and observed signals. This could be achieved by including more types of stretching force constants. However, including more variables will not give more significant information about the compound, and therefore this expansion of variables was not performed.

*Table 4.7 Comparison of the observed and calculated frequencies for the  $[Mn^{III}Mn^{IV}_3O_6(bpea)_4]^{3+}$  compound. The overall  $C_s$  symmetry is assumed, the bending force constants are set at zero, and the stretching force constants are:  $f_{r_{IV}} = 3.10$  mdyn/Å,  $f_{r_{III}} = 2.45$  mdyn/Å,  $f_{r_{Or}} = 0.40$ , and  $f_{r_{Mnr}} = 0.15$  mdyn/Å (see also Appendix 4.\*). (The normal modes are organized as in the  $T_d$  Table 4.5.)*

$C_s$	$^{16}O$ (cm $^{-1}$ )		$^{18}O$ (cm $^{-1}$ )		$\Delta$ (cm $^{-1}$ )	
	Obs.	Calc.	Obs.	Calc.	Obs.	Calc.
A' / A' A''	~745	747 / 726 747	~705	710 / 674 710	~40	37 / 35 37
A' / A' A''	493	492 / 478 464	481	476 / 463 449	12	16 / 15 15
A' A'' / A''	680	685 726 / 689	653	653 692 / 656	27	32 34 / 33
A' A''	–	505 500	–	488 485	–	17 15
A'	–	466	–	450	–	16

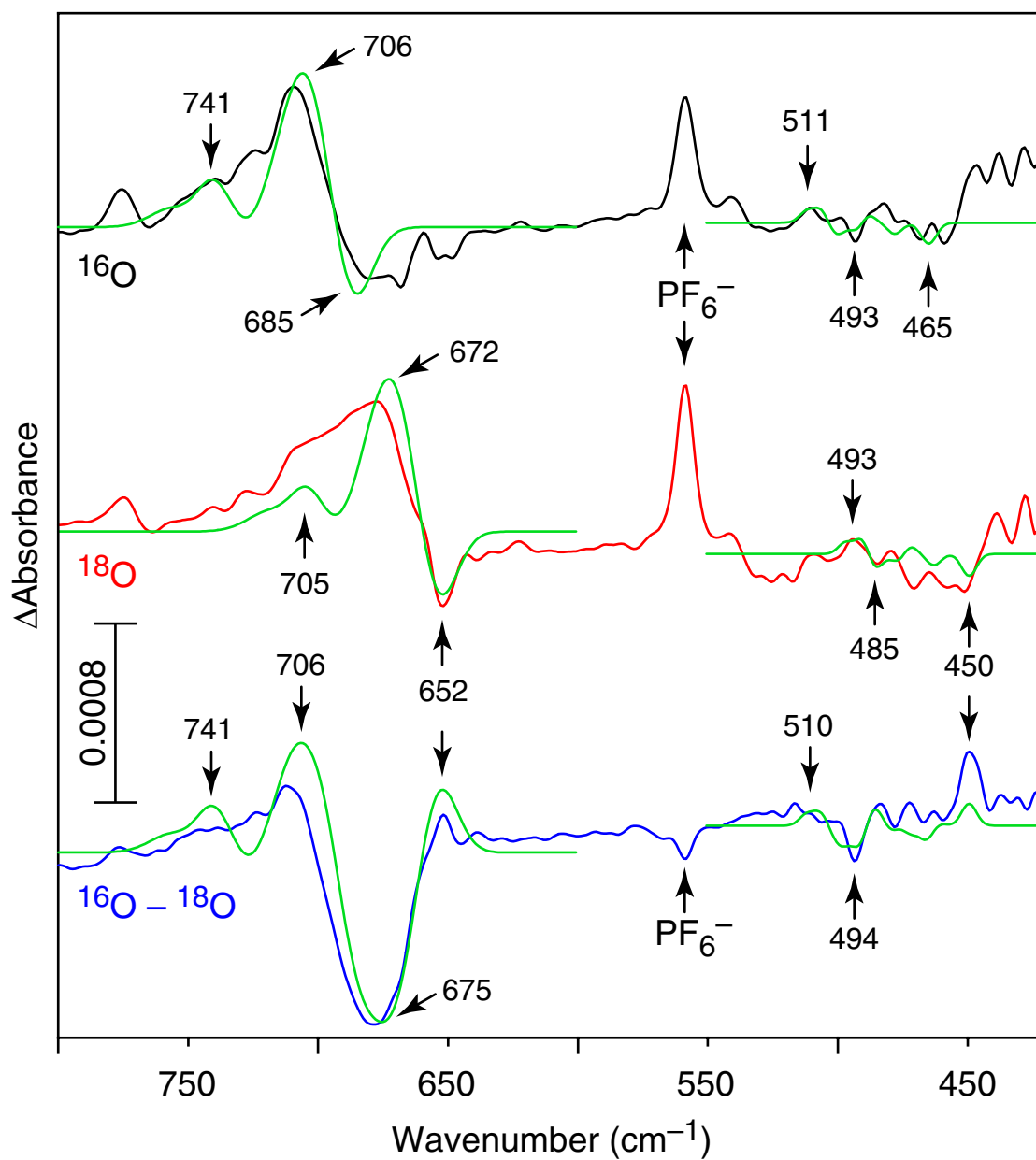


Figure 4.8 A comparison of the observed  $^{16}\text{O}$  (black) and  $^{18}\text{O}$  (red) (oxidized-reduced) difference spectra and the ( $^{16}\text{O} - ^{18}\text{O}$ ) difference-difference spectrum (blue) with the simulated spectra (green). The simulated spectra are obtained using the calculated frequencies of  $S_4$  symmetry for the  $\text{Mn}^{\text{IV}}_4$  species, Table 4.6, and  $C_s$  symmetry for the  $\text{Mn}^{\text{III}}\text{Mn}^{\text{IV}}_3$  species, Table 4.7 (see also Appendix 4.6). The arrows indicate the frequencies that were optimized.

## 4.5 Discussion

Several assumptions were required to perform a normal-mode analysis of the adamantane-like compound. One of the assumptions was that the bpea modes and the Mn–O core modes could be treated separately. However, if these vibrational modes do interact, a small  $^{16}\text{O} \rightarrow ^{18}\text{O}$  isotopic effect is expected on the bpea modes. In the (oxidized – reduced) difference spectra reversible signals are observed which do not shift between the  $^{16}\text{O}$  and  $^{18}\text{O}$  spectra, and which are absent in the ( $^{16}\text{O} - ^{18}\text{O}$ ) difference-difference spectrum. This indicates that these modes are not sensitive to the  $^{16}\text{O} \rightarrow ^{18}\text{O}$  exchange. All of these difference signals are at positions of the vibrational modes of terminal ligand, bpea (Figure 4.2). Therefore, it is concluded that these reversible signals are caused by changes in the terminal ligand, bpea, upon a change in oxidation state of a Mn atom. This supports the assumption that the modes of the terminal ligand bpea are not influenced by the Mn–O core, and can indeed be treated separately.

To reduce the number of force constant variables it was assumed that the stretching and bending modes could be treated separately. Consequently, the bending force constants were set at zero, during the simulations of the stretching normal modes. In appendix 4.6 it is shown, that stretching and bending modes do interact. Including bending modes in the calculations causes shifts in frequencies of the stretching modes. However, these shifts can be corrected by slight alterations of the stretching force constants,  $\sim 0.1 \text{ mdyn}/\text{\AA}$ . These corrections of the force constants are on the same order as the changes needed to optimize the calculated modes when a different overall symmetry is assumed. Therefore, omitting the bending force constants is assumed to be reasonable given the error of the normal-mode calculations.



A good match between the calculated and observed vibrational modes is obtained, without including the terminal ligand Mn–N interactions. Therefore, the assumption, that the terminal ligand Mn–N interaction is much weaker than the  $\mu$ -oxo bridge Mn–O interaction, seems to be valid. This agrees with the results Sheats et al.<sup>55</sup> obtained for the vibrational modes of the mono- $\mu$ -oxo compound. However, it is questionable whether this assumption will apply to the OEC. As indicated in Chapter 1 and section 4.1 most of the terminal ligands to the Mn-cluster are carboxylate groups. The terminal carboxylate Mn–O ligand interactions in the OEC will be much stronger than the terminal ligand Mn–N interactions in the adamantane-like compound. Therefore, the terminal ligand Mn–O interactions will have to be included for normal-mode analysis of the OEC.

Another influence on the bridging Mn–O interaction is the number of bridging oxygens to the Mn atom. As expected, the force constant of a Mn<sup>III</sup>–O bond,  $f_{r,III} = 2.45$  mdyn/Å, is weaker than that of the Mn<sup>IV</sup>–O bond,  $f_{r,IV} = 3.10$  mdyn/Å. However, both these values are smaller than to the value found for the Mn<sup>III</sup>–O bond,  $f_{r,III} = 3.34$  mdyn/Å, of the mono- $\mu$ -oxo compound studied by Sheats et al.<sup>55</sup> (see also Table 4.2). This is an indication that the strength of the Mn–X bond depends not only on the oxidation state of Mn and the electronegativity of X, but also on the character of the other bridging ligands. The manganese atoms in the adamantane-like compound have three  $\mu$ -oxo bridge oxygens. Most likely, the number of  $\mu$ -oxo bridges influences the strength of the Mn–O bonds. Therefore, it is imperative that more manganese compounds are studied to provide further insight into the behavior of these Mn–O vibrational modes and to provide more accurate models of the OEC.

## **4.6 Appendix - Normal-mode analysis.**

### **4.6.1 Definition of the *G* & *F* matrices for the adamantane-like compound**

The observed frequencies, the isotopic shifts, and changes due to the redox chemistry can be used to learn more about vibrational force constants of Mn–O bonds. A normal-mode analysis of the compound is required to understand and extract this information from IR spectra. Comprehensive descriptions of normal-mode analysis are given in Wilson et al.<sup>85</sup> and Herzberg,<sup>86</sup> and summarized here briefly using the adamantane-like compound as an example.

The adamantane-like compound consists of 146 atoms, which translate into  $(3 \times N - 6 =)$  432 degrees of vibrational freedom - i.e. vibrational normal modes. To reduce the magnitude of the analysis some simplifications are required. Our main interest is in the Mn–O vibrations. Therefore, the focus will be on the manganese-oxygen core of the compound, as shown in Figure 4.6.1. Using this reduction, 10 atoms are involved and only 24 normal modes need to be analyzed.

This approach implicates some assumptions for the interaction between certain vibrations. One of the assumptions is that the Mn–O core and the terminal bpea ligands can be treated separately, i.e. there is no (or only a very weak) coupling between vibrations of the bpea ligand and the Mn–O core. There are indications in the IR difference spectra of the two electrochemical species that are consistent with this assumption. Upon oxidation, reversible difference signals of bpea are observed in Figures 4.4 and 4.5 which do not shift upon <sup>16</sup>O and <sup>18</sup>O exchange. This indicates that there is no coupling between this vibration of the bpea ligand and the Mn–O core vibrations. Another assumption is that there is no (or only very weak) coupling between

the terminal Mn–N(bpea) vibrations and those of the Mn–O core. This can be the case only when the Mn–N bond constants are much weaker than those of the Mn–O bonds. The Mn–N bond constants are indeed weaker, Mn–N vibrations occur around  $300\text{ cm}^{-1}$  (Table 4.1), but they are still significant compared to Mn–O bonds. Nevertheless, this assumption has been used successfully applied by Sheats et al.<sup>55</sup> for a di-manganese mono- $\mu$ -oxo compound. Therefore, as a first approximation the Mn–N bonds are not included in this normal-mode analysis.

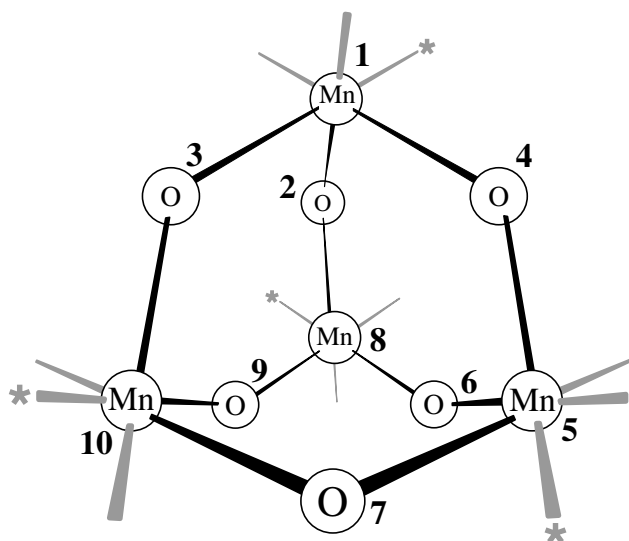


*Figure 4.9 The Mn–O core of the adamantane-like compound. The Mn–N(bpea) terminal ligands are indicated by gray, and the non-aromatic nitrogens are indicated by an asterisk. The indices for each atom in the Mn–O core are used in Table 4.8 to define the internal bond and angle coordinates.*

The first step in a normal-mode analysis is the definition of the internal coordinates. Figure 4.9 shows the Mn–O core of the adamantane-like compound with an index for each atom. Using these indices, each bond and valence angle is defined in Table 4.8. As can be seen from Table 4.8 the number of internal coordinates, 30, exceeds

the degrees of vibrational freedom of the Mn–O core, 24. This indicates that not all internal coordinates are independent of each other. Therefore, some redundant conditions exist which will combine the internal coordinates into a set of independent coordinates. The number of these independent coordinates should equal 24. Consequently, there are 6 different redundant conditions. These redundant conditions in general can be extracted during the normal-mode analysis and used as a double-check of the calculations. For cyclic structures, such as the adamantane-like compound, finding these redundant conditions is not trivial.<sup>87</sup> However, it is not necessary to obtain the redundant conditions, because the independent coordinates will easily be derived during the calculations. Therefore, no extra effort is taken here to find the formal expression of the redundant conditions.

*Table 4.8 The definition of the internal coordinates used for the normal-mode analysis of the Mn–O core of the adamantane-like compound. The indices of the atoms are defined in Figure 4.9.*

Bond	Atoms	Bond	Atoms	Angle	Atoms	Angle	Atoms
r <sub>1</sub>	1 - 2	r <sub>7</sub>	4 - 5	α <sub>1</sub>	2 - 1 - 4	α <sub>10</sub>	6 - 5 - 7
r <sub>2</sub>	1 - 4	r <sub>8</sub>	6 - 5	α <sub>2</sub>	3 - 1 - 4	α <sub>11</sub>	4 - 5 - 7
r <sub>3</sub>	1 - 3	r <sub>9</sub>	7 - 5	α <sub>3</sub>	2 - 1 - 3	α <sub>12</sub>	5 - 6 - 8
r <sub>4</sub>	2 - 8	r <sub>10</sub>	3 - 10	α <sub>4</sub>	1 - 2 - 8	α <sub>13</sub>	5 - 7 - 10
r <sub>5</sub>	6 - 8	r <sub>11</sub>	7 - 10	α <sub>5</sub>	2 - 8 - 6	α <sub>14</sub>	3 - 10 - 7
r <sub>6</sub>	9 - 8	r <sub>12</sub>	9 - 10	α <sub>6</sub>	6 - 8 - 9	α <sub>15</sub>	3 - 10 - 9
				α <sub>7</sub>	2 - 8 - 9	α <sub>16</sub>	7 - 10 - 9
				α <sub>8</sub>	1 - 4 - 5	α <sub>17</sub>	8 - 9 - 10
				α <sub>9</sub>	4 - 5 - 6	α <sub>18</sub>	1 - 3 - 10

Beside bonds and valence angles other internal coordinates can be defined, such as out of plane angles and torsion angles (which is the angle between two non-connected bonds). However, due to the cyclic character of the molecule these two additional internal coordinates are correlated to the already defined internal coordinates. Therefore, including these coordinates will increase only the number of internal coordinates, and no additional vibrational modes are added. Consequently, only the number of redundant coordinates would increase. Therefore, no additional internal coordinates are included.

To obtain analytical expressions for the normal mode vibrations Newton's equation needs to be solved for the set of defined internal coordinates, which can be written as:

$$\begin{aligned} \frac{d}{dt} \left( \frac{\partial T}{\partial \dot{R}} \right) + \frac{\partial V}{\partial R} &= 0 \\ 2T &= \dot{R}^T G^{-1} \dot{R} \\ 2V &= R^T F R \end{aligned} \quad (\text{eq. 4.1})$$

where  $R$  is the vector with all the displacements of the internal coordinates, i.e. stretching of the bonds and bending of the valence angles.  $\dot{R}$  is the time derivative of  $R$ . The matrix  $F$  contains the force constants involved in the vibrations, which is needed for the potential energy,  $V$ . Matrix  $G$  contains structural information about the compound, which is necessary to calculate the kinetic energy,  $T$ . Both the  $F$  and  $G$  matrices are symmetric around their diagonal and will be defined later in more detail. Equation 4.1 can be rewritten into:

$$\begin{vmatrix} \sum G_{1r} F_{r1} - \lambda & \sum G_{1r} F_{r2} & \cdots \\ \sum G_{2r} F_{r1} & \sum G_{2r} F_{r2} - \lambda & \cdots \\ \vdots & \vdots & \ddots \end{vmatrix} \equiv |GF - \lambda E| = 0 \quad (\text{eq. 4.2})$$

where  $E$  is the unit matrix, and  $\lambda$  (force constant per mass) are the eigenvalues of this equation and are related to the wavenumber,  $\nu$ , by the relation  $\lambda = 4\pi^2 c^2 \nu^2$ . These eigenvalues correspond to frequencies in the IR spectra with the appropriate values for the force constant variables.

The force constant matrix,  $F$ , is defined as:

$$F = \begin{bmatrix} f_{r_1} & f_{r_1 r_2} & \cdots & f_{r_1 r_{10}} & f_{r_1 \alpha_1} & f_{r_1 \alpha_2} & \cdots & f_{r_1 \alpha_{18}} \\ f_{r_1 r_2} & f_{r_2} & \cdots & f_{r_2 r_{10}} & f_{r_2 \alpha_1} & f_{r_2 \alpha_2} & \cdots & f_{r_2 \alpha_{18}} \\ \vdots & \vdots & \ddots & \vdots & \vdots & \vdots & \vdots & \vdots \\ f_{r_1 r_{10}} & f_{r_2 r_{10}} & \cdots & f_{r_{10}} & f_{r_{10} \alpha_1} & f_{r_{10} \alpha_2} & \cdots & f_{r_{10} \alpha_{18}} \\ f_{r_1 \alpha_1} & f_{r_2 \alpha_1} & \cdots & f_{r_{10} \alpha_1} & f_{\alpha_1} & f_{\alpha_1 \alpha_2} & \cdots & f_{\alpha_1 \alpha_{18}} \\ f_{r_1 \alpha_2} & f_{r_2 \alpha_2} & \cdots & f_{r_{10} \alpha_2} & f_{\alpha_1 \alpha_2} & f_{\alpha_2} & \cdots & f_{\alpha_2 \alpha_{18}} \\ \vdots & \vdots & \cdots & \vdots & \vdots & \vdots & \ddots & \vdots \\ f_{r_1 \alpha_{18}} & f_{r_2 \alpha_{18}} & \cdots & f_{r_{10} \alpha_{18}} & f_{\alpha_1 \alpha_{18}} & f_{\alpha_2 \alpha_{18}} & \cdots & f_{\alpha_{18}} \end{bmatrix} \quad (\text{eq. 4.3})$$

where  $f_{r_x}$  is the stretching force constant (mdyn/Å) for internal bond coordinate  $r_x$ , and  $f_{\alpha_x}$  is the bending force constant for internal angle coordinate  $\alpha_x$ . The other three force constants  $f_{r_x r_y}$ ,  $f_{\alpha_x \alpha_y}$ , and  $f_{r_x \alpha_y}$  are the coupling constants between two bond stretches, two angle bendings, and between a bond stretch and angle bend, respectively.

The structural information matrix,  $G$ , can be defined as:<sup>85,86,88</sup>

$$G = S \cdot M^{-1} \cdot S^T \quad (\text{eq. 4.4})$$

$$M^{-1} = \begin{bmatrix} \mu_1 & 0 & & & 0 \\ 0 & \mu_2 & & & \\ & & \ddots & & \\ & & & \mu_9 & 0 \\ 0 & & & 0 & \mu_{10} \end{bmatrix}$$

where  $M$  is a diagonal matrix whose components are the reciprocal of the mass of the  $i^{\text{th}}$  atoms,  $\mu_i$ . The  $S$ -matrix links the displacement of  $i^{\text{th}}$  atoms in a vibration to the changes in internal coordinates. Wilson et al.<sup>85</sup> give some general rules to create the  $S$ -matrix.

The first step in this analysis is to define internal displacement vectors, which give the largest change in internal coordinates with the smallest delocalization of vectors. Figure 4.10 shows the internal displacement vectors for bond stretching and valence angle bending.

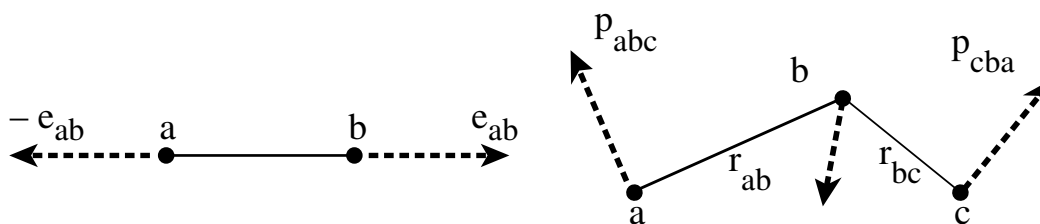


Figure 4.10 The internal displacement vectors for the two internal coordinates, i.e. bonds and valence angles.

In this method a stretch is described with two unit vectors opposite to one another and in line with the bond that is stretched. In Figure 4.10 these stretch vectors are denoted with  $e_{ab}$ , where the indices indicate the two atoms involved in the bond. In the following calculations, all the displacement vectors on the Mn atoms have the same sign, while the displacement vectors on the O atoms are of opposite sign (see Table 4.9). For example the stretching of bond  $r_1$ ,  $\Delta r_1$ , is described by displacement vector  $e_{12}$  indicating the displacement of atom 1(Mn) and  $-e_{12}$  describes the displacement of atom 2(O).

In-plane bending is described by two unit vectors perpendicular to the bonds that are bending, indicated in Figure 4.10 as  $p_{xyz}$ . One vector indicates the direction of displacement of one of the end atoms, the other vector indicates the direction of the other end atom. The first two indices of these vectors indicate the bond to which this vector is perpendicular, and all three indices define the plane in which these two vectors lie. Upon bending the amount of displacement of the end atom is equivalent to the inverse of the

bond distance between the end atom and the apex atom, i.e.  $1/r_{ab}$ . The apex atom moves by an equal amount to the sum of both end atoms, however in the opposite direction. For example, for the bending of  $\alpha_1$ , the displacement vector of atom 2(O) is  $p_{214}/r_{12}$  and for atom 4(O) it is  $p_{412}/r_{14}$ , then for the apex atom 1(Mn) the displacement vector is  $-p_{214}/r_{12}-p_{412}/r_{14}$ . From this definition it can be seen that the stretching and bending displacement vectors are perpendicular, therefore the S-matrix can be blocked out into two sub-matrices (eq. 4.5); a vectorial stretch sub-matrix,  $A(r)$  and a vectorial angular sub-matrix,  $B(\alpha)$ . The two sub-matrices,  $A(r)$  and  $B(\alpha)$  are given in Table 4.9 and 4.10, respectively.

$$S = \begin{bmatrix} A(r) & 0 \\ 0 & B(\alpha) \end{bmatrix} \quad (\text{eq. 4.5})$$

Table 4.9 The vectorial stretching sub-matrix,  $A(r)$ , of the S-matrix.

	1(Mn)	2(O)	3(O)	4(O)	5(Mn)	6(O)	7(O)	8(Mn)	9(O)	10(Mn)
$\Delta r_1$	$e_{12}$	$-e_{12}$	0	0	0	0	0	0	0	0
$\Delta r_2$	$e_{14}$	0	0	$-e_{14}$	0	0	0	0	0	0
$\Delta r_3$	$e_{13}$	0	$-e_{13}$	0	0	0	0	0	0	0
$\Delta r_4$	0	$-e_{28}$	0	0	0	0	0	$e_{28}$	0	0
$\Delta r_5$	0	0	0	0	0	$-e_{68}$	0	$e_{68}$	0	0
$\Delta r_6$	0	0	0	0	0	0	0	$e_{89}$	$-e_{89}$	0
$\Delta r_7$	0	0	0	$-e_{45}$	$e_{45}$	0	0	0	0	0
$\Delta r_8$	0	0	0	0	$e_{56}$	$-e_{56}$	0	0	0	0
$\Delta r_9$	0	0	0	0	$e_{57}$	0	$-e_{57}$	0	0	0
$\Delta r_{10}$	0	0	$-e_{310}$	0	0	0	0	0	0	$e_{310}$
$\Delta r_{11}$	0	0	0	0	0	0	$-e_{710}$	0	0	$e_{710}$
$\Delta r_{12}$	0	0	0	0	0	0	0	0	$-e_{910}$	$e_{910}$



Table 4.10 The vectorial angular sub-matrix,  $B(\alpha)$ , of the  $S$ -matrix.

	1(Mn)	2(O)	3(O)	4(O)	5(Mn)	6(O)	7(O)	8(Mn)	9(O)	10(Mn)
$\Delta\alpha_1$	$-p_{214}/r_1$ $-p_{412}/r_2$	$p_{214}/r_1$	0	$p_{412}/r_2$	0	0	0	0	0	0
$\Delta\alpha_2$	$-p_{314}/r_3$ $-p_{413}/r_2$	0	$p_{314}/r_3$	$p_{413}/r_2$	0	0	0	0	0	0
$\Delta\alpha_3$	$-p_{213}/r_1$ $-p_{312}/r_3$	$p_{213}/r_1$	$p_{312}/r_3$	0	0	0	0	0	0	0
$\Delta\alpha_4$	$p_{128}/r_1$	$-p_{128}/r_1$ $-p_{821}/r_4$	0	0	0	0	0	$p_{821}/r_4$	0	0
$\Delta\alpha_5$	0	$p_{286}/r_4$	0	0	0	$p_{682}/r_5$	0	$-p_{286}/r_4$ $-p_{682}/r_5$	0	0
$\Delta\alpha_6$	0	0	0	0	0	$p_{689}/r_5$	0	$-p_{689}/r_5$ $-p_{986}/r_6$	$p_{986}/r_6$	0
$\Delta\alpha_7$	0	$p_{289}/r_4$	0	0	0	0	0	$-p_{289}/r_4$ $-p_{982}/r_6$	$p_{982}/r_6$	0
$\Delta\alpha_8$	$p_{145}/r_2$	0	0	$-p_{145}/r_2$ $-p_{541}/r_7$	$p_{541}/r_7$	0	0	0	0	0
$\Delta\alpha_9$	0	0	0	$p_{456}/r_7$	$-p_{456}/r_7$ $-p_{654}/r_8$	$p_{654}/r_8$	0	0	0	0
$\Delta\alpha_{10}$	0	0	0	0	$-p_{657}/r_8$ $-p_{756}/r_9$	$p_{657}/r_8$	$p_{756}/r_9$	0	0	0
$\Delta\alpha_{11}$	0	0	0	$p_{457}/r_7$	$-p_{457}/r_7$ $-p_{754}/r_9$	0	$p_{754}/r_9$	0	0	0
$\Delta\alpha_{12}$	0	0	0	0	$p_{568}/r_8$	$-p_{568}/r_8$ $-p_{865}/r_5$	0	$p_{865}/r_5$	0	0
$\Delta\alpha_{13}$	0	0	0	0	$p_{5710}/r_9$	0	$-p_{5710}/r_9$ $-p_{1075}/r_{11}$	0	0	$p_{1075}/r_{11}$
$\Delta\alpha_{14}$	0	0	$p_{3107}/r_{10}$	0	0	0	$p_{7103}/r_{11}$	0	0	$-p_{3107}/r_{10}$ $-p_{7103}/r_{11}$
$\Delta\alpha_{15}$	0	0	$p_{3109}/r_{10}$	0	0	0	0	0	$p_{9103}/r_{12}$	$-p_{3109}/r_{10}$ $-p_{9103}/r_{12}$
$\Delta\alpha_{16}$	0	0	0	0	0	0	$p_{7109}/r_{11}$	0	$p_{9107}/r_{12}$	$-p_{7109}/r_{11}$ $-p_{9107}/r_{12}$
$\Delta\alpha_{17}$	0	0	0	0	0	0	0	$p_{8910}/r_6$	$-p_{8910}/r_6$ $-p_{1098}/r_{12}$	$p_{1098}/r_{12}$
$\Delta\alpha_{18}$	$p_{1310}/r_3$	0	$-p_{1310}/r_3$ $-p_{1031}/r_{10}$	0	0	0	0	0	0	$p_{1031}/r_{10}$

To simplify the calculation of the  $G$ -matrix the bending displacement vector can be expressed in terms of the stretching displacement vectors. The plane which is formed by two bonds can be defined by the outerproduct of two stretch displacement vectors. For example, for the bending of angle  $\alpha_1$  the plane which contains both bonds can be defined as;  $\mathbf{e}_{14} \otimes \mathbf{e}_{12}$ . This outerproduct is a vector which is perpendicular to the plane (a right handed axis-system is used). For normalization this vector needs to be divided by  $\sin \alpha_1$ . Now the angular displacement vector  $\mathbf{p}_{214}$  can be expressed as the outer product of  $\mathbf{e}_{12}$  and the plane vector. These outerproducts can be reduced to a series of innerproducts and the bending displacement vector of angle  $\alpha_1$ ,  $\mathbf{p}_{214}$  and  $\mathbf{p}_{412}$  can be expressed as:

$$\mathbf{p}_{214} = (\sin \alpha_1)^{-1} \mathbf{e}_{12} \otimes [\mathbf{e}_{14} \otimes \mathbf{e}_{12}] = (\sin \alpha_1)^{-1} [(\mathbf{e}_{12} \cdot \mathbf{e}_{12}) \cdot \mathbf{e}_{14} - (\mathbf{e}_{12} \cdot \mathbf{e}_{14}) \cdot \mathbf{e}_{12}]$$

$$\mathbf{p}_{412} = (\sin \alpha_1)^{-1} [\mathbf{e}_{14} \otimes \mathbf{e}_{12}] \otimes \mathbf{e}_{12} = (\sin \alpha_1)^{-1} [(\mathbf{e}_{14} \cdot \mathbf{e}_{14}) \cdot \mathbf{e}_{12} - (\mathbf{e}_{12} \cdot \mathbf{e}_{14}) \cdot \mathbf{e}_{14}]$$

All the other conversions of the bending displacement vectors into expressions of stretching vectors are given in Table 4.11.

After converting the bending displacement vectors the  $G$ -matrix contains the  $r_x$  and  $\alpha_x$  variables and a set of inner products of the stretch displacement vectors. These inner products can be exchanged for the cosine of the angle between the two vectors (using the cosine rule). Three different kinds of inner products can be distinguished: between two connected bonds (Table 4.12), between two bonds separated by one bond (Table 4.13), and two bonds separated by two bonds (Table 4.14). The angles between two connected bonds have been defined already as the internal angle coordinates. The other two angles are defined by the inner products given in Table 4.13 and 4.14.

Table 4.11 The conversion of all the bending displacement vectors into expressions of stretching vectors.

$p_{214} = (\sin \alpha_1)^{-1}[(e_{12} \cdot e_{12}) \cdot e_{14} - (e_{12} \cdot e_{14}) \cdot e_{12}]$	$p_{756} = (\sin \alpha_{10})^{-1}[(e_{57} \cdot e_{57}) \cdot e_{56} - (e_{56} \cdot e_{57}) \cdot e_{57}]$
$p_{412} = (\sin \alpha_1)^{-1}[(e_{14} \cdot e_{14}) \cdot e_{12} - (e_{12} \cdot e_{14}) \cdot e_{14}]$	$p_{657} = (\sin \alpha_{10})^{-1}[(e_{56} \cdot e_{56}) \cdot e_{57} - (e_{56} \cdot e_{57}) \cdot e_{56}]$
$p_{314} = (\sin \alpha_2)^{-1}[(e_{13} \cdot e_{13}) \cdot e_{14} - (e_{14} \cdot e_{13}) \cdot e_{13}]$	$p_{457} = (\sin \alpha_{11})^{-1}[(e_{45} \cdot e_{45}) \cdot e_{57} - (e_{57} \cdot e_{45}) \cdot e_{45}]$
$p_{413} = (\sin \alpha_2)^{-1}[(e_{14} \cdot e_{14}) \cdot e_{13} - (e_{14} \cdot e_{13}) \cdot e_{14}]$	$p_{754} = (\sin \alpha_{11})^{-1}[(e_{57} \cdot e_{57}) \cdot e_{45} - (e_{57} \cdot e_{45}) \cdot e_{57}]$
$p_{213} = (\sin \alpha_3)^{-1}[(e_{12} \cdot e_{12}) \cdot e_{13} - (e_{13} \cdot e_{12}) \cdot e_{12}]$	$p_{568} = (\sin \alpha_{12})^{-1}[(e_{68} \cdot e_{56}) \cdot e_{56} - (e_{56} \cdot e_{56}) \cdot e_{68}]$
$p_{312} = (\sin \alpha_3)^{-1}[(e_{13} \cdot e_{13}) \cdot e_{12} - (e_{13} \cdot e_{12}) \cdot e_{13}]$	$p_{865} = (\sin \alpha_{12})^{-1}[(e_{68} \cdot e_{56}) \cdot e_{68} - (e_{68} \cdot e_{68}) \cdot e_{56}]$
$p_{128} = (\sin \alpha_4)^{-1}[(e_{12} \cdot e_{28}) \cdot e_{12} - (e_{12} \cdot e_{12}) \cdot e_{28}]$	$p_{5710} = (\sin \alpha_{13})^{-1}[(e_{57} \cdot e_{710}) \cdot e_{57} - (e_{57} \cdot e_{57}) \cdot e_{710}]$
$p_{821} = (\sin \alpha_4)^{-1}[(e_{12} \cdot e_{28}) \cdot e_{28} - (e_{28} \cdot e_{28}) \cdot e_{12}]$	$p_{1075} = (\sin \alpha_{13})^{-1}[(e_{57} \cdot e_{710}) \cdot e_{710} - (e_{710} \cdot e_{710}) \cdot e_{57}]$
$p_{286} = (\sin \alpha_5)^{-1}[(e_{28} \cdot e_{28}) \cdot e_{68} - (e_{68} \cdot e_{28}) \cdot e_{28}]$	$p_{3107} = (\sin \alpha_{14})^{-1}[(e_{310} \cdot e_{310}) \cdot e_{710} - (e_{710} \cdot e_{310}) \cdot e_{310}]$
$p_{682} = (\sin \alpha_5)^{-1}[(e_{68} \cdot e_{68}) \cdot e_{28} - (e_{68} \cdot e_{28}) \cdot e_{68}]$	$p_{7103} = (\sin \alpha_{14})^{-1}[(e_{710} \cdot e_{710}) \cdot e_{310} - (e_{710} \cdot e_{310}) \cdot e_{710}]$
$p_{689} = (\sin \alpha_6)^{-1}[(e_{68} \cdot e_{68}) \cdot e_{89} - (e_{89} \cdot e_{68}) \cdot e_{68}]$	$p_{3109} = (\sin \alpha_{15})^{-1}[(e_{310} \cdot e_{310}) \cdot e_{910} - (e_{910} \cdot e_{310}) \cdot e_{310}]$
$p_{986} = (\sin \alpha_6)^{-1}[(e_{89} \cdot e_{89}) \cdot e_{68} - (e_{89} \cdot e_{68}) \cdot e_{89}]$	$p_{9103} = (\sin \alpha_{15})^{-1}[(e_{910} \cdot e_{910}) \cdot e_{310} - (e_{910} \cdot e_{310}) \cdot e_{910}]$
$p_{289} = (\sin \alpha_7)^{-1}[(e_{28} \cdot e_{28}) \cdot e_{89} - (e_{28} \cdot e_{89}) \cdot e_{28}]$	$p_{7109} = (\sin \alpha_{16})^{-1}[(e_{710} \cdot e_{710}) \cdot e_{910} - (e_{710} \cdot e_{910}) \cdot e_{710}]$
$p_{982} = (\sin \alpha_7)^{-1}[(e_{89} \cdot e_{89}) \cdot e_{28} - (e_{28} \cdot e_{89}) \cdot e_{89}]$	$p_{9107} = (\sin \alpha_{16})^{-1}[(e_{910} \cdot e_{910}) \cdot e_{710} - (e_{710} \cdot e_{910}) \cdot e_{910}]$
$p_{145} = (\sin \alpha_8)^{-1}[(e_{14} \cdot e_{45}) \cdot e_{14} - (e_{14} \cdot e_{14}) \cdot e_{45}]$	$p_{8910} = (\sin \alpha_{17})^{-1}[(e_{910} \cdot e_{89}) \cdot e_{89} - (e_{89} \cdot e_{89}) \cdot e_{910}]$
$p_{541} = (\sin \alpha_8)^{-1}[(e_{14} \cdot e_{45}) \cdot e_{45} - (e_{45} \cdot e_{45}) \cdot e_{14}]$	$p_{1098} = (\sin \alpha_{17})^{-1}[(e_{910} \cdot e_{89}) \cdot e_{910} - (e_{910} \cdot e_{910}) \cdot e_{89}]$
$p_{654} = (\sin \alpha_9)^{-1}[(e_{56} \cdot e_{56}) \cdot e_{45} - (e_{45} \cdot e_{56}) \cdot e_{56}]$	$p_{1310} = (\sin \alpha_{18})^{-1}[(e_{13} \cdot e_{310}) \cdot e_{13} - (e_{13} \cdot e_{13}) \cdot e_{310}]$
$p_{456} = (\sin \alpha_9)^{-1}[(e_{45} \cdot e_{45}) \cdot e_{56} - (e_{45} \cdot e_{56}) \cdot e_{45}]$	$p_{1031} = (\sin \alpha_{18})^{-1}[(e_{13} \cdot e_{310}) \cdot e_{310} - (e_{310} \cdot e_{310}) \cdot e_{13}]$

Table 4.12 Conversion of the inner product of the stretch displacement vectors of two connected bonds.

$e_{12} \cdot e_{13} = \cos \alpha_3$	$e_{28} \cdot e_{68} = \cos \alpha_5$	$e_{56} \cdot e_{68} = \cos \alpha_{12}$
$e_{12} \cdot e_{14} = \cos \alpha_1$	$e_{28} \cdot e_{89} = \cos \alpha_7$	$e_{56} \cdot e_{57} = \cos \alpha_{10}$
$e_{12} \cdot e_{28} = \cos \alpha_4$	$e_{310} \cdot e_{710} = \cos \alpha_{14}$	$e_{57} \cdot e_{710} = \cos \alpha_{13}$
$e_{13} \cdot e_{310} = \cos \alpha_{18}$	$e_{310} \cdot e_{910} = \cos \alpha_{15}$	$e_{68} \cdot e_{89} = \cos \alpha_6$
$e_{14} \cdot e_{13} = \cos \alpha_2$	$e_{45} \cdot e_{56} = \cos \alpha_9$	$e_{710} \cdot e_{910} = \cos \alpha_{16}$
$e_{14} \cdot e_{45} = \cos \alpha_8$	$e_{45} \cdot e_{57} = \cos \alpha_{11}$	$e_{89} \cdot e_{910} = \cos \alpha_{17}$

Table 4.13 Conversion of the inner product of the stretch displacement vectors of two bonds separated by one bond.

$e_{12} \cdot e_{45} = \cos \beta_1$	$e_{13} \cdot e_{710} = \cos \beta_7$	$e_{45} \cdot e_{68} = \cos \beta_{13}$	$e_{56} \cdot e_{710} = \cos \beta_{19}$
$e_{12} \cdot e_{310} = \cos \beta_2$	$e_{13} \cdot e_{910} = \cos \beta_8$	$e_{45} \cdot e_{710} = \cos \beta_{14}$	$e_{56} \cdot e_{89} = \cos \beta_{20}$
$e_{12} \cdot e_{68} = \cos \beta_3$	$e_{14} \cdot e_{28} = \cos \beta_9$	$e_{28} \cdot e_{56} = \cos \beta_{15}$	$e_{57} \cdot e_{68} = \cos \beta_{21}$
$e_{12} \cdot e_{89} = \cos \beta_4$	$e_{14} \cdot e_{310} = \cos \beta_{10}$	$e_{28} \cdot e_{910} = \cos \beta_{16}$	$e_{57} \cdot e_{910} = \cos \beta_{22}$
$e_{13} \cdot e_{28} = \cos \beta_5$	$e_{14} \cdot e_{56} = \cos \beta_{11}$	$e_{310} \cdot e_{57} = \cos \beta_{17}$	$e_{68} \cdot e_{910} = \cos \beta_{23}$
$e_{13} \cdot e_{45} = \cos \beta_6$	$e_{14} \cdot e_{57} = \cos \beta_{12}$	$e_{310} \cdot e_{89} = \cos \beta_{18}$	$e_{89} \cdot e_{710} = \cos \beta_{24}$

Table 4.14 Conversion of the inner product of the stretch displacement vectors of two bonds separated by two bonds.

$e_{12} \cdot e_{910} = \cos \delta_1$	$e_{13} \cdot e_{56} = \cos \delta_7$	$e_{28} \cdot e_{45} = \cos \delta_{13}$	$e_{310} \cdot e_{68} = \cos \delta_{19}$
$e_{12} \cdot e_{710} = \cos \delta_2$	$e_{13} \cdot e_{57} = \cos \delta_8$	$e_{28} \cdot e_{310} = \cos \delta_{14}$	$e_{45} \cdot e_{89} = \cos \delta_{20}$
$e_{12} \cdot e_{56} = \cos \delta_3$	$e_{14} \cdot e_{68} = \cos \delta_9$	$e_{28} \cdot e_{57} = \cos \delta_{15}$	$e_{45} \cdot e_{910} = \cos \delta_{21}$
$e_{12} \cdot e_{57} = \cos \delta_4$	$e_{14} \cdot e_{89} = \cos \delta_{10}$	$e_{28} \cdot e_{710} = \cos \delta_{16}$	$e_{56} \cdot e_{910} = \cos \delta_{22}$
$e_{13} \cdot e_{68} = \cos \delta_5$	$e_{14} \cdot e_{710} = \cos \delta_{11}$	$e_{310} \cdot e_{45} = \cos \delta_{17}$	$e_{57} \cdot e_{89} = \cos \delta_{23}$
$e_{13} \cdot e_{89} = \cos \delta_6$	$e_{14} \cdot e_{910} = \cos \delta_{12}$	$e_{310} \cdot e_{56} = \cos \delta_{18}$	$e_{68} \cdot e_{710} = \cos \delta_{24}$

At this point, the  $G$ -matrix is a  $30 \times 30$  matrix, which contains four types of variables  $r_x$ ,  $\alpha_x$ ,  $\beta_x$ , and  $\delta_x$ , amounting to 76 different variables, which all can be extracted from the crystal structure. As can be seen from Eq. 4.3 the  $F$ -matrix is also a  $30 \times 30$  matrix, containing 465 different force constants. Consequently it would be convenient to reduce the number of variables and the size of the matrices  $G$  and  $F$ . This can be achieved by utilizing some of the symmetry of the adamantane-like compound.

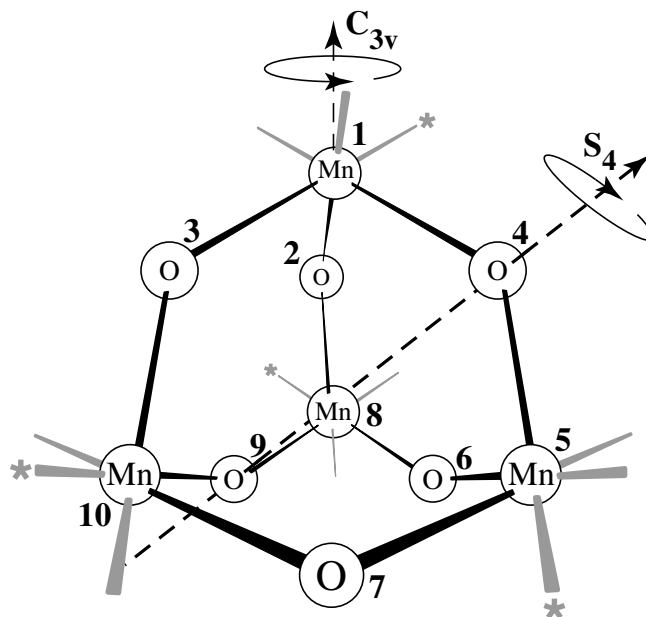


Figure 4.11 Some of the symmetry operations of the adamantane-like compound for  $T_d$  symmetry. Each Mn atom has a  $C_3$  proper rotation axis and three  $\sigma_d$  mirror planes, which contain the three Mn–O–Mn moieties the Mn atom is attached to. In addition, there are three improper rotation axis which bisect two opposite Mn–O–Mn moieties. For the exact definition of all the symmetry operations see Table 4.15.

#### 4.6.2 Normal-mode analysis for the $T_d$ symmetry

The first step in the simplification of the  $F$  and  $G$  matrices requires establishing the overall symmetry of the compound. For the  $\text{Mn}^{\text{IV}}_4$  compound  $T_d$  symmetry can be assumed, with the assumption that no differences in the Mn–O bonds are caused by the bpea ligand. From the crystal structure it is known that there is a slight effect on the Mn–O due to the difference between aromatic and non-aromatic Mn–N bonds. However, as a first approach this influence of the terminal ligand on the overall symmetry is neglected. The next step is to define the symmetry operations. The  $T_d$  symmetry consists

of four proper  $C_3$  rotation axis, six  $\sigma_d$  mirror planes, and three improper  $S_4$  rotation axis. One of the proper  $C_3$  rotation axis is represented in Figure 4.11, the other three are through the other three manganese atoms. The six mirror planes contain one of the Mn–O–Mn moieties and the oxygen on the opposite mono- $\mu$ -oxo moiety. The improper  $S_4$  rotation axis bisects two opposite Mn–O–Mn moieties, see Figure 4.11. The atoms which are involved in the various symmetry operations are given in Table 4.15.

*Table 4.15 Definition of the symmetry operations for the adamantane-like compound in  $T_d$  symmetry.*

Sym. oper.	Atoms that are on the symmetry operation
$C_3$	1(Mn) and through the middle of the 6(O)7(O)9(O) plane
$C_3'$	5(Mn) and through the middle of the 2(O)3(O)9(O) plane
$C_3''$	10(Mn) and through the middle of the 2(O)4(O)6(O) plane
$C_3'''$	8(Mn) and through the middle of the 3(O)4(O)7(O) plane
$S_4$	2(O) and 7(O)
$S_4'$	4(O) and 9(O)
$S_4''$	3(O) and 6(O)
$\sigma_1$	1(Mn)-2(O)-8(Mn) and 7(O)
$\sigma_2$	1(Mn)-4(O)-5(Mn) and 9(O)
$\sigma_3$	1(Mn)-3(O)-10(Mn) and 6(O)
$\sigma_4$	5(Mn)-6(O)-8(Mn) and 3(O)
$\sigma_5$	8(Mn)-9(O)-10(Mn) and 4(O)
$\sigma_6$	5(Mn)-7(O)-10(Mn) and 2(O)

When the overall  $T_d$  symmetry is assumed for the adamantane-like compound the symmetry representations of the 24 vibrational modes are: 2  $A_1$ , 2  $E$ , 2  $T_1$ , and 4  $T_2$ . The  $E$  symmetry representations are doubly degenerate modes, while the  $T_x$  symmetry representations are triply degenerate levels. Of these modes only the  $T_2$  vibrations are IR

active, and only the  $T_1$  vibrations are Raman active (Figure 4.7). To find the mathematical expression of these vibrational modes the internal coordinates,  $R$ , need to be transformed into symmetry coordinates,  $R^S$ , as in described in equation 4.6.

$$R^S = U \cdot R \quad (\text{eq. 4.6})$$

where  $U$  is constructed by using:

$$R_i^S = N \sum_k \chi_i(K) K(\Delta I) \quad (\text{eq. 4.7})$$

where  $N$  is the normalization constant,  $i$  is the symmetry representation,  $\Delta I$  is an internal coordinate and  $\chi(K)$  is the character of the symmetry operation  $K$ .  $K(\Delta I)$  is the internal coordinate, which  $\Delta I$  is transformed into when symmetry operation  $K$  is applied. The  $F$  and  $G$  matrix block-out into symmetry representation sub-matrices by using the symmetry coordinates, and are calculated as in eq. 4.8.

$$G_s = U \cdot G \cdot U^T = \begin{bmatrix} G_s(A) & 0 & 0 & 0 \\ 0 & G_s(E) & 0 & 0 \\ 0 & 0 & G_s(T_1) & 0 \\ 0 & 0 & 0 & G_s(T_2) \end{bmatrix}$$

$$F_s = U \cdot F \cdot U^T = \begin{bmatrix} F_s(A) & 0 & 0 & 0 \\ 0 & F_s(E) & 0 & 0 \\ 0 & 0 & F_s(T_1) & 0 \\ 0 & 0 & 0 & F_s(T_2) \end{bmatrix} \quad (\text{eq. 4.8})$$

Table 4.16 and 4.17 show the result of each symmetry operation on the internal coordinates, which are necessary to obtain the  $U$ -matrix.

Table 4.16 The result of the  $T_d$  symmetry operations working on the internal coordinates of the Mn model compound. The improper rotation operations are given in Table 4.17.

	E	$C_3$	$C_3^2$	$C_3'$	$C_3^{2'}$	$C_3''$	$C_3^{2''}$	$C_3'''$	$C_3^{2'''}$	S table	$\sigma_1$	$\sigma_2$	$\sigma_3$	$\sigma_4$	$\sigma_5$	$\sigma_6$
$\Gamma_1$	$\Gamma_1$	$\Gamma_3$	$\Gamma_2$	$\Gamma_{10}$	$\Gamma_6$	$\Gamma_5$	$\Gamma_7$	$\Gamma_8$	$\Gamma_{12}$		$\Gamma_1$	$\Gamma_3$	$\Gamma_2$	$\Gamma_{12}$	$\Gamma_8$	$\Gamma_4$
$\Gamma_2$	$\Gamma_2$	$\Gamma_1$	$\Gamma_3$	$\Gamma_{11}$	$\Gamma_5$	$\Gamma_4$	$\Gamma_8$	$\Gamma_9$	$\Gamma_{10}$		$\Gamma_3$	$\Gamma_2$	$\Gamma_1$	$\Gamma_{11}$	$\Gamma_7$	$\Gamma_5$
$\Gamma_3$	$\Gamma_3$	$\Gamma_2$	$\Gamma_1$	$\Gamma_{12}$	$\Gamma_4$	$\Gamma_6$	$\Gamma_9$	$\Gamma_7$	$\Gamma_{11}$		$\Gamma_2$	$\Gamma_1$	$\Gamma_3$	$\Gamma_{10}$	$\Gamma_9$	$\Gamma_6$
$\Gamma_4$	$\Gamma_4$	$\Gamma_{10}$	$\Gamma_7$	$\Gamma_3$	$\Gamma_{12}$	$\Gamma_8$	$\Gamma_2$	$\Gamma_5$	$\Gamma_6$		$\Gamma_4$	$\Gamma_{10}$	$\Gamma_7$	$\Gamma_6$	$\Gamma_5$	$\Gamma_1$
$\Gamma_5$	$\Gamma_5$	$\Gamma_{12}$	$\Gamma_9$	$\Gamma_2$	$\Gamma_{11}$	$\Gamma_7$	$\Gamma_1$	$\Gamma_6$	$\Gamma_4$		$\Gamma_6$	$\Gamma_{11}$	$\Gamma_8$	$\Gamma_5$	$\Gamma_4$	$\Gamma_2$
$\Gamma_6$	$\Gamma_6$	$\Gamma_{11}$	$\Gamma_8$	$\Gamma_1$	$\Gamma_{10}$	$\Gamma_9$	$\Gamma_3$	$\Gamma_4$	$\Gamma_5$		$\Gamma_5$	$\Gamma_{12}$	$\Gamma_9$	$\Gamma_4$	$\Gamma_6$	$\Gamma_3$
$\Gamma_7$	$\Gamma_7$	$\Gamma_4$	$\Gamma_{10}$	$\Gamma_9$	$\Gamma_8$	$\Gamma_1$	$\Gamma_5$	$\Gamma_{11}$	$\Gamma_3$		$\Gamma_{10}$	$\Gamma_7$	$\Gamma_4$	$\Gamma_9$	$\Gamma_2$	$\Gamma_8$
$\Gamma_8$	$\Gamma_8$	$\Gamma_6$	$\Gamma_{11}$	$\Gamma_7$	$\Gamma_9$	$\Gamma_2$	$\Gamma_4$	$\Gamma_{12}$	$\Gamma_1$		$\Gamma_{12}$	$\Gamma_9$	$\Gamma_5$	$\Gamma_8$	$\Gamma_1$	$\Gamma_7$
$\Gamma_9$	$\Gamma_9$	$\Gamma_5$	$\Gamma_{12}$	$\Gamma_8$	$\Gamma_7$	$\Gamma_3$	$\Gamma_6$	$\Gamma_{10}$	$\Gamma_2$		$\Gamma_{11}$	$\Gamma_8$	$\Gamma_6$	$\Gamma_7$	$\Gamma_3$	$\Gamma_9$
$\Gamma_{10}$	$\Gamma_{10}$	$\Gamma_7$	$\Gamma_4$	$\Gamma_6$	$\Gamma_1$	$\Gamma_{12}$	$\Gamma_{11}$	$\Gamma_2$	$\Gamma_9$		$\Gamma_7$	$\Gamma_4$	$\Gamma_{10}$	$\Gamma_3$	$\Gamma_{11}$	$\Gamma_{12}$
$\Gamma_{11}$	$\Gamma_{11}$	$\Gamma_8$	$\Gamma_6$	$\Gamma_5$	$\Gamma_2$	$\Gamma_{10}$	$\Gamma_{12}$	$\Gamma_3$	$\Gamma_7$		$\Gamma_9$	$\Gamma_5$	$\Gamma_{12}$	$\Gamma_2$	$\Gamma_{10}$	$\Gamma_{11}$
$\Gamma_{12}$	$\Gamma_{12}$	$\Gamma_9$	$\Gamma_5$	$\Gamma_4$	$\Gamma_3$	$\Gamma_{11}$	$\Gamma_{10}$	$\Gamma_1$	$\Gamma_8$		$\Gamma_8$	$\Gamma_6$	$\Gamma_{11}$	$\Gamma_1$	$\Gamma_{12}$	$\Gamma_{10}$
$\alpha_1$	$\alpha_1$	$\alpha_3$	$\alpha_2$	$\alpha_{14}$	$\alpha_6$	$\alpha_5$	$\alpha_9$	$\alpha_{10}$	$\alpha_{15}$		$\alpha_3$	$\alpha_2$	$\alpha_1$	$\alpha_{16}$	$\alpha_9$	$\alpha_5$
$\alpha_2$	$\alpha_2$	$\alpha_1$	$\alpha_3$	$\alpha_{16}$	$\alpha_5$	$\alpha_7$	$\alpha_{10}$	$\alpha_{11}$	$\alpha_{14}$		$\alpha_2$	$\alpha_1$	$\alpha_3$	$\alpha_{14}$	$\alpha_{11}$	$\alpha_6$
$\alpha_3$	$\alpha_3$	$\alpha_2$	$\alpha_1$	$\alpha_{15}$	$\alpha_7$	$\alpha_6$	$\alpha_{11}$	$\alpha_9$	$\alpha_{16}$		$\alpha_1$	$\alpha_3$	$\alpha_2$	$\alpha_{15}$	$\alpha_{10}$	$\alpha_7$
$\alpha_4$	$\alpha_4$	$\alpha_{18}$	$\alpha_8$	$\alpha_{18}$	$\alpha_{17}$	$\alpha_{12}$	$\alpha_8$	$\alpha_{12}$	$\alpha_{17}$		$\alpha_4$	$\alpha_{18}$	$\alpha_8$	$\alpha_{17}$	$\alpha_{12}$	$\alpha_4$
$\alpha_5$	$\alpha_5$	$\alpha_{15}$	$\alpha_{11}$	$\alpha_2$	$\alpha_{16}$	$\alpha_9$	$\alpha_1$	$\alpha_6$	$\alpha_7$		$\alpha_7$	$\alpha_{14}$	$\alpha_9$	$\alpha_6$	$\alpha_5$	$\alpha_1$
$\alpha_6$	$\alpha_6$	$\alpha_{16}$	$\alpha_{10}$	$\alpha_1$	$\alpha_{14}$	$\alpha_{11}$	$\alpha_3$	$\alpha_7$	$\alpha_5$		$\alpha_6$	$\alpha_{16}$	$\alpha_{10}$	$\alpha_5$	$\alpha_7$	$\alpha_2$
$\alpha_7$	$\alpha_7$	$\alpha_{14}$	$\alpha_9$	$\alpha_3$	$\alpha_{15}$	$\alpha_{10}$	$\alpha_2$	$\alpha_5$	$\alpha_6$		$\alpha_5$	$\alpha_{15}$	$\alpha_{11}$	$\alpha_7$	$\alpha_6$	$\alpha_3$
$\alpha_8$	$\alpha_8$	$\alpha_4$	$\alpha_{18}$	$\alpha_{13}$	$\alpha_{12}$	$\alpha_4$	$\alpha_{12}$	$\alpha_{13}$	$\alpha_{18}$		$\alpha_{18}$	$\alpha_8$	$\alpha_4$	$\alpha_{13}$	$\alpha_8$	$\alpha_{12}$
$\alpha_9$	$\alpha_9$	$\alpha_7$	$\alpha_{14}$	$\alpha_{11}$	$\alpha_{10}$	$\alpha_1$	$\alpha_5$	$\alpha_{16}$	$\alpha_3$		$\alpha_{15}$	$\alpha_{11}$	$\alpha_5$	$\alpha_{10}$	$\alpha_1$	$\alpha_9$
$\alpha_{10}$	$\alpha_{10}$	$\alpha_6$	$\alpha_{16}$	$\alpha_9$	$\alpha_{11}$	$\alpha_2$	$\alpha_7$	$\alpha_{15}$	$\alpha_1$		$\alpha_{16}$	$\alpha_{10}$	$\alpha_6$	$\alpha_9$	$\alpha_3$	$\alpha_{11}$
$\alpha_{11}$	$\alpha_{11}$	$\alpha_5$	$\alpha_{15}$	$\alpha_{10}$	$\alpha_9$	$\alpha_3$	$\alpha_6$	$\alpha_{14}$	$\alpha_2$		$\alpha_{14}$	$\alpha_9$	$\alpha_7$	$\alpha_{11}$	$\alpha_2$	$\alpha_{10}$
$\alpha_{12}$	$\alpha_{12}$	$\alpha_{17}$	$\alpha_{13}$	$\alpha_8$	$\alpha_{13}$	$\alpha_8$	$\alpha_4$	$\alpha_{17}$	$\alpha_4$		$\alpha_{17}$	$\alpha_{13}$	$\alpha_{12}$	$\alpha_{12}$	$\alpha_4$	$\alpha_8$
$\alpha_{13}$	$\alpha_{13}$	$\alpha_{12}$	$\alpha_{17}$	$\alpha_{12}$	$\alpha_8$	$\alpha_{18}$	$\alpha_{17}$	$\alpha_{18}$	$\alpha_8$		$\alpha_{13}$	$\alpha_{12}$	$\alpha_{17}$	$\alpha_8$	$\alpha_{18}$	$\alpha_{13}$
$\alpha_{14}$	$\alpha_{14}$	$\alpha_9$	$\alpha_7$	$\alpha_6$	$\alpha_1$	$\alpha_{15}$	$\alpha_{16}$	$\alpha_2$	$\alpha_{11}$		$\alpha_{11}$	$\alpha_5$	$\alpha_{15}$	$\alpha_2$	$\alpha_{14}$	$\alpha_{16}$
$\alpha_{15}$	$\alpha_{15}$	$\alpha_{11}$	$\alpha_5$	$\alpha_7$	$\alpha_3$	$\alpha_{16}$	$\alpha_{14}$	$\alpha_1$	$\alpha_{10}$		$\alpha_9$	$\alpha_7$	$\alpha_{14}$	$\alpha_3$	$\alpha_{16}$	$\alpha_{15}$
$\alpha_{16}$	$\alpha_{16}$	$\alpha_{10}$	$\alpha_6$	$\alpha_5$	$\alpha_2$	$\alpha_{14}$	$\alpha_{15}$	$\alpha_3$	$\alpha_9$		$\alpha_{10}$	$\alpha_6$	$\alpha_{16}$	$\alpha_1$	$\alpha_{15}$	$\alpha_{14}$
$\alpha_{17}$	$\alpha_{17}$	$\alpha_{13}$	$\alpha_{12}$	$\alpha_4$	$\alpha_{18}$	$\alpha_{13}$	$\alpha_{18}$	$\alpha_4$	$\alpha_{12}$		$\alpha_{12}$	$\alpha_{17}$	$\alpha_{13}$	$\alpha_4$	$\alpha_{17}$	$\alpha_{18}$
$\alpha_{18}$	$\alpha_{18}$	$\alpha_8$	$\alpha_4$	$\alpha_{17}$	$\alpha_4$	$\alpha_{17}$	$\alpha_{13}$	$\alpha_8$	$\alpha_{13}$		$\alpha_8$	$\alpha_4$	$\alpha_{18}$	$\alpha_{18}$	$\alpha_{13}$	$\alpha_{17}$



Table 4.17 The result of the of the improper rotation operations working on the internal coordinates of the Mn model compound.

	E	S <sub>4</sub>	C <sub>2</sub>	S <sub>4</sub> <sup>2</sup>	S <sub>4</sub> <sup>1</sup>	C <sub>2</sub> <sup>1</sup>	S <sub>4</sub> <sup>21</sup>	S <sub>4</sub> <sup>11</sup>	C <sub>2</sub> <sup>11</sup>	S <sub>4</sub> <sup>211</sup>
r <sub>1</sub>	r <sub>1</sub>	r <sub>9</sub>	r <sub>4</sub>	r <sub>11</sub>	r <sub>10</sub>	r <sub>9</sub>	r <sub>5</sub>	r <sub>6</sub>	r <sub>11</sub>	r <sub>7</sub>
r <sub>2</sub>	r <sub>2</sub>	r <sub>8</sub>	r <sub>6</sub>	r <sub>10</sub>	r <sub>12</sub>	r <sub>7</sub>	r <sub>6</sub>	r <sub>4</sub>	r <sub>12</sub>	r <sub>9</sub>
r <sub>3</sub>	r <sub>3</sub>	r <sub>7</sub>	r <sub>5</sub>	r <sub>12</sub>	r <sub>11</sub>	r <sub>8</sub>	r <sub>4</sub>	r <sub>5</sub>	r <sub>10</sub>	r <sub>8</sub>
r <sub>4</sub>	r <sub>4</sub>	r <sub>11</sub>	r <sub>1</sub>	r <sub>9</sub>	r <sub>3</sub>	r <sub>11</sub>	r <sub>8</sub>	r <sub>12</sub>	r <sub>9</sub>	r <sub>2</sub>
r <sub>5</sub>	r <sub>5</sub>	r <sub>12</sub>	r <sub>3</sub>	r <sub>7</sub>	r <sub>1</sub>	r <sub>10</sub>	r <sub>9</sub>	r <sub>10</sub>	r <sub>8</sub>	r <sub>3</sub>
r <sub>6</sub>	r <sub>6</sub>	r <sub>10</sub>	r <sub>2</sub>	r <sub>8</sub>	r <sub>2</sub>	r <sub>12</sub>	r <sub>7</sub>	r <sub>11</sub>	r <sub>7</sub>	r <sub>1</sub>
r <sub>7</sub>	r <sub>7</sub>	r <sub>5</sub>	r <sub>12</sub>	r <sub>3</sub>	r <sub>6</sub>	r <sub>2</sub>	r <sub>12</sub>	r <sub>1</sub>	r <sub>6</sub>	r <sub>11</sub>
r <sub>8</sub>	r <sub>8</sub>	r <sub>6</sub>	r <sub>10</sub>	r <sub>2</sub>	r <sub>4</sub>	r <sub>3</sub>	r <sub>11</sub>	r <sub>3</sub>	r <sub>5</sub>	r <sub>10</sub>
r <sub>9</sub>	r <sub>9</sub>	r <sub>4</sub>	r <sub>11</sub>	r <sub>1</sub>	r <sub>5</sub>	r <sub>1</sub>	r <sub>10</sub>	r <sub>2</sub>	r <sub>4</sub>	r <sub>12</sub>
r <sub>10</sub>	r <sub>10</sub>	r <sub>2</sub>	r <sub>8</sub>	r <sub>6</sub>	r <sub>9</sub>	r <sub>5</sub>	r <sub>1</sub>	r <sub>8</sub>	r <sub>3</sub>	r <sub>5</sub>
r <sub>11</sub>	r <sub>11</sub>	r <sub>1</sub>	r <sub>9</sub>	r <sub>4</sub>	r <sub>8</sub>	r <sub>4</sub>	r <sub>3</sub>	r <sub>7</sub>	r <sub>1</sub>	r <sub>6</sub>
r <sub>12</sub>	r <sub>12</sub>	r <sub>3</sub>	r <sub>7</sub>	r <sub>5</sub>	r <sub>7</sub>	r <sub>6</sub>	r <sub>2</sub>	r <sub>9</sub>	r <sub>2</sub>	r <sub>4</sub>
α <sub>1</sub>	α <sub>1</sub>	α <sub>10</sub>	α <sub>7</sub>	α <sub>14</sub>	α <sub>15</sub>	α <sub>11</sub>	α <sub>6</sub>	α <sub>7</sub>	α <sub>16</sub>	α <sub>11</sub>
α <sub>2</sub>	α <sub>2</sub>	α <sub>9</sub>	α <sub>6</sub>	α <sub>15</sub>	α <sub>16</sub>	α <sub>9</sub>	α <sub>7</sub>	α <sub>5</sub>	α <sub>15</sub>	α <sub>10</sub>
α <sub>3</sub>	α <sub>3</sub>	α <sub>11</sub>	α <sub>5</sub>	α <sub>16</sub>	α <sub>14</sub>	α <sub>10</sub>	α <sub>5</sub>	α <sub>6</sub>	α <sub>14</sub>	α <sub>9</sub>
α <sub>4</sub>	α <sub>4</sub>	α <sub>13</sub>	α <sub>4</sub>	α <sub>13</sub>	α <sub>18</sub>	α <sub>13</sub>	α <sub>12</sub>	α <sub>17</sub>	α <sub>13</sub>	α <sub>8</sub>
α <sub>5</sub>	α <sub>5</sub>	α <sub>16</sub>	α <sub>3</sub>	α <sub>11</sub>	α <sub>3</sub>	α <sub>14</sub>	α <sub>10</sub>	α <sub>15</sub>	α <sub>10</sub>	α <sub>2</sub>
α <sub>6</sub>	α <sub>6</sub>	α <sub>15</sub>	α <sub>2</sub>	α <sub>9</sub>	α <sub>1</sub>	α <sub>15</sub>	α <sub>11</sub>	α <sub>14</sub>	α <sub>9</sub>	α <sub>3</sub>
α <sub>7</sub>	α <sub>7</sub>	α <sub>14</sub>	α <sub>1</sub>	α <sub>10</sub>	α <sub>2</sub>	α <sub>16</sub>	α <sub>9</sub>	α <sub>16</sub>	α <sub>11</sub>	α <sub>1</sub>
α <sub>8</sub>	α <sub>8</sub>	α <sub>12</sub>	α <sub>17</sub>	α <sub>18</sub>	α <sub>17</sub>	α <sub>8</sub>	α <sub>17</sub>	α <sub>4</sub>	α <sub>17</sub>	α <sub>13</sub>
α <sub>9</sub>	α <sub>9</sub>	α <sub>6</sub>	α <sub>15</sub>	α <sub>2</sub>	α <sub>7</sub>	α <sub>2</sub>	α <sub>16</sub>	α <sub>3</sub>	α <sub>6</sub>	α <sub>14</sub>
α <sub>10</sub>	α <sub>10</sub>	α <sub>7</sub>	α <sub>14</sub>	α <sub>1</sub>	α <sub>5</sub>	α <sub>3</sub>	α <sub>14</sub>	α <sub>2</sub>	α <sub>5</sub>	α <sub>15</sub>
α <sub>11</sub>	α <sub>11</sub>	α <sub>5</sub>	α <sub>16</sub>	α <sub>3</sub>	α <sub>6</sub>	α <sub>1</sub>	α <sub>15</sub>	α <sub>1</sub>	α <sub>7</sub>	α <sub>16</sub>
α <sub>12</sub>	α <sub>12</sub>	α <sub>17</sub>	α <sub>18</sub>	α <sub>8</sub>	α <sub>4</sub>	α <sub>18</sub>	α <sub>13</sub>	α <sub>18</sub>	α <sub>12</sub>	α <sub>18</sub>
α <sub>13</sub>	α <sub>13</sub>	α <sub>4</sub>	α <sub>13</sub>	α <sub>4</sub>	α <sub>12</sub>	α <sub>4</sub>	α <sub>18</sub>	α <sub>8</sub>	α <sub>4</sub>	α <sub>17</sub>
α <sub>14</sub>	α <sub>14</sub>	α <sub>1</sub>	α <sub>10</sub>	α <sub>7</sub>	α <sub>10</sub>	α <sub>5</sub>	α <sub>3</sub>	α <sub>9</sub>	α <sub>3</sub>	α <sub>6</sub>
α <sub>15</sub>	α <sub>15</sub>	α <sub>2</sub>	α <sub>9</sub>	α <sub>6</sub>	α <sub>11</sub>	α <sub>6</sub>	α <sub>1</sub>	α <sub>10</sub>	α <sub>2</sub>	α <sub>5</sub>
α <sub>16</sub>	α <sub>16</sub>	α <sub>3</sub>	α <sub>11</sub>	α <sub>5</sub>	α <sub>9</sub>	α <sub>7</sub>	α <sub>2</sub>	α <sub>11</sub>	α <sub>1</sub>	α <sub>7</sub>
α <sub>17</sub>	α <sub>17</sub>	α <sub>18</sub>	α <sub>8</sub>	α <sub>12</sub>	α <sub>8</sub>	α <sub>17</sub>	α <sub>8</sub>	α <sub>13</sub>	α <sub>8</sub>	α <sub>4</sub>
α <sub>18</sub>	α <sub>18</sub>	α <sub>8</sub>	α <sub>12</sub>	α <sub>17</sub>	α <sub>13</sub>	α <sub>12</sub>	α <sub>4</sub>	α <sub>12</sub>	α <sub>18</sub>	α <sub>12</sub>

The  $U$ -matrix now can be derived from Eq. 4.7, the information in Table 4.16 and 4.17, and the  $T_d$  character table. The result of this procedure does not always give orthogonal symmetry coordinates for the degenerate vibrational modes, such as for the E,  $T_1$  and  $T_2$  symmetry representations. However, the orthogonal symmetry coordinates can be found by making linear combinations of the non-orthogonal symmetry coordinates. Table 4.18 and 4.19 give the orthogonalized symmetry coordinates for the stretching and bending modes, respectively. Table 4.18 and 4.19 show that the  $A_1$ , E, and  $T_2$  symmetry representations have three, six, and fifteen vibrational modes, respectively. However, based on symmetry considerations only two, four, and twelve vibrational modes are anticipated for the  $A_1$ , E, and  $T_2$  symmetry representations, respectively. Therefore, one redundant condition applies to the  $A_1$  symmetry representation, and two and three for the E and  $T_2$  symmetry representations, respectively.

Table 4.18 The orthogonalized symmetry bond displacement coordinates of the adamantane-like compound for the various symmetry representations, assuming the  $T_d$  symmetry.  $N$  is the normalization factor of the symmetry internal coordinates.

N	A	E		T <sub>1</sub>			T <sub>2</sub>					
	$\frac{1}{2\sqrt{3}}$	$\frac{1}{2\sqrt{6}}$	$\frac{1}{2\sqrt{2}}$	$\frac{1}{4}$	$\frac{1}{4\sqrt{3}}$	$\frac{1}{\sqrt{6}}$	$\frac{1}{4\sqrt{2}}$	$\frac{1}{4\sqrt{2}}$	$\frac{1}{4}$	$\frac{1}{2\sqrt{6}}$	$\frac{1}{2\sqrt{3}}$	$\frac{1}{2}$
$\Delta r_1$	1	2	0	2	0	0	4	0	0	0	0	0
$\Delta r_2$	1	-1	1	-1	3	0	1	-1	-1	3	0	0
$\Delta r_3$	1	-1	-1	-1	-3	0	1	-1	1	1	-1	-1
$\Delta r_4$	1	2	0	-2	0	0	0	4	0	0	0	0
$\Delta r_5$	1	-1	-1	1	-1	1	-1	1	-1	1	-1	1
$\Delta r_6$	1	-1	1	1	1	-1	-1	1	1	-1	-2	0
$\Delta r_7$	1	-1	1	1	-3	0	-1	1	1	1	2	0
$\Delta r_8$	1	-1	-1	-1	1	-1	1	-1	1	-1	1	1
$\Delta r_9$	1	2	0	0	2	1	-2	-2	2	0	0	0
$\Delta r_{10}$	1	-1	-1	1	3	0	-1	1	-1	-1	1	-1
$\Delta r_{11}$	1	2	0	0	-2	-1	-2	-2	-2	0	0	0
$\Delta r_{12}$	1	-1	1	-1	-1	1	1	-1	-1	-3	0	0
$\Delta \alpha_x$	0	0	0	0	0	0	0	0	0	0	0	0

Table 4.19 The orthogonalized symmetry angle displacement coordinates of the adamantane-like compound for the various symmetry representations, assuming the  $T_d$  symmetry.  $N$  is the normalization factor of the symmetry internal coordinates.

N	A		E				$T_1$			$T_2$								
	$\frac{1}{2\sqrt{3}}$	$\frac{1}{\sqrt{6}}$	$\frac{1}{2\sqrt{6}}$	$\frac{1}{2\sqrt{3}}$	$\frac{1}{2}$	$\frac{1}{2\sqrt{2}}$	$\frac{1}{4}$	$\frac{1}{4\sqrt{3}}$	$\frac{1}{\sqrt{6}}$	$\frac{1}{4\sqrt{2}}$	$\frac{1}{4\sqrt{2}}$	$\frac{1}{4}$	$\frac{1}{2\sqrt{6}}$	$\frac{1}{2\sqrt{3}}$	$\frac{1}{2}$	$\frac{1}{\sqrt{2}}$	$\frac{1}{\sqrt{2}}$	$\frac{1}{\sqrt{2}}$
$\Delta r_x$	0	0	0	0	0	0	0	0	0	0	0	0	0	0	0	0	0	0
$\Delta\alpha_1$	1	0	2	0	0	0	2	0	0	4	0	0	0	0	0	0	0	0
$\Delta\alpha_2$	1	0	-1	0	0	1	-1	3	0	1	-1	-1	1	2	0	0	0	0
$\Delta\alpha_3$	1	0	-1	0	0	-1	-1	-3	0	1	-1	1	-1	1	1	0	0	0
$\Delta\alpha_4$	0	1	0	2	0	0	0	0	0	0	0	0	0	0	0	1	0	0
$\Delta\alpha_5$	1	0	-1	0	0	-1	-1	1	1	1	-1	1	1	-1	-1	0	0	0
$\Delta\alpha_6$	1	0	-1	0	0	1	1	-3	0	-1	1	1	3	0	0	0	0	0
$\Delta\alpha_7$	1	0	2	0	0	0	0	2	-1	-2	-2	2	0	0	0	0	0	0
$\Delta\alpha_8$	0	1	0	-1	1	0	0	0	0	0	0	0	0	0	0	0	1	0
$\Delta\alpha_9$	1	0	-1	0	0	1	-1	-1	-1	1	-1	-1	-1	-2	0	0	0	0
$\Delta\alpha_{10}$	1	0	-1	0	0	-1	1	3	0	-1	1	-1	1	-1	1	0	0	0
$\Delta\alpha_{11}$	1	0	2	0	0	0	0	-2	1	2	-2	-2	0	0	0	0	0	0
$\Delta\alpha_{12}$	0	1	0	-1	-1	0	0	0	0	0	0	0	0	0	0	0	0	1
$\Delta\alpha_{13}$	0	1	0	2	0	0	0	0	0	0	0	0	0	0	0	-1	0	0
$\Delta\alpha_{14}$	1	0	-1	0	0	-1	1	-1	-1	-1	1	-1	-1	1	-1	0	0	0
$\Delta\alpha_{15}$	1	0	-1	0	0	1	1	1	1	-1	1	1	-3	0	0	0	0	0
$\Delta\alpha_{16}$	1	0	2	0	0	0	-2	0	0	0	4	0	0	0	0	0	0	0
$\Delta\alpha_{17}$	0	1	0	-1	1	0	0	0	0	0	0	0	0	0	0	0	-1	0
$\Delta\alpha_{18}$	0	1	0	-1	-1	0	0	0	0	0	0	0	0	0	0	0	0	-1

Not only can the  $T_d$  symmetry be used to reduce the  $F$  and  $G$  matrices into smaller sub-matrices, but it also can be used to reduce the number of variables in  $F$  and  $G$  matrices. The 465 force constants in the  $F$ -matrix can be reduced to 30 constants when the  $T_d$  symmetry is applied.

Chapter 4

For the  $T_d$  symmetry all bonds are equivalent. Therefore the 12 stretch force constant are also equivalent and can be reduced to 1 constant.

$$f_{r1} \equiv \{f_{r2}, f_{r3}, f_{r4}, f_{r5}, f_{r6}, f_{r7}, f_{r8}, f_{r9}, f_{r10}, f_{r11}, f_{r12}\}$$

The 66 stretch-stretch coupling force constant can be reduced to 5 constants.

$$f_{r1r2} \equiv \{f_{r2r3}, f_{r1r3}, f_{r4r5}, f_{4r6}, f_{r5r6}, f_{r7r8}, f_{r7r9}, f_{r8r9}, f_{r10r11}, f_{r10r12}, f_{r11r12}\}$$

$$f_{r1r4} \equiv \{f_{r2r7}, f_{r3r10}, f_{r5r8}, f_{r6r12}, f_{r9r11}\}$$

$$f_{r1r5} \equiv \{f_{r1r6}, f_{r1r7}, f_{r1r10}, f_{r2r4}, f_{r2r8}, f_{r2r9}, f_{r2r10}, f_{r3r4}, f_{r3r7}, f_{r3r11}, f_{r3r12}, f_{r4r8}, f_{r4r12}, f_{r5r7}, f_{r5r9}, f_{r5r12}, f_{r6r8}, f_{r6r10}, f_{r6r11}, f_{r7r11}, f_{r8r11}, f_{r9r10}, f_{r9r12}\}$$

$$f_{r1r8} \equiv \{f_{r1r12}, f_{r2r5}, f_{r2r11}, f_{r3r6}, f_{r3r9}, f_{r4r7}, f_{r4r10}, f_{r5r11}, f_{r6r9}, f_{r7r10}, f_{r8r12}\}$$

$$f_{r1r9} \equiv \{f_{r1r11}, f_{r2r6}, f_{r2r12}, f_{r3r5}, f_{r3r8}, f_{r4r9}, f_{r4r11}, f_{r5r10}, f_{r6r7}, f_{r7r12}, f_{r8r10}\}$$

The 18 bending force constant can be reduced to 2 constants.

$$f_{\alpha1} \equiv \{f_{\alpha2}, f_{\alpha3}, f_{\alpha4}, f_{\alpha5}, f_{\alpha6}, f_{\alpha7}, f_{\alpha9}, f_{\alpha10}, f_{\alpha11}, f_{\alpha14}, f_{\alpha15}, f_{\alpha16}\}$$

$$f_{\alpha4} \equiv \{f_{\alpha8}, f_{\alpha11}, f_{\alpha12}, f_{\alpha17}, f_{\alpha18}\}$$

The 153 bend-bend coupling force constant can be reduced to 11 constants.

$$f_{\alpha1\alpha2} \equiv \{f_{\alpha1\alpha3}, f_{\alpha2\alpha3}, f_{\alpha5\alpha6}, f_{\alpha5\alpha7}, f_{\alpha6\alpha7}, f_{\alpha9\alpha10}, f_{\alpha9\alpha11}, f_{\alpha10\alpha11}, f_{\alpha14\alpha15}, f_{\alpha14\alpha16}, f_{\alpha15\alpha16}\}$$

$$f_{\alpha1\alpha4} \equiv \{f_{\alpha1\alpha8}, f_{\alpha2\alpha8}, f_{\alpha2\alpha18}, f_{\alpha3\alpha4}, f_{\alpha3\alpha18}, f_{\alpha4\alpha5}, f_{\alpha5\alpha12}, f_{\alpha6\alpha12}, f_{\alpha6\alpha17}, f_{\alpha4\alpha7}, f_{\alpha7\alpha17}, f_{\alpha8\alpha9}, f_{\alpha9\alpha12}, f_{\alpha10\alpha12},$$

$$f_{\alpha10\alpha13}, f_{\alpha8\alpha11}, f_{\alpha11\alpha13}, f_{\alpha13\alpha14}, f_{\alpha14\alpha18}, f_{\alpha15\alpha17}, f_{\alpha15\alpha18}, f_{\alpha13\alpha16}, f_{\alpha16\alpha17}\}$$

$$f_{\alpha1\alpha5} \equiv \{f_{\alpha1\alpha9}, f_{\alpha2\alpha11}, f_{\alpha2\alpha14}, f_{\alpha3\alpha7}, f_{\alpha3\alpha15}, f_{\alpha5\alpha9}, f_{\alpha6\alpha10}, f_{\alpha6\alpha16}, f_{\alpha7\alpha15}, f_{\alpha10\alpha16}, f_{\alpha11\alpha14}\}$$

$$f_{\alpha1\alpha6} \equiv \{f_{\alpha1\alpha10}, f_{\alpha1\alpha14}, f_{\alpha1\alpha15}, f_{\alpha2\alpha5}, f_{\alpha2\alpha7}, f_{\alpha2\alpha10}, f_{\alpha2\alpha16}, f_{\alpha3\alpha6}, f_{\alpha3\alpha9}, f_{\alpha3\alpha11}, f_{\alpha3\alpha16}, f_{\alpha5\alpha11}, f_{\alpha5\alpha15}, f_{\alpha5\alpha16},$$

$$f_{\alpha6\alpha11}, f_{\alpha6\alpha14}, f_{\alpha7\alpha14}, f_{\alpha7\alpha9}, f_{\alpha7\alpha10}, f_{\alpha9\alpha14}, f_{\alpha9\alpha16}, f_{\alpha10\alpha15}, f_{\alpha11\alpha15}\}$$

$$f_{\alpha1\alpha7} \equiv \{f_{\alpha1\alpha11}, f_{\alpha2\alpha9}, f_{\alpha2\alpha15}, f_{\alpha3\alpha5}, f_{\alpha3\alpha14}, f_{\alpha5\alpha10}, f_{\alpha6\alpha9}, f_{\alpha6\alpha15}, f_{\alpha7\alpha16}, f_{\alpha10\alpha14}, f_{\alpha11\alpha16}\}$$

$$f_{\alpha1\alpha12} \equiv \{f_{\alpha2\alpha13}, f_{\alpha3\alpha17}, f_{\alpha5\alpha8}, f_{\alpha6\alpha13}, f_{\alpha7\alpha18}, f_{\alpha4\alpha9}, f_{\alpha10\alpha17}, f_{\alpha11\alpha18}, f_{\alpha8\alpha14}, f_{\alpha4\alpha15}, f_{\alpha12\alpha16}\}$$

$$\begin{aligned}
f_{\alpha 1 \alpha 13} &\equiv \{f_{\alpha 1 \alpha 17}, f_{\alpha 2 \alpha 12}, f_{\alpha 2 \alpha 17}, f_{\alpha 3 \alpha 12}, f_{\alpha 2 \alpha 13}, f_{\alpha 5 \alpha 13}, f_{\alpha 5 \alpha 18}, f_{\alpha 6 \alpha 8}, f_{\alpha 6 \alpha 18}, f_{\alpha 7 \alpha 8}, f_{\alpha 7 \alpha 13}, f_{\alpha 9 \alpha 17}, f_{\alpha 9 \alpha 18}, \\
&f_{\alpha 4 \alpha 10}, f_{\alpha 10 \alpha 18}, f_{\alpha 4 \alpha 11}, f_{\alpha 11 \alpha 17}, f_{\alpha 4 \alpha 14}, f_{\alpha 12 \alpha 14}, f_{\alpha 8 \alpha 15}, f_{\alpha 12 \alpha 15}, f_{\alpha 4 \alpha 16}, f_{\alpha 8 \alpha 16}\} \\
f_{\alpha 1 \alpha 16} &\equiv \{f_{\alpha 2 \alpha 6}, f_{\alpha 3 \alpha 10}, f_{\alpha 5 \alpha 14}, f_{\alpha 7 \alpha 11}, f_{\alpha 9 \alpha 15}\} \\
f_{\alpha 1 \alpha 18} &\equiv \{f_{\alpha 2 \alpha 4}, f_{\alpha 3 \alpha 8}, f_{\alpha 5 \alpha 17}, f_{\alpha 4 \alpha 6}, f_{\alpha 7 \alpha 12}, f_{\alpha 9 \alpha 13}, f_{\alpha 8 \alpha 10}, f_{\alpha 11 \alpha 12}, f_{\alpha 14 \alpha 17}, f_{\alpha 13 \alpha 15}, f_{\alpha 16 \alpha 18}\} \\
f_{\alpha 4 \alpha 8} &\equiv \{f_{\alpha 4 \alpha 12}, f_{\alpha 4 \alpha 17}, f_{\alpha 4 \alpha 18}, f_{\alpha 8 \alpha 12}, f_{\alpha 8 \alpha 13}, f_{\alpha 8 \alpha 18}, f_{\alpha 12 \alpha 13}, f_{\alpha 12 \alpha 17}, f_{\alpha 13 \alpha 17}, f_{\alpha 13 \alpha 18}, f_{\alpha 17 \alpha 18}\} \\
f_{\alpha 4 \alpha 13} &\equiv \{f_{\alpha 8 \alpha 17}, f_{\alpha 12 \alpha 18}\}
\end{aligned}$$

The 216 stretch-bend coupling force constant can be reduced to 11 constants.

$$\begin{aligned}
f_{r 1 \alpha 1} &\equiv \{f_{r 1 \alpha 3}, f_{r 2 \alpha 1}, f_{r 2 \alpha 2}, f_{r 3 \alpha 2}, f_{r 3 \alpha 3}, f_{r 4 \alpha 5}, f_{r 4 \alpha 7}, f_{r 5 \alpha 5}, f_{r 5 \alpha 6}, f_{r 6 \alpha 6}, f_{r 6 \alpha 7}, f_{r 7 \alpha 9}, f_{r 7 \alpha 11}, f_{r 8 \alpha 9}, f_{r 8 \alpha 10}, f_{r 9 \alpha 10}, \\
&f_{r 9 \alpha 11}, f_{r 10 \alpha 14}, f_{r 10 \alpha 15}, f_{r 11 \alpha 14}, f_{r 11 \alpha 16}, f_{r 12 \alpha 15}, f_{r 12 \alpha 16}\} \\
f_{r 1 \alpha 2} &\equiv \{f_{r 2 \alpha 3}, f_{r 3 \alpha 1}, f_{r 4 \alpha 6}, f_{r 5 \alpha 7}, f_{r 6 \alpha 5}, f_{r 7 \alpha 10}, f_{r 8 \alpha 11}, f_{r 9 \alpha 9}, f_{r 10 \alpha 16}, f_{r 11 \alpha 15}, f_{r 12 \alpha 14}\} \\
f_{r 1 \alpha 4} &\equiv \{f_{r 2 \alpha 8}, f_{r 3 \alpha 18}, f_{r 4 \alpha 4}, f_{r 5 \alpha 12}, f_{r 6 \alpha 17}, f_{r 7 \alpha 8}, f_{r 8 \alpha 12}, f_{r 9 \alpha 13}, f_{r 10 \alpha 18}, f_{r 11 \alpha 13}, f_{r 12 \alpha 17}\} \\
f_{r 1 \alpha 5} &\equiv \{f_{r 1 \alpha 7}, f_{r 2 \alpha 9}, f_{r 2 \alpha 11}, f_{r 3 \alpha 14}, f_{r 3 \alpha 15}, f_{r 4 \alpha 1}, f_{r 4 \alpha 3}, f_{r 5 \alpha 9}, f_{r 5 \alpha 10}, f_{r 6 \alpha 15}, f_{r 6 \alpha 16}, f_{r 7 \alpha 1}, f_{r 7 \alpha 2}, f_{r 8 \alpha 5}, f_{r 8 \alpha 6}, \\
&f_{r 9 \alpha 14}, f_{r 9 \alpha 16}, f_{r 10 \alpha 2}, f_{r 10 \alpha 3}, f_{r 11 \alpha 10}, f_{r 11 \alpha 11}, f_{r 12 \alpha 6}, f_{r 12 \alpha 7}\} \\
f_{r 1 \alpha 6} &\equiv \{f_{r 2 \alpha 10}, f_{r 3 \alpha 16}, f_{r 4 \alpha 2}, f_{r 5 \alpha 11}, f_{r 6 \alpha 14}, f_{r 7 \alpha 3}, f_{r 8 \alpha 7}, f_{r 9 \alpha 15}, f_{r 10 \alpha 1}, f_{r 11 \alpha 9}, f_{r 12 \alpha 5}\} \\
f_{r 1 \alpha 8} &\equiv \{f_{r 1 \alpha 18}, f_{r 2 \alpha 4}, f_{r 2 \alpha 18}, f_{r 3 \alpha 4}, f_{r 3 \alpha 8}, f_{r 4 \alpha 12}, f_{r 4 \alpha 17}, f_{r 5 \alpha 4}, f_{r 5 \alpha 17}, f_{r 6 \alpha 4}, f_{r 6 \alpha 12}, f_{r 7 \alpha 12}, f_{r 7 \alpha 13}, f_{r 8 \alpha 8}, f_{r 8 \alpha 13}, \\
&f_{r 9 \alpha 8}, f_{r 9 \alpha 12}, f_{r 10 \alpha 13}, f_{r 10 \alpha 17}, f_{r 11 \alpha 17}, f_{r 11 \alpha 18}, f_{r 12 \alpha 13}, f_{r 12 \alpha 18}\} \\
f_{r 1 \alpha 9} &\equiv \{f_{r 1 \alpha 15}, f_{r 2 \alpha 5}, f_{r 2 \alpha 14}, f_{r 3 \alpha 7}, f_{r 3 \alpha 11}, f_{r 4 \alpha 9}, f_{r 4 \alpha 15}, f_{r 5 \alpha 1}, f_{r 5 \alpha 16}, f_{r 6 \alpha 3}, f_{r 6 \alpha 10}, f_{r 7 \alpha 5}, f_{r 7 \alpha 14}, f_{r 8 \alpha 1}, f_{r 8 \alpha 16}, \\
&f_{r 9 \alpha 2}, f_{r 9 \alpha 6}, f_{r 10 \alpha 7}, f_{r 10 \alpha 11}, f_{r 11 \alpha 2}, f_{r 11 \alpha 6}, f_{r 12 \alpha 3}, f_{r 12 \alpha 10}\} \\
f_{r 1 \alpha 10} &\equiv \{f_{r 1 \alpha 16}, f_{r 2 \alpha 6}, f_{r 2 \alpha 16}, f_{r 3 \alpha 6}, f_{r 3 \alpha 10}, f_{r 4 \alpha 11}, f_{r 4 \alpha 14}, f_{r 5 \alpha 2}, f_{r 5 \alpha 14}, f_{r 6 \alpha 2}, f_{r 6 \alpha 11}, f_{r 7 \alpha 7}, f_{r 7 \alpha 15}, f_{r 8 \alpha 3}, f_{r 8 \alpha 15}, \\
&f_{r 9 \alpha 3}, f_{r 9 \alpha 7}, f_{r 10 \alpha 5}, f_{r 10 \alpha 9}, f_{r 11 \alpha 1}, f_{r 11 \alpha 5}, f_{r 12 \alpha 1}, f_{r 12 \alpha 9}\} \\
f_{r 1 \alpha 11} &\equiv \{f_{r 1 \alpha 14}, f_{r 2 \alpha 7}, f_{r 2 \alpha 15}, f_{r 3 \alpha 5}, f_{r 3 \alpha 9}, f_{r 4 \alpha 10}, f_{r 4 \alpha 16}, f_{r 5 \alpha 3}, f_{r 5 \alpha 15}, f_{r 6 \alpha 1}, f_{r 6 \alpha 9}, f_{r 7 \alpha 6}, f_{r 7 \alpha 16}, f_{r 8 \alpha 2}, f_{r 8 \alpha 14}, \\
&f_{r 9 \alpha 1}, f_{r 9 \alpha 5}, f_{r 10 \alpha 6}, f_{r 10 \alpha 10}, f_{r 11 \alpha 3}, f_{r 11 \alpha 7}, f_{r 12 \alpha 2}, f_{r 12 \alpha 11}\}
\end{aligned}$$

Chapter 4

$$f_{r1\alpha12} \equiv \{f_{r1\alpha17}, f_{r2\alpha12}, f_{r2\alpha13}, f_{r3\alpha13}, f_{r3\alpha17}, f_{r4\alpha8}, f_{r4\alpha18}, f_{r5\alpha8}, f_{r5\alpha13}, f_{r6\alpha13}, f_{r6\alpha18}, f_{r7\alpha4}, f_{r7\alpha18}, f_{r8\alpha4}, f_{r8\alpha17}, f_{r9\alpha17}, f_{r9\alpha18}, f_{r10\alpha4}, f_{r10\alpha8}, f_{r11\alpha8}, f_{r11\alpha12}, f_{r12\alpha4}, f_{r12\alpha12}\}$$

$$f_{r1\alpha13} \equiv \{f_{r2\alpha17}, f_{r3\alpha12}, f_{r4\alpha13}, f_{r5\alpha18}, f_{r6\alpha8}, f_{r7\alpha17}, f_{r8\alpha18}, f_{r9\alpha4}, f_{r10\alpha12}, f_{r11\alpha4}, f_{r12\alpha8}\}$$

Even though the number of force-constant variables has been reduced greatly, there are still too many variables. Therefore, some additional assumptions need to be made. Table 4.2 shows that the bending force constant or stretch-stretch coupling force constants are about 5 to 10 times smaller than the stretching force constants. While the bend-bend coupling constants are an additional factor of 10 smaller. Therefore, the bend-bend force constants are assumed to be negligible in this analysis,  $f_{\alpha\alpha\alpha} = 0$ , because our main interest is in the Mn–O stretch modes of the adamantane-like compound. In addition, it is expected that the stretch-bend coupling constants are about the same size, or even smaller, than the bend-bend coupling constants. Therefore, the stretch-bend coupling constants are also assumed insignificant, i.e.  $f_{r\alpha\alpha} = 0$ . Another assumption is that the stretch-stretch coupling constants have a value only when the two stretching bonds have a common atom, i.e.  $f_{r1r5} = 0, f_{r1r8} = 0, f_{r1r9} = 0$ .

With these assumptions the number of force constant variables has been reduced to 5. There is one Mn<sup>IV</sup>–O stretch constant,  $f_{r1} = f_{r\nu}$ , and two bend constants with either a Mn atom,  $f_{\alpha1} = f_{\alpha Mn}$ , or an O atom,  $f_{\alpha1} = f_{\alpha O}$ , at the apex. The only coupling constants included in this analysis are the stretch-stretch coupling constants with either Mn,  $f_{r1r2} = f_{rMnr}$ , or O,  $f_{r1r4} = f_{rOr}$  at the apex.

Not only are the variables in the  $F$ -matrix reduced, but also the structural variables in the  $G$ -Matrix. For the  $T_d$  symmetry all bonds are the same. Therefore, the 12 bond length variables can be reduced to 1 variable.

$$r_1 = \{r_2, r_3, r_4, r_5, r_6, r_7, r_8, r_9, r_{10}, r_{11}, r_{12}\}$$

The 18 valence angle variables can be reduced to 2 variables.

$$\alpha_1 = \{\alpha_2, \alpha_3, \alpha_5, \alpha_6, \alpha_7, \alpha_9, \alpha_{10}, \alpha_{11}, \alpha_{14}, \alpha_{15}, \alpha_{16}\}$$

$$\alpha_4 = \{\alpha_8, \alpha_{12}, \alpha_{13}, \alpha_{17}, \alpha_{18}\}$$

The 24  $\beta$  angle variables can be reduced to 1 variable.

$$\beta_1 = \{\beta_2, \beta_3, \beta_4, \beta_5, \beta_6, \beta_7, \beta_8, \beta_9, \beta_{10}, \beta_{11}, \beta_{12}, \beta_{13}, \beta_{14}, \beta_{15}, \beta_{16}, \beta_{17}, \beta_{18}, \beta_{19}, \beta_{20}, \beta_{21}, \beta_{22}, \beta_{23}, \beta_{24}\}$$

The 24  $\delta$  angle variables can be reduced to 2 variables.

$$\delta_1 = \{\delta_3, \delta_6, \delta_8, \delta_9, \delta_{11}, \delta_{13}, \delta_{14}, \delta_{17}, \delta_{22}, \delta_{23}, \delta_{24}\}$$

$$\delta_2 = \{\delta_4, \delta_5, \delta_7, \delta_{10}, \delta_{12}, \delta_{15}, \delta_{16}, \delta_{18}, \delta_{19}, \delta_{20}, \delta_{21}\}$$

The crystal structure data<sup>80</sup> are used to calculate the averaged values for these structural parameters of the  $G$ -matrix, and are presented in Table 4.20.

Table 4.20 The calculated structural parameters of the adamantane-like compound for the  $T_d$  symmetry.

	average	st. dev.		average	st. dev.
$r_1$ (Å)	1.799	0.012	$\beta_1$	114.08	2.79
$\alpha_1$	98.08	2.24	$\delta_1$	17.59	1.55
$\alpha_4$	128.89	1.40	$\delta_2$	100.61	3.80



With all this information the eigenvalues of the  $G_s \cdot F_s$  matrix can be calculated (eq. 4.2), and the observed IR frequencies can be simulated by optimizing the force constant variables,  $f_{r^{IV}}$ ,  $f_{rMnr}$ ,  $f_{rOr}$ . The optimal calculated frequencies for the  $Mn^{IV}_4$  adamantane-like compound are presented in Table 4.21. This table also shows that when the bending modes are included in the normal-mode analysis, the stretching modes are shifting. These shifts can be corrected by changing the stretching force constants a small amount (last column in Table 4.21).

*Table 4.21 Comparison of the observed and calculated frequencies for the  $Mn^{IV}_4$  adamantane-like compound, assuming  $T_d$  symmetry. The stretching force constants are:  $f_{r^{IV}} = 3.15$  mdyn/Å,  $f_{rMnr} = 0.20$  mdyn/Å, and  $f_{rOr} = 0.55$  mdyn/Å, except for the last column. The bending constants,  $f_{\alpha Mn}$  and  $f_{\alpha O}$ , are varied, to investigate the effect of the bending modes on the stretching modes. The units of  $f_{\alpha Mn}$  and  $f_{\alpha O}$  are mdyn/Å, and the units of the frequencies are  $cm^{-1}$ .*

$T_d$	Observed		$f_{\alpha Mn} = 0$ & $f_{\alpha O} = 0$		$f_{\alpha Mn} = 0.4$ & $f_{\alpha O} = 0$		$f_{\alpha Mn} = 0$ & $f_{\alpha O} = 0.4$		$f_{\alpha Mn} = 0.2$ & $f_{\alpha O} = 0.2$		& $f_{r^{IV}} = 3.05$ $f_{rOr} = 0.45$ $f_{rMnr} = 0.20$	
	$^{16}O$	$^{18}O$	$^{16}O$	$^{18}O$	$^{16}O$	$^{18}O$	$^{16}O$	$^{18}O$	$^{16}O$	$^{18}O$	$^{16}O$	$^{18}O$
$T_2$	745	705	746	709	746	709	754	717	750	713	750	713
	510	490	508	492	534	514	511	493	522	504	508	491
$T_1$	707	677	706	673	706	673	710	677	708	675	708	675
E	–	–	511	496	545	527	512	496	529	512	514	498
$A_1$	–	–	503	485	510	490	512	491	511	490	499	479

### 4.6.3 Normal-mode analysis for the $S_4$ symmetry

In the  $T_d$  normal-mode analysis the influence of the bpea on the compound was ignored. However, from the crystal structure it is known that the bpea does have an influence on the Mn–O core, and the overall symmetry approaches  $S_4$ . Due to the lower symmetry most of the symmetry operations are removed, and only the improper rotation axis through the oxygen 2 and 7 remains for the  $S_4$  symmetry, see also Figure 4.11 and Table 4.15. Due to the lower  $S_4$  symmetry, the symmetry representations change into: 7A, 7B and 5E (Figure 4.7). Of these modes the doubly degenerate E vibrational modes are IR and Raman active. While B symmetry representations are only IR active, and the A levels are only Raman active. As described in section 4.6.2, the symmetry coordinates,  $R^S$ , obtained by using equation 4.6 and 4.7, are used to block-out the  $G$  and  $F$  matrices into sub-matrices (eq. 4.9). To execute Equation 4.6 and 4.7 the result of the symmetry operations on the internal coordinates need to be known, which are presented in Table 4.22.

$$G_s = U \cdot G \cdot U^T = \begin{bmatrix} G_s(A) & 0 & 0 \\ 0 & G_s(B) & 0 \\ 0 & 0 & G_s(E) \end{bmatrix}$$

$$F_s = U \cdot F \cdot U^T = \begin{bmatrix} F_s(A) & 0 & 0 \\ 0 & F_s(B) & 0 \\ 0 & 0 & F_s(E) \end{bmatrix} \quad (\text{eq. 4.9})$$

Table 4.22 The result of the  $S_4$  symmetry operations working on the internal coordinates of the Mn model compound.

	E	$S_4$	$C_2$	$S_4^2$
$r_1$	$r_1$	$r_9$	$r_4$	$r_{11}$
$r_2$	$r_2$	$r_8$	$r_6$	$r_{10}$
$r_3$	$r_3$	$r_7$	$r_5$	$r_{12}$
$r_4$	$r_4$	$r_{11}$	$r_1$	$r_9$
$r_5$	$r_5$	$r_{12}$	$r_3$	$r_7$
$r_6$	$r_6$	$r_{10}$	$r_2$	$r_8$
$r_7$	$r_7$	$r_5$	$r_{12}$	$r_3$
$r_8$	$r_8$	$r_6$	$r_{10}$	$r_2$
$r_9$	$r_9$	$r_4$	$r_{11}$	$r_1$
$r_{10}$	$r_{10}$	$r_2$	$r_8$	$r_6$
$r_{11}$	$r_{11}$	$r_1$	$r_9$	$r_4$
$r_{12}$	$r_{12}$	$r_3$	$r_7$	$r_5$

	E	$S_4$	$C_2$	$S_4^2$
$\alpha_1$	$\alpha_1$	$\alpha_{10}$	$\alpha_7$	$\alpha_{14}$
$\alpha_2$	$\alpha_2$	$\alpha_9$	$\alpha_6$	$\alpha_{15}$
$\alpha_3$	$\alpha_3$	$\alpha_{11}$	$\alpha_5$	$\alpha_{16}$
$\alpha_4$	$\alpha_4$	$\alpha_{13}$	$\alpha_4$	$\alpha_{13}$
$\alpha_5$	$\alpha_5$	$\alpha_{16}$	$\alpha_3$	$\alpha_{11}$
$\alpha_6$	$\alpha_6$	$\alpha_{15}$	$\alpha_2$	$\alpha_9$
$\alpha_7$	$\alpha_7$	$\alpha_{14}$	$\alpha_1$	$\alpha_{10}$
$\alpha_8$	$\alpha_8$	$\alpha_{12}$	$\alpha_{17}$	$\alpha_{18}$
$\alpha_9$	$\alpha_9$	$\alpha_6$	$\alpha_{15}$	$\alpha_2$
$\alpha_{10}$	$\alpha_{10}$	$\alpha_7$	$\alpha_{14}$	$\alpha_1$
$\alpha_{11}$	$\alpha_{11}$	$\alpha_5$	$\alpha_{16}$	$\alpha_3$
$\alpha_{12}$	$\alpha_{12}$	$\alpha_{17}$	$\alpha_{18}$	$\alpha_8$
$\alpha_{13}$	$\alpha_{13}$	$\alpha_4$	$\alpha_{13}$	$\alpha_4$
$\alpha_{14}$	$\alpha_{14}$	$\alpha_1$	$\alpha_{10}$	$\alpha_7$
$\alpha_{15}$	$\alpha_{15}$	$\alpha_2$	$\alpha_9$	$\alpha_6$
$\alpha_{16}$	$\alpha_{16}$	$\alpha_3$	$\alpha_{11}$	$\alpha_5$
$\alpha_{17}$	$\alpha_{17}$	$\alpha_{18}$	$\alpha_8$	$\alpha_{12}$
$\alpha_{18}$	$\alpha_{18}$	$\alpha_8$	$\alpha_{12}$	$\alpha_{17}$

The orthogonalized symmetry coordinates for the stretching and bending modes are presented in Table 4.23 and 4.24. These tables show that the A, B and E symmetry representations contain eight, eight, and fourteen vibrational modes, respectively. However, based on symmetry considerations only seven, seven, and ten vibrational modes are anticipated for the A, B, and E symmetry representations, respectively. Therefore, both the A and B symmetry representation have one redundancy, and the E representations has four redundancies.

Table 4.23 The orthogonalized symmetry bond displacement coordinates of the adamantane-like compound for the various symmetry representations, assuming the  $S_4$  symmetry.  $N$  is the normalization factor of the symmetry internal coordinates.

N	A			B			E					
	$\frac{1}{2}$	$\frac{1}{2}$	$\frac{1}{2}$	$\frac{1}{2}$	$\frac{1}{2}$	$\frac{1}{2}$	$\frac{1}{\sqrt{2}}$	$\frac{1}{\sqrt{2}}$	$\frac{1}{\sqrt{2}}$	$\frac{1}{\sqrt{2}}$	$\frac{1}{\sqrt{2}}$	$\frac{1}{\sqrt{2}}$
$r_1$	1	0	0	1	0	0	1	0	0	0	0	0
$r_2$	0	1	0	0	1	0	0	1	0	0	0	0
$r_3$	0	0	1	0	0	1	0	0	1	0	0	0
$r_4$	1	0	0	1	0	0	-1	0	0	0	0	0
$r_5$	0	0	1	0	0	1	0	0	-1	0	0	0
$r_6$	0	1	0	0	1	0	0	-1	0	0	0	0
$r_7$	0	0	1	0	0	-1	0	0	0	1	0	0
$r_8$	0	1	0	0	-1	0	0	0	0	0	1	0
$r_9$	1	0	0	-1	0	0	0	0	0	0	0	1
$r_{10}$	0	1	0	0	-1	0	0	0	0	0	-1	0
$r_{11}$	1	0	0	-1	0	0	0	0	0	0	0	-1
$r_{12}$	0	0	1	0	0	-1	0	0	0	-1	0	0
$\Delta\alpha_x$	0	0	0	0	0	0	0	0	0	0	0	0

Table 4.24 The orthogonalized symmetry angle displacement coordinates of the adamantane-like compound for the various symmetry representations, assuming  $S_4$  symmetry.  $N$  is the normalization factor of the symmetry internal coordinates.

N	A					B					E								
	$\frac{1}{2}$	$\frac{1}{2}$	$\frac{1}{2}$	$\frac{1}{\sqrt{2}}$	$\frac{1}{2}$	$\frac{1}{2}$	$\frac{1}{2}$	$\frac{1}{2}$	$\frac{1}{\sqrt{2}}$	$\frac{1}{2}$	$\frac{1}{\sqrt{2}}$	$\frac{1}{\sqrt{2}}$	$\frac{1}{\sqrt{2}}$	$\frac{1}{\sqrt{2}}$	$\frac{1}{\sqrt{2}}$	$\frac{1}{\sqrt{2}}$	$\frac{1}{\sqrt{2}}$	$\frac{1}{\sqrt{2}}$	
$\Delta r_x$	0	0	0	0	0	0	0	0	0	0	0	0	0	0	0	0	0	0	0
$\alpha_1$	1	0	0	0	0	1	0	0	0	0	1	0	0	0	0	0	0	0	0
$\alpha_2$	0	1	0	0	0	0	1	0	0	0	0	1	0	0	0	0	0	0	0
$\alpha_3$	0	0	1	0	0	0	0	1	0	0	0	0	1	0	0	0	0	0	0
$\alpha_4$	0	0	0	1	0	0	0	0	1	0	0	0	0	0	0	0	0	0	0
$\alpha_5$	0	0	1	0	0	0	0	1	0	0	0	0	-1	0	0	0	0	0	0
$\alpha_6$	0	1	0	0	0	0	1	0	0	0	0	-1	0	0	0	0	0	0	0
$\alpha_7$	1	0	0	0	0	1	0	0	0	0	-1	0	0	0	0	0	0	0	0
$\alpha_8$	0	0	0	0	1	0	0	0	0	1	0	0	0	1	0	0	0	0	0
$\alpha_9$	0	1	0	0	0	0	-1	0	0	0	0	0	0	0	1	0	0	0	0
$\alpha_{10}$	1	0	0	0	0	-1	0	0	0	0	0	0	0	0	0	1	0	0	0
$\alpha_{11}$	0	0	1	0	0	0	0	-1	0	0	0	0	0	0	0	0	1	0	0
$\alpha_{12}$	0	0	0	0	1	0	0	0	0	-1	0	0	0	0	0	0	0	1	0
$\alpha_{13}$	0	0	0	1	0	0	0	0	-1	0	0	0	0	0	0	0	0	0	0
$\alpha_{14}$	1	0	0	0	0	-1	0	0	0	0	0	0	0	0	0	-1	0	0	0
$\alpha_{15}$	0	1	0	0	0	0	-1	0	0	0	0	0	0	0	-1	0	0	0	0
$\alpha_{16}$	0	0	1	0	0	0	0	-1	0	0	0	0	0	0	0	0	-1	0	0
$\alpha_{17}$	0	0	0	0	1	0	0	0	0	1	0	0	0	-1	0	0	0	0	0
$\alpha_{18}$	0	0	0	0	1	0	0	0	0	-1	0	0	0	0	0	0	0	0	-1

As for the  $T_d$  normal-mode analysis, the  $S_4$  symmetry can be used to reduced the number of force constant variables. However, in this case the same reduction of constants is used as for the  $T_d$  symmetry 465 force constants are reduced to 5 variables. However, for the  $G$ -matrix the change in symmetry is included resulting in 19 structural parameters. The 12 bond length parameters are reduced to 3 parameters.

$$r_1 = \{r_4, r_9, r_{11}\}, r_2 = \{r_6, r_8, r_{10}\}, \text{ and } r_3 = \{r_5, r_7, r_{12}\}$$

The 18 valence angle parameters can be reduced to 5 parameters.

$$\alpha_1 = \{\alpha_7, \alpha_{10}, \alpha_{14}\}, \alpha_2 = \{\alpha_6, \alpha_9, \alpha_{15}\}, \text{ and } \alpha_3 = \{\alpha_5, \alpha_{11}, \alpha_{16}\}$$

$$\alpha_4 = \{\alpha_{13}\} \text{ and } \alpha_8 = \{\alpha_{12}, \alpha_{17}, \alpha_{18}\}$$

The 24  $\beta$  angle parameters can be reduced to 4 parameters.

$$\beta_1 = \{\beta_3, \beta_5, \beta_7, \beta_{14}, \beta_{16}, \beta_{21}, \beta_{22}\} \text{ and } \beta_2 = \{\beta_4, \beta_9, \beta_{12}, \beta_{15}, \beta_{17}, \beta_{19}, \beta_{24}\}$$

$$\beta_6 = \{\beta_8, \beta_{13}, \beta_{23}\} \text{ and } \beta_{10} = \{\beta_{11}, \beta_{18}, \beta_{20}\}$$

The 24  $\delta$  angle variables can be reduced to 7 variables.

$$\delta_1 = \{\delta_8, \delta_{13}, \delta_{24}\}, \delta_3 = \{\delta_{11}, \delta_{14}, \delta_{23}\}, \text{ and } \delta_6 = \{\delta_9, \delta_{17}, \delta_{22}\}$$

$$\delta_2 = \{\delta_4, \delta_{15}, \delta_{16}\}, \delta_5 = \{\delta_{21}\}, \delta_7 = \{\delta_{12}, \delta_{19}, \delta_{20}\}, \text{ and } \delta_{10} = \{\delta_{18}\}$$

These parameters are calculated from the crystal structure data<sup>80</sup> and are presented in Table 4.25. Now the parameters and variables of the  $G$  and  $F$  matrices are defined and the IR frequencies of the modes can be calculated, using equation 4.2.

Table 4.25 The calculated structural parameters of the adamantane-like compound for the  $S_4$  symmetry.

	average	st. dev.		average	st. dev.
$r_1$ (Å)	1.786	0.005	$\beta_1$	112.42	0.44
$r_2$ (Å)	1.804	0.008	$\beta_2$	115.89	2.18
$r_3$ (Å)	1.808	0.009	$\beta_6$	117.37	0.84
$\alpha_1$	95.15	0.32	$\beta_{10}$	110.49	0.61
$\alpha_2$	98.70	0.52	$\delta_1$	19.50	0.26
$\alpha_3$	100.37	0.71	$\delta_2$	99.98	0.47
$\alpha_4$	130.78	0.23	$\delta_3$	15.78	0.33
$\alpha_8$	127.94	0.45	$\delta_5$	94.61	0.01
			$\delta_6$	17.48	0.27
			$\delta_7$	100.81	1.13
			$\delta_{10}$	107.44	0.16

#### 4.6.4 Normal-mode analysis for the $C_s$ symmetry

When the influence of the terminal ligand bpea on the reduced adamantane-like compound ( $Mn^{III}Mn^{IV}_3$ ) is ignored, the overall  $C_s$  symmetry can be assumed. The  $C_{3v}$  symmetry cannot be applied for the reduced compound, because the crystal structure<sup>80</sup> shows a significant Jahn-Teller distortion of the  $Mn^{III}$  atom. When it is assumed that the 5(Mn) atom is reduced, the only symmetry operation that remains for the  $C_s$  symmetry is the mirror plane  $\sigma_2$ ; see also Figure 4.11 and Table 4.15. The symmetry representations change into 14A' and 10A'' vibrational modes, which are both IR and Raman active (Figure 4.7). As described in section 4.6.2, the symmetry coordinates,  $R^S$ , obtained by using equations 4.6 and 4.7, are used block-out the  $G$  and  $F$  matrices into sub-matrices (Equation 4.9). To execute equations 4.6 and 4.7 the result of the symmetry operations on the internal coordinates need to be known, which are presented in Table 4.26.

$$G_s = U \cdot G \cdot U^T = \begin{bmatrix} G_s(A') & 0 \\ 0 & G_s(A'') \end{bmatrix}$$

$$F_s = U \cdot F \cdot U^T = \begin{bmatrix} F_s(A') & 0 \\ 0 & F_s(A'') \end{bmatrix} \quad (\text{eq. 4.10})$$



Table 4.26 The result of the  $C_s$  symmetry operations working on the internal coordinates of the Mn model compound.

$C_s$	E	$\sigma_2$	$C_s$	E	$\sigma_2$
$r_1$	$r_1$	$r_3$	$\alpha_1$	$\alpha_1$	$\alpha_2$
$r_2$	$r_2$	$r_2$	$\alpha_2$	$\alpha_2$	$\alpha_1$
$r_3$	$r_3$	$r_1$	$\alpha_3$	$\alpha_3$	$\alpha_3$
$r_4$	$r_4$	$r_{10}$	$\alpha_4$	$\alpha_4$	$\alpha_{18}$
$r_5$	$r_5$	$r_{11}$	$\alpha_5$	$\alpha_5$	$\alpha_{14}$
$r_6$	$r_6$	$r_{12}$	$\alpha_6$	$\alpha_6$	$\alpha_{16}$
$r_7$	$r_7$	$r_7$	$\alpha_7$	$\alpha_7$	$\alpha_{15}$
$r_8$	$r_8$	$r_9$	$\alpha_8$	$\alpha_8$	$\alpha_8$
$r_9$	$r_9$	$r_8$	$\alpha_9$	$\alpha_9$	$\alpha_{11}$
$r_{10}$	$r_{10}$	$r_4$	$\alpha_{10}$	$\alpha_{10}$	$\alpha_{10}$
$r_{11}$	$r_{11}$	$r_5$	$\alpha_{11}$	$\alpha_{11}$	$\alpha_9$
$r_{12}$	$r_{12}$	$r_6$	$\alpha_{12}$	$\alpha_{12}$	$\alpha_{13}$
			$\alpha_{13}$	$\alpha_{13}$	$\alpha_{12}$
			$\alpha_{14}$	$\alpha_{14}$	$\alpha_5$
			$\alpha_{15}$	$\alpha_{15}$	$\alpha_7$
			$\alpha_{16}$	$\alpha_{16}$	$\alpha_6$
			$\alpha_{17}$	$\alpha_{17}$	$\alpha_{17}$
			$\alpha_{18}$	$\alpha_{18}$	$\alpha_4$

The orthogonalized symmetry coordinates for the stretching and bending modes are presented in Table 4.27 and 4.28. These tables show that the A' and A'' symmetry representations contain eighteen and twelve vibrational modes, respectively. However, based on symmetry considerations only fourteen and ten vibrational modes are anticipated for the A' and A'' symmetry representations, respectively. Therefore, four redundant conditions apply to the A' symmetry representation and two for the A'' symmetry representation.

Table 4.27 The orthogonalized symmetry bond displacement coordinates of the adamantane-like compound for the various symmetry representations, assuming  $C_s$  symmetry.  $N$  is the normalization factor of the symmetry internal coordinates.

N	A'							A''				
	$\frac{1}{\sqrt{2}}$	1	$\frac{1}{\sqrt{2}}$	$\frac{1}{\sqrt{2}}$	$\frac{1}{\sqrt{2}}$	1	$\frac{1}{\sqrt{2}}$	$\frac{1}{\sqrt{2}}$	$\frac{1}{\sqrt{2}}$	$\frac{1}{\sqrt{2}}$	$\frac{1}{\sqrt{2}}$	
$r_1$	1	0	0	0	0	0	0	1	0	0	0	0
$r_2$	0	1	0	0	0	0	0	0	0	0	0	0
$r_3$	1	0	0	0	0	0	0	-1	0	0	0	0
$r_4$	0	0	1	0	0	0	0	0	1	0	0	0
$r_5$	0	0	0	1	0	0	0	0	0	1	0	0
$r_6$	0	0	0	0	1	0	0	0	0	0	1	0
$r_7$	0	0	0	0	0	1	0	0	0	0	0	0
$r_8$	0	0	0	0	0	0	1	0	0	0	0	1
$r_9$	0	0	0	0	0	0	1	0	0	0	0	-1
$r_{10}$	0	0	1	0	0	0	0	0	-1	0	0	0
$r_{11}$	0	0	0	1	0	0	0	0	0	-1	0	0
$r_{12}$	0	0	0	0	1	0	0	0	0	0	-1	0
$\Delta\alpha_x$	0	0	0	0	0	0	0	0	0	0	0	0

Table 4.28 The orthogonalized symmetry angle displacement coordinates of the adamantane-like compound for the various symmetry representations, assuming  $C_s$  symmetry.  $N$  is the normalization factor of the symmetry internal coordinates.

N	A'											A''						
	$\frac{1}{\sqrt{2}}$	1	$\frac{1}{\sqrt{2}}$	$\frac{1}{\sqrt{2}}$	$\frac{1}{\sqrt{2}}$	$\frac{1}{\sqrt{2}}$	1	$\frac{1}{\sqrt{2}}$	1	$\frac{1}{\sqrt{2}}$	1	$\frac{1}{\sqrt{2}}$	$\frac{1}{\sqrt{2}}$	$\frac{1}{\sqrt{2}}$	$\frac{1}{\sqrt{2}}$	$\frac{1}{\sqrt{2}}$	$\frac{1}{\sqrt{2}}$	
$\Delta r_x$	0	0	0	0	0	0	0	0	0	0	0	0	0	0	0	0	0	0
$\alpha_1$	1	0	0	0	0	0	0	0	0	0	0	1	0	0	0	0	0	0
$\alpha_2$	1	0	0	0	0	0	0	0	0	0	0	-1	0	0	0	0	0	0
$\alpha_3$	0	1	0	0	0	0	0	0	0	0	0	0	0	0	0	0	0	0
$\alpha_4$	0	0	1	0	0	0	0	0	0	0	0	0	1	0	0	0	0	0
$\alpha_5$	0	0	0	1	0	0	0	0	0	0	0	0	0	1	0	0	0	0
$\alpha_6$	0	0	0	0	1	0	0	0	0	0	0	0	0	0	1	0	0	0
$\alpha_7$	0	0	0	0	0	1	0	0	0	0	0	0	0	0	0	1	0	0
$\alpha_8$	0	0	0	0	0	0	1	0	0	0	0	0	0	0	0	0	0	0
$\alpha_9$	0	0	0	0	0	0	0	1	0	0	0	0	0	0	0	0	1	0
$\alpha_{10}$	0	0	0	0	0	0	0	0	1	0	0	0	0	0	0	0	0	0
$\alpha_{11}$	0	0	0	0	0	0	0	1	0	0	0	0	0	0	0	0	-1	0
$\alpha_{12}$	0	0	0	0	0	0	0	0	0	1	0	0	0	0	0	0	0	1
$\alpha_{13}$	0	0	0	0	0	0	0	0	0	1	0	0	0	0	0	0	0	-1
$\alpha_{14}$	0	0	0	1	0	0	0	0	0	0	0	0	0	-1	0	0	0	0
$\alpha_{15}$	0	0	0	0	0	1	0	0	0	0	0	0	0	0	-1	0	0	0
$\alpha_{16}$	0	0	0	0	1	0	0	0	0	0	0	0	0	-1	0	0	0	0
$\alpha_{17}$	0	0	0	0	0	0	0	0	0	0	1	0	0	0	0	0	0	0
$\alpha_{18}$	0	0	1	0	0	0	0	0	0	0	0	0	-1	0	0	0	0	0

As for the  $T_d$  normal-mode analysis, the  $C_s$  symmetry can be used to reduce the number of force constants variables. Like the  $T_d$  symmetry the stretch-bend,  $f_{rx\alpha y}$ , and bend-bend coupling,  $f_{\alpha x\alpha y}$ , constants are set at zero. It is also assumed that the bending force constant and the stretch-stretch coupling constant are independent of the oxidation state of the manganese atoms. Consequently, there are still only two bending force constants,  $f_{\alpha Mn}$  and  $f_{\alpha O}$ , and two stretch-stretch coupling constants,  $f_{rMnr}$  and  $f_{rOr}$ .

Additionally, it is assumed that no distinction is made between non-Jahn-Teller and Jahn-Teller bond stretching force constants, nor is a distinction made whether a  $\text{Mn}^{\text{IV}}\text{-O}$  bond is connected to a  $\text{Mn}^{\text{IV}}\text{-O}$  or  $\text{Mn}^{\text{III}}\text{-O}$  bond. Therefore the stretch force constants are reduced to:

$$f_{,IV} \equiv \{f_{r1}, f_{r2}, f_{r3}, f_{r4}, f_{r5}, f_{r6}, f_{r10}, f_{r11}, f_{r12}\}$$

$$f_{,III} \equiv \{f_{r7}, f_{r8}, f_{r9}\}$$

Including the  $C_s$  symmetry for the  $G$ -matrix, the 78 structural parameters are reduced to 43 parameters. The 12 bond length parameters are reduced to 7 parameters.

$$r_1 = \{r_3\}, r_2, r_4 = \{r_{10}\}, r_5 = \{r_{11}\}, r_6 = \{r_{12}\}, r_7, \text{ and } r_8 = \{r_9\}$$

The 18 valence angle parameters can be reduced to 11 parameters.

$$\alpha_1 = \{\alpha_2\}, \alpha_3, \alpha_5 = \{\alpha_{14}\}, \alpha_6 = \{\alpha_{16}\}, \alpha_7 = \{\alpha_{15}\}, \alpha_9 = \{\alpha_{11}\}, \text{ and } \alpha_{10}$$

$$\alpha_4 = \{\alpha_{18}\}, \alpha_8, \alpha_{12} = \{\alpha_{13}\}, \text{ and } \alpha_{17}$$

The 24  $\beta$  angle parameters can be reduced to 12 parameters.

$$\beta_1 = \{\beta_6\}, \beta_2 = \{\beta_5\}, \beta_3 = \{\beta_7\}, \beta_4 = \{\beta_8\}, \beta_9 = \{\beta_{10}\}, \beta_{11} = \{\beta_{12}\}, \beta_{13} = \{\beta_{14}\}, \beta_{15} = \{\beta_{17}\},$$

$$\beta_{16} = \{\beta_{18}\}, \beta_{19} = \{\beta_{21}\}, \beta_{20} = \{\beta_{22}\}, \text{ and } \beta_{23} = \{\beta_{24}\}$$

The 24  $\delta$  angle variables can be reduced to 13 variables.

$$\delta_1 = \{\delta_6\}, \delta_3 = \{\delta_8\}, \delta_9 = \{\delta_{11}\}, \delta_{13} = \{\delta_{17}\}, \delta_{14}, \delta_{22} = \{\delta_{23}\}, \text{ and } \delta_{24}$$

$$\delta_2 = \{\delta_5\}, \delta_4 = \{\delta_7\}, \delta_{10} = \{\delta_{12}\}, \delta_{15} = \{\delta_{18}\}, \delta_{16} = \{\delta_{19}\}, \text{ and } \delta_{20} = \{\delta_{21}\}$$

These parameters are calculated from the crystal structure data<sup>80</sup> and are presented in Table 4.25. Now the parameters and variables of the  $G$  and  $F$  matrices are defined and the IR frequencies of the modes can be calculated, using Equation 4.2.

Table 4.29 The calculated structural parameters of the adamantane-like compound in  $C_s$  symmetry.

	average	st. dev.		average	st. dev.		average	st. dev.
$r_1$ (Å)	1.801	0.014	$\beta_1$	114.87	1.87	$\delta_1$	19.95	0.94
$r_2$ (Å)	1.774	–	$\beta_2$	115.36	2.93	$\delta_2$	98.00	2.21
$r_4$ (Å)	1.795	0.005	$\beta_3$	112.02	2.85	$\delta_3$	17.32	1.90
$r_5$ (Å)	1.789	0.021	$\beta_4$	115.26	1.76	$\delta_4$	100.37	0.54
$r_6$ (Å)	1.801	0.005	$\beta_9$	110.84	4.28	$\delta_9$	14.55	1.01
$r_7$ (Å)	1.877	–	$\beta_{11}$	115.17	3.89	$\delta_{10}$	105.65	3.31
$r_8$ (Å)	1.807	0.001	$\beta_{13}$	114.95	2.00	$\delta_{13}$	17.54	.96
$\alpha_1$	98.33	1.80	$\beta_{15}$	115.34	2.48	$\delta_{14}$	15.21	–
$\alpha_3$	100.01	–	$\beta_{16}$	110.36	4.66	$\delta_{15}$	103.54	3.81
$\alpha_4$	128.89	1.73	$\beta_{19}$	113.30	1.58	$\delta_{16}$	101.00	0.28
$\alpha_5$	98.63	2.25	$\beta_{20}$	111.43	3.53	$\delta_{20}$	97.17	2.35
$\alpha_6$	100.91	0.47	$\beta_{23}$	117.79	2.97	$\delta_{22}$	15.97	0.69
$\alpha_7$	96.49	2.02				$\delta_{24}$	18.06	–
$\alpha_8$	125.91	–						
$\alpha_9$	99.73	0.24						
$\alpha_{10}$	95.61	–						
$\alpha_{12}$	128.55	1.69						
$\alpha_{17}$	127.29	–						

**4.6.4 The gaussians used to simulate the ( $^{16}\text{O} - ^{18}\text{O}$ ) difference-difference FTIR spectrum**

Table 4.30 The position, width at half peak height and amplitude of the gaussian curves used to simulate the difference-difference spectrum in the 620 - 720  $\text{cm}^{-1}$  range. The intensities of the  $\text{Mn}^{\text{IV}}_4$  compound are derived from the ( $^{16}\text{O} - ^{18}\text{O}$ ) difference spectrum (Figure 4.3). Degenerate levels split upon reduction and their intensity is divided equally over the single modes.

	Redox state	Symmetry		Position ( $\text{cm}^{-1}$ )	Width ( $\text{cm}^{-1}$ )	Amplitude
		$T_d$	$S_4/C_s$			
$^{16}\text{O}$	$\text{Mn}^{\text{IV}}_4$	$T_2$	E	748	15	0.0001
			B	742	10	0.0001
		$T_1$	E	707	15	0.0003
			A	705	10	0.0001
	$\text{Mn}^{\text{III}}\text{Mn}^{\text{IV}}_3$	$T_2$	A'	747	10	0.00005
			A'	709	10	0.00005
			A''	747	10	0.00005
		$T_1$	A'	685	10	0.0001
			A''	726	10	0.00005
			A''	689	10	0.0001
$^{18}\text{O}$	$\text{Mn}^{\text{IV}}_4$	$T_2$	E	711	15	0.0001
			B	706	10	0.0001
		$T_1$	E	673	15	0.0003
			A	672	10	0.0001
	$\text{Mn}^{\text{III}}\text{Mn}^{\text{IV}}_3$	$T_2$	A'	710	10	0.00005
			A'	674	10	0.00005
			A''	710	10	0.00005
		$T_1$	A'	653	10	0.0001
			A''	692	10	0.00005
			A''	656	10	0.0001

Table 4.31 The position, width at half peak height and amplitude of the gaussian curves used to simulate the difference-difference spectrum in the 420 - 520  $\text{cm}^{-1}$  range. The intensities of the doubly degenerate levels are twice the value of single modes.

	Redox state	Symmetry		Position ( $\text{cm}^{-1}$ )	Width ( $\text{cm}^{-1}$ )	Amplitude
		$T_d$	$S_4/C_s$			
$^{16}\text{O}$	$\text{Mn}^{\text{IV}}_4$	$T_2$	E	506	4	0.000025
			B	489	4	0.00005
		E	B	512	4	0.000025
	$\text{Mn}^{\text{III}}\text{Mn}^{\text{IV}}_3$	$T_2$	A''	482	4	0.000025
			A'	511	4	0.000025
			A'	497	4	0.000025
		E	A''	505	4	0.000025
			A'	501	4	0.000025
		A <sub>1</sub>	A'	488	4	0.000025
	$^{18}\text{O}$	$\text{Mn}^{\text{IV}}_4$	$T_2$	E	490	4
B				473	4	0.00005
E			B	497	4	0.000025
$\text{Mn}^{\text{III}}\text{Mn}^{\text{IV}}_3$		$T_2$	A''	468	4	0.000025
			A'	485	4	0.000025
			A'	480	4	0.000025
		E	A''	489	4	0.000025
			A'	501	4	0.000025
		A <sub>1</sub>	A'	470	4	0.000025

## 4.7 References

- (1) Kok, B.; Forbush, B.; McGloin, M. *Photochem. Photobiol.* **1970**, *11*, 457-475.
- (2) Zouni, A.; Witt, H. T.; Kern, J.; Fromme, P.; Krauss, N.; Saenger, W.; Orth, P. *Nature* **2001**, *409*, 739-743.
- (3) Kirby, J. A.; Goodin, D. B.; Wydrzynski, T.; Robertson, A. S.; Klein, M. P. *J. Am. Chem. Soc.* **1981**, *103*, 5537-5542.
- (4) Liang, W.; Roelofs, T. A.; Cinco, R. M.; Rompel, A.; Latimer, M. J.; Yu, W. O.; Sauer, K.; Klein, M. P.; Yachandra, V. K. *J. Am. Chem. Soc.* **2000**, *122*, 3399-3412.
- (5) Penner-Hahn, J. E. *Struct. Bonding (Berlin)* **1998**, *90*, 1-36.
- (6) Robblee, J. H.; Cinco, R. M.; Yachandra, V. K. *Biochim. Biophys. Acta* **2001**, *1503*, 7-23.
- (7) Yachandra, V. K.; Sauer, K.; Klein, M. P. *Chem. Rev.* **1996**, *96*, 2927-2950.
- (8) Liang, W.; Latimer, M. J.; Dau, H.; Roelofs, T. A.; Yachandra, V. K.; Sauer, K.; Klein, M. P. *Biochemistry* **1994**, *33*, 4923-4932.
- (9) Messinger, J.; Robblee, J. H.; Yu, W. O.; Sauer, K.; Yachandra, V. K.; Klein, M. P. *J. Am. Chem. Soc.* **1997**, *119*, 11349-11350.
- (10) Miller, A. F.; Brudvig, G. W. *Biochim. Biophys. Acta* **1991**, *1056*, 1-18.
- (11) Peloquin, J. M.; Britt, R. D. *Biochim. Biophys. Acta* **2001**, *1503*, 96-111.
- (12) Debus, R. J. *Biochim. Biophys. Acta* **1992**, *1102*, 269-352.
- (13) Debus, R. J. In *Manganese and Its Role in Biological Processes*; Sigel, A., Sigel, H., Eds.; Marcel Dekker, Inc.: New York, 2000; Vol. 37, pp 657-711.
- (14) Vrettos, J. S.; Limburg, J.; Brudvig, G. W. *Bioch. Biophys Acta* **2001**, *1503*, 229-245.



- (15) Messinger, J.; Robblee, J. H.; Bergmann, U.; Fernandez, C.; Glatzel, P.; Visser, H.; Cinco, R. M.; McFarlane, K. L.; Bellacchio, E.; Pizarro, S. A.; Cramer, S. P.; Sauer, K.; Klein, M. P.; Yachandra, V. K., manuscript in preparation.
- (16) Roelofs, T. A.; Liang, M. C.; Latimer, M. J.; Cinco, R. M.; Rompel, A.; Andrews, J. C.; Sauer, K.; Yachandra, V. K.; Klein, M. P. *Proc. Natl. Acad. Sci. U. S. A.* **1996**, *93*, 3335-3340.
- (17) Ono, T.; Noguchi, T.; Inoue, Y.; Kusunoki, M.; Matsushita, T.; Oyanagi, H. *Science* **1992**, *258*, 1335-1337.
- (18) Iuzzolino, L.; Dittmer, J.; Dörner, W.; Meyer-Klaucke, W.; Dau, H. *Biochemistry* **1998**, *37*, 17112-17119.
- (19) Cinco, R. M.; Rompel, A.; Visser, H.; Aromí, G.; Christou, G.; Sauer, K.; Klein, M. P.; Yachandra, V. K. *Inorg. Chem.* **1999**, *38*, 5988-5998.
- (20) Cooper, S. R.; Calvin, M. *J. Am. Chem. Soc.* **1977**, *99*, 6623-6630.
- (21) Kirby, J. A.; Robertson, A. S.; Smith, J. P.; Thompson, A. C.; Cooper, S. R.; Klein, M. P. *J. Am. Chem. Soc.* **1981**, *103*, 5529-5537.
- (22) Pecoraro, V. L.; Baldwin, M. J.; Gelasco, A. *Chem. Rev.* **1994**, *94*, 807-826.
- (23) Pecoraro, V. L.; Hsieh, W.-Y. In *Manganese and Its Role in Biological Processes*; Sigel, A., Sigel, H., Eds.; Marcel Dekker Inc.: New York, 2000; Vol. 37, pp 429-504.
- (24) Visser, H.; Anxolabéhère-Mallart, E.; Bergman, U.; Glatzel, P.; Robblee, J. H.; Cramer, S. P.; Girerd, J.-J.; Sauer, K.; Klein, M. P.; Yachandra, V. K. *submitted for publication* **2001**.
- (25) Wieghardt, K. *Angew. Chem.-Int. Edit. Engl.* **1989**, *28*, 1153-1172.

- (26) Chu, H.-A.; Hillier, W.; Law, N. A.; Sackett, H.; Haymond, S.; Babcock, G. T. *Biochim. Biophys. Acta* **2000**, *1459*, 528-532.
- (27) Noguchi, T.; Inoue, Y.; Tang, X. S. *Biochemistry* **1999**, *38*, 10187-10195.
- (28) Noguchi, T.; Ono, T. A.; Inoue, Y. *Biochim. Biophys. Acta* **1993**, *1143*, 333-336.
- (29) Noguchi, T.; Ono, T. A.; Inoue, Y. *Biochimica Et Biophysica Acta* **1995**, *1232*, 59-66.
- (30) Noguchi, T.; Sugiura, M. *Biochemistry* **2000**, *39*, 10943-10949.
- (31) Steenhuis, J. J.; Hutchison, R. S.; Barry, B. A. *J. Biol. Chem.* **1999**, *274*, 14609-14616.
- (32) Chu, H. A.; Hillier, W.; Law, N. A.; Babcock, G. T. *Biochimica Et Biophysica Acta* **2001**, *1503*, 69-82.
- (33) Chu, H.-A.; Gardner, M. T.; O'Brien, J. P.; Babcock, G. T. *Biochemistry* **1999**, *38*, 4533-4541.
- (34) Hawkins, G. J.; Hunneman, R.; Gardner, M. T.; Babcock, G. T. *Infrared Phys. Technol.* **1998**, *39*, 297-306.
- (35) Cua, A.; Stewart, D. H.; Reifler, M. J.; Brudvig, G. W.; Bocian, D. F. *J. Am. Chem. Soc.* **2000**, *122*, 2069-2077.
- (36) Baxter, R.; Krausz, E.; Wydrzynski, T.; Pace, R. J. *J. Am. Chem. Soc.* **1999**, *121*, 9451-9452.
- (37) Boussac, A.; Girerd, J.-J.; Rutherford, A. W. *Biochemistry* **1996**, *35*, 6984-6989.
- (38) Boussac, A.; Kuhl, H.; Un, S.; Roegner, M.; Rutherford, A. W. *Biochemistry* **1998**, *37*, 8995-9000.
- (39) Dismukes, G. C.; Mathis, P. *FEBS Lett.* **1984**, *178*, 51-54.

- (40) Shreve, A. P.; Cherepy, N. J.; Franzen, S.; Boxer, S. G.; Mathies, R. A. *Proc. Natl. Acad. Sci. U. S. A.* **1991**, *88*, 11207-11211.
- (41) Shreve, A. P.; Cherepy, N. J.; Mathies, R. A. *Appl. Spectrosc.* **1992**, *46*, 707-711.
- (42) Czernuscewicz, R. S.; Su, Y. O.; Stern, M. K.; Macor, K. A.; Kim, D.; Groves, J. T.; Spiro, T. G. *J. Am. Chem. Soc.* **1988**, *110*, 4158-4165.
- (43) Collins, T. J.; Powell, R. D.; Sledobnick, C.; Uffelman, E. S. *J. Am. Chem. Soc.* **1990**, *112*, 899-901.
- (44) Workman, J. M.; Powell, R. D.; Procyk, A. D.; Collins, T. J.; Bocian, D. F. *Inorg. Chem.* **1992**, *31*, 1548-1550.
- (45) Gonzalez-Vilchez, F.; Griffith, W. P. *J.C.S. Dalton Trans.* **1972**, 1416-1421.
- (46) Noda, L. K.; Ribeiro, M. C. C.; Goncalves, N. S.; Jubert, A. H.; Sala, O. *J. Raman Spectrosc.* **1999**, *30*, 697-704.
- (47) Tarte, P.; Thelen, J. *Spectrochim. Acta, Part A* **1972**, *28*, 5-14.
- (48) Baran, E. J.; Aymonino, P. J. *Spectrochim. Acta, Part A* **1968**, *24*, 291-295.
- (49) Jubert, A. H.; Varetti, E. L. *J. Mol. Struct.* **1982**, *79*, 285-288.
- (50) Kiefer, W.; Bernstein, H. J. *Appl. Spectrosc.* **1971**, *25*, 609-613.
- (51) Kiefer, W.; Bernstein, H. J. *Mol. Phys.* **1972**, *23*, 835-851.
- (52) Dave, B. C.; Czernuszewicz, R. S. *Inorg. Chim. Acta* **1998**, *281*, 25-35.
- (53) Gultneh, Y.; Ahvazi, B.; Khan, A. R.; Butcher, R. J.; Tuchagues, J. P. *Inorg. Chem.* **1995**, *34*, 3633-3645.
- (54) Mimoun, H.; Saussine, L.; Menage, S.; Girerd, J.-J. In *New Developments in Selective Oxidation*; Trifiro, F., Centi, G., Eds.; Elsevier Science Publishers: Amsterdam, 1990; pp 97-107.

- (55) Sheats, J. E.; Czernuszewicz, R. S.; Dismukes, G. C.; Rheingold, A. L.; Petrouleas, V.; Stubbe, J.; Armstrong, W. H.; Beer, R. H.; Lippard, S. J. *J. Am. Chem. Soc.* **1987**, *109*, 1435-1444.
- (56) Pal, S.; Armstrong, W. H. *Inorg. Chem.* **1992**, *31*, 5417-5423.
- (57) Schardt, B. C.; Hollander, F. J.; Hille, C. L. *J. Am. Chem. Soc.* **1982**, *104*, 3964-3972.
- (58) Brewer, K. J.; Calvin, M.; Lumpkin, R. S.; Otvos, J. W.; Spreer, L. O. *Inorg. Chem.* **1989**, *28*, 4446-4451.
- (59) Dave, B. C.; Czernuszewicz, R. S. *Inorg. Chim. Acta* **1994**, *227*, 33-41.
- (60) Gamelin, D. R.; Kirk, M. L.; Stemmler, T. L.; Pal, S.; Armstrong, W. H.; Penner-Hahn, J. E.; Solomon, E. I. *J. Am. Chem. Soc.* **1994**, *116*, 2392-2399.
- (61) Hagen, K. S.; Armstrong, W. H.; Hope, H. *Inorg. Chem.* **1988**, *27*, 967-969.
- (62) Pal, S.; Gohdes, J. W.; Wilisch, W. C. A.; Armstrong, W. H. *Inorg. Chem.* **1992**, *31*, 713-716.
- (63) Pal, S.; Olmstead, M. M.; Armstrong, W. H. *Inorg. Chem.* **1995**, *34*, 4708-4715.
- (64) Boucher, L. J.; Coe, C. G. *Inorg. Chem.* **1975**, *14*, 1289-1295.
- (65) Hoof, D. L.; Tisley, D. G.; Walton, R. A. *Inorg. Nucl. Chem. Letters* **1973**, *9*, 571-576.
- (66) Libby, E.; Webb, R. J.; Streib, W. E.; Folting, K.; Huffman, J. C.; Hendrickson, D. N.; Christou, G. *Inorg. Chem.* **1989**, *28*, 4037-4040.
- (67) Pal, S.; Chan, M. K.; Armstrong, W. H. *J. Am. Chem. Soc.* **1992**, *114*, 6398-6406.
- (68) Hage, R.; Krijnen, B.; Warnaar, J. B.; Hartl, F.; Stufkens, D. J.; Snoeck, T. L. *Inorg. Chem.* **1995**, *34*, 4973-4978.

- (69) Wieghardt, K.; Bossek, U.; Nuber, B.; Weiss, J.; Bonvoisin, J.; Corbella, M.; Vitols, S. E.; Girerd, J. J. *J. Am. Chem. Soc.* **1988**, *110*, 7398-7411.
- (70) Li, H.; Jiang, T.-L.; Butler, I. S. *J. Raman Spectr.* **1989**, *20*, 569-574.
- (71) Cavaluzzo, M.; Chen, Q.; Zubieta, J. *J. Chem. Soc., Chem. Commun.* **1993**, 131-133.
- (72) Edwards, H. G. M.; Ware, M. J.; Woodward, L. A. *Chem. Commun.* **1968**, 540-541.
- (73) Edwards, H. G. M.; Woodward, L. A.; Gall, M. J.; Ware, M. J. *Spectrochim. Acta, Part A* **1970**, *26*, 287-290.
- (74) Varetti, E. L.; Müller, A. *Z. anorg. allg. Chem.* **1978**, *422*, 230-234.
- (75) Varetti, E. L.; Filgueira, R. R.; Müller, A. *Spectrochim. Acta* **1981**, *37A*, 369-373.
- (76) Goher, M. A. S.; Abu-Youssef, M. A. M.; Mautner, F. A.; Popitsch, A. *Polyhedron* **1993**, *12*, 1751-1756.
- (77) Goldstein, M.; Unsworth, W. D. *Inorg. Chim. Acta* **1970**, *4*, 342-346.
- (78) Goldstein, M.; Unsworth, W. D. *Spectrochim. Acta, Part A* **1972**, *28*, 1297-1304.
- (79) Johnson, M. K.; Powell, D. B.; Cannon, R. D. *Spectrochim. Acta, Part A* **1981**, *37*, 995-1006.
- (80) Dube, C. E.; Wright, D. W.; Pal, S.; Bonitatebus, P. J.; Armstrong, W. H. *J. Am. Chem. Soc.* **1998**, *120*, 3704-3716.
- (81) Wieghardt, K.; Bossek, U.; Gebert, W. *Angew. Chem.-Int. Edit. Engl.* **1983**, *22*, 328-329.
- (82) Visser, H.; Curtright, A. E.; McCusker, J. K.; Sauer, K. submitted for publication to *Anal. Chem.*
- (83) Milosevic, M.; Sting, D.; Rein, A. *Spectroscopy* **1995**, *10*, 44-49.

- (84) Sheridan, R. E.; Rein, A. J. *R&D* **1991**, 33, 100-102.
- (85) Wilson, E. B.; Decius, J. C.; Cross, P. C. *Molecular Vibrations: The Theory of Infrared and Raman Vibrational Spectra*; Dover Publications, Inc.: New York, 1955.
- (86) Herzberg, G. *Molecular Spectra and Molecular Structure - Volume II Infrared and Raman Spectra of Polyatomic Molecules*; Krieger Publishing Company: Malabar, FL, 1945.
- (87) Califano, S.; Crawford, B., Jr. *Z. Elektrochemie* **1960**, 64, 571-575.
- (88) Cotton, F. A. *Chemical Applications of Group Theory*; 3rd ed.; John Wiley & Sons: New York, 1963.



# **Chapter 5**

## **Future Directions**



## 5.1 X-ray spectroscopy

Few Mn compounds have been studied by Mn K-edge XANES and Mn K $\beta$  XES spectroscopy, as indicated in Chapters 1 and 2. Therefore, it is essential to study the effect of ligand environment, symmetry, and oxidation state of the Mn on the X-ray spectra using a large library of model compounds. Such empirical studies will provide insights for the development of a theoretical model for the Mn K-edge XANES spectra.

One of the controversial issues is the effect of ligands on the Mn K-edge. This effect is especially pronounced when comparing Mn model compounds with aromatic or non-aromatic ligands. When aromatic ligands are present, a shoulder in the Mn K-edge is present. It has been suggested that this shoulder is due to an 1s(metal) to  $\pi^*$ (ligand) transition. The presence of this shoulder has a major effect on the IPE of the Mn K-edge spectra. Hence it is important to understand the origins of this feature.

In Chapter 2, Figure 2.10 shows a strong shoulder in the main edge of the di- $\mu$ -oxo compound K-edge XANES spectra. The terminal ligand environment of the di- $\mu$ -oxo compound is provided by 1,10-phenanthroline, which provides only aromatic nitrogen ligands to the Mn atoms. The mono- $\mu$ -oxo compound shows only a very weak shoulder (Figure 2.11.). The ligand environment of the mono- $\mu$ -oxo compound is a mixture of aromatic (2), non-aromatic (2), and phenoxy (1) ligands. Figure 5.1 shows a simplified atomic model of the main transitions involved in the Mn K-edge XANES; the electric-dipole forbidden pre-edge 1s $\rightarrow$ 3d transition, the main-edge 1s(Mn) $\rightarrow$ 4p(Mn) transition, and the 1s(Mn) $\rightarrow\pi^*(L)$  transition. It is anticipated that the  $\pi^*$  orbital will have a lower energy when the aromaticity of the ligand is more extensive. (There have been no reports of strong UV/vis absorption bands for the di- $\mu$ -oxo compound which have been assigned

to the  $3d(M) \rightarrow \pi^*(L)$  transition.)

To verify whether the  $\pi^*$  orbital has a lower energy with a more extensive aromaticity of the ligand, mono-nuclear  $Mn^{2+}$  compounds could be studied with the ligands; 1,4,7-triazacyclonane (tacn), hydrotris(1-pyrazolyl)borate ( $HB(pz)_3$ ), 2,2'-bipyridine (bipy), and 1,10-phenantroline (phen), in order of increasing aromaticity (Figure 5.1). This study of mono-nuclear compounds can be expanded to di-nuclear compounds, either mono- $\mu$ -oxo or di- $\mu$ -oxo compounds, which can be studied in various oxidation states.

Figure 5.2A shows structures of the mono- $\mu$ -oxo compounds with either the non-aromatic ligand tacn,<sup>1-3</sup> or the aromatic ligand  $HB(pz)_3$ .<sup>4,5</sup> Each compound has been synthesized in the  $Mn^{III}Mn^{III}$  oxidation state and can be electrochemically converted to the  $Mn^{III}Mn^{IV}$  oxidation state. The  $HB(pz)_3$  compound can also be converted to the  $Mn^{IV}Mn^{IV}$  oxidation state. Figure 5.2B shows the di- $\mu$ -oxo compounds which could be used to study the effect of the  $1s \rightarrow \pi^*$  transition on the XANES spectra. For the non-aromatic compounds there are two ligands available 1,4,7,10-tetrazacyclododecane (cyclen)<sup>6</sup> and 1,4,8,11-tetraazacyclotetradecane (cyclam).<sup>7,8</sup> There are two aromatic di- $\mu$ -oxo compounds available with a difference in aromaticity: bipy<sup>9-11</sup> or phen.<sup>12,13</sup> The non-aromatic and aromatic compounds are synthesized in the  $Mn^{III}Mn^{IV}$  oxidation state and can be electrochemically converted to the  $Mn^{IV}Mn^{IV}$  state. Reduction to the  $Mn^{III}Mn^{III}$  of the non-aromatic compounds is possible, but the aromatic di- $\mu$ -oxo compounds are unstable during this electrochemical step.

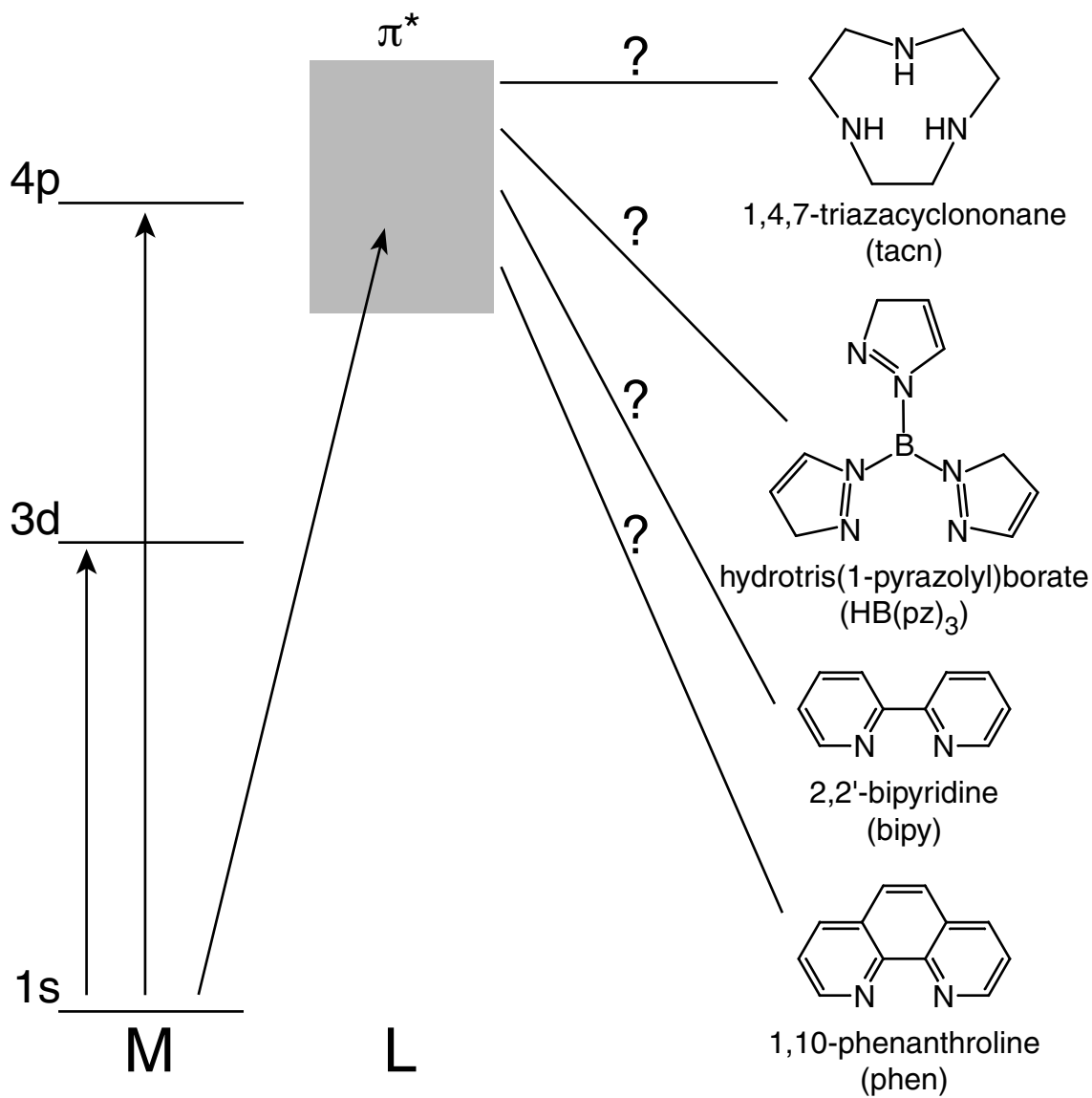
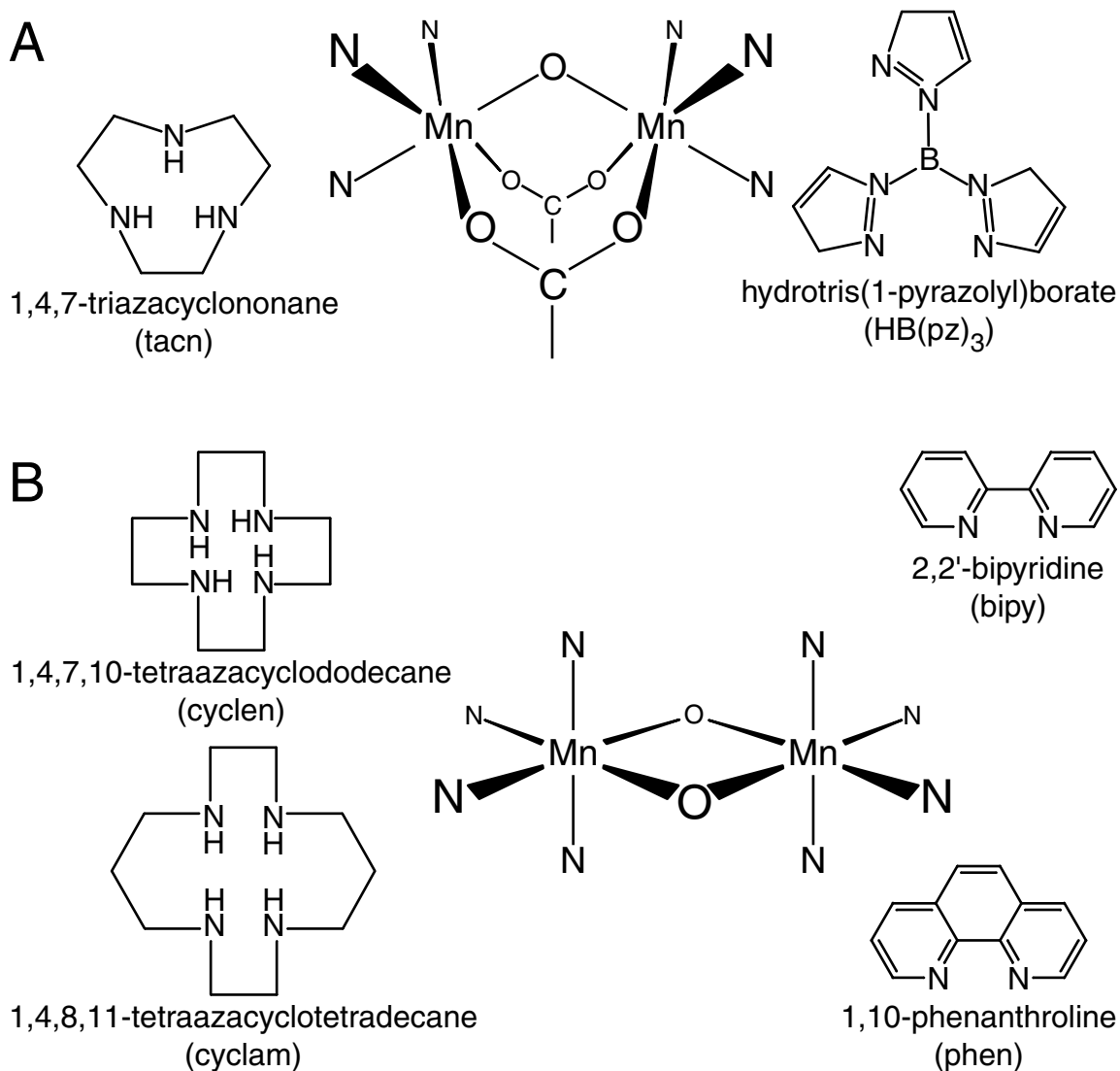


Figure 5.1 Energy diagram of the Mn (M) and ligand (L) orbitals involved in the Mn K-edge XANES. The question is whether the  $1s(M) \rightarrow \pi^*(L)$  transition is observed in XANES spectra, and how much the energy level of  $\pi^*$  orbital depends on the aromaticity of the ligand.



*Figure 5.2 The mono- $\mu$ -oxo (A) and di- $\mu$ -oxo (B) compounds and the ligands that can be used to study the effect of aromaticity of the terminal ligand environment on the Mn K-edge XANES spectra.*

The aromaticity of the terminal ligand environment also has an influence on the pre-edge feature in the Mn K-edge spectra. Therefore, it is relevant to study the pre-edge feature also in more detail. There is a theoretical model available to analyze the pre-edge features of the K-edge spectra, which uses a simplified model of the local symmetry around the metal atoms. However, so far this approach has been used only on mono-nuclear compounds.<sup>14,15</sup> It will be difficult to distinguish individual features for multi-nuclear compounds, especially for multi-valence compounds. Therefore, it would be of interest to have an additional X-ray technique which can provide information about the oxidation state of the metal and the ligand environment. L-edge spectroscopy, which observes the 2p→3d transition, is such a technique. L-edge spectroscopy has the advantage over K-edge that it directly probes the 3d orbitals. Two well resolved transitions are observed due to the spin-orbit coupling,  $J=1/2$  and  $J=3/2$ , as shown in Figure 5.3. Additionally, an adequate theoretical model is available to interpret L-edge spectra.<sup>16</sup> The disadvantage of L-edge spectroscopy is that the Mn L-edge (638 eV) is near the oxygen K-edge (543 eV). When there is a large concentration of oxygen present in the sample the oxygen K-edge obscures the Mn L-edge. Consequently, this technique works only for model compounds, because there is too much X-ray absorption by the oxygens present in the biological samples. However, another technique is available which provides L-edge-like information: Resonant Inelastic X-ray scattering spectroscopy (RIXS).

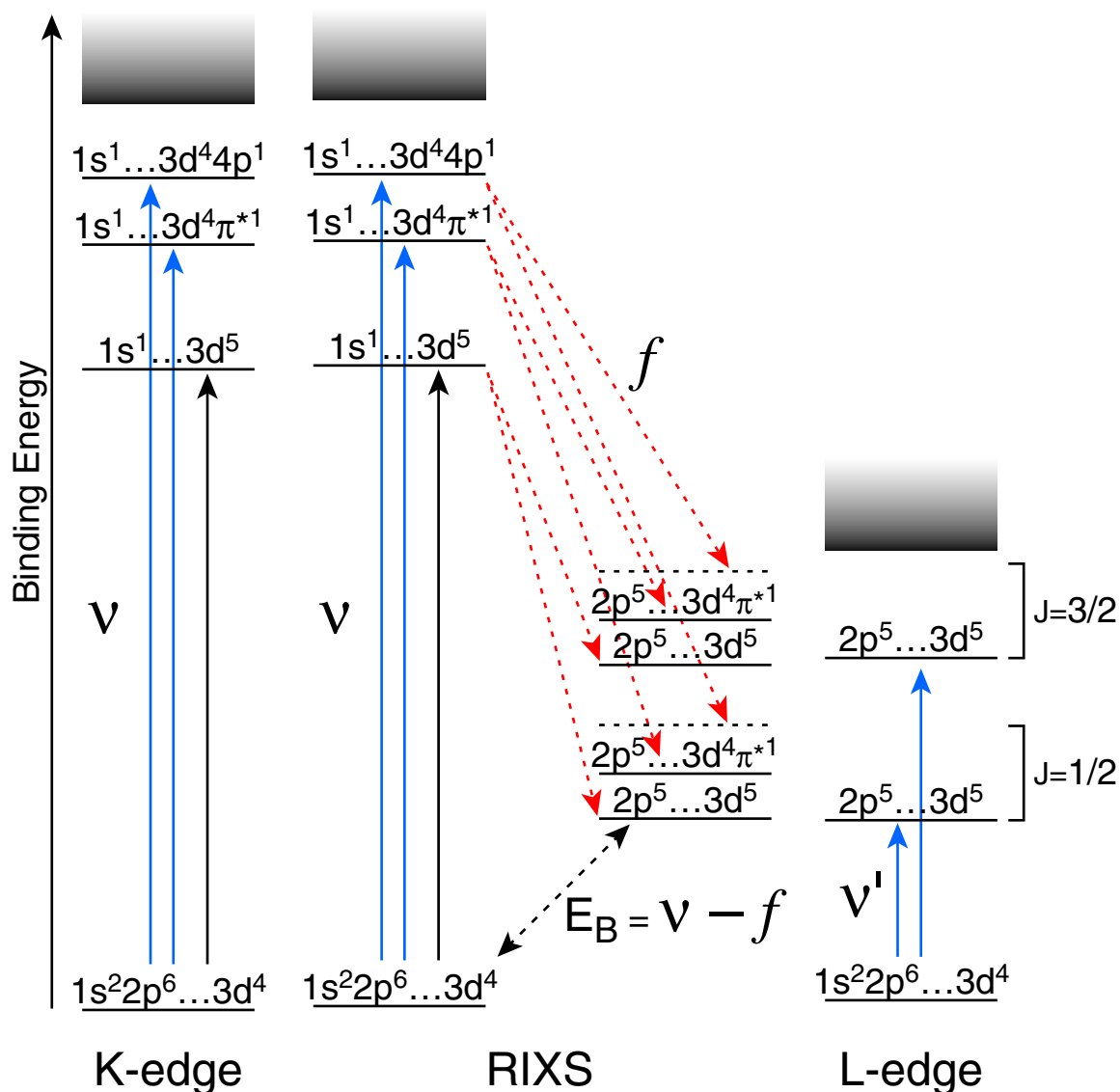


Figure 5.3 The electronic energy diagram of the transitions that occur in Mn K-edge, L-edge and RIXS spectroscopy. L-edge like information is extracted from RIXS by subtracting the emission energy,  $f$ , from the excitation energy,  $v$ . However, more final states are present in the RIXS spectra than in the L-edge spectra. Therefore, RIXS gives a wealth of information about the Mn oxidation state, ligand environment and local symmetry. Blue arrows indicate electric-dipole allowed excitations, black arrows indicate electric-dipole forbidden excitations, and the red dashed arrows indicate emission transitions.

Figure 5.3 shows the electronic state transition diagram of the processes that are involved in RIXS and a comparison to Mn K-edge and L-edge spectroscopy. As can be seen, RIXS is a two dimensional technique. The excitation energy is scanned through the Mn K-edge, while the emission is analyzed for the  $1s^1 2p^6 \rightarrow 1s^2 2p^5$  transition. Both the excitation and emission energy are well above the K-edge of oxygen absorption. Consequently, RIXS can be used on model compounds and biological systems.

The L-edge-like information (630 - 680 eV) of the RIXS is extracted by calculating the difference between the excitation and emission spectroscopy  $E_B = \nu - f$ . RIXS spectra are plotted in contour plots with the excitation,  $\nu$ , and difference between excitation and emission,  $E_B$ , as the x,y axis. Consequently, RIXS spectroscopy contains more information than L-edge spectroscopy, because certain final states in RIXS spectroscopy (Figure 5.3) are allowed which are electric-dipole forbidden in the L-edge spectroscopy. Therefore, RIXS is helpful in providing information on oxidation state of the Mn atoms and the nature of the ligand environment. This additional information might be useful for the development of a theory of Mn K-edge XANES.<sup>17</sup>

## 5.2 Vibrational spectroscopy

Vibrational spectra and normal mode analysis of Mn compounds are indispensable for the interpretation of the IR and Raman spectra of the oxygen-evolving complex (OEC). Table 4.1 gives a selection of Mn complexes that have been studied by IR and/or Raman spectroscopy. However, the list of compounds that additionally were analyzed by normal-mode analysis is very limited, as shown in Table 4.2. It is critical for the understanding of the vibrational spectra of the OEC that more Mn complexes in

different oxidation states are studied, as was done for the adamantane-like compound in Chapter 4. As was shown in Chapter 1, in Tables 1.1 through 1.7, there is a wide variety of Mn complexes that have been synthesized. In principle, vibrational analysis of each of these compounds will provide information about the OEC, however there are some compounds that are of special interest.

One of the assumptions of the normal-mode analysis in Chapter 4 is that the vibrations of the terminal ligand do not couple to the 'core' Mn–O vibrations. However, there are some indications that this assumption is not completely true. Consequently, an analysis of the influence of the terminal ligand on the 'core' Mn–O vibrational modes is needed. This involves a normal-mode analysis of the whole complex, which includes the Mn–O 'core' and the terminal ligand. To study the vibrations of the terminal ligand isotopic exchange of the N or O atoms which ligate to the Mn is helpful. In addition, it would be useful to study different types of terminal ligands, to identify ligands that have weak or strong coupling to the Mn–O 'core' vibrational modes. Coupling between vibrational modes is determined by the strength of the bonds and symmetry considerations, i.e. modes in the same plane have a stronger coupling than orthogonal modes. Oxygen is more electronegative than nitrogen, and oxygen ligands in general have also a negative charge, causing a stronger Mn–O ligand interaction compared to the Mn–N ligands. Therefore, terminal ligands which provide Mn–O ligation, such as carboxylate groups, will have a stronger influence than when the ligating atom is N. Most likely there will also be differences between aromatic and non-aromatic ligands. Consequently, comparison of the vibrational spectra of compounds with all terminal aromatic or non-aromatic nitrogen ligands, or oxygen ligands (bridging or terminal)



would be useful.

Especially, the influence of the carboxylate groups are of interest, because several studies of PS II have focused on the carboxylate vibrations in the 1800 - 1000  $\text{cm}^{-1}$ , instead of the Mn–O vibrational modes (900 - 400  $\text{cm}^{-1}$ ).<sup>18-22</sup> When carboxylate groups are ligated to Mn their vibrational modes occur in the 1410 - 1350  $\text{cm}^{-1}$  ( $\nu_{\text{sym}}$ ) and 1600 - 1550  $\text{cm}^{-1}$  ( $\nu_{\text{asym}}$ ) region.<sup>23</sup> There are some difficulties in distinguishing carboxylate vibrations from vibrational modes of other components in photosystem II, which occur in the same spectral region. Therefore, it might be beneficial to study carboxylate vibrations in conjunction with the Mn–O modes. Studying the carboxylate and Mn–O ‘core’ modes will give insight as to how these two groups influence each other's vibrational modes, when the oxidation state of Mn changes. This kind of study will aid the identification of the carboxylate vibrational modes of the OEC in the 1400 - 1600  $\text{cm}^{-1}$  range.

Therefore, Mn compounds which contain Mn–O–Mn bridges and carboxylate groups, either terminal or bridging, need to be studied in different oxidation states, as described in Chapters 3 and 4. Initially, one would like to start with some rudimentary examples, such as mono- $\mu$ -oxo or di- $\mu$ -oxo compounds. There is a variety of mono- $\mu$ -oxo and di- $\mu$ -oxo compounds which contain carboxylate bridges which can be prepared in different oxidation states (see Tables 1.2 and 1.3). After these initial studies, more complex systems can be studied such as the mono- $\mu_3$ -oxo tri-nuclear (Table 1.4), the ‘cubane’ (Table 1.6) or the ‘butterfly’ (Table 1.7) complexes. Isotopic exchange  $^{16}\text{O} \rightarrow ^{18}\text{O}$  of the Mn–O ‘core’ and of the carboxylate groups is required to aid an extensive vibrational analysis, and give a complete insight in how these two groups

influence each other.

Another interesting set of compounds is where one of the ligand coordinates can be occupied by either H<sub>2</sub>O, OH<sup>-</sup>, or a halide (specifically Cl<sup>-</sup>), but the rest of the coordination environment stays intact. There are some indications that Cl<sup>-</sup> is ligated to the OEC cluster in the S<sub>3</sub> state but not necessarily in the other catalytic states.<sup>24</sup> However, in contrast it has been proposed also that Cl<sup>-</sup> is bound to Mn in the earlier stages during the catalytic cycle and replaced by H<sub>2</sub>O or OH<sup>-</sup> in later stages.<sup>25</sup> Vibrational spectra of the OEC can help in resolving this issue, either by directly identifying the Mn–Cl vibration or, indirectly, by the change observed in the Mn–O ‘core’ vibrations when Cl<sup>-</sup> is exchange by H<sub>2</sub>O or OH<sup>-</sup>.

Figure 5.4 shows four different compounds where Cl<sup>-</sup> can be replaced by OH<sup>-</sup>/H<sub>2</sub>O or another halide. Only minor structural changes occur upon exchange, due to the difference in size and electronegativity of Cl<sup>-</sup> vs. OH<sup>-</sup>/H<sub>2</sub>O. In case of the mono- $\mu$ -oxo compound<sup>26</sup>, the other ligands are provided by two carboxylate groups and two aromatic nitrogen ligands. There are no electrochemical data available on the di- $\mu$ -oxo compound<sup>27,28</sup>. The terminal ligands of the di- $\mu$ -oxo compound are all non-aromatic nitrogen ligands. Both oxidation and reduction of the tri-nuclear compound has been published<sup>29,30</sup>. However, oxidation of the tri-nuclear compound is the most interesting, because in that case the Mn<sub>A</sub> is oxidized. The Mn<sub>A</sub> atom is the atom to which the OH<sup>-</sup>, F<sup>-</sup>, Cl<sup>-</sup> binds. An oxidation state change of the Mn<sub>A</sub> atom will give more information about this bond than a change in oxidation state of the Mn<sub>B</sub> atoms. The ligand environment of the Mn<sup>A</sup> atom is a mixture of two aromatic and one non-aromatic nitrogen ligands, while the Mn<sup>B</sup> atoms have an additional carboxylate bridge. The

'cubane' model compound has a (III<sub>3</sub>,IV) starting oxidation state, with the Mn<sup>IV</sup> as the atom that is not connected to X. A variety of oxidation states can be prepared electrochemically. The other ligands are three carboxylate bridges and six alkoxy terminal ligands.

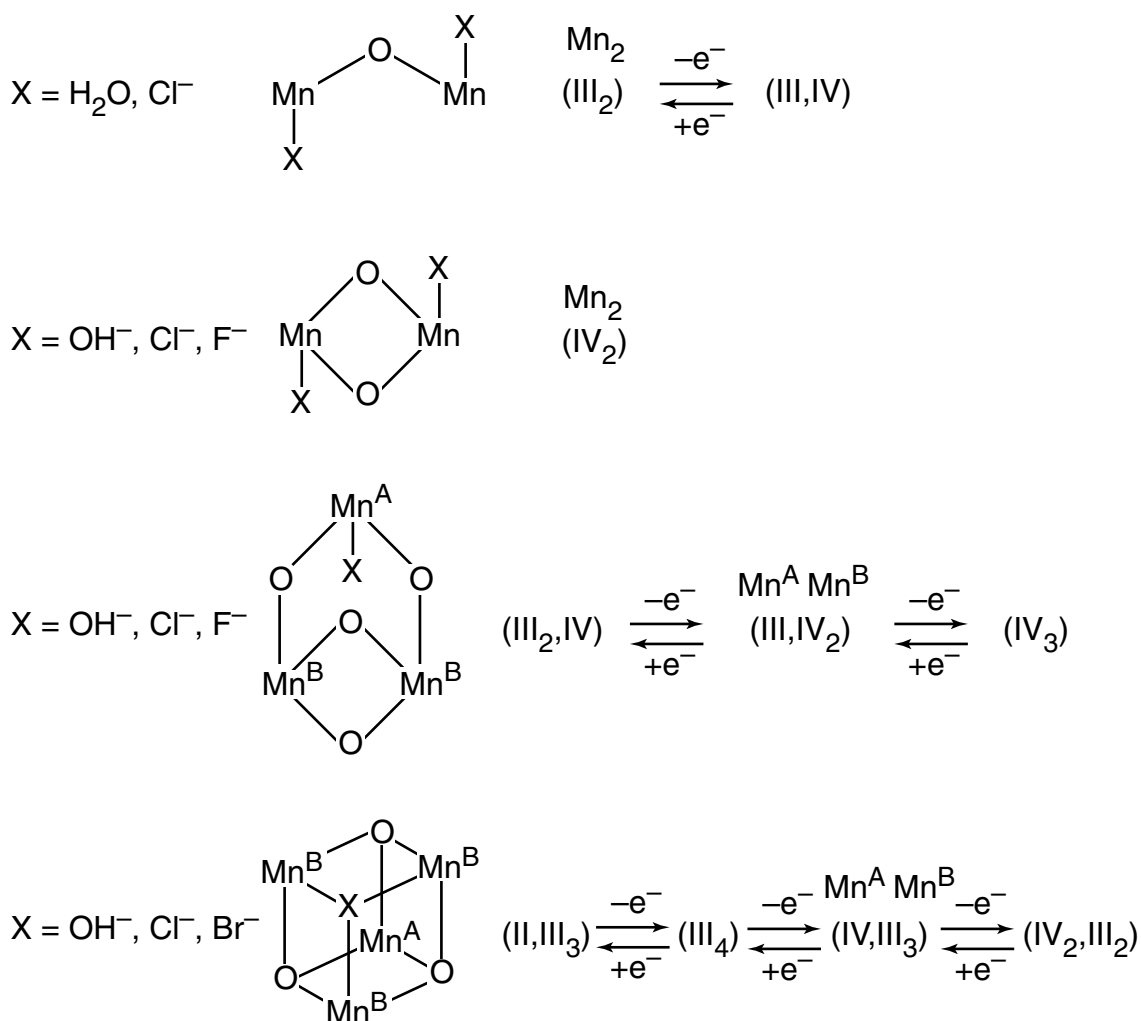


Figure 5.4 Mn complexes of interest to study the influence of replacement of one OH<sup>-</sup> or H<sub>2</sub>O by a halide. The mono- $\mu$ -oxo compound<sup>26</sup> has the starting ox. state (III,III), and can be oxidized to (III,IV). No electrochemistry is reported for the di- $\mu$ -oxo compound.<sup>27,28</sup> Oxidation and reduction steps are available for both the tri-nuclear<sup>29,30</sup> and the cubane<sup>31,32</sup> compounds.

So far, studies of compounds have been proposed where there are minor structural changes either by an oxidation state change or a small change in ligand environment. During the  $S_1 \rightarrow S_2$  state transition of the OEC there are indeed only minor changes. However, for the  $S_0 \rightarrow S_1$ <sup>33</sup> and the  $S_2 \rightarrow S_3$ <sup>34</sup> state transitions there is evidence that the Mn–Mn distances change significantly. Therefore, it might be relevant to study the effect of a major structural change in the Mn–O ‘core’, while the rest of the ligand environment stays intact. Figure 5.5 shows such a compound, where a ‘dimer-of-dimers’ compound can be transformed into an ‘adamantane-like’ compound, by either chemical reaction or reduction.<sup>29</sup> This would be a very interesting compound to study with vibrational spectroscopy, especially because some information about the ‘adamantane-like’ compound is already known (Chapter 4).

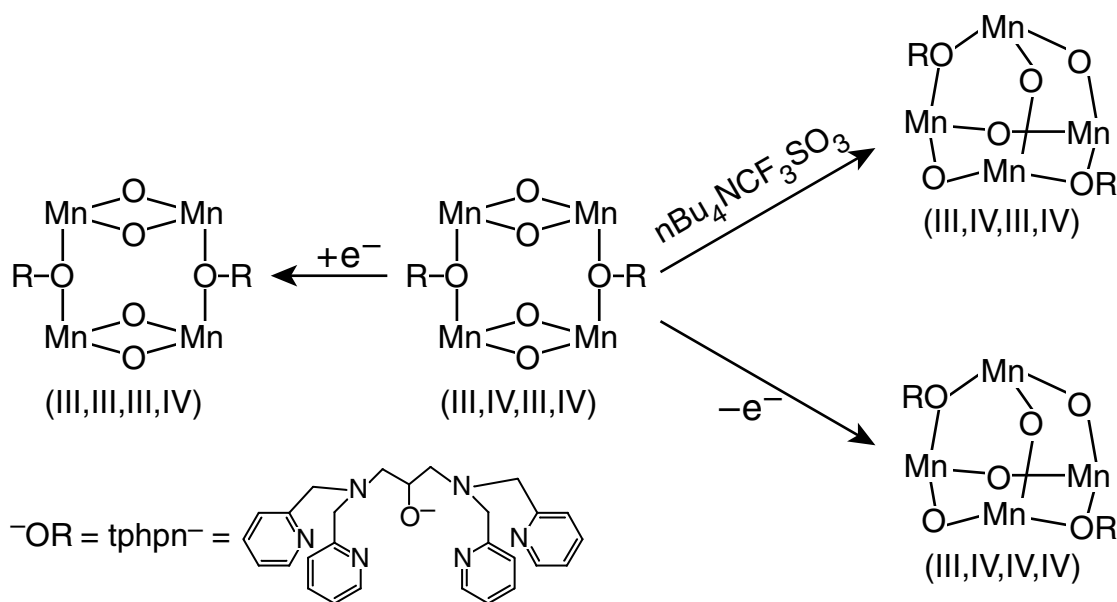


Figure 5.5 The reduction of a dimer-of-dimer compound, and the conversion into an adamantane-like compound, either by chemical reaction or oxidation.<sup>29</sup>

Until now most of the vibrational data available for PS II and, specifically, the OEC are steady state spectra, i.e. the spectra are of PS II frozen in its S-states. There are a few kinetic studies of PS II with a focus on Quinone A and Tyrosine Z.<sup>35-37</sup> Even though no kinetic data are yet available on the OEC, time-resolved vibrational experiments (either IR or Raman) of some Mn complexes might show interesting kinetic behavior. For this type of IR experiment biomimetic systems could be used, i.e. systems that mimic PS II. These systems contain inorganic complexes which upon illumination transfer an electron to a electron acceptor and extract an electron from a Mn compound. Figure 5.6 shows such a system where upon light absorption (532 nm) by the Ru complex an electron is transferred to the electron acceptor  $[\text{Co}(\text{NH}_3)_5\text{Cl}]^{2+}$ . The Ru complex extracts an electron by way of a phenyl group from a Mn di-nuclear compound (halftime  $\sim 30$  ms). The Mn di-nuclear compound is the linear mono- $\mu$ -oxo compound of Chapter 2.<sup>38</sup> Even though this biomimetic system decomposes after a few flashes, step-scan FTIR spectroscopy is still possible because the system dissolves in acetonitrile, a solvent with few IR features (see Chapters 3 and 4). Using a liquid system, one can use a stop-flow cell, which renews the sample for each new mirror position of the FTIR spectrometer. Using this kind of equipment, a time resolution of  $\sim 20$  ns can be obtained.<sup>39</sup> It would be interesting if this biomimetic system could be combined with other Mn complexes, such as the dimer-of-dimer complex described in Figure 5.5 which has a major structural change upon reduction.

Step-scan FTIR spectroscopy is not possible for the OEC, because under the conditions required for this experiment the OEC is not stable enough. Repeated laser illuminations are required of the PS II for each mirror position for step-scan

spectroscopy. There are about 600 mirror positions for a range of  $1000\text{ cm}^{-1}$  at a  $4\text{ cm}^{-1}$  resolution. Additionally, the water content of the PS II sample is reduced as much as possible to minimize the IR absorption. Water, even  $\text{D}_2\text{O}$ , absorbs too much IR radiation in the region of interest,  $400 - 1000\text{ cm}^{-1}$ , of the OEC. Low water content in the PS II sample makes the sample less stable. Consequently, it is unlikely that no changes will occur in the OEC during the 600 laser illuminations.

No stop-flow set-up can be used to work around the instability of PS II, because so far no alternative solvents are known in which PS II is stable and which has minor IR absorption bands in the  $400 - 1000\text{ cm}^{-1}$  range. Consequently, the only way of acquiring time-resolved IR spectra is by using rapid-scan FTIR spectroscopy. The time resolution of rapid-scan is around 20 ms ( $4\text{ cm}^{-1}$  resolution), which is fast enough to measure some of the relaxation processes of the OEC at room temperature. Nevertheless, rapid-scan spectroscopy has still several problems associated with it, such as low detector sensitivity in the  $400 - 600\text{ cm}^{-1}$  region.

More promising might be time resolved Raman spectroscopy, because here you can use a liquid system, and therefore carry out a stop-flow experiment. One would use the near-infrared band of the OEC to measure the resonance Raman spectra as was proposed by Cua et al.,<sup>40</sup> see also Chapter 4. Advancing the OEC through its catalytic cycle can be achieved with a green laser pulse. Using time-resolved Raman spectroscopy, a time resolution on the picosecond time scale has been achieved for studies of bacteriorhodopsin.<sup>41-44</sup>

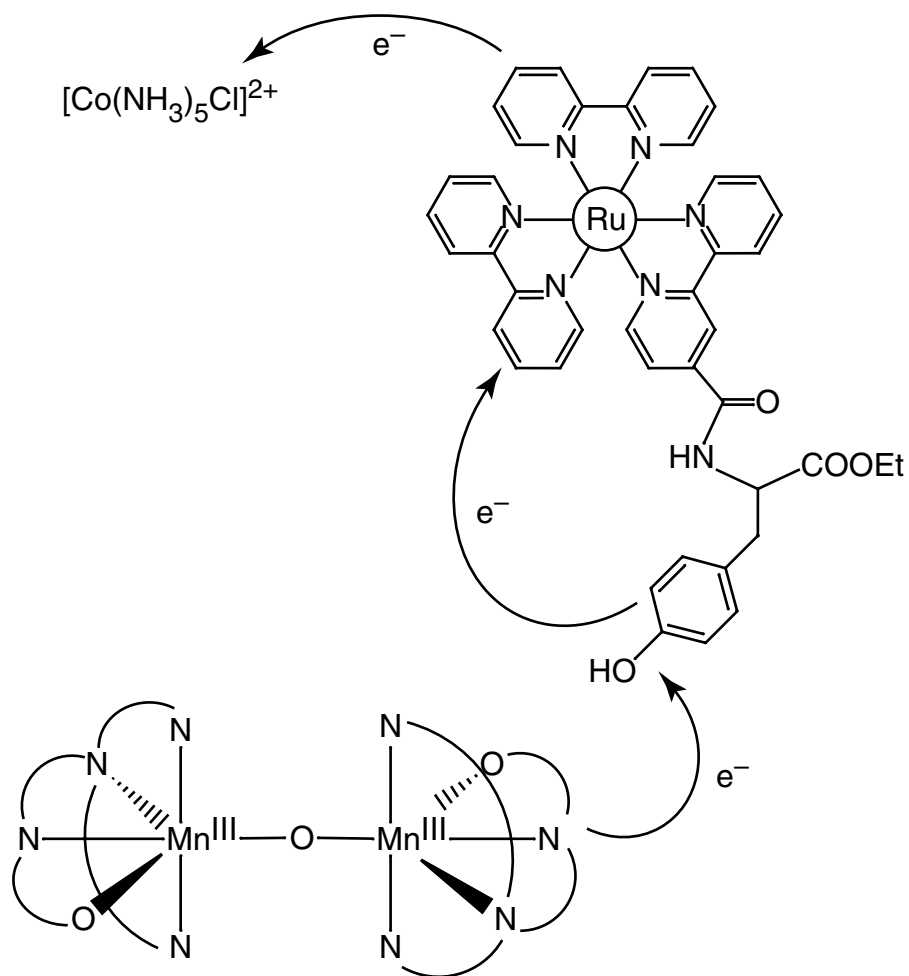


Figure 5.6 A biomimetic system of PS II. The Ru complex excited at 532 nm transfers an electron to the electron acceptor  $[\text{Co}(\text{NH}_3)_5\text{Cl}]^{2+}$ . The Ru complex extracts an electron from the Mn complex by way of the phenyl group - half-time  $\sim 30$  ms. The Mn compound is the same compound as the mono- $\mu$ -oxo compound of Chapter 2. [Adapted from Magnuson et al.<sup>38</sup>]

### 5.3 References

- (1) Bossek, U.; Wieghardt, K.; Nuber, B.; Weiss, J. *Inorg. Chim. Acta* **1989**, *165*, 123-129.
- (2) Wieghardt, K.; Bossek, U.; Ventur, D.; Weiss, J. *J. Chem. Soc., Chem. Commun.* **1985**, 347-349.
- (3) Wieghardt, K.; Bossek, U.; Bonvoisin, J.; Beauvillain, P.; Girerd, J.-J.; Nuber, B.; Weiss, J.; Heinze, J. *Angew. Chem., Int. Ed. Engl.* **1986**, *25*, 1030-1031.
- (4) Sheats, J. E.; Czernuszewicz, R. S.; Dismukes, G. C.; Rheingold, A. L.; Petrouleas, V.; Stubbe, J.; Armstrong, W. H.; Beer, R. H.; Lippard, S. J. *J. Am. Chem. Soc.* **1987**, *109*, 1435-1444.
- (5) Wu, F. J.; Kurtz, D. M.; Hagen, K. S.; Nyman, P. D.; Debrunner, P. G.; Vankai, V. *A. Inorg. Chem.* **1990**, *29*, 5174-5183.
- (6) Goodson, P. A.; Hodgson, D. J.; Glerup, J.; Michelsen, K.; Weihe, H. *Inorg. Chim. Acta* **1992**, *197*, 141-147.
- (7) Brewer, K. J.; Calvin, M.; Lumpkin, R. S.; Otvos, J. W.; Spreer, L. O. *Inorg. Chem.* **1989**, *28*, 4446-4451.
- (8) Goodson, P. A.; Hodgson, D. J. *Inorg. Chim. Acta* **1990**, *172*, 49-57.
- (9) Jensen, A. F.; Su, Z. W.; Hansen, N. K.; Larsen, F. K. *Inorg. Chem.* **1995**, *34*, 4244-4252.
- (10) Plaksin, P. M.; Stoufer, R. C.; Mathew, M.; Palenik, G. J. *J. Am. Chem. Soc.* **1972**, *94*, 2121-2122.
- (11) Wilson, C.; Larsen, F. K.; Figgis, B. N. *Acta Crystallogr., Sect. C* **1998**, *54*, 1797-1799.



- (12) Manchanda, R.; Brudvig, G. W.; Degala, S.; Crabtree, R. H. *Inorg. Chem.* **1994**, *33*, 5157-5160.
- (13) Stebler, M.; Ludi, A.; Bürgi, H.-B. *Inorg. Chem* **1986**, *25*, 4743-4750.
- (14) DuBois, J. L.; Mukherjee, P.; Stack, T. D. P.; Hedman, B.; Solomon, E. I.; Hodgson, K. O. *J. Am. Chem. Soc.* **2000**, *122*, 5775-5787.
- (15) Westre, T. E.; Kennepohl, P.; DeWitt, J. G.; Hedman, B.; Hodgson, K. O.; Solomon, E. I. *J. Am. Chem. Soc.* **1997**, *119*, 6297-6314.
- (16) Cramer, S. P.; Degroot, F. M. F.; Ma, Y.; Chen, C. T.; Sette, F.; Kipke, C. A.; Eichhorn, D. M.; Chan, M. K.; Armstrong, W. H.; Libby, E.; Christou, G.; Brooker, S.; McKee, V.; Mullins, O. C.; Fuggle, J. C. *J. Am. Chem. Soc.* **1991**, *113*, 7937-7940.
- (17) Bergmann, U.; Glatzel, P.; Rodriguez, J. H., personal communication about the practical and theoretical aspects of Mn K-edge, L-edge, and RIXS spectroscopy.
- (18) Chu, H.-A.; Hillier, W.; Law, N. A.; Sackett, H.; Haymond, S.; Babcock, G. T. *Biochim. Biophys. Acta* **2000**, *1459*, 528-532.
- (19) Chu, H.-A.; Debus, R. J.; Babcock, G. T. *Biochemistry* **2001**, *40*, 2312-2316.
- (20) Noguchi, T.; Ono, T.-A.; Inoue, Y. *Biochim. Biophys. Acta* **1995**, *1232*, 59-66.
- (21) Noguchi, T.; Sugiura, M. *Biochemistry* **2001**, *40*, 1497-1502.
- (22) Hillier, W.; Babcock, G. T. *Biochemistry* **2001**, *40*, 1503-1509.
- (23) Chu, H.-A.; Hillier, W.; Law, N. A.; Babcock, G. T. *Biochim. Biophys. Acta* **2001**, *1503*, 69-82.

- (24) Fernandez, C.; Cinco, R. M.; Robblee, J. H.; Messinger, J.; Pizarro, S. A.; Sauer, K.; Klein, M. P.; Yachandra, V. K. In *Photosynthesis: Mechanisms and Effects*; Garab, G., Ed.; Kluwer Academic Publishers: Dordrecht, 1998; Vol. 2, pp 1399-1402.
- (25) Hoganson, C. W.; Babcock, G. T. *Science* **1997**, *277*, 1953-1956.
- (26) Vincent, J. B.; Tsai, H. L.; Blackman, A. G.; Wang, S.; Boyd, P. D. W.; Folting, K.; Huffman, J. C.; Lobkovsky, E. B.; Henderickson, D. N.; Christou, G. *J. Am. Chem. Soc.* **1993**, *115*, 12353-12361.
- (27) Wieghardt, K.; Bossek, U.; Zsolnai, L.; Huttner, G.; Blondin, G.; Girerd, J.-J.; Babonneau, F. *J. Chem. Soc., Chem. Commun.* **1987**, 651-653.
- (28) Wieghardt, K.; Bossek, U.; Nuber, B.; Weiss, J.; Bonvoisin, J.; Corbella, M.; Vitols, S. E.; Girerd, J.-J. *J. Am. Chem. Soc.* **1988**, *110*, 7398-7411.
- (29) Armstrong, W. H., personal communication.
- (30) Pal, S.; Armstrong, W. H. *Inorg. Chem.* **1992**, *31*, 5417-5423.
- (31) Aromí, G.; Wemple, M. W.; Aubin, S. J.; Folting, K.; Hendrickson, D. N.; Christou, G. *J. Am. Chem. Soc.* **1998**, *120*, 5850-5851.
- (32) Wang, S.; Tsai, H. L.; Libby, E.; Folting, K.; Streib, W. E.; Hendrickson, D. N.; Christou, G. *Inorg. Chem.* **1996**, *35*, 7578-7589.
- (33) Robblee, J. H.; Messinger, J.; Cinco, R. M.; McFarlane, K. L.; Fernandez, C.; Pizarro, S. A.; Sauer, K.; Yachandra, V. K., manuscript in preparation.
- (34) Liang, W.; Roelofs, T. A.; Cinco, R. M.; Rompel, A.; Latimer, M. J.; Yu, W. O.; Sauer, K.; Klein, M. P.; Yachandra, V. K. *J. Am. Chem. Soc.* **2000**, *122*, 3399-3412.

- (35) Zhang, H. M.; Razeghifard, M. R.; Fischer, G.; Wydrzynski, T. *Biochemistry* **1997**, *36*, 11762-11768.
- (36) Zhang, H.; Fischer, G.; Wydrzynski, T. *Plant Physiol.* **1997**, *114*, 1033-1033.
- (37) Zhang, H. M.; Fischer, G.; Wydrzynski, T. *Biochemistry* **1998**, *37*, 5511-5517.
- (38) Magnuson, A.; Frapart, Y.; Abrahamsson, M.; Horner, O.; Åkermark, B.; Sun, L.; Girerd, J.-J.; Hammarström, L.; Styring, S. *J. Am. Chem. Soc.* **1999**, *121*, 89-96.
- (39) Curtright, A. E.; McCusker, J. K. *The Journal of Physical Chemistry A* **1999**, *103*, 7032-7041.
- (40) Cua, A.; Stewart, D. H.; Reifler, M. J.; Brudvig, G. W.; Bocian, D. F. *J. Am. Chem. Soc.* **2000**, *122*, 2069-2077.
- (41) Kaminaka, S.; Mathies, R. A. *Laser Chem.* **1999**, *19*, 165-168.
- (42) Kim, J. E.; McCamant, D. W.; Zhu, L. Y.; Mathies, R. A. *J. Phys. Chem. B* **2001**, *105*, 1240-1249.
- (43) Kochendoerfer, G. G.; Mathies, R. A. *Isr. J. Chem.* **1995**, *35*, 211-226.
- (44) Zhu, L. Y.; Kim, J.; Mathies, R. A. *J. Raman Spectrosc.* **1999**, *30*, 777-783.